Programa de Doctorado en Química y Tecnologías Químicas. Materiales y Nanotecnología.
Departamento de Química Inorgánica, Cristalografía y Mineralogía.
Facultad de Ciencias, Universidad de Málaga

*"Humidity control inside metallized film capacitors.
Development of design rules for operating under harsh
environmental conditions of high humidity and temperature."*

TESIS DOCTORAL

Azahara Mª Albéndiz García

Dirigida por:
Dr. Enrique Rodríguez Castellón
Dr. David Peláez Millas

Málaga, 2021

UNIVERSIDAD
DE MÁLAGA

AUTOR: Azahara María Albéndiz García

https://orcid.org/0000-0003-4119-246X

HUMIDITY CONTROL INSIDE METALLIZED FILM CAPACITORS. DEVELOPMENT OF DESIGN RULES FOR OPERATING UNDER HARSH ENVIRONMENTAL CONDITIONS OF HIGH HUMIDITY AND TEMPERATURE.

MEMORIA presentada por la Ingeniera Química y Máster Universitario en

Química Avanzada. Preparación y Caracterización de Materiales

Dª Azahara Mª Albéndiz García para aspirar al grado de Doctora en

Ciencias, Sección de Ciencias e Ingeniería de Materiales, con la mención de

"**Doctorado Industrial** "por la Universidad de Málaga

Fdo.: Ms. Sc. Azahara Mª Albéndiz García

Los Directores,

Fdo.:

Dr. D Enrique Rodríguez Castellón

Catedrático de Química Inorgánica

Universidad de Málaga

Fdo.:

Dr. D David Peláez Millas

Director Global de Technology en TDK

Electronics Components, S.A.U.

UNIVERSIDAD DE MÁLAGA

TDK

AUTORIZACIÓN DE LOS DIRECTORES DE TESIS

Enrique Rodríguez Castellón, Catedrático de Química Inorgánica del Departamento de Química Inorgánica, Cristalografía y Mineralogía de la Facultad de Ciencias de la Universidad de Málaga, Y David Peláez Millas, Director Global del grupo Technology de I+D de TDK Electronics Components, S.A.U.

CERTIFICAN:

Que la presente Tesis doctoral titulada "*Humidity control inside metallized film capacitors. Development of design rules for operating under harsh environmental conditions of high humidity and temperature.*" ha sido realizada por Dª. Azahara Mª Albéndiz García bajo nuestra dirección o tutela. Cumpliendo los criterios de idoneidad estipulados en el Reglamento de los Estudios de Doctorado de la Universidad de Málaga, autorizamos su presentación.

Málaga, a 8 de Julio de 2021.

Fdo. Prof. Dr. Enrique Rodríguez Castellón   Fdo. Dr. David Peláez Millas

UNIVERSIDAD DE MÁLAGA

DECLARACIÓN DE AUTORÍA Y ORIGINALIDAD DE LA TESIS PRESENTADA PARA OBTENER EL TÍTULO DE DOCTOR

D./Dña AZAHARA Mª ALBÉNDIZ GARCIA

Estudiante del programa de doctorado QUÍMICA Y TECNOLOGÍAS QUIMICAS, MATERIALES Y NANOTECNOLOGÍA de la Universidad de Málaga, autor/a de la tesis, presentada para la obtención del título de doctor por la Universidad de Málaga, titulada: HUMIDITY CONTROL INSIDE OF METALLIZED FILM CAPACITORS. DEVELOPMENT OF DESIGN RULES FOR OPERATING UNDER HARSH ENVIRONMENTAL CONDITIONS OF HIGH HUMIDITY AND TEMPERATURE.

Realizada bajo la tutorización de ENRIQUE RODRÍGUEZ CASTELLÓN y dirección de ENRIQUE RODRÍGUEZ CASTELLÓN Y DAVID PELÁEZ MILLAS (si tuviera varios directores deberá hacer constar el nombre de todos)

DECLARO QUE:

La tesis presentada es una obra original que no infringe los derechos de propiedad intelectual ni los derechos de propiedad industrial u otros, conforme al ordenamiento jurídico vigente (Real Decreto Legislativo 1/1996, de 12 de abril, por el que se aprueba el texto refundido de la Ley de Propiedad Intelectual, regularizando, aclarando y armonizando las disposiciones legales vigentes sobre la materia), modificado por la Ley 2/2019, de 1 de marzo.

Igualmente asumo, ante a la Universidad de Málaga y ante cualquier otra instancia, la responsabilidad que pudiera derivarse en caso de plagio de contenidos en la tesis presentada, conforme al ordenamiento jurídico vigente.

En Málaga, a 9 de JULIO de 2021

Fdo.: AZAHARA ALBÉNDIZ GARCÍA Doctorando/a	Fdo.: ENRIQUE RODRÍGUEZ CASTELLÓN Tutor/a

Fdo.:

ENRIQUE RODRÍGUEZ CASTELLÓN   DAVID PELÁEZ MILLAS

Director/es de tesis

AGRADECIMIENTOS

Y por supuesto a mis compañeros de batalla en la empresa en los momentos más críticos de esta tesis: gracias Paco Torreblanca porque has sido mi apoyo número 1 en muchas ocasiones en la producción de las muestras definidas de forma tan "mijita", porque no es fácil producir muestras de condensadores con materiales, procesos y configuraciones no estándares y ahí estabas siempre con una sonrisa. Gracias a Bernardo Corpas, por tener siempre actitud y predisposición a que salgan las cosas adelante y hacer que parezca sencillo lo que puede ser un gran reto técnico o logístico cuando se hace sin ganas. Gracias a Tim Li, Luis Li y a Freddy Esteban, por su apoyo en la producción de las muestras del estudio del schoop que se fabricaron en la planta de Zhuhai (China) y a Dr. Märit Djupmyr, Manuel Blasco y Dr. Lucía Cabo por su apoyo en las muestras del estudio del schoop producidas en la planta de Heidenheim (Alemania). Gracias a Fran Barbero, porque le tocó cuando era becario echar muchas fotos para los análisis visuales y hacer montajes de excell que se bloqueaban cada dos por tres. A María Libera por el ingente número de órdenes de producción que tuvo que ayudarme a meter en SAP para las muestras. A Miguel Ángel Atencia y Mari Jose, por tantas medidas en el laboratorio eléctrico. A Pedro Sánchez, a Andrés Toledo, a Domingo, a Dani Botín, por su apoyo en fábrica cada vez que aparecía con una resina nueva y me tocaba hacer pucheretes en la primera etapa.

Indudablemente, mi infinito agradecimiento a mis padres, Paqui y Antonio, por vuestro amor y paciencia, por ayudarme a cultivar y canalizar mi pasión por entender el mundo y por enseñarme con vuestro ejemplo que con humildad, esfuerzo y perseverancia se consigue cualquier reto. Gracias a mis hermanas Sandra y Lucía y a mi cuñado Jorge, por estar siempre ahí.

Gracias a mis amigos y familia en general (de sangre y política), a Mango, mi gran apoyo para gestionar el estrés; y muy especialmente a la bisabuela Felicísima García Martín (Feli), porque ha sido un ejemplo a seguir muchas veces y ha marcado de forma significativa quien soy hoy profesional y personalmente, gracias.

Finalmente, mis gracias infinitas a mi familia maravillosa. A mis hijos Adrián y Lara, porque todavía están en esa etapa maravillosa en la que se les iluminan los ojos de admiración cuando dicen que tienen una madre científica e investigadora, sólo eso ya es motivo suficiente para esforzarse cada día por la Ciencia. Y a mi compañero de vida, a Tomás, porque la tesis es sólo una baldosa más de lo que llevamos andado juntos estos más de 17 años. Gracias por entenderme, acompañarme, sostenerme y cuidarme con tanta paciencia y amor.

Table of Contents

0. RESUMEN

RESUMEN BREVE DE LA TESIS

La industria electrónica requiere que los condensadores de lámina delgada metalizada superen requisitos cada vez más exigentes de ensayos de operación bajo tensión en un ambiente de alta humedad y temperatura. En la presente tesis se lleva a cabo el estudio de los distintos materiales (resina de encapsulado, plásticos inyectados como envase y metal depositado por spray para contactar la bobina) que actúan como barrera frente a la humedad para que ésta no degrade la metalización de la cinta que actúa como electrodo. Así como las distintas interfaces del condensador para garantizar el contacto entre superficies y, por consiguiente, la vida útil del dispositivo bajo las condiciones extremas de calor húmedo. Para la mejora de la adhesión en dichas interfaces, se estudian diferentes tratamientos de limpieza y funcionalización de superficies. Todos los estudios se han abordado tanto a través de la caracterización de los materiales como de los ensayos de operación de los dispositivos. Como consecuencia de dichos estudios, se definen unas reglas de diseño de condensadores de lámina delgada que se recogen en la patente con Nº de Publicación Internacional WO 2019/141388 A1 de la cual Azahara Albéndiz es la inventora principal. Es por ello, que el presente manuscrito recoge sólo los resultados experimentales e interpretación de los mismos del estudio específico del metal depositado por spray y compila como anexos diversas evidencias que demuestran los estudios referentes a los otros materiales e interfaces. El comportamiento de los condensadores obtenido durante la prueba combinada acelerada de temperatura/humedad/tensión (a 305Vac, 85ºC y 85% de humedad relativa) demostró que el cumplimiento de las reglas de diseño permite operar durante al menos 1000h bajo las más estrictas condiciones ambientales perdiendo menos de un 10% de la capacidad inicial.

RESUMEN

Las industrias de electrónica de potencia y de automoción están demandando progresivamente que los condensadores de lámina delgada superen ensayos muy exigentes donde los dispositivos son sometidos a tensión (continua o alterna) bajo un ambiente de alta humedad y temperatura. En los condensadores de cinta, los electrodos están compuestos por capas muy finas de metal, normalmente zinc y/o aluminio, depositadas sobre la superficie de una lámina delgada polimérica. La corrosión electroquímica es uno de los mecanismos de fallo más comunes en estos condensadores debido a la entrada de humedad dentro de los componentes. La entrada de agua puede darse por diferentes mecanismos:

- entrada directa de vapor de agua o humedad condensada a través de los canales o poros presentes en las resinas de encapsulado o debido a la falta de adhesión entre superficies de contacto,

- difusión de vapor de agua a través de las matrices poliméricas que constituyen el material que encapsulan el electrodo del condensador de cinta.

Cuando comienza la corrosión del electrodo, se observa en el condensador una pérdida de capacidad.

Todos los polímeros que constituyen el condensador sufren una degradación por el hecho de estar sometidos a condiciones ambientales. La presencia de cavidades en la interfaz entre la resina de encapsulado y el envase termoplástico, puede conducir a la aparición de grietas debido a la rotura de enlaces por concentración de tensiones mecánicas, creando caminos para la entrada directa de la humedad dentro del condensador. Esto produce la migración de oxígeno (aire) y/o humedad hacia el electrodo interno, iniciándose así el proceso de corrosión.

Los polímeros seleccionados para usarse como aislantes, normalmente se desarrollan para cumplir una serie de requisitos muy exigentes, como pueden ser: presentar una buena procesabilidad, precisas propiedades mecánicas, una alta estabilidad dimensional, que sean inertes químicamente, propiedades no inflamables, buenos conductores térmicos que ayuden a disipar el calor generado por las pérdidas eléctricas, etc, además de funcionar como aislante eléctrico.

La mayoría de los problemas que presentan las resinas de vertido (principalmente poliuretanos o epoxis) están relacionados con los aditivos presentes en su formulación, que migran a la superficie una vez el contacto superficial se ha establecido, causando posteriormente una falta de adhesión en determinados puntos o zonas.

El segundo tipo de material polimérico involucrado en la interfaz envase/resina de encapsulado es el termoplástico inyectado como envase del condensador. La fibra de vidrio se incorpora junto con ingredientes activos a una gran variedad de termoplásticos como el polietileno, polipropileno, poliamidas, cloruro de polivinilo (PVC), etc. En la mayoría de las formulaciones, es necesario el uso de agentes dispersantes o aglomerantes para minimizar las diferencias de polaridad entre los distintos agentes donde pueden juntarse algunos altamente polares con otros no polares. Las poliolefinas son los componentes termoplásticos más atractivos en estos composites debido a sus propiedades y precio. Sin embargo, las reacciones de funcionalización de superficies usadas en las técnicas de química húmeda convencional no son apropiadas por la naturaleza inerte de las poliolefinas. Las tecnologías por plasma son más adecuadas para la funcionalización de este tipo de materiales debido a que los procesos secos se llevan a cabo en un intervalo más amplio de presiones, modificando exclusivamente las capas más superficiales del sustrato expuesto al plasma y, por tanto, dejando inalteradas las propiedades del resto del volumen del material. Además, este tipo de tecnologías son muy eficientes energéticamente.

Asimismo, durante su funcionamiento, los condensadores bobinados se ven sometidos al estrés térmico asociado a los cambios rápidos de temperatura que provocan una pérdida de adhesión entre el envase y la resina de encapsulado, haciendo necesario reforzar dicho contacto por medio de una adhesión química durante el proceso de curado de la resina.

Se pueden usar distintas técnicas de funcionalización de superficies. En la presente tesis, se han estudiado diferentes tipos de plasmas y tratamientos Corona, considerando tanto la funcionalización conseguida como los aspectos económicos y medioambientales. Los dos tratamientos de

funcionalización de superficie que finalmente se seleccionaron y se han aplicado para su estudio experimental y caracterización han sido:

- Plasma generado con oxígeno por microondas a baja presión. Los mecanismos de reacción del gas implican la interacción de especies neutras con especies cargadas creadas en el plasma, incluyendo radicales libres, iones de cada polaridad, electrones y fotones. Estas interacciones crean especies inestables de corta vida en la superficie del polímero que actúan como centros reactivos frente a la resina de encapsulado produciendo fuertes interacciones. El oxígeno es el gas generador de plasma que se ha encontrado lo suficientemente energético como para modificar la energía superficial de los sustratos a tratar pero llevando a cabo una funcionalización no-destructiva de la superficie polimérica. El objetivo es conseguir una reducción del ángulo de contacto con el solvente polar y un aumento de la energía libre superficial para aumentar la adhesión en la interfaz del polímero tratado (envase) y la resina vertida.

- Plasma frío atmosférico. Se han estudiado diferentes tecnologías de plasma atmosférico pero finalmente se seleccionó el sistema Openair® con la tobera de rotación RD1004 y el generador de plasma FG5001 de Plasmatreat GmbH (*Figura 0.1*). El tratamiento se realiza mediante un canal de plasma libre de potencial que sale de la boquilla con cierta inclinación, esto implica que la pieza no está expuesta a alta tensión, por lo tanto, tanto los plásticos (envase y bobina) como el metal (schoop y terminales) pueden tratarse eficazmente con el mismo sistema. El chorro gira y, como consecuencia, el plasma se aplica uniformemente en la superficie de la muestra. El plasma se genera mediante una descarga de alta tensión a presión atmosférica (1kW) en la cámara de reacción del inyector, creando una descarga que sale de la boquilla a gran velocidad sobre la superficie del material a tratar. El gas de trabajo es aire comprimido sin aceite ni agua (2,5 m^3/h) y la rotación del inyector es superior a 2800 r.p.m.. La frecuencia de trabajo del inyector de rotación es de 23 kHz, como la frecuencia de salida de la unidad generadora. Se realizaron diferentes diseños de experimento (DOE de sus siglas en inglés) para definir las condiciones del proceso, siendo la velocidad lineal del soporte con la muestra y la distancia sustrato/plasma, las dos variables estudiadas. En todas las fábricas de TDK Electronics, todas las máquinas de producción de condensadores de cinta trabajan con una velocidad entre 0,5-1,8 m/min, por lo que la velocidad del tratamiento con plasma se definió en 2 m/min para que no fuera una limitación en la producción. Como resultado de los DOE realizados, para la velocidad fijada se definió una distancia muestra/plasma entre 6-10 mm para obtener una energía libre superficial de 75±10 mN/m (por medio del ángulo de contacto tanto con disolvente polar como no polar).

Figura 0.1. Vista general de la instalación del sistema de plasma atmosférico de Plasmatreat GmbH (izda.) y detalle del inyector de rotación Openair® RD1004 (dcha.)

Los tratamientos superficiales de funcionalización se aplicaron a dos tipos diferentes de materiales:

- Materiales poliméricos. A las caras interiores de los envases plásticos para estudiar la adhesión de la interfaz resina/envase.
- Materiales conductores eléctricos. A dos tipos de muestras metálicas diferentes, pero con la misma composición química:
    - Chapas lisas
    - Material rugoso depositado por spray (schoop) como lámina y también en las bobinas con los terminales soldados.

Finalmente, la efectividad de los tratamientos superficiales se comprobó sobre los condensadores en ensayos de operación bajo tensión alterna (AC), con un 85% de humedad relativa a 85ºC de temperatura durante 500 y 1000h en comparación con el comportamiento que mostraron los mismos condensadores en el mismo ensayo pero sin tratamiento plasma y producidos con el proceso estándar.

Durante el proceso de vertido de resina de encapsulado es clave conseguir un contacto óptimo entre el material polimérico del envase y la resina que encapsula el electrodo; y ésta y los terminales y el schoop, porque dichos contactos van a influir de forma determinante en el tiempo de vida del condensador de lámina delgada. Por tanto, debe minimizarse la presencia de cavidades, burbujas y/o falta de contacto en las interfaces cuando posteriormente los dispositivos vayan a ser sometidos bajo condiciones aceleradas de temperatura y humedad.

Considerando todos estos aspectos junto con los efectos que provocan las condiciones ambientales durante la fabricación de los condensadores y en la propia aplicación y el hecho de estar sometidos a tensión eléctrica, los condensadores de lámina delgada metalizada sufren diferentes mecanismos de pérdida de capacidad, normalmente debido a las regeneraciones, que implican la pérdida de área metalizada del electrodo, y debido a su corrosión.

El diseño de un condensador basado en una correcta selección de materiales y teniendo en cuenta la combinación de más de una resina de aislamiento hace posible optimizar su rendimiento en la aplicación; de modo que los mecanismos de pérdida de capacidad que se han descrito puedan reducirse

significativamente, a pesar de intensificarse cuando las condiciones de operación implican un alto estrés térmico y de humedad.

La memoria de esta tesis describe con detalle el estudio llevado a cabo en los distintos materiales metálicos depositados por spray generado con arco eléctrico sobre los laterales de la bobina para llevar a cabo su contacto eléctrico, denominado bajo la terminología *schoop*, justo antes de encapsularlo con la resina dentro del envase plástico (Target 4 descrito en el Capítulo 3).

El resto de estudios y resultados desarrollados bajo los targets 2, 3, 5 y 6 no se han expuesto en detalle en la memoria de tesis por tratarse de los argumentos relevantes y evidencias experimentales que apoyan la publicación de la patente internacional nº WO 2019/141388 A1 (Anexo A) de la cual Azahara Albéndiz es la inventora principal.

Como resultado de dichos estudios, se definieron en TDK Electronics Group unas reglas de diseño interno de condensadores MKP capaces de operar bajo condiciones extremas de humedad. Estas reglas de diseño internas incluyen: la selección del material de envase plástico y de la resina de encapsulado, si es necesaria la combinación de más de un tipo de resina, las distancias mínimas de resina que deben rodear a la bobina en las diferentes zonas para garantizar una baja difusión del vapor de agua a través del material, el diseño mecánico del envase, la necesidad de llevar a cabo tratamientos superficiales para mejorar la adhesión en las distintas interfaces y/o el diseño de los terminales para garantizar el paso (distancia) entre ellos y simultáneamente cumplir el requisito de distancia mínima entre la bobina y el envase plástico, entre otras.

En el estudio del schoop (Target 4) que se detalla en la memoria, todos los ensayos de operación que se han llevado a cabo sobre condensadores completos, éstos se han fabricado de acuerdo a las reglas de diseño definidas y recogidas en la patente internacional (Anexo A).

Asimismo, como evidencia de algunos de los resultados obtenidos durante esta tesis de los objetivos no descritos en detalle en la memoria, las siguientes publicaciones se han adjuntado como anexos al manuscrito.

- ❖ Anexo A. Patente internacional publicada, IP Nr. WO 2019/141388 A1.

- ❖ Anexo B. Artículo en revista de cuartil Q1. Albéndiz García, A., Rodríguez-Castellón, E. and Peláez Millas, D. *Surface modification of thermoplastics by low-pressure microwave O_2 plasma treatment for enhancement of the adhesion of the interface box/encapsulating resin and the influence on film capacitors operating under extreme humidity conditions.* Applied Surface Science 513 (2020) 145764

- ❖ Anexo C. Contribuciones a congresos internacionales, seminarios y/o jornadas:

  - ▪ Anexo C.1. Contribución oral (investigación, validación, redacción y presentación) en el European Polymer Congress EPF celebrado en Dresden (Alemania) en Junio de 2015

bajo el código NANO-P-146 y titulada *Encapsulation of film capacitors for power electronics. Study and characterization of adhesion between polymeric materials*.

- Anexo C.2. Contribución de póster (investigación, validación, redacción y exposición) en el European Polymer Congress EPF celebrado en Dresden (Alemania) en Junio de 2015 bajo el código NANO-P-147 y titulado *Characterization of transport properties of oxygen and water vapor in polymers for the encapsulation of metallized film capacitors as protection against humidity*.

- Anexo C.3. Contribución oral (investigación, validación, redacción y presentación) en el 16th European Conference on Applications of Surface and Interface Analysis (ECASIA'15) celebrado en Granada (Spain) en Septiembre de 2015 bajo el código de sesión oral O7-W-R4-SFWET1 y titulado *Improvement of performance by a low-pressure microwave O_2 plasma treatment in the interface of polymeric encapsulation of film capacitors for power electronics.*

- Anexo C.4. Oral contribution (investigación, validación, redacción y presentación) en el European Center for Power Electronics e.V. (ECPE) Workshop "*Humidity and condensation in Power Electronics Systems – Degradation mechanisms and lifetime modelling*" celebrado en Bremen (Alemania) en Junio de 2019. La session oral llevó por título *Studies on metal spray metallization as humidity barrier in film capacitors*.

- Anexo C.5. Contribución oral (investigación, validación y redacción) en el Seminario organizado por CELCORR (Technical University of Denmark) '*Climatic reliability of Electronics: Global challenges and perspectives*' celebrado en Lyngby (Dinamarca) en Marzo de 2020 bajo el título *Studies on sprayed metal (schoopage) as humidity barrier in film capacitor*.

Todas estas publicaciones son resultado, al menos, de uno de los objetivos de la presente tesis. La *Figura 0.2.* ilustra los resultados indicando qué objetivos han contribuido a las diferentes publicaciones y viceversa, en los resultados de qué estudio están basadas las publicaciones anexadas.
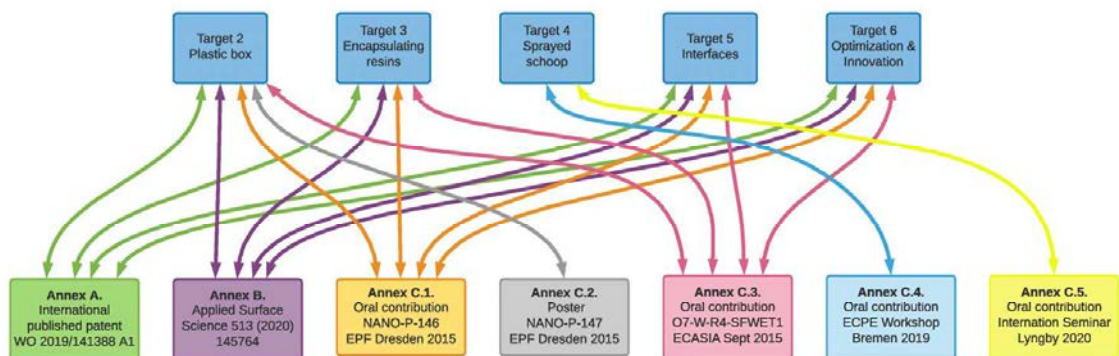
Figura 0.2. Conexiones entre objetivos y publicaciones anexadas en la tesis.

En el estudio del schoop metalizado como barrera frente a la humedad en los condensadores de cinta, se han analizado tres tipos diferentes de muestras:

- Metal depositado por spray como láminas (Figura 0.3.). Este tipo de muestra se ha procesado con la misma técnica (spray generado por arco eléctrico) y bajo las mismas condiciones que las bobinas y/o los condensadores y con los mismos espesores de acuerdo a lo definido para el tipo de condensador MKP seleccionado. Todos los schoops producidos tenían espesores entre 0.2 y 0.5 mm. El ancho y longitud de las láminas no son relevantes, ya que no influyen en las propiedades a caracterizar, ni en la correlación que se quiere establecer con los resultados de los ensayos operacionales sobre los componentes eléctricos. En ese tipo de muestra, todas las caracterizaciones de materiales se han llevado a cabo de acuerdo al esquema de la Figura 0.7.

Figura 0.3. Ejemplo de schoop pulverizado como lámina.

- Bobinas desnudas (Figura 0.4.). Se han llevado a cabo ensayos operacionales sobre bobinas desnudas, sin el encapsulado ni el envase de plástico, con el objetivo de analizar el comportamiento sin la influencia de la interacción con la resina, el envase plástico y/o las mejoras definidas internamente como reglas de diseño. Por medio de las bobinas desnudas, las posibles diferencias de comportamiento que se puedan observar podrán correlacionarse mejor con los mecanismos de envejecimiento de la variable en estudio (los diferentes tipos de schoop) y con los resultados obtenidos en la caracterización de materiales sobre las láminas de schoop.
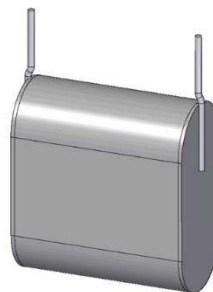
Figura 0.4. Bobina desnuda del tipo de condensador seleccionado.

- Condensadores DC (*Figura 0.5.*). Para el estudio de rendimiento de los condensadores MKP con diferentes schoops se ha seleccionado un condensador supresor de interferencias electromagnéticas (EMI) resistente a la humedad con 6 µF (± 10%) de capacidad, 305 Vrms de tensión nominal, terminales paralelos de 1mm de diámetro estañados y libres de plomo, una versión de 2 pins y con un paso entre terminales de 37.5 mm.
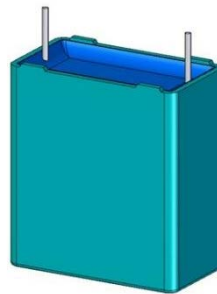
Figura 0.5. Condensador DC seleccionado para el estudio.

Asimismo, el estudio del schoop incluye la caracterización y testeo de las siguientes composiciones y configuraciones de acuerdo al número de capas de schoop depositadas:

- Capa de schoop simple: 100% zinc (Zn)

- Capa de schoop simple: estaño-cobre (3% en peso de cobre) (SnCu3)

- Capa de schoop simple: zinc-aluminio (15% en peso de aluminio) (ZnAl)

- Dos capas combinadas de schoop: una primera capa depositada primero de 100% zinc y una segunda capa, sobre la anterior, de estaño-cobre (3% en peso de cobre) (Zn + SnCu3) (*Figura 0.6. (b)*).
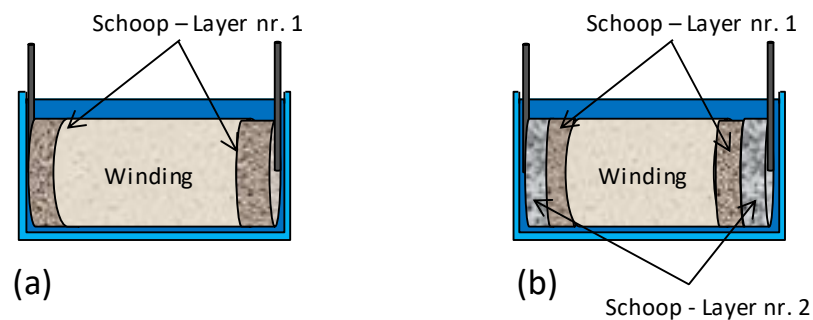
Figura 0.6. Esquema de configuración de schoop con una capa simple (a) o combinación de dos capas (b) (esquema no escalado).

La *Figura 0.7.* muestra las composiciones de schoops que se han empleado tanto en bobinas desnudas como en condensadores, así como también recoge qué técnica de caracterización se ha aplicado a qué composición de schoop depositada como lámina.

Todas las técnicas de caracterización listadas en el esquema se han aplicado a schoops de 100%Zn, SnCu3 y ZnAl depositados como capa única; sin embargo, la variante de Zn + SnCu3 que combina ambas capas, como lámina sólo se ha caracterizado la tasa de transmission de vapor de agua (WVTR de sus siglas en inglés) por ser la única propiedad asociada al espesor completo de la capa y no puede extrapolarse lo obtenido para las capas individuales. Por otro lado, las capas de schoop simples de 100%Zn y ZnAl; y la de Zn + SnCu3 como configuración de capas combinadas se han estudiado en las bobinas desnudas y en los condensadores encapsulados de cinta metalizada. Todas las variantes se han caracterizado antes y después de ser envejecidas durante 1100h a 85ºC y 85% humedad relativa como lámina de material, así como su comportamiento en los componentes eléctricos.
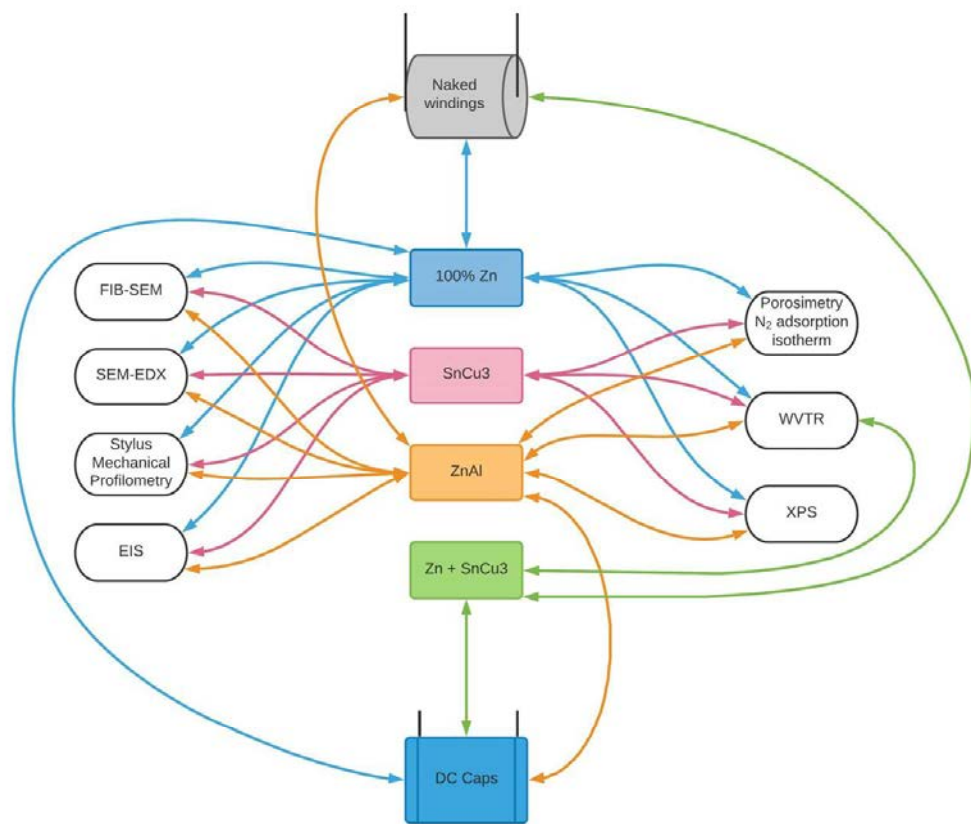
Figura 0.7. Composiciones de schoop vs. tipo de muestra y técnicas de caracterización de materiales aplicadas.

El estudio del schoop como barrera frente a la humedad dentro del condensador se ha abordado por medio de caracterizaciones de materiales para comprender el comportamiento individual del material, el schoop, y a su vez en conjunto considerando las interacciones con el resto de materiales a través del rendimiento de los condensadores.

La Figura 0.7. muestra un diagrama que recopila todas las técnicas de caracterización aplicadas junto con todos los ensayos funcionales y los relaciona con el tipo de muestra sobre el que se ha estudiado.
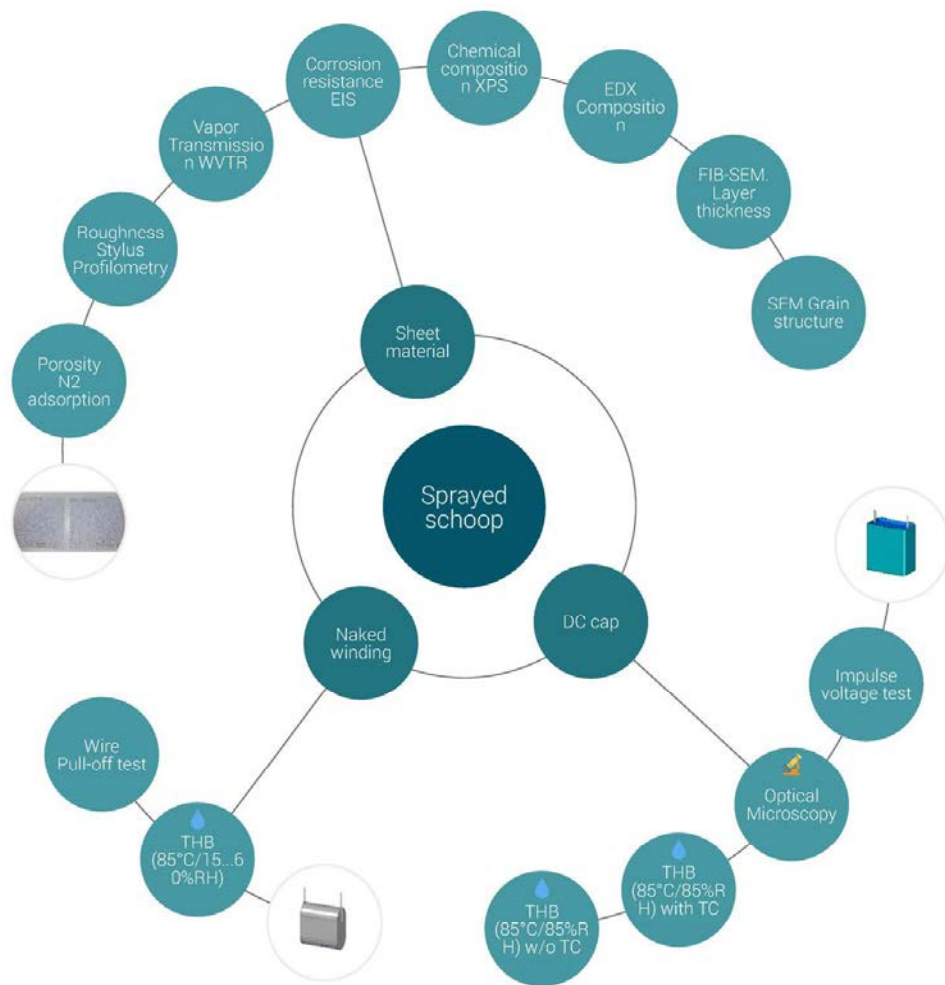
Figura 0.8. Técnicas y ensayos aplicados a cada tipo de muestra para estudiar el schoop.

En las bobinas desnudas se evaluó: (i) la robustez de los terminales a través de un ensayo de tracción y (ii) el ensayo de temperatura/humedad/voltaje (THB de sus siglas en inglés). Mientras que los condensadores fueron sometidos a: (i) ensayo de THB (85°C/85%RH/305V_{rms}) sin ciclos térmicos intermedios, (ii) ensayo de THB (85°C/85%RH/305V_{rms}) con ciclos térmicos intermedios como estrés adicional, (iii) tras los ensayos THB se analizaron las piezas fallo y cada variante de schoop se evaluó por microscopía óptica para confirmar que los espesores depositados estaban dentro de los parámetros definidos por diseño o si diferencias de espesor podían estar influenciando los resultados observados en los ensayos de THB además de la variable de estudio; y (iv) test de pulsos de corriente sobre piezas nuevas.

Como resultado de las caracterizaciones sobre el material se encontró que todos los schoops presentaban un tamaño de poro equivalente y una distribución de ancho de poro entre 25 Å y 2300 Å antes de aplicar ningún programa de envejecimiento. La variante constituida solamente por zinc mostró el doble del volumen total de poros en comparación con los schoops de ZnAl15 y SnCu3; en

cualquier caso, todas las variantes presentaron valores muy bajos de volumen y superficie de poro (~0.0009-0.0018 cm^3/g según el modelo DFT). Una vez aplicado el envejecimiento (1100h a 85ºC y 85% de humedad relativa), todos los schoops redujeron el volumen total de poros y estrecharon la distribución de tamaño de poro a un rango mesoporoso, mostrando un ancho de poro en el rango de los 25 Å y 200 Å. Sin embargo, entre las distintas variantes de schoop no se observaron diferencias en la caracterización de rugosidad superficial (Ra, Rq or Rt) previamente al programa de envejecimiento.

El schoop compuesto por SnCu3 fue el que mostró el menor valor de WVTR. A su vez, el WVTR del schoop de Zn + SnCu3 fue un orden de magnitud menor que los valores de WVTR obtenidos para los schoops de 100%Zn y ZnAl. Tras el programa de envejecimiento, los WVTR de los schoops de 100% Zn y SnCu3 cayeron significativamente, llegando a reducirse dos órdenes de magnitud en el caso del zinc puro. La evolución del WVTR antes y después del envejecimiento va en concordancia con los resultados obtenidos de porosidad.

De la caracterización por EIS se concluyó que en el caso del schoop hecho de ZnAl15, sus medidas de impedancia tras 90 min. de inmersión en el electrolito estaban fundamentalmente controladas por el mecanismo de difusión. Este comportamiento sugería que el schoop de ZnAl15 presentaría la mayor resistencia a la corrosión porque además era la única variante que no mostró transferencia de carga durante todo el tiempo que estuvo inmerso en el electrolito. De cualquier modo, las medidas de impedancia también revelaron que el schoop de ZnAl15 no se pasivaba durante el test de inmersión. Por lo que comparando los resultados obtenidos tras 90 min. y tras 24h de inmersión, se podía concluir que los productos de corrosión del schoop de ZnAl15 estaban aplicando un efecto barrera adicional.

Los resultados obtenidos con EIS de los mecanismos de corrosión y la resistencia a la corrosión para períodos cortos de inmersión en el electrolito (0-3h) concordaron con las diferencias obtenidas de comportamiento en los condensadores en la prueba de THB. Los componentes producidos con schoop de Zn + SnCu3 mostraron la mayor resistencia a la corrosión al presentar la mayor estabilidad tanto en capacidad como en el factor de pérdidas a las dos frecuencias evaluadas (1 y 10 kHz).

Sin embargo, el comportamiento de las bobinas desnudas en la prueba THB (donde el schoop se encuentra expuesto de forma directa al ambiente de humedad extrema) no estuvo de acuerdo a lo esperado considerando los resultados obtenidos de resistencia a la corrosión a tiempos de inmersión altos (24h), donde se esperaba que la variante de bobinas con schoop de Zn + SnCu3 fuera la que presentara la mayor estabilidad en la capacidad y factores de pérdidas (a 1 y 10kHz). De todos modos, se comprobó en el ensayo de tracción, que la unión de los terminales en esta variante era la menos robusta (impactando en el factor de pérdidas durante el test THB) pudiendo afectar de forma significativa en los resultados obtenidos. La fortaleza de la soldadura se debilita con el tiempo, influyendo también ese factor en los resultados obtenidos. Esto demuestra la importancia que tiene en el proceso de producción de los condensadores llevar a cabo el encapsulado de la bobina con la resina en el tiempo definido para ello. Además de todo esto, en la prueba THB de bobinas desnudas, hubo una

gran manipulación de los terminales durante las mediciones intermedias en el test, debilitando mecánicamente así la unión de estos al schoop, especialmente al compuesto de Zn + SnCu3, por ser la única variante hecha por la combinación de dos capas de menor espesor que las otras dos variantes de 100% Zn y ZnAl.

En el caso de los condensadores encapsulados, estos inconvenientes descritos influyeron en mucha menor medida en los resultados gracias a la robustez mecánica que la resina de encapsulado proporciona a la unión terminal/schoop.

En general, del estudio de corte transversal con FIB y su observación por SEM se comprendió que la oxidación natural del schoop hecho de 100% zinc no suponía un debilitamiento de sus propiedades morfológicas y químicas. El porcentaje del área intergranular fue de un 9%. Esta interfaz, en el caso de que durante el proceso de metalización del schoop no se alcance una unión metalúrgica completa entre granos y sólo se dé una unión mecánica, es lo que explica que se dé la trasmisión de vapor de agua (u otros fluidos) a través del schoop en el condensador. El hecho de que durante el proceso de metalización por spray las partículas metálicas lleguen totalmente fundidas al sustrato y no se haya iniciado la solidificación del grano antes de su impacto contra la superficie, es la clave para producir un schoop con la menor área intergranular y que por tanto actúe mejor como barrera para impedir que la humedad (u otros fluidos) alcancen el electrodo.

La oxidación natural del schoop constituido un 85% en peso de zinc y un 15% en peso de aluminio provocó un cambio morfológico importante en el tamaño de la estructura en dicha capa superficial, quien mostraba la misma morfología que el resto del volumen del material pero con menor tamaño. En el corte transversal por FIB se observó muy baja presencia de cavidades, resultando complejo distinguir los poros/cavidades de las zonas oscuras compuestas de aluminio. Las micrografías de SEM sugirieron que el tipo de microestructura, laminar y de islas que se observaba, podría corresponder a la transformación eutectoide a α-Al/β-Zn.

El corte transversal con FIB del schoop de SnCu3 mostró claramente los límites de grano. Se apreciaron bolsas de aire atrapadas entre gotas de cobre de distinto tamaño durante la solidificación del sustrato; sin embargo, no se hallaron grietas intergranulares ni delaminación como causas de fallo mecánico.

Respecto a la caracterización por XPS, se evidenció que la capa superficial de los tres schoops en estudio estaban compuestas químicamente por enlaces CH_2-CH_2, C-O y O-C=O (carboxilatos) asociados a la presencia de contaminantes orgánicos en la superficie que provienen de la atmósfera ambiental y que desaparecen una vez se desbasta los primeros nanómetros de superficie. Además, el schoop de 100% Zn mostró componentes O asociados al oxígeno de la red en el óxido de zinc y también a los enlaces O-H debidos a los grupos hidroxilo o a las moléculas de H_2O absorbidas en la película de óxido.

El schoop de ZnAl15 mostró hidróxidos y óxidos de aluminio en la capa superficial. Sin embargo, 14 minutos de sputtering con iones de argón de 4kV no parecieron suficientes para eliminar por completo

la capa oxidada. Esto puede deberse bien porque la tasa de desbastado sea inferior a la esperada debido a la estructura evidenciada por esta composición de schoop por FIB-SEM; o bien puede deberse a que la capa superficial fuera más gruesa que en los casos de los schoop hechos de 100%Zn y SnCu3.

El análisis XPS del schoop hecho de SnCu3 no registró ninguna señal de la región de Cu $2p$ en la superficie. Además, tras el sputtering se encontraron valores de energía de enlace para el Cu $2p$ similares a los reportados en literatura para el CuO. Por otro lado, se registró el nivel de núcleo de Sn $3d$ y se detectaron dos componentes ($3d_{5/2}$ y $3d_{3/2}$) con picos de doblete de espín-órbita que se asociaron en la capa superficial a Sn^{4+} y Sn^{2+}, mientras que tras el desbastado con iones argón durante 14 min. se atribuyeron principalmente a Sn^0, pero también una pequeña cantidad a Sn^{2+}. Tras bombardear la superficie durante 14 min. se predijo que la composición principal de entre todos los óxidos presentes pareció ser CuO, debido a que la composición atómica detectada para el Cu $2p$ fue de $10,7 \pm 0,7$ % atómico cuando su proporción en el schoop es de un 3% en peso frente al 97% de estaño.

En cuanto a la resistencia de la soldadura, se encontró una gran dispersión en los resultados encontrados en el ensayo de tracción de terminales, siendo el schoop combinado de Zn + SnCu3 la variante que mostró la menor dispersión a pesar de confirmarse ser la más débil de las uniones evaluadas. La unión del terminal con el schoop compuesto por ZnAl fue la más robusta de la comparativa.

Por lo que respecta al comportamiento de las bobinas desnudas en la prueba THB (85ºC/15…60%R.H.), el schoop de Zn + SnCu3 presentó la mayor pérdida de capacidad alcanzando un -32.7% tras 1274h de test; mientras que las otras variantes no habían perdido más de un 10% de capacidad llevando 385h más de test que las bobinas de Zn + SnCu3.

En relación con las pérdidas, éstas se dispararon a partir de las 1500h de ensayo THB (a 85ºC/45% de humedad relativa/305Vac) en las bobinas con schoop de 100% Zn y ZnAl. Ambas pérdidas aumentaron, aquellas relacionadas con el dieléctrico (medición a 1kHz) así como las medidas a 10 kHz y asociadas a los contactos (terminales, schoop, metalización de la cinta que actúa de electrodo…).

Las causas de fallo durante el test en bobinas desnudas fueron: la rotura de terminales en el caso del schoop de Zn + SnCu3, terminales desoldados en el schoop de ZnAl y derretimiento del dieléctrico debido al auto-calentamiento por pérdidas en el schoop de 100% Zn.

Para confirmar el comportamiento de los condensadores encapsulados, se llevaron a cabo análisis dimensionales y visuales con el microscopio óptico. Todos los parámetros evaluados estuvieron en concordancia a las especificaciones definidas tanto de diseño como de proceso.

En el test de pulsos de corriente, todos los condensadores, indistintamente del tipo de schoop que llevaran, mostraron una capacidad estable tras someterlos incluso a 60A/m. Los dispositivos con schoop de Zn + SnCu3 aumentaron el factor pérdidas a ambas frecuencias a los 55A/m. Sin embargo, los condensadores de 100% Zn y de ZnAl aumentaron sus pérdidas dieléctricas (medidas a 1kHz) a los 55A/m pero fue a 60A/m de corriente cuando incrementaron las pérdidas relacionadas a los contactos

(medidas a 10kHz). Por tanto, los contactos de los condensadores hechos con schoops de zinc puro y ZnAl mostraron mayor resistencia a los pulsos de corriente que los que tenían el schoop de Zn + SnCu3.

A pesar de ello, en el ensayo THB (85ºC/85% de humedad relativa/305Vrms) sobre condensadores encapsulados, aquellos que estaban hechos con schoop de Zn + SnCu3 permanecieron tras 1000h de prueba con una gran estabilidad en su capacidad, llegando a perder al final tan solo un -0.9% de su capacidad inicial, en comparación con la pérdida del -4.3% DC/C que mostraron los schoops de ZnAl y 100% Zn. Pero en cuanto al factor de pérdidas, las piezas hechas con schoops de 100% Zn y los de Zn + SnCu3 finalizaron la prueba operacional triplicando su valor inicial del factor de pérdidas medido a 1kHz (energía perdida en polarizar y repolarizar el dieléctrico en dos direcciones opuestas para semiciclos sucesivos de tensión alterna y relacionada con las pérdidas óhmicas) y duplicándolo a 10kHz (suma de resistencias de contacto). En cuanto a los condensadores con schoop de ZnAl, estos dispararon sus factores de pérdidas (1 y 10kHz) tras 750h de ensayo.

Conclusiones

De acuerdo con los objetivos definidos y con los resultados obtenidos y descritos, se concluye que:

- Como resultado de los estudios de la presente tesis se definieron en TDK Electronics Group las reglas de diseño de condensadores de lámina delgada bobinados y encapsulados MKP para poder trabajar bajo condiciones extremas de humedad, dando lugar a la patente internacional publicada bajo el código internacional WO 2019/141388 A1 (Anexo A9) donde Azahara Albéndiz es la inventora principal.

- La memoria de tesis se centra en la descripción en detalle del objetivo que estudia los diferentes materiales metálicos depositados por spray con arco eléctrico en el lateral de la bobina para contactarla, denominado schoop. Los condensadores testeados en pruebas operacionales se produjeron de acuerdo a las reglas de diseño definidas y recogidas en la patente internacional. El comportamiento de dichos condensadores durante la prueba combinada acelerada de temperatura/humedad/tensión (THB de sus siglas inglesas, a 305Vac, 85ºC y 85% de humedad relativa) demostró que el cumplimiento de las reglas de diseño permite operar durante al menos 1000h bajo las más estrictas condiciones ambientales perdiendo menos de un 10% de la capacidad inicial (el peor valor obtenido fue de aproximadamente un 4% de caída de capacidad).

Por todo ello, se considera que los objetivos planteados para esta tesis se han logrado.

1. STATE OF THE ART

1.1.   INTRODUCTION

Power electronic and automotive industries are progressively demanding that film capacitors pass very aggressive tests where devices are submitted to voltage in a harsh humid environment under high temperature. The electrodes on metallized film capacitors are made of very thin layers of metal, usually zinc or aluminum, evaporated onto the surface of a polymeric thin film. Electrochemical corrosion in metallized film capacitors encapsulated with polymeric materials is one of the most common mechanisms of failure due to the water ingress inside the device. This water entry may derive from different mechanisms:

- direct penetration of water vapour or condensed humidity through created channels or pores in the encapsulating materials or due to lack of adhesion between substances at interfaces.

- diffusion of water vapour through the polymeric materials that are encapsulating the capacitor electrode.

A drop in the capacitance of the capacitor is found when corrosion of the electrode begins [1-3].

All the polymers playing the role of insulating materials undergo a slow degradation due to the submitted conditions. The presence of cavities in the interface between the resin of encapsulation and the plastic box may lead to cracks by the breakage of bonds, creating paths for the direct penetration of water vapor inside the device. This generates the migration of oxygen and/or moisture to the electrode, initiating the process of corrosion [4].

The polymers used as encapsulation usually are developed to fulfill good processability, advanced mechanical properties, dimensional stability, chemical inertness, non-flammable properties, etc. in addition to their function as electrical isolator. Most of the adhesion problems in casting resins are usually related to the additives in the formulation of these polyurethane or epoxy resins, which migrate to the surface once the adhesive joint is established, causing further a lack of adhesion [5-7].

The second polymeric material involved in the interface of the joint is thermoplastic injected as a box. Fiberglass and active ingredients have been incorporated into a wide variety of thermoplastics as polyethylene, polypropylene, polyamides, polyvinyl chloride, etc. [8-14]. In most of the formulations, the use of dispersing and/or coupling agents is required to minimize the dissimilar nature of highly polar and nonpolar agents. Polyolefins are the most attractive thermoplastic components in these composites due to their properties and cost. However, surface functionalization reactions using conventional wet chemistry techniques are not adequate due to the chemical inertness of polyolefins. Plasma technologies are most appropriate for the functionalization of this type of materials because dry processes take place over a wide pressure range, altering only the very top layers of the plasma exposed surface and, hence leaving the bulk properties of the substrates unchanged, and they are energy efficient [15-17].

Furthermore, during operation, the devices are submitted to thermal stress due to rapid changes of temperature, leading to a mechanical loss of adhesion between the box and the casting resin that might

be necessary to compensate with an additional chemical adhesion during the curing process. Several techniques of functionalization of surfaces can be used. In this thesis, different plasmas and Corona treatment were studied and characterized in the materials of interest, being the final selected treatment the application of low-pressure microwave plasma with oxygen, considering additionally economic and environmental aspects.

During the process of potting the encapsulating resin, to get an adequate adhesion between the polymeric material of the box and the one that is encapsulating the electrode is a fundamental contributor to the lifetime of the film capacitor. Thus, voids and lack of adhesion should be minimized when the device is submitted to temperature-humidity accelerations [18, 19].

All of these considerations under the effects of an application environment, the ambient working conditions and an applied electric field, are promoting that the metallized film capacitor suffers from various capacitance loss mechanisms typically due to self-healings resulting in a loss of metallized electrode area and its oxidations.

By designing a capacitor with the right selection of materials and considering the combination of more than one insulating resin, it is possible to optimize the performance in such a manner that the above mentioned capacitance loss mechanisms, which may be intensified under high thermal stress, can be significantly reduced.

1.2. METALLIZED FILM CAPACITORS

Fixed capacitors with plastic film dielectrics might be termed with different names: film capacitors, film dielectric capacitors, plastic film capacitors, polymer film capacitors or also FK capacitors due to its acronyms in German.

Film capacitors, together with ceramic and electrolytic capacitors, are the most common capacitor types for use in electronic equipment.

The capacitance (C) of a capacitor is determined by the equation (Equation 1.1.),

$$C = \varepsilon \cdot \frac{A}{t} \qquad \textbf{(Equation 1.1.)}$$

where,

C is the capacitance,

ε is the dielectric constant of the dielectric,

A is the surface of the electrodes, and

t is the thickness of the dielectric.

To obtain the maximum capacitance density is needed to select a dielectric with a high dielectric constant, a large electrode surface area and a thin dielectric.

1.2.1. Classifications of film capacitors

During the early development of film capacitors, some large manufacturers have tried to standardize the names of film materials and film capacitor type.

The characteristics and possible applications of film capacitors are so deeply affected by the dielectric used that capacitors are grouped and designated according to the type of dielectric. Short identification codes for the type of construction, describing the dielectric and the basic technology applied, are defined in standard DIN EN 60062:2005 [20].

The short identification code is prefixed with M if the capacitor is made of metallized films and the last character of the short code indicates the type of dielectric (*Figure 1.1.*):

T for polyethylene terephthalate (PET)

P for polypropylene (PP)

N for polyethylene naphthalate (PEN)
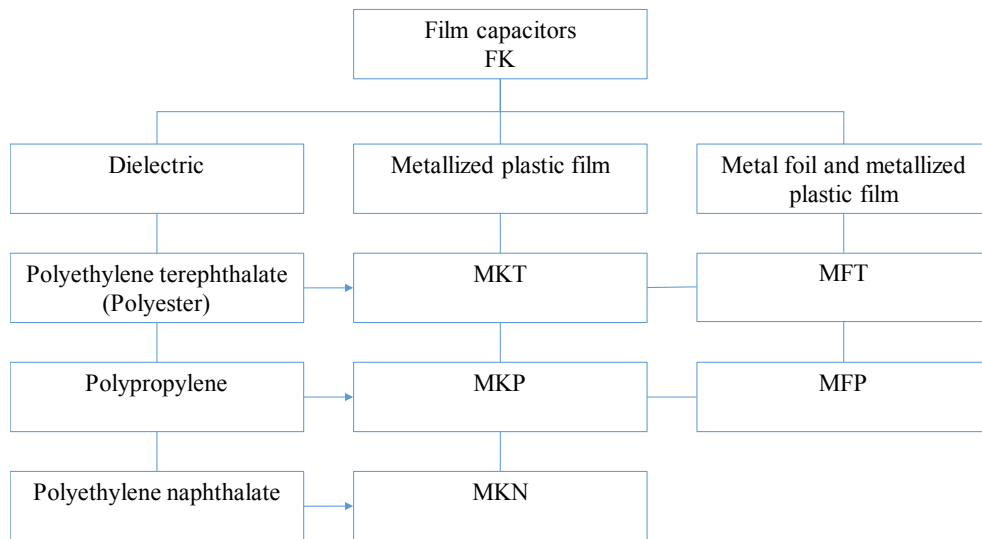
Figure 1.1. Classification of film capacitors according to DIN EN 60062:2005.

1.2.2. Production processes

For a better understanding of the internal construction of film capacitors, Figure 1.2. shows some typical film arrangement.
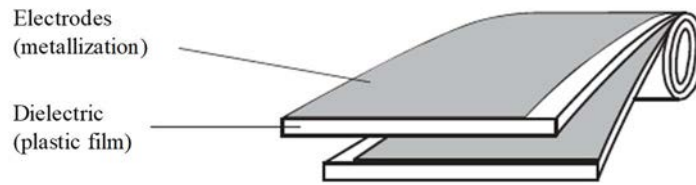
Figure 1.2. Example of typical film arrangement.

In the conventional production process, capacitors are made by individually rolling the metallized films or the film into cylindrical rolls and then covering them with an insulating material (Figure 1.3.) [21].

At TDK Electronics, the MKT, MKP and foil type series production range includes capacitors with space-saving flattened wound bodies with insulating coatings or inside plastic casings, as well as cylindrical wound capacitors. Flat windings are produced by compressing the cylindrical roll before they are placed in casings, so that the casing form is optimally used.
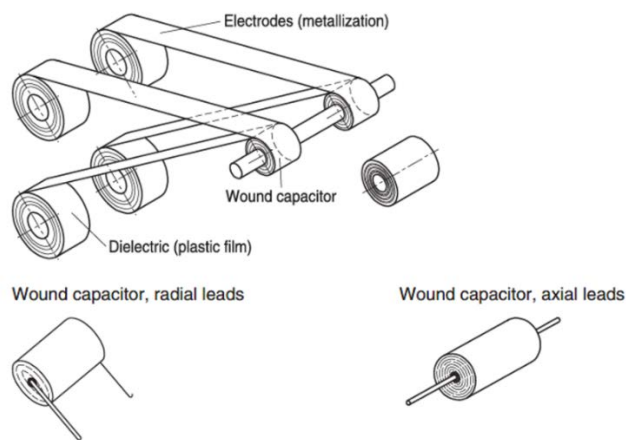
Figure 1.3. Conventional production process in wound technology [20].

In film capacitors, a minimum of two films are wound in parallel to produce a capacitor element (or winding). The electrodes in metallized film capacitors are comprised of very thin layers of metal, usually zinc and/or aluminum, evaporated onto the surface of a polymeric thin film on one side. Aluminum is commonly selected as metal because its general resistance to corrosion due to its surface protective oxide formation, its good bonding to polypropylene, and the ease with which it can be vacuum coated in very thin layers. Typical compositions of metallization containing aluminum are:

- 100% aluminum,
- 10% aluminum and 90% zinc,
- 5% aluminum and 95% zinc,

Being the combined metallization of zinc and aluminum the selected for AC applications.

Each strip has a clear edge without metallization. As *Figure 1.4* shows in the cross section of a cylindrical metallized capacitor winding, the strips are deposited in the manner that each clear edge is at opposite ends of the winding, and the metallizations on both faces either the inner or the outer diameter of the winding. The opposite edge to the clear edge usually has a thicker coating of the same metal than is used in the schoopage, termed a "heavy edge", to provide higher conductivity and robustness for the external connection.

After the two trips are co-wound, a plasma arc (or gas) is used to spray a metallic coating, usually zinc, at each end of the winding. These schooping metallizations selectively connect to the heavy edge of each strip [22]. The free margin prevents simultaneous connection of the complementary strip to the same end as schemed in Figure 1.4. Wires are then soldered or welded to each schoop to provide external connections to the capacitor.
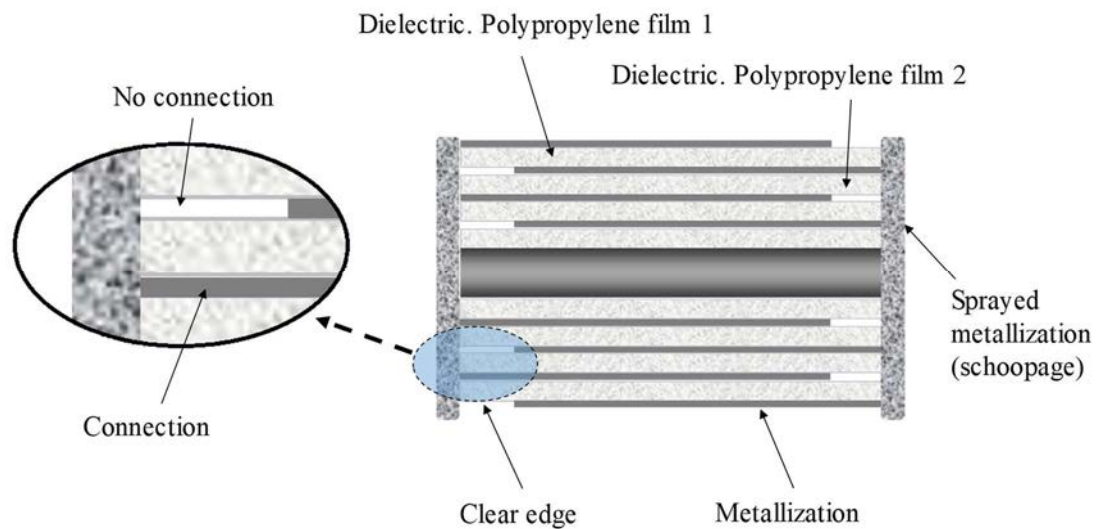
Figure 1.4. Schematic cross section of a cylindrical metallized capacitor winding.

1.2.3. Film capacitor failure modes

Metallized film capacitors mostly fail due to be decreased the capacitance below the required tolerance. This degradation usually takes place after the expected lifetime given by the manufacturer. Additionally, this drop of capacitance uses to be associated to an increase of the loss factor, tan δ.

From a basic point of view, the causes of the capacitor failures are related to bad design, bad processes or unsuitable operation conditions.

During the design stage, the selection of a dielectric film too thin, inappropriate selection of materials to encapsulate the device, too small insulation distances, metallization layer too thick or too thin or a wrong size of the conductor, are typical causes that may lead to failure.

In production process, usual contributors to failure are for example: poor mechanical tension control during winding, bad drying process leaving too high humidity content inside the capacitor, or bad encapsulation. And finally, over-voltages in the application, higher temperature or rapid changes on it and a harsh humid ambient are characteristic root causes of failure on film capacitors during operation in field (Table 1.1.).

Table 1.1. Typical causes of film capacitor failures.

Failure Causes			
Nr.	**Design**	**Process**	**Operation**
1	Mechanical design		
2	Conductor sizing		
3	Film thickness		
4	Insulation distance		
5	Electrode resistance		
6	Material selection		
7		Heat treatment	
8		Compactness	
9		Impregnation	
10			Humidity
11			Thermal cycles/shocks
12			Application design
13			Over-voltages
14			Ripple voltage pulses

In regards to the failure modes, it is not easy to describe them because different causes or the combination between them may lead to the same failure mode as Table 1.2. shows. Furthermore, in Figure 1.5. is schemed a summary of the possible failure modes and effects and consequences which may take place in metallized film capacitors.

Table 1.2. Summary of film capacitor failure modes and possible causes from Table 1.1.

Failure Modes		Causes
Nr.	**Mode**	
1	Mechanical rupture	1, 6 and 11
2	Joule losses	2 and 5
3	Insulation resistance	3 and 7
4	Corona effect	3, 7, 8, 9 and 10
5	Corrosion	6 and 10
6	Partial discharge	10
7	Uncontrolled self-healing	3, 5, 12, 13 and 14

For instance, a poor space factor control during winding process (failure cause nr. 8 in Table 1.1.) will originate the electrode corona demetallization, leading to a faster capacitance decreasing and consequently to the capacitor loss of functionality.

An additional example would be a wrong selection of the encapsulating material (failure cause nr. 6 in Table 1.1.), this may lead to a mechanical rupture in the case of a plastic box and/or a loss of capacitance due to corrosion because a higher diffusion of humidity through the selected polymer (resin or box) to inside the capacitor can be involved. This bad material choice will cause a capacitance loss if the failure is corrosion, finally occurring the function loss of the device.

Furthermore, a bad choice of the metallization resistance value, or poor metallization control during the process (failure cause nr. 5 in Table 1.1.) will lead to a deteriorated self-healing capability, which will mechanically degrade the dielectric film and will generate heat which is conducted locally to the adjacent film layers. At this local point, the dielectric strength of the film falls and breakdown may occur. As consequence, chimneys of melted polypropylene can be created through the winding. This originated channel is conductive, motivating a drop in the insulation resistance and an increase in leakage current which may generate enough heat to melt the dielectric and thus increase the internal pressure of the device. If this effect is combined with a wrong metallization resistance, in the worst case, can lead to an event of fire or even a capacitor explosion.
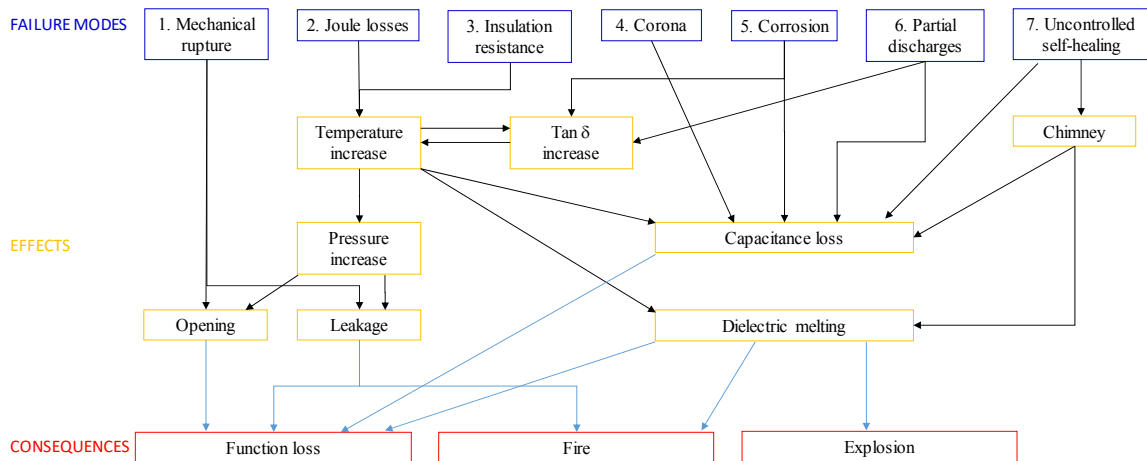
Figure 1.5. Scheme of metallized film capacitors failure modes and their effects and consequences.

The most commonly observed capacitor failure mode is usually originated by high currents, which increase the device temperature, conducting to a reduction of the breakdown voltage and, occasionally, even melting the capacitor. Respect of this failure, the geometry of the capacitor is key. For high power applications, to design short elements to reduce the current path length and increase the number of parallel layers, is very important to minimize the self-heating.

Furthermore, the presence of humidity in the capacitor is one of the most critical causes affecting its right performance, especially if the device is contained in a plastic case. This humidity can proceed due to a poor drying process during the manufacture of the capacitor, or because the moisture permeability of the selected encapsulating material was too high, or due to the relative humidity in the field is too high. Anyway, the presence of humidity leads to three different failure modes with diverse effects and consequences:

- Electrode corrosion. This failure mode slowly increases the series resistance over time, due to the reduction of the electrode thickness and consequently an increase of the loss factor is observed. The rise of temperature catalyzes the capacitance loss due to the decrease of the dielectric strength with temperature, concluding with the loss of functionality of the capacitor.

- Corona effect. This failure mode is due either to a reduction of the dielectric strength of the gas present in the gaps between the dielectric layers in the case of oil-free capacitors, or to a bad space factor control of the films. The larger the gap, the worse the malfunction. The space factor characterizes the gap thickness, but this is very difficult to control in curves of flat windings. Only winding machines can reach a right space factor control by means of the mechanical tension control of the films during the winding process.

- Reduction of insulation resistance (parallel resistance of the capacitor). A decrease in insulation resistance involves an increase of the leakage current from one electrode to the other because of the presence of water dipoles. This effect is observed at low frequencies, and it may be measured by either the capacitor loss factor (tan δ) or the DC resistance, R_p (as defined in Section 1.2.4.1. and Equation 1.11). This failure mode may involve a chain reaction. The reduction of the insulation resistance generates heat, and the more the temperature rises, the more the insulation is decreased. This phenomenon may lead to the appearance of chimneys and the final melting of the dielectric.

Moreover, the failure modes of film capacitors can be classified by its circuit electrical answer. According to this criterion, Table 1.3. makes a compilation of possible failure mechanisms resulting on these failure modes [25].

Table 1.3. Possible causes of the main failure modes of film/foil capacitors.

Failure mode	Possible failure mechanisms
Open circuit	1. Broken encapsulating resin (epoxy or polyurethane) and corrosion.
	2. End-termination damage.
	3. Lead-attach damage
	4. Fusing of the interface between the electrode and termination, when the current flow in the capacitor is too large for the electrode thickness.
	5. High AC ripple current, when the bond between the electrodes and the device termination is poor enough that its resistance is exceptionally high.
Short circuit	1.Weakening of film dielectric with time and temperature exposure, the dielectrics being sensitive to defects in the film (cracks, pinholes, wrinkles, contamination).
	2. Caught moisture, resulting dielectric degradation.
	3. Overvoltage punch-through.
	4. Ionic contamination on the body
	5. Electrode-spacing change.
Winding resistance and quality factor outside the specification tolerance	Corrosion of the wire may lead to failure by parameter drift. It is possible for turns severely damaged by corrosion due to continuity still exists by an electrically conductive path through the corrosion products.

1.2.4. Electrical characteristics

1.2.4.1. Equivalent circuit diagram

Any real capacitor can be modeled by its equivalent circuits (Figure 1.6.).
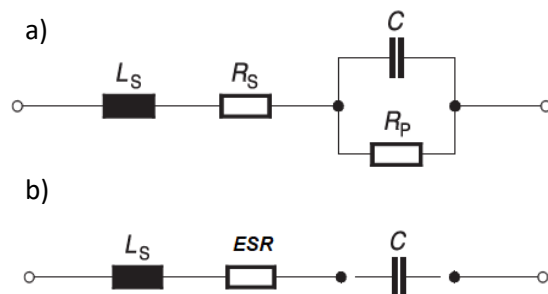
Figure 1.6. Diagram of complete (a) and simplified (b) equivalent circuit of a capacitor [21].

where,

L_s is the series inductance,

R_s is the series resistance

R_p is the parallel resistance,

ESR is the equivalent series resistance, and

C is the capacitance.

The capacitance, the series resistance and series inductance are magnitudes that vary in the frequency domain (AC). The series resistance in a film capacitor is due to the contacts as it can be leads, sprayed metal (schoop), connecting strips and film metallization. However, the parallel resistance is a magnitude defined in DC and is produced by the insulation resistance of the dielectric.

In the simplified equivalent circuit, ESR is representing the total active power in the capacitor.

1.2.4.2. Capacitance

Capacitance is the amount of electrically charged carriers that a capacitor can store per unit of voltage. The rated capacitance (C_R) of a capacitor is the value for which it is designed. Capacitance is measured under standard conditions to IEC 60068-1:2013 (Table 1.4.). Prior to being measured, a capacitor must be stored under measuring conditions until the complete capacitor has reached the measuring temperature and humidity.

Table 1.4. Reference conditions defined in IEC 60068-1:2013 [24].

Measuring conditions	Standard conditions	Referee conditions
Temperature	15-35 ºC	(23$\pm$1) ºC
Relative humidity	45-75 % RH	(50 $\pm$2) % RH
Ambient atmospheric pressure	86-106 kPa	86-106 kPa

The capacitance tolerance is the permissible relative deviation of the real capacitance from the rated value, expressed in percent. The measuring conditions are the same as for the rated capacitance.

Capacitance will undergo a reversible change within a range of temperature between the upper and lower category temperatures. The gradient of the capacitance/temperature curve is given by the temperature coefficient α_c of the capacitance, which is defined as the average capacitance change, in relation to the capacitance measured at (20 $\pm$ 2) ºC,

occurring within the temperature range T_1 to T_2. It is expressed in units of 10^{-6}/K (Equation 1.2.).

$$\alpha_C = \frac{C_2 - C_1}{C_1 \cdot (T_2 - T_1)} \qquad \textbf{(Equation 1.2.)}$$

being,

C_1 the capacitance measured at temperature T_1,

C_2 the capacitance measured at temperature T_2, and

C_3 the reference capacitance measured at (20 ± 2) ºC.

The temperature coefficient is basically determined by the properties of the dielectric, the capacitor construction and the process parameters. Polypropylene capacitors have negative temperature coefficients, whilst polyester capacitors present positive temperature coefficients (Table 1.5.) [21].

Table 1.5. Temperature coefficient of different polymeric dielectrics.

Dielectric		PP	PET	PEN
Temperature coefficient α_c	10^{-6}/K	-250	+600	+200

Furthermore, **reversible changes** of capacitance with temperature are usually expressed as $\Delta C/C$. Figure 1.7 shows typical temperature characteristics of different capacitor styles.
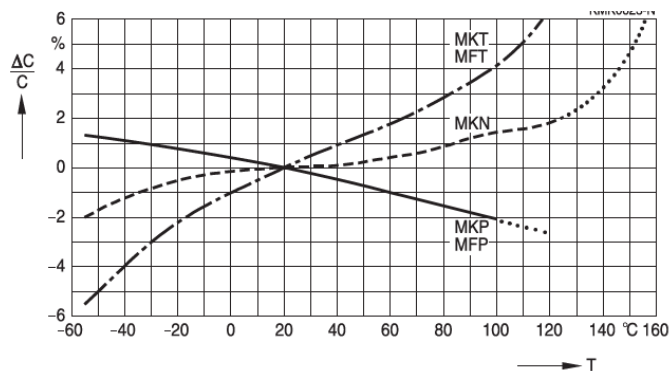
Figure 1.7. Relative capacitance change $\Delta C/C$ vs. temperature T (typical values) [21].

However, when the capacitor is submitted to a temperature cycle from the reference temperature to T_{min}, then up to T_{max} and back to the reference temperature, a small

irreversible change may be observed between the initial and the final capacitance (Figure 1.8.) [21]. This deviation is denominated temperature cyclic capacitance drift, and is expressed as a percentage of the reference capacitance. For film capacitors it is usually very small.
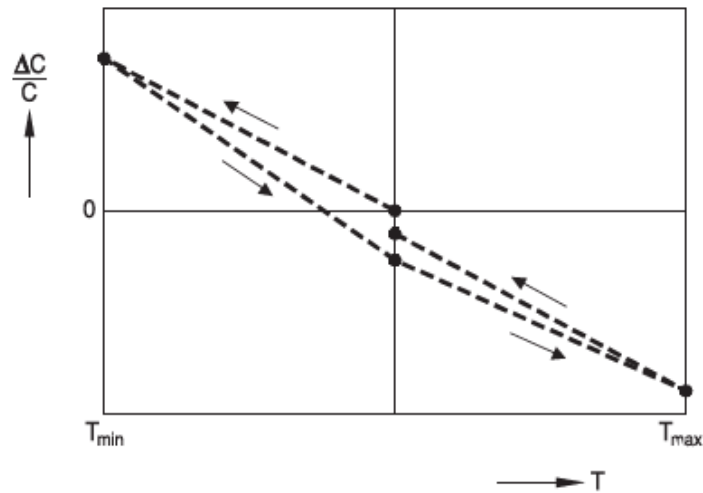
Figure 1.8. Capacitance change ΔC/C vs. temperature T (schematic curve).

In addition, when film capacitors are uncoated, it should be considered that when measurements are carried out, every temperature change is accompanied by a relative humidity change, which will influence the measurement. However, if those are performed under standard conditions and the temperature cycles are not too long, the changes affected by humidity variations remain within the limits specified for α_c.

The capacitance of a polymeric film capacitor will endure a reversible change of value related to any modification in ambient humidity. In function of the type of capacitor design, both the dielectric and the effective air gap between films will respond to changes in the ambient humidity, which will then influence the measured capacitance.

The humidity coefficient β_c is defined as the relative capacitance change measured for a 1% change in humidity, being constant the temperature (Equation 1.3.).

$$\beta_C = \frac{2 \cdot (C_2 - C_1)}{(C_2 + C_1) \cdot (F_2 - F_1)}$$ **(Equation 1.3.)**

being,

C_1 the capacitance measured at relative humidity F_1,

C_2 the capacitance measured at relative humidity F_2.

Table 1.6. Humidity coefficient β_c of different polymeric dielectrics [21].

Dielectric		PP	PET	PEN
Humidity coefficient β_c (50 … 95 %RH)	10^{-6}/% R.H.	40-100	500-700	700-900

The values of humidity coefficient β_c shown in Table 1.6. are valid in the range of a relative humidity of 50% to 95%. At relative humidity below 30%, the humidity coefficient is relatively low. Wide changes are expected to be found when relative humidity above 85%.

Typical characteristics of capacitance/humidity in capacitors based on different plastic dielectrics are plotted in Figure 1.9.
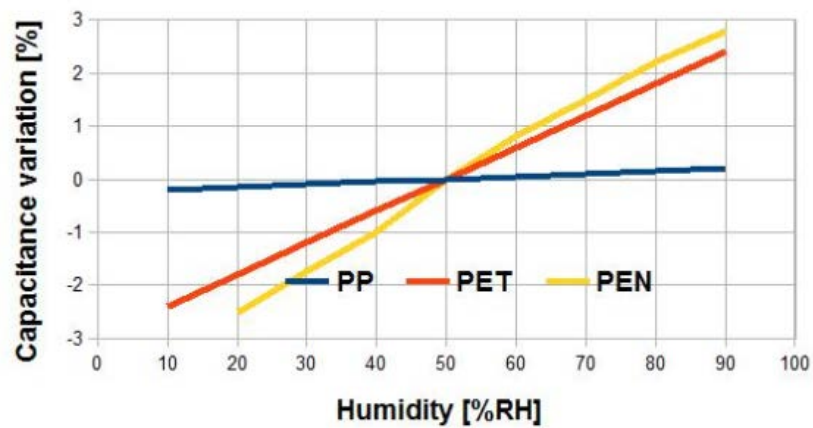
Figure 1.9. Relative capacitance/variation, DC/C, vs. relative humidity (%RH) (typical values).

Irreversible effects in film capacitors will be discussed in section 1.2.6.

1.2.4.3. ESR and dissipation factor

For a film capacitor submitted to a given AC voltage signal of determined frequency, as discussed in section 1.2.4.1., the equivalent circuit diagram can be simplified to a series connection of the capacitance C, an equivalent series resistance (ESR) and the series inductance L_s.
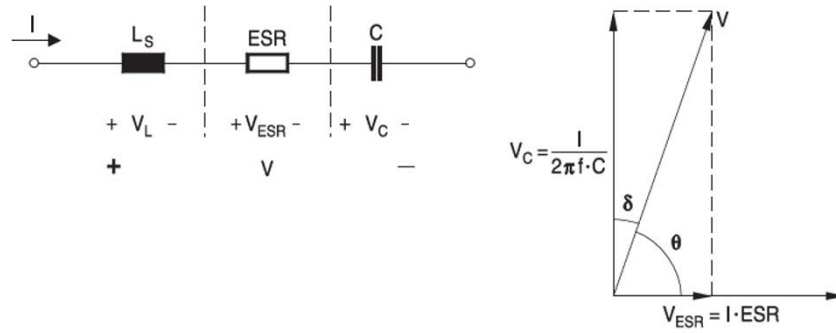
Figure 1.10. Simplified capacitor model AC. Complex voltage calculation.

L_s, V_L are very small when the frequencies are significantly below the natural resonant frequency. The phase variation between current and voltage is slightly less than 90º due to the equivalent series resistance. The shift from 90º to the phase angle θ is the defect angle δ, measured by means of the dissipation factor $\tan \delta$, for instance the ratio of ESR to the capacitive reactance X_c,

$$X_C = \frac{1}{2}\pi f \cdot C \quad (Equation\ 1.4.)$$

$$\tan \delta = ESR \cdot 2\pi f \cdot C \quad (Equation\ 1.5.)$$

Then, it can be concluded that dissipation factor is also the rate of effective power (i.e. power dissipation) to reactive power. Power dissipation is a function of the voltage through the equivalent series resistance (V_{ESR}) or the current I across it:

$$P = \frac{V_{ESR}^2}{ESR} = ESR \cdot I^2 \quad (Equation\ 1.6.)$$

Since,

$$V_{ESR}^2 = \frac{ESR^2}{ESR^2 + (\frac{1}{2\pi f \cdot C})^2} \cdot V^2 \quad (Equation\ 1.7.)$$

In the case of film capacitors $\tan \delta = 2\pi f \cdot C \cdot ESR \ll 0.1$, thus,

$$V_{ESR}^2 = ESR^2 \cdot (2\pi f \cdot C)^2 \cdot V^2 \quad (Equation\ 1.8.)$$

The power can be expressed as:

P = 2πf · C · tan δ · V² or P = (2πf · C)² · ESR · V² (Equation 1.9.)

The power dissipation of a capacitor, then also its self-heating, is defined by both ESR and tan δ.

Generic standards define the same measuring conditions for dissipation factor tan δ as for capacitance (paragraph 1.2.4.2.).

If the inductance L_s is considered to be negligible for frequencies well below the natural resonant frequency, the dissipation factor tan δ is considered a combination of a parallel component tan $δ_P$, a series component tan $δ_S$ and a dielectric component tan $δ_D$ that it is a characteristic of the dielectric:

$$\tan δ = \tan δ_P + \tan δ_S + \tan δ_D \qquad (\text{Equation } 1.10.)$$

$$\tan δ_P = \frac{1}{R_P \cdot 2\pi f \cdot C} \qquad (\text{Equation } 1.11.)$$

$$\tan δ_S = R_S \cdot 2\pi f \cdot C \qquad (\text{Equation } 1.12.)$$

The insulation resistance (parallel resistor R_P in Figure X) influences the **parallel component tan $δ_P$**. As the insulation resistance is extremely high, this component can be considered negligible in the complete frequency range.

The **dielectric component tan $δ_D$** measures the losses related to the dielectric, as it can be the energy wasted under AC voltage for successive half-cycles to polarize and repolarize the dielectric in two opposite directions. This component determines self-heating at low frequencies (at 1kHz). In polypropylene film capacitors, tan $δ_D$ stays without variations with frequency and typically shows a value of approximately 10^{-4}. However, in polyester film capacitors, tan $δ_D$ is much higher and grows with frequency.

The **series component tan $δ_S$** is defined by the series resistance (R_S in Figure X), which compiles every contact resistances and the resistances of leads, schoopage and electrode. This component is highly influenced by frequency and also increases with capacitance.

For film capacitors with polypropylene dielectric, the dissipation factor is broadly unaffected by temperature changes; however, polyester capacitors show at approximately 80ºC (at 1kHz) a minimum characteristic dissipation factor (Figure 1.11.) [21].
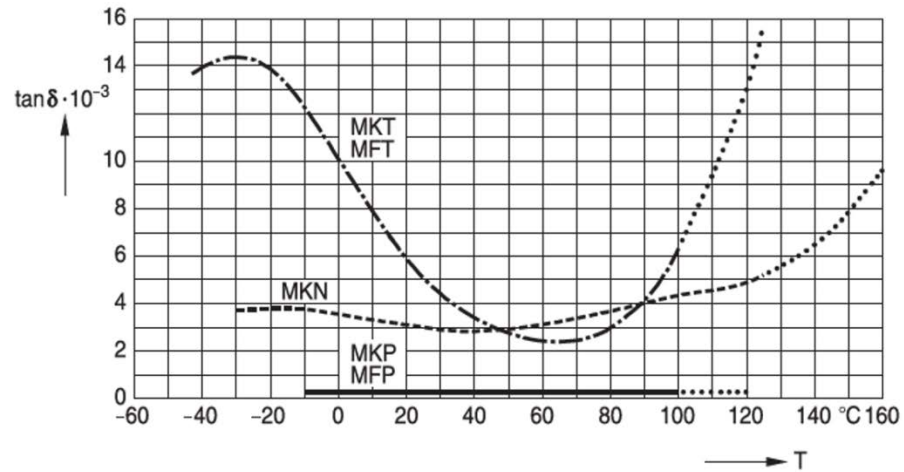
Figure 1.11. Dissipation factor tan δ vs. temperature T for 1kHz (typical values).

Under normal operation range, the variation of dissipation factor is negligible with voltage, but it may increase as well under humid conditions do it.

On the other hand, since ESR can be defined as:

$$ESR = \frac{\tan \delta}{2\pi f \cdot C} \quad (Equation\ 1.14.)$$

Then ESR compiles all the phenomena, just defined for the dissipation factor that can provide resistivity.

In general, at very low frequencies, the leakage will be prevalent and, at low frequencies, the dielectric losses are the most important part of ESR, but these losses show an inversely proportional decrease with respect to frequency. At medium to high frequencies, ESR will vary poorly because losses are mainly due to ohmic losses in the conductors (electrode, sprayed metal layers and leads), R_S. At very high frequencies the losses increase due to the skin effect in the conductors.

1.2.4.4. Insulation resistance (R_{iso})

Under a stationary DC voltage, a leakage current flows across the dielectric and over the capacitor surfaces. The measurement of a capacitor resistivity in DC is denominated insulation resistance, R_{iso}. Its measurement is determined by the ratio of the applied DC voltage to the consequent leakage current flowing through the capacitor, once the initial charging current has concluded (this usually occurs after 1min ± 5s).

For fixed film capacitors for use in electronic equipment, the measuring voltage is specified in the standard IEC 60384-1:2016 [26] and is a function of the rated voltage.

The specified measuring temperature is 20ºC. Since insulation resistance is affected by temperature, at any other temperature, a correction multiplying the measured value by the specific correction factor should be made to get the equivalent result for 20ºC (Table 1.7.) [21].

Table 1.7. Correction factors vs measuring temperatures for different capacitors.

Measuring temperature (ºC)	Correction factors (average values) according to the sectional specification		
	MKT, MFT	MKN	MKP, MFP
15	0.79	0.79	0.75
20	1.00	1.00	1.00
23	1.15	1.15	1.25
27	1.38	1.38	1.50
30	1.59	1.59	1.75
35	2.00	2.00	2.00

Usually a referee measurement at 20ºC and (50 ± 2) % RH is conducted to confirm.

Insulation resistance is also affected substantially by humidity in an inverse relation: insulation resistance decreases as humidity increases.

1.2.4.5. Self-inductance

The series inductance L_S or self-inductance of a film capacitor is produced by the magnetic field created by the current in the film metallization and the connections. Therefore, in fixed film capacitors for use in electronic equipment, the winding structure, the design geometry and the length and thickness of the contact paths will determine L_S. Because of the special kind of contacting in self-healing capacitors, a large area metal spraying covering all windings, the self-inductance is particularly low. The resonant frequency is accordingly high for all capacitors. In addition to be calculated from the resonant frequency, for MKP capacitors there is a general rule of estimating L_S with a maximum value of 1nH per mm of lead length and capacitor length.

1.2.4.6. Impedance and resonant frequency

The impedance Z depicts the component's opposition to the current flow and is both resistive and reactive character. Then, it is especially important in AC and ripple current filtering.

According to the capacitor model schematized in Figure 1.10, Z is defined as the magnitude of the vector sum of the total reactance (inductive reactance X_L minus capacitive reactance X_C) and ESR (equations 1.15. and 1.16.).

$$Z = \sqrt{ESR^2 + (2\pi f \cdot L_S - \frac{1}{2\pi f \cdot C})^2} \quad (Equation\ 1.15)$$

$$Z = \sqrt{ESR^2 + (X_L + X_C)^2} \quad (Equation\ 1.16.)$$

As plotted in Figure 1.12., Z is strongly frequency dependent:
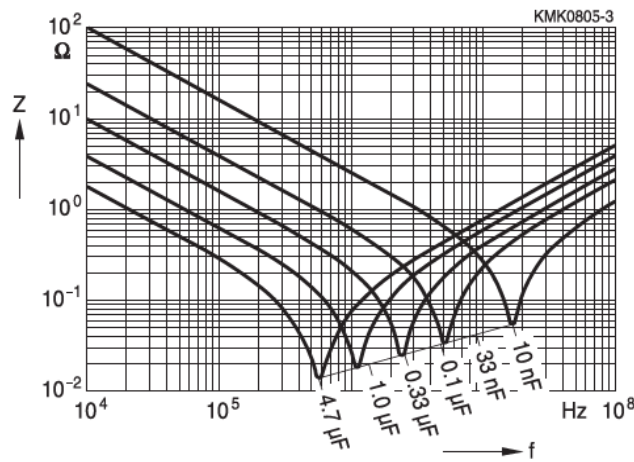
Figure 1.12. Typical impedance characteristics of film capacitors [21].

For low frequencies, capacitive reactance, X_C, predominates, whilst at very high frequencies the inductive reactance, X_L, prevails. The natural resonant frequency is the frequency at which the capacitive reactance equals to inductive reactance and natural resonance takes place (Equation 1.17.). At this frequency impedance is equivalent to ESR due to reactances cancel each other out.

$$2\pi f_{res} \cdot L_S = \frac{1}{2\pi f_{res} \cdot C} \rightarrow f_{res} = \frac{1}{2\pi\sqrt{L_s C}} \quad (Equation\ 1.17.)$$

1.2.5. Operation

DC voltage for which a capacitor is designed is termed as rated voltage, V_R. It is defined as the maximum DC voltage at which the capacitor terminals can be submitted in continuous at any temperature between

the lower category temperature T_{min} and the rated temperature T_R. V_R is influenced by the dielectric material and the film thickness.

During the final capacitor inspection in production, the device is submitted to a DC test voltage (100% electrical inspection). Every capacitor type has defined a value and an application time according to IEC 60384-1:2016, section 4.6 [26]. This is also applicable to the qualification approval test with a duration of 60 s and to lot by lot quality compliance inspection for 2 s of duration.

The category temperature range of a capacitor defines the upper and lower category temperatures (T_{min} and T_{max}) at which a capacitor can operate within this range continuously.

Within this range, there is a rated temperature T_R defined as the maximum ambient temperature at which a capacitor can continuously operate under the rated voltage V_R. It is a function of the dielectric material (Table 1.8.).

Table 1.8. Rated temperature values for different dielectric materials.

Dielectric	T_R
Polyester (PET), Polypropylene (PP)	85 ºC
Polyethylene naphthalate (PEN)	125 ºC

On further consideration, the maximum voltage that may be applied to a capacitor in continuous for a given temperature defines the category voltage V_C (Figure 1.13.).
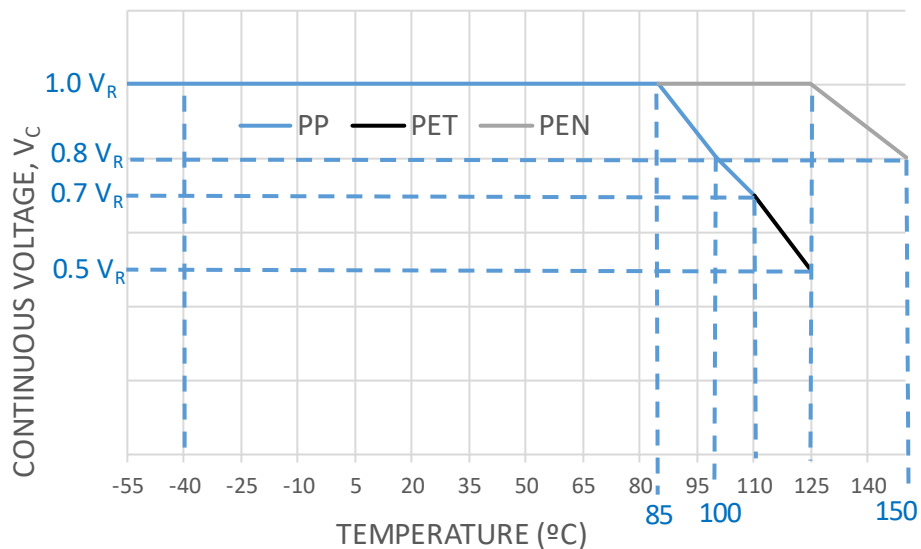

Figure 1.13. Maximum permissible continuous voltage vs. temperature.

Within the lower category temperature T_{min} and the rated temperature T_R, the maximum continuous voltage is the rated voltage, V_R. Whilst between the rated temperature T_R and the upper category

temperature Tmax, to apply a derating factor is necessary. Typically for PET and PP this will be 1.25% per ºC and for PEN 0.8% per ºC [21].

On the other hand, the rated AC voltage, V_{RMS}, is the maximum RMS voltage at specified frequency, usually 50Hz, at which a capacitor can continuously operate at any temperature within the rated temperature T_R and the lower category temperature T_{min}.

The capability of a capacitor to endure a continuous (sine-wave) alternating voltage load V_{RMS} or alternating current I_{RMS} is defined by the frequency and is constrained by 3 different factors (Figure 1.14.):

- **Region (a).** Limit at which corona discharge starts to occur VCD. Below a certain frequency limit f_1, the applied AC voltage should not pass the threshold voltage VCD at which corona discharge would be initiated in air gaps in the capacitor. It may degrade the film metallization and sporadically endanger its dielectric strength.

- **Region (b).** Limit due to thermal power dissipation. Higher than a given frequency limit f_1 to keep the power generated in the capacitor element (P_{gen}) below the power that its surface is able to dissipate (P_{diss}), then the permissible alternating voltage load must be decreased with increasing frequency.

  $P_{gen} < P_{diss}$

  These powers are defined as:

  $P_{gen} = V^2_{RMS} \cdot 2\pi f \cdot C \cdot \tan\delta$ (Equation 1.18.)

  $P_{diss} = \alpha \cdot A \cdot \Delta T$ (Equation 1.19.)

  where,

  α is the heat transfer coefficient,

  ΔT is the self-heating or at the hottest part of the capacitor surface, the stabilized and kept over-temperature in relation to the surrounding ambient, and

  A is the surface area of the capacitor element.

- **Region (c).** Limit due to maximum current handling capability. Higher than other frequency limit f_2, the permissible AC voltage load is restricted by the maximum current I_C than can pass through the connection between sprayed metal and film metallization, without generating overheating due to resistive losses related. This region, in practice, is only presented by mall capacitors with short contact lengths.
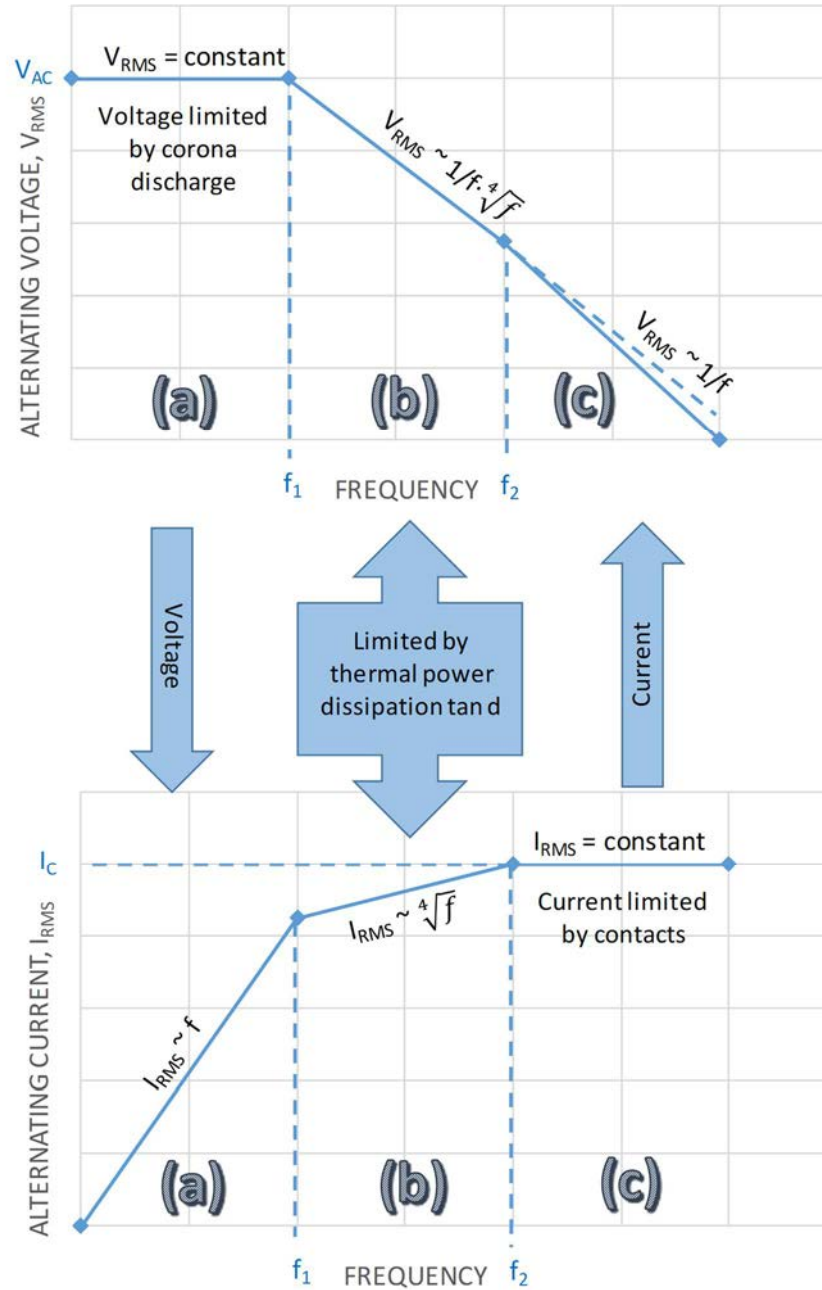
Figure 1.14. Alternating voltage and alternating current load limits.

Furthermore, during operation, a key characteristic to be taken into consideration is that the capacitor should be pulse withstanding. Voltage pulses together with rapid voltage changes incite strong peak currents in a capacitor. These currents create heat in the contact regions between the sprayed metal and the electrode (film metallization). Therefore, the pulse that can be applied to a specific capacitor must be limited to keep the heat dissipated below the maximum permissible that will damage these regions.

The parameters that define the pulse handling capability of a capacitor are:

- the maximum voltage pulse slope, dV/dt and

- pulse characteristic k_0, characteristic factor of a pulse wave-form, providing its energy content. The maximum permissible k_0 defines the capability of a capacitor to withstand pulses involving several current peaks.

1.2.6. Climatic stress

1.2.6.1. Climatic category

According to the standard IEC 60068-1:2013, Appendix A, the climatic category of a capacitor is specified by three values separated by slashes, $T_{min}/T_{max}/Duration$, for example:

55/100/56, where,

-55ºC would be the absolute value of the lower category temperature T_{min}. This is the minimum ambient temperature for which a capacitor is designed to run continuously.

100ºC would be the upper category temperature T_{max}. A capacitor is designed to operate in continuous at this maximum ambient temperature. In addition, T_{max} is the temperature for test Ba (dry heat) defined at IEC 60068-2-2:2007. For capacitors operating under AC, the specific self-heating will increase its surface temperature above the ambient one. It is crucial to consider this in order to not exceed the upper category temperature.

56 days would be the longest duration in days of test Ca (damp heat, steady state) to IEC 60068-2-78:2001. The most severe test conditions are (93 +2/-3) %RH and 40ºC as ambient temperature [29].

1.2.6.2. Effect of temperature

This section addressed the irreversible effects on electrical characteristics produced by an excessive exposure to temperatures above T_{max}. This will lead to a thermal aging on the film according to the Arrhenius' law. In addition, dimensional changes in the capacitor will be caused by the film shrinkage.

1.2.6.3. Effect of Humidity

The number of permanent dipoles inside the capacitor is increased by the absorption of moisture, producing reversible effects on electrical characteristics as described in previous sections. These can be reversed by a drying process when occurred for a relative humidity lower than 93%RH for a limited time.

These reversible changes are unassociated with construction and finish capacitor, it is only due to the differences in the rate of moisture absorption/desorption, which will be determined by:

- Capacitor finish. Moisture will penetrate and diffuse faster into uncoated components than into coated ones.
- Ambient temperature, and

- Humidity.

Typical values of time for humidity absorption/desorption fluctuate between 12h, in uncoated capacitors, and several weeks in capacitors with plastic cases.

Regarding irreversible effects, these will be caused by a long contact between the film capacitor and humidity. Film metallization is ultimately removed and then destroyed the capacitor when occur:

- Direct contact with liquid water, especially in uncoated capacitors,
- Excess exposure to a high ambient humidity, and/or
- Condensation.

For film capacitors operating under AC, if these causes occur, the effect is observed with a brief contact between the moisture and the film metallization.

Simulations of the effect of humidity are done using the humidity test defined in the climatic category.

Under more severe conditions, accelerated tests can be performed taking into consideration the relative severities. The severity S of any humidity test can be defined as the product of two factors (Equation 1.20.):

$S = \rho \cdot F_D$ (Equation 1.20.)

where

ρ is the density of water vapor in air, which is a function of both temperature and relative humidity. These data can be taken from standardized psychrometric charts (for instance, $\rho = 47$ gr/m^3 for T = 313K and humidity = 93%).

F_D is the thermal acceleration factor for diffusion (according to Arrhenius' law):

$$F_D = e^{(-E/RT)} \qquad (Equation\ 1.21.)$$

    E is the activation energy for diffusion, 10^{+4} cal/mol

    R is universal molar constant for gases, 1.987 cal/mol K, and

    T is the temperature in Kelvins, T (in °C) + 273.

The test severity S helps to compare the conditions of humidity tests. Table 1.9. compares the data for some common test conditions and referred to the standard ones (40 °C/93%, S' = 1).

Table 1.9. Severities for different humidity tests.

Temperature (ºC)	Temperature (K)	Humidity (%)	ρ (g/m³)	S	S'
40	313	93	47	$4.89 \cdot 10^{-6}$	1.0
65	338	95	151	$5.14 \cdot 10^{-5}$	10.5
85	358	85	294	$2.31 \cdot 10^{-4}$	47.3

1.2.6.4. Storage conditions

In general, film capacitors can be stored at any temperature within the complete category temperature range during a short period. However, for a long storage period, the storage conditions should be:

- Storage temperature between -40ºC to +40ºC,
- Maximum relative humidity 80% without condensation on the capacitor, and
- A maximum duration of 5 years of storage.

1.2.7. Mechanical test

1.2.7.1. Lead robustness

Film capacitors are devices liable to be submitted to mechanical stress during normal assembly or handling operations. The mechanical robustness of the leads is then tested according to the standard IEC 60068-2-21:2006, that defines the applicable tests depending on the component and if the stress is submitted to the device being mounted or not (Table 1.10) [27].

Table 1.10 Applicable tests according to IEC 60068-2-21:2006.

Test	Type	Component	Mounted/not mounted
Ua_1	Tensile	Leaded devices	Not mounted
Ua_2	Thrust	Leaded devices	Not mounted
Ub	Bending	Leaded devices	Not mounted
Uc	Torsion	Leaded devices	Not mounted
Ud	Torque	Threaded stud or screw termination	Not mounted
Ue_1	Bending	Surface mounted devices	Mounted
Ue_2	Pull/push	Surface mounted devices	Mounted
Ue_3	Shear	Surface mounted devices	Mounted

1.2.7.2. Resistance to vibration

During operation, capacitors should withstand specified severities of sinusoidal vibration. Thus the device mechanical weakness and/or degradation is tested according to the IEC 60068-2-6:2007 (Table 1.11) [28]. The standard procedure to determine the capacitor robustness typically used continuous vibration and varying continuously the frequency and the following severities:

Table 1.11. Typical test conditions of resistance to vibration in capacitors.

Test Fc: vibration, sinusoidal	Test conditions
Amplitude of displacement (below 57.6 Hz transition frequency)	0.75 mm
Amplitude of acceleration (above 57.6 Hz transition frequency)	98 m/s^2
Frequency range	10 Hz…500 Hz
Test duration (in 3 orthogonal axes)	3…120 min.

In addition, film capacitors especially designed for more severe vibration regimes during operation can be found, mainly in automotive applications. Hence, specific mounting conditions are defined in function of the lead space.

- Capacitors smaller than 22.5mm of lead space shall be mechanically fixed by the leads, and
- Capacitors with lead spaces higher than 22.5mm shall be fixed by the leads but the body must be additionally clamped in a proper manner.

1.2.7.3. Flammability

Flammability of film capacitors are studied by different type of flammability tests:

- Passive flammability. This test is intended to ensure that components contribute less energy to combustion in their immediate proximity than is required to ignite them.
- Then, any fire that may occur will be localized and contained. For this test, capacitors are submitted to a standardized flame to evaluate the combustion behavior determining if the flame persists for longer than the maximum permissible period time or not. The test severity is basically determined by the test flame and the exposure period. In general, the smaller the capacitor, the more easily it will be flammable. Different specifications define passive flammability

tests: UL1414:2000-9, IEC 60695-2-2:1991, IEC 60384-14:2013, UL 60384-14:2014, etc.

- ▪ Active flammability. This test is exclusively applied to EMI suppression capacitors, being the objective to ensure that capacitors do not ignite at a defined electrical overload. This is a destructive test and the failure condition is that cheesecloth around the capacitor shall not burn with a flame.

- ▪ Flammability of materials. Some specifications request additionally to check the flammability of materials with UL 94. These standards define the material test to conduct on test specimens for classifying the flammability of plastics. In the test according to UL94 V, the specimens are arranged vertically and exposed to a flame twice. The plastics are then classified into flammability categories in function of the thickness of the test specimen. The unique objective of UL94 is to enable a comparative method of the relative flammability of different materials, but it is not providing information related to the combustion characteristics of a capacitor.

1.2.8. Safety characteristics

1.2.8.1. Self-healing process

The most important reliability feature of film capacitors is their self-healing capability; this is their ability to clear faults under the influence of a voltage.

The electrode in film capacitors is a metal coating, vacuum-deposited directly onto the plastic film, only 20-50 nm thick. If the dielectric breakdown field strength is exceeded locally at a weak point (such as impurity or pore in the film), a dielectric breakdown occurs. The high temperatures reached in the breakdown channel (up to 6000 K) transform the dielectric into a highly compressed plasma that forces its exit. The thin metal coating in the vicinity of the channel is totally evaporated by interaction with the plasma, retreating from the breakdown channel. The rapid expansion of the plasma causes it to cool after a few microseconds, thus quenching the discharge before a greater loss of voltage takes place. The insulated region thus resulting around the former faulty area will keep the capacitor operating normally, with a minimal loss of capacitance.

Figure 1.15. schemes the described self-healing process, defining the numeration:

1. Dielectric,
2. Metallized electrodes,
3. Material displacing shock wave,
4. Air gap with metal vapor,

5, 6. Plasma zone,

7.   Boundary layer between gas phase dielectric and plasma,

8.   Breakdown channel,

9.   Gas phase dielectric, and

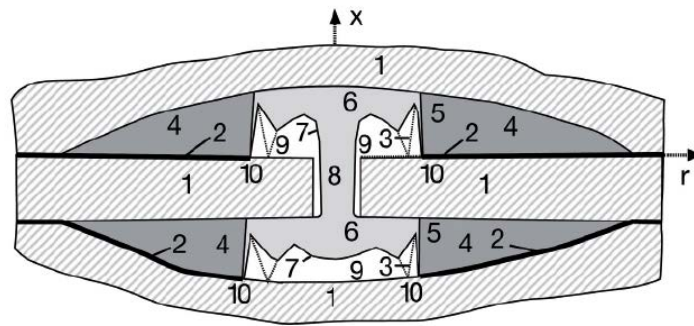10.   Zone of displaced metallization and dielectric (insulating region).

Figure 1.15. Schematic of the self-healing area during electrical breakdown.

The self-healing capabilities of a capacitor increase as the surface square resistance of the electrode increases, due to the reduced quantity of metal should be vaporized during the event. Consequently, the nominal field strength of a capacitor type could be increased by reducing the film thickness and compensating this by using a very thin metallization layer as electrode or high surface resistance. However, the ohmic losses in the electrode will be then increased proportionally to the resistance gaining and its current handling capability would be decreased.

Additionally, at low voltages, anodic oxidation of the metal coatings leads to an electrochemical self-healing process.

1.2.8.2. Corona discharges

The capacitors present in and around them air inside and micro-gaps (such as inside and between the films, near the corners) that may get ionized, leading to a destructive process known as corona effect.

This takes place when the intensity of the electric field in the capacitor exceeds the dielectric rigidity of the air. Under these conditions, small corona discharges occur, producing two undesirable effects:

  ▪   removal of the film metallization edges dropping then the capacitance, and

- structural damages caused by the bombardment of the film with ions and electrons might occur occasionally as well. This provokes a reduction of the breakdown voltage level of the dielectric, and finally might result to a short-circuit or fire.

This phenomenon is initiated at a voltage termed corona starting voltage VCD and its value is mainly determined by the internal construction of the capacitors (which determines the field strength at the edges). The VCD also depends, to a lesser degree, on the thickness of the dielectric. This voltage limit can be raised, in particular, by using internal series connection designs. However, if a capacitor is used below VCD, no corona effect will be observed and the corresponding degradation can be omitted.

1.2.8.3. Dielectric absorption

The dielectric absorption describes the effect that occurs in a capacitor that has remained charged for a long period of time and submitted to a brief discharge in short-circuit. During seconds or minutes, the voltage on the capacitor will try to recover to a fixed percentage of its original value (typically between 0.01% and 2% in film capacitors). The recharging originates in polarization processes in the dielectric material, and is mainly independent of the capacitance of a capacitor and the thickness of its dielectric.

The phenomenon has a particular adverse effect in sample and hold applications, in which charges should be stored for comparison or measuring goals. Test procedure for measuring of dielectric absorption is defined in the international standard IEC 60384-1:2016. However, typical values found for the mainly used dielectric are compiled on Table 1.12.

Table 1.12. Typical values of dielectric absorption.

Dielectric		PP	PET	PEN
Dielectric absorption	%	0.05	0.2	1.2

1.2.8.4. Buzz noise

When a film capacitor operates under AC regime, buzzing noise is produced by the mechanical vibration of the films, due to the Coulomb force existing between electrodes with opposite polarity. Buzz noise becomes louder if the applied voltage waveform presents distortion and/or high frequency harmonics.

Buzz noise does not affect the capacitor structure, nor its electrical characteristics or reliability.

1.3. MARKET STUDY

The global film capacitor market is leaded by companies such as TDK Corporation (Japan), Mitsubishi Shindoh Co. Ltd (Japan), AVX Corporation (U.S.), Electro Tecknik Industries, Inc. (U.S.), Custom Electronics, Inc. (U.S.), Aerovox Corporation (U.S.), Cornell Dubilier Electronics Inc. (U.S.), KEMET Corporation (U.S.), Vishay Intertechnology Inc. (U.S.), Nichicon Corporation (Japan), Panasonic Corporation (Japan), and Xiamen Faratronic Co. Ltd. (China), among others.

The prominent companies are focused to penetrate the new film capacitor products in the market. These products may be further used in next-generation applications such as artificial intelligence, machine learning, quantum computing, robotics and others.

The global film capacitor market is branched based on different criteria such as capacitor type, applications, end-users or region.

The types are divided into AC film capacitors, DC film capacitors, power film capacitors and others. The applications are segmented into electronic circuits, radio frequency interference suppression film capacitors, power film capacitors, lighting ballasts, damping capacitors and others. The market sections based on end users are automotive, industries, consumer electronics, power and utilities, government and defense and others. The regional analysis of film capacitor market is being studied for region such as Asia Pacific, North America, Europe and rest of the world. North America is one of the main leader in terms of market share in film capacitor market as this region has a strong demand in many sectors like automotive, defense, industries and others.

The film capacitor market in Europe region is expected to evidence a rapid growth in the next period. Whereas, Asia-Pacific countries such as China, Japan and South Korea is an emerging market for film capacitor market and expected to be the highest Compound Annual Growth Rate (CAGR) in the coming. Being defined the CAGR as the annual average rate of return for an investment over a period of time.

The global film capacitor market was pegged at USD 2.12 Billion in 2018; and without considering the effects of the Corona virus disease in the economic situation, is expected to grow at USD ~2.59 Billion by 2026, at a ~2.5 % CAGR of between 2019 and 2026. (Figure 1.16.) [30-32].
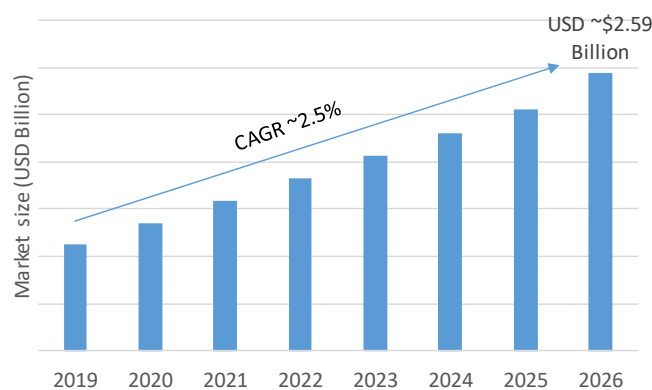

Figure 1.16. Global film capacitor market.

High demand of film capacitor in consumer electronics is major driving variable behind the market. Furthermore, rise in demand for high-temperature film capacitors and high incorporation of film capacitors in the electric vehicle system have expanded the growth of the global film capacitor industry. However, increase in severity of manufacturing rules and environmental conditions and low pricing margins slow the market down. Degradation due to humidity is nowadays the major issue in the film capacitor which could hamper the growth of market. This expected trend for the environmental conditions to be fulfilled by film capacitors is in line with the observations of the last decade.

The evolution of the environmental requirements since year 2010 to the present in global film capacitor market shows a clear trend to increase the severity of the operation ambient. A decade ago, more than half of the customer specifications required to pass environmental test without being electrically stressed the film capacitors and at 40ºC with 93% relative humidity. And the most stringent environmental conditions (85% relative humidity at 85ºC) with electric load were the 5% of the total specifications with environmental requirements defined. However, nowadays, the environmental requirements without electrical stress at 40ºC and 93%R.H. reveals a reduction of demand of 20%, being distributed to more severe conditions (Figure 1.17):

- 5% gained by 40ºC with 93%R.H. and electrical load tested during 1000 hours,
- 5% gained by 60ºC with 95%R.H. and electrical load tested during 1000 hours, and
- 10% gained by the most severe conditions, 85ºC with 85%R.H. and voltage.
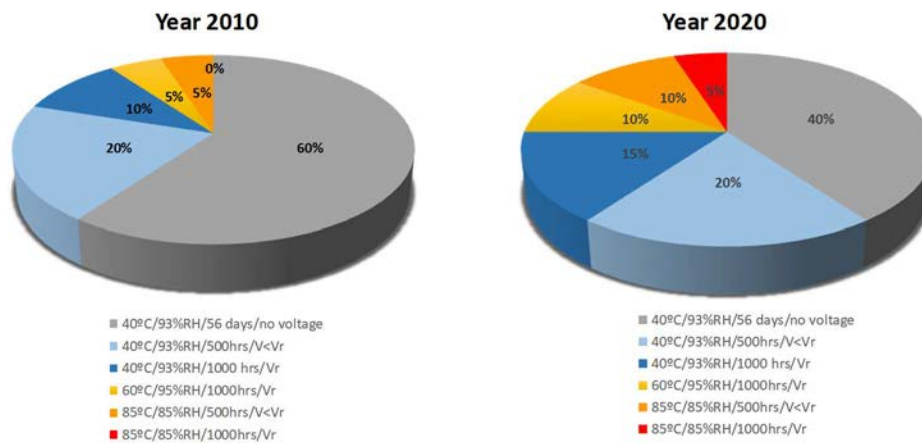

Figure 1.17. Distribution of environmental requirements in Global film capacitor market.

Source: TDK CAP FILM I&A DC marketing department.

This rise in severity makes necessary to design robust film capacitors with high reliability and suitable to operate under extreme environmental conditions, a fact that should be tested by means of a temperature, humidity, bias test (THB) at 85ºC and 85% relative humidity with a rated voltage applied for 500h or 1000h. To achieve this objective, it is key a right selection of the materials to be used,

being thermoplastic and polymeric materials which absorb very small moisture the trend of the new series introduced in the last years in the market to feature high humidity resistance and high safety.

1.4.   TDK CORPORATION IN THE MARKET

TDK Corporation is a Japan-based company mainly engaged in the manufacture and sale of passive components and magnetic application products. The Company has three business segments. The Passive Component segment is engaged in the manufacture and sale of ceramic capacitors, inductive devices, high frequency wave parts, piezoelectric material components, circuit protection components, aluminium electrolytic capacitors, film capacitors and sensors, among others. The Magnetic Application Product segment is involved in the manufacture and sale of recording devices, electrical power supplies, magnets and recording media, among others. The Others segment is engaged in the manufacture and sale of energy devices such as secondary batteries, as well as manufacturing facilities such as mechatronics equipment, among others.

TDK purchased EPCOS in 2007 in an effort to expand their dielectric capabilities to include other dielectrics other than their traditional ceramic line and EPCOS offered TDK a gateway into film capacitors, aluminum capacitors and a variety of thermistor and sensor products as well as SAW filter technology. EPCOS film capacitor production is largely in Spain and Brazil and the company is a major competitor in both the AC and DC film capacitor markets worldwide.

1.5. References

[1] D.F. Taylor, *On the Mechanism of Aluminum Corrosion in Metallized Film AC Capacitors*. IEEE Transactions on Electrical Insulation. EI-19, Issue 4 (1984) 288-293.

[2] H. Wang, F. Blaabjerg. *Reliability of capacitors for DC-link applications – An overview.* IEEE Transactions on Ind. Appl. 50 (5) (2014) 3569-3578.

[3] R. Brown. *Linking corrosion and catastrophic failure in low-power metallized polypropylene capacitors.* IEEE Trans. Device Mater. Reliab. 6 (2) (2006) 326-333.

[4] E. Yildiz, A. Güngor, H. Yildirim, B.M. Baysal, *Synthesis and characterization of uv-curable acrylated urethane prepolymers, I. Effects of reactive diluents and relative humidity on physical properties*. Macromolecular Materials and Engineering. 219, Issue 1 (1994) 55-66.

[5] M.M. Pastor-Blas, J.M. Martín-Martínez, J.G.Dillard. *Surface characterization of synthetic vulcanized rubber treated with oxygen plasma.* Surf. Interface Anal. 26 (1998) 385

[6] G.H. Meng, B.Y. Zhang, H. Liu, G.J. Yang, T. Xu, C.X. Li, C.J. Li, *Vacuum heat treatment mechanisms promoting the adhesion strength of thermally sprayed metallic coatings*, Surf. Coat. Technol. 344 (2018) 102-110.

[7] M. Michelazzi, E. Boni, D. Montanari, L. Barbieri, T. Chow, E. Matero, S. Sartini, F. Bergamaschi, *RFI X2 Capacitors for High Humidity Environment*, CARTS International (2014)

[8] M. Mrad, Y. Ben Amor, L. Dhouibi, M.F. Montemor, *Corrosion prevention of AA2024-T3 aluminum alloy with a polyaniline/poly(γ-glycidoxypropyltrimethoxysilane) bi-layer coating: Comparative study with polyaniline mono-layer feature,* Surf. Coat. Technol. 337 (2018) 1-11.

[9] R.E.Jacobson, M.S.Engineer, D.F. Caufield, R.M.Rowell, A.R. Sanadi, *Proceedings of Second Biomass Conference of the Americas: Energy, Environment, Agriculture, and Industry* (1995) 1171-1180.

[10] A.R Sanadi, D.F. Caufield, R.M. Rowell. *Reinforcing polypropylene with natural fibers*. Plastic Eng. L(4) (1994) 27-28.

[11] S.V. Gnedenkov, S.L. Sinebryukhov, V.S. Egorkin, I.E. Vyaliy, *Wettability and electrochemical properties of the highly hydrophobic coatings on PEO-pretreated aluminum alloy*, Surf. Coat. Technol. 307 (2016) 1241-1248.

[12] V. Svorcík; A. Reznícková; P. Sajdl; Z. Kolská; Z. Makajová; P. Slepicka. *Au nanoparticles grafted on plasma treated polymers*. Journal Materials Science. 46. (2011) 7917-7922.

[13] V. Scorcík; A. Chaloupka; P. Rezanka; P. Slepicka; Z. Kolská; N. Kasálková; T. Hubácek; J. Siegel. *Au-nanoparticles grafted on plasma treated PE.* Radiation Physics and Chemistry. 79 (2010) 315-317.

[14] N. Slepicková Kasálková; P. Slepicka; Z. Kolská; P. Sajdl;L. Bacáková; S. Rimpelová; V. Svorcík. *Cell adhesion and proliferation on polyethylene grafted with Au nanoparticles*. Nuclear Instruments and Methods in Physics Research B. 272 (2012) 391-395.

[15] F.S. Denes, S.Manolache. *Macromolecular plasma-chemistry: an emerging field of polymer science*. Prog.Polym. Sci. 29 (2004) 815-885.

[16] F. Denes, S. Manolache, R.A. Young. *Synthesis and surface functionalization under cold-plasma conditions*. Journal of Photopolym. Sci. and Techn. 12, Nr.1 (1999) 27-38.

[17] D. Liu, P. Chen, M. Chen, Z. Liu. *Improved interfacial adhesion in PBO fiber/bismaleimide composite with oxygen plasma plus aging and humid resistance properties*. Materials Science and Engineering A 532 (2012) 78-83.

[18] J.N. Borges, T. Belmonte, J. Guillot, D. Duday, M. Moreno-Couranjou, P. Choquet, H.N. Migeon. *Functionalization of Copper Surfaces by Plasma Treatments to Improve Adhesion of Epoxy Resins*. Plasma Process. Polym. 6 Issue S1 (2009) 490-495.

[19] S.P. Sim, R.W.Lawson. *The influence of encapsulant and passivation layers on the corrosion of thin aluminum films subjected to humidity stress*. Proceedings of 17th Annual Reliability Physics Symposium (1979) 103-112.

[20] DIN EN 60062:2005

[21] EPCOS AG – TDK Group Company. *Film Capacitors. General technical information*. (June 2018)

[22] Shaw, D. G., Cichanowski, S. W. and Yializis, A. *A changing capacitor technology - Failure mechanisms and design innovations*, IEEE Trans. Elect. Insul., Vol. EI-16, no. 5 (Oct 1981) 399–413

[23] Sarjeant, W. J. and MacDougall F. W., *Capacitors for high power electronics*, in Proc. IEEE Annu. Rep. - Conf. Elect. Insul. Dielect. Phenomena, Minneapolis, MN, Vol. 1 (Oct. 19–22, 1997) 113–120.

[24] IEC 60068-1:2013. *International Standard. Ed. 7.0. Environmental testing – Part 1. General and guidance* (July 2013)

[25] Bâzu, M. I. and Bajenescu, T. M. I. *Failure Analysis. A practical guide for manufacturers of electronic components and systems*. John Wiley and Sons Ltd. ISBN 978-0-470-74824-4 (2011)

[26] IEC 60384-1:2016. *International Standard. Fixed capacitors for use in electronic equipment – Part 1: Generic specification* (Feb 2016)

[27] IEC 60068-2-21:2006. *International Standard. Ed. 6.0. Environmental testing – Part 2-21: Tests-Test U: Robustness of terminations and integral mounting devices*. ISBN 978-2-88912-734-4 (June 2006)

[28] IEC 60068-2-6:2007. *International Standard. Ed. 7.0. Environmental testing – Part 2-6: Tests-Test Fc: Vibration (sinusoidal)*. ISBN 2-8318-9490-5 (December 2007)

[29] IEC 60068-2-78:2001. *International Standard. Ed. 1.0. Environmental testing - Part 2-78: Tests - Test Cab: Damp heat, steady state.* (August 2001)

2. OBJECTIVES

As previously discussed in the *Introduction,* a self-healing metallized film capacitor which may be used for various applications typically consists of a winding element housed in a plastic or metal housing impregnated with insulating material. The metallized film capacitor is generally designed to operate in ambient environment of -40ºC to a maximum of 125ºC. Under the effects of an application environment, the ambient working conditions and an applied electric field, the metallized film capacitor suffers from various capacitance loss mechanisms. The capacitance loss mechanisms are typically due to self-healings resulting in a loss of metallized electrode area and electrode oxidation.

Occasionally, the metallized film capacitor fails due to a high capacitance drift. The failure should normally occur after the expected end of life of the capacitor. Drift in the capacitance is generally associated with an increase in the loss factor.

Present day applications demand key components to withstand higher amount of electrical as well as environmental stresses. Capacitors are required to operate at higher ambient temperatures in the presence of high relative humidity conditions while achieving higher lifetime and reliability for the products.

Capacitance loss mechanisms are accelerated under harsh environmental working condition. In particular, the presence of humidity lead to corrosion on the metallized film. The capacitance loss phenomenon affects either an active electrode surface or an electrode edge. In electrochemical corrosion, the series resistance of the capacitor increases over a period of time causing further increase in loss factor due to de-metallization of the metallized electrode leading to an increase in local hotspot temperatures. Higher ambient temperatures further accelerate this failure mechanism.

There is a growing demand for the capacitors capable to withstand high temperature of 85ºC, under high relative humidity of 85%. As discussed above, under these exigent ambient working conditions, the capacitance loss mechanisms are accelerated. Hence, this situation calls for new design considerations to be adopted in the metallized film capacitor.

Accordingly, the general objective of the present thesis is to design an optimized metallized film capacitor able to extend the lifetime under harsh environmental conditions of temperature and humidity with applied voltage in comparison with the standard design. The achievement of this general aim is based on the following specific objects:

❖ To deep understand the failure mechanisms on metallized film capacitors due to the presence of humidity in the metallized film

❖ To define the types of barriers against the humidity

❖ To identify the key interfaces involved in a metallized film capacitor

❖ To define the key properties of the encapsulating materials to ensure a good performance in terms of thermal and mechanicals requirements, electrical insulation and humidity barriers.

❖ To design the metallized film capacitor to reduce the stress applied to the encapsulating materials and ensuring the adhesion in the interfaces.

The validity of the found improvements in the material characterizations was additionally checked by operational tests with temperature and humidity bias (THB) test on the metallized film capacitors.

3. PROJECT ORGANIZATION
(Targets and tasks)

TDK Electronics Components S.A.U. in the plant of Málaga (Spain) is manufacturing two different families of metallized film capacitors for applications of consumption devices and for power electronics. The specific aims will be met based on TDK experimental results and know-how.

The project plan is divided into different targets and tasks as schemed in Figure 3.1. and described as follows.
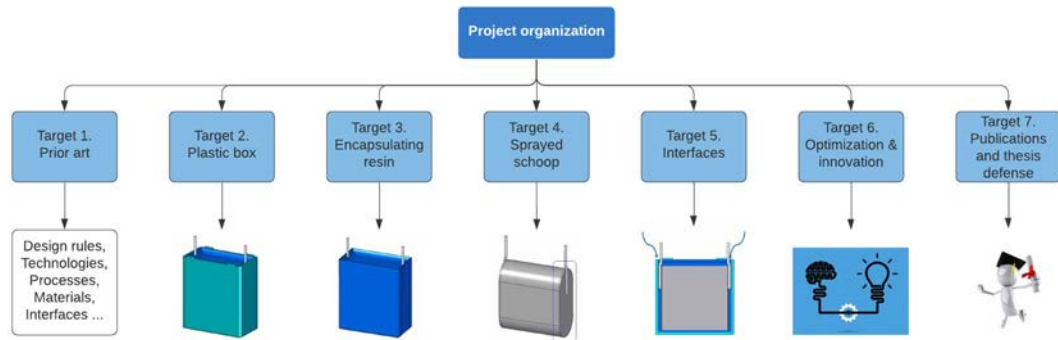
Figure 3.1. Project organization.

- Target1: Prior Art: To make an exhaustive study of the prior art about the encapsulation of metallized film capacitors (MFC) in different working conditions.

  o Task 1.1. Study of design rules of MFC in function of the application requirements.

  o Task 1.2. Study of product families and technologies of MFC focused in polypropylene film as dielectric.

  o Task 1.3. Study and analysis of production processes of MFC applied to automotive industry

  o Task 1.4. Study of the behavior of the standard design of MFC under the new harsher requirements of 85ºC and 85% of relative humidity and applied voltage.

  o Task 1.5. Analysis of the elements on a MFC as soldering wires, metal sprayed to contact the electrode, encapsulating resins, plastic housing, etc.

  o Task 1.6. Study of plastic materials acting as humidity barrier.

  o Task 1.7. Study of different processes to increase the adhesion on MFC interfaces.

- Target 2: Characterization of standard materials used for housing the metallized film capacitor.

- Task 2.1. Analysis of the MFC performance under THB test with the standard materials injected as housing of MFC.

- Task 2.2. Characterization of standard plastic materials injected as housing in MFC before being submitted to environmental and working conditions. The characterization compiles studies of the chemical composition, wettability and polarity of the surfaces, roughness, water vapor permeability, etc.

- Task 2.3. Characterization of standard plastic materials injected as housing in MFC during the temperature and humidity bias test. The characterization compiles studies of the chemical composition, wettability and polarity of the surfaces, roughness, water vapor permeability, etc.

- Task 2.4. Analysis of failure mechanisms on MFC in function of the plastic material selected as box.

- Target 3: Characterization of standard materials used for encapsulating the metallized film capacitor.

  - Task 3.1. Analysis of the MFC performance under THB test with the standard polymeric resins used to fill the capacitors.

  - Task 3.2. Characterization of standard polymeric resins used to fill a MFC before being submitted to environmental and working conditions. The characterization compiles studies of the chemical composition, wettability and polarity of the surfaces, roughness, water vapor permeability, etc.

  - Task 3.3. Characterization of standard polymeric resins used to fill a MFC during the temperature and humidity bias test. The characterization compiles studies of the chemical composition, wettability and polarity of the surfaces, roughness, water vapor permeability, etc.

  - Task 3.4. Analysis of the results and definition of the failure mechanisms on MFC related to the potting material selected as encapsulation of the electrode.

- Target 4: Characterization of standard alloys sprayed onto the winding (denominated *schoop*) of the metallized film capacitor.

  - Task 4.1. Analysis of the MFC performance under THB test with every alloy selected as schoop.

- o Task 4.2. Characterization of every specific schoop before being submitted to environmental and working conditions. The characterization compiles studies of the chemical composition, wettability and polarity of the surfaces, roughness, water vapor and oxygen permeability, morphology, grain size analysis, grain distribution study, etc.

- o Task 4.3. Characterization of every specific schoop during the temperature and humidity bias test. The characterization compiles studies of the chemical composition, wettability and polarity of the surfaces, roughness, water vapor and oxygen permeability, morphology, grain size analysis, grain distribution study, etc.

- o Task 4.4. Analysis of the results and definition of failure mechanisms on MFC related to the schoop composition and grain morphology.

- Target 5: Characterization of the interfaces on the metallized film capacitor.

  - o Task 5.1. Study of the adhesion in the interface between the plastic housing and the encapsulating resin with standard materials and processes.

  - o Task 5.2. Study of the adhesion in the interface between the plastic housing and the encapsulating resin with new materials and processes.

  - o Task 5.3. Study of the adhesion in the interface between the encapsulating resin and the wire terminal with standard materials and processes.

  - o Task 5.4. Study of the adhesion in the interface between the encapsulating resin and the wire terminal with new materials and processes.

- Target 6: Optimization of the standard design of MFC to withstand an ambient of 85ºC of temperature and 85% of relative humidity and the nominal voltage of the device.

  - o Task 6.1. To submit the optimized MFC to the temperature and humidity bias (THB) test.

  - o Task 6.2. Analysis of THB test results.

- Target 7: Publications, dissemination of results and thesis defense

  - o Task 7.1. Dissemination of results in congress, journals, patents, workshops, etc. taking into consideration TDK's rights including copyright, trademark, patent, and any other confidential information intellectual property rights and industrial.

4. EXPERIMENTAL. MATERIALS AND METHODS

4.1. MATERIALS

4.1.1. Metallized plastic film capacitor

The present thesis studies the humidity protection of metallized plastic film capacitors, but focused in the series using polypropylene as dielectric, denominated MKP capacitors.

The selected type for the study as reference is a MKP wound boxed capacitor (humidity resistant X2 EMI suppressor) of 6 μF ($\pm$ 10%) of capacitance, 305 V_{AC} of voltage, parallel wire leads of 1 mm of diameter which are lead-free tinned, in a 2-pin version and a lead spacing of 37.5 mm. The external dimensions of the box are (20.2 x 39.7 x 42.0) mm^3, made of polybutylene terephthalate (PBT) without reinforcement of glass fiber (0% GF). The encapsulating resin surrounding the winding element is an epoxy. Both polymers, the thermoplastic case and the epoxy resin for sealing are in compliance with the standard of flammability UL 94, V-0 category [59]. The type of metallization selected to be sprayed onto the lateral side of the winding (schoop) before being encapsulated with the epoxy resin was firstly 100% of zinc and a second layer of an alloy composed by tin and copper according to DIN EN 29453 (3% in weight of copper, Cu) (Figure 4.1.).
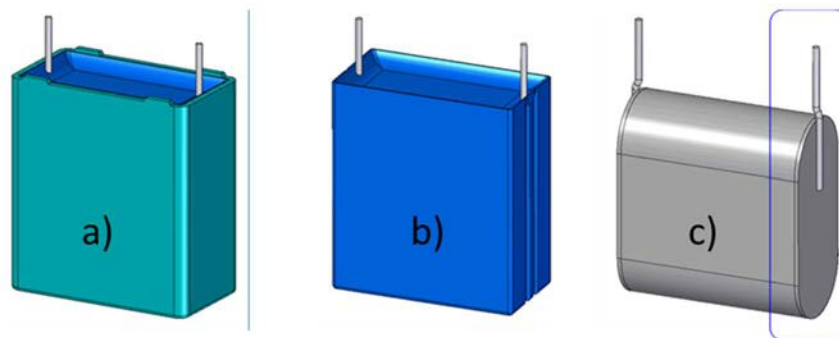
Figure 4.1. A 2-pin version of a metallized film capacitor encapsulated with resin and box (a), only with resin (b) and a winding with sprayed schoops (blue square).

The film used as reference is a biaxially oriented polypropylene (BOPP) dielectric of 6.0 μm of thickness with a metallization made of 95% zinc and 5% aluminum with a resistivity of 10 Ω in the flat area and lower than 3 Ω in the heavy edge (*Figure 4.2.*).
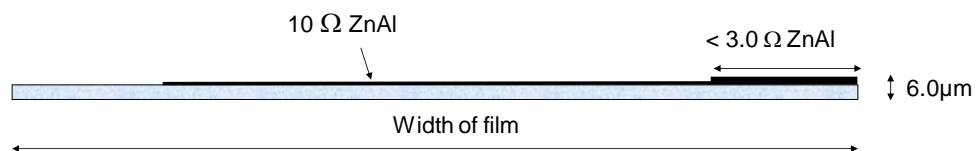
Figure 4.2. Film of reference used in MKP wound box capacitor of 2-pins.

Related to environmental regulations, all the standard and new materials involved in the production of metallized film capacitors are in compliance with the following regulations:

1. GAD-SL
2. RoHS (2011/65/EU)
3. ELV Directive and its amendments (2000/53/EC)
4. REACH Regulation (EC) No. 1907/2006
5. China management measures on electronic information products pollution control (China RoHS)
6. Act for resource recycling of electrical and electronic equipment and vehicles (Korea RoHS)
7. Japan: revised law for promotion of effective utilization of resources (J·MoSS)
8. California electronic waste recycling act SB 20, amended by SB 50 and AB 575
9. Swiss Ordenance on risk reduction related to the use of certain particularly dangerous substances. Preparations and articles (Ordinance on Chemical Risk Reduction) (ORRChem)
10. Louisiana mercury risk reduction act
11. Rhode Island General law chapter 23-24.9 (Mercury Reduction and Education Act) and Amendment of 2007
12. Vermont: "Act relating to comprehensive management of exposure to mercury"
13. Directive 94/62/EC on Packaging and packaging waste (EU Packaging Directive)
14. Directive 2006/66/EC on Batteries and accumulators and waste batteries and accumulators (EU Battery Directive): "Non-Alkaline Zinc Manganese Dioxide Batteries"
15. China: GB 24427-2009. Limitation of mercury cadmium and lead contents for alkaline and non-alkaline zinc manganese dioxide batteries
16. Taiwan: restrictions on the manufacture, import and sale of dry cell batteries
17. South Korea: quality management and safety control of industrial products act. Battery regulation
18. California: Perchlorate contamination prevention act: enforced on January 1, 2007
19. New York Environmental conservation law. Title 7-27-0719. Battery management and disposal
20. IEC 62474
21. EU Directive 2005/84/EC
22. IPC-4101
23. IEC 61249-2-21
24. US EPA TSCA
25. Swiss Ordinance on reduction of risk from chemical products
26. EU Reg. No. 842/2006

27. Austria-BGB | 1990/194 Formaldehydverordnung, S2, 12/2/1990

28. Montreal Protocol

29. EU EC No. 2037/2000

30. US Clean Air Act

31. EU Regulation (EC) No. 850/2004

32. Canadian Environmental Protection Act SOR/SOR/2008-178

33. Japan law concerning the evaluation of chemical substances

34. EU-D 96/29/Euratom

35. Japan law for the regulation of nuclear source material, nuclear fuel material and reactors, 1986

36. US NRC

37. Norway product regulations FOR-2004-06-01-922

38. EU Commission Decision (2009/251/EC)

39. DIGITALEUROPE/CECED/AeA/EERA Guidance

40. Japan Water Pollution Control Law

41. US Dodd-Frank Wall Street reform and consumer protection act. Section 1502

42. Stockholm Convention on persistent organic pollutants

43. Delegated directive 2015/863/EU amending Annex II to Directive 2011/65/EU

44. Prohibition requirement from Japanese Industries (JEITA)

4.1.2. Windings with schoop

All the studies of improvement of protection under harsh humid environment are validated by operational tests over the selected metallized film capacitor. However, for target 4 described in Section 3, (the study of schoop as humidity barrier) was included as sample type additionally naked winding with schoop to isolate the variable under study (the schoop) without the influence of the encapsulating resin and the plastic box (Figure 4.1. c)). The winding characteristics are described above in paragraph 4.1.1. The tested naked windings are studied with the terminals joined by welding (no adding material in the soldering).

4.1.3. Encapsulating resins

The filling material of reference to encapsulate the electrode of the capacitor was an epoxy resin with an electrical comparative tracking index (CTI) of 600V (IEC 60112), a hardness of 90 ShoreD, a water vapor transmission rate (WVTR) of 0.3 g·mm/(m^2·day) (ASTM F1249-06), a glass transition temperature (Tg) of 90 ºC (ASTM E 1356, IEC 1006), a tensile strength of 55 N/mm^2 (ISO 527) and a modulus of elasticity (Young's modulus) of 3500-4700 N/mm^2 (ISO 527-2). This epoxy is classified as V-0 according to the standard of safety of flammability of plastic materials for parts in devices and appliances testing, UL 94. The standard design is encapsulated exclusively with this material.

However, in target 3 (described in section 3) additional encapsulating resins with different configurations were characterized and tested in the MKP wound boxed capacitors. Potting with only one material and also with two different resins (one as main encapsulation of the winding element and the second as closing layer) were analyzed with materials with different compilation of properties, with the purpose of analyzing the dominant failure mechanisms in every case.

In addition to the reference, the studied encapsulating resins (not only as material characterization but also in the device under temperature/humidity/bias (THB) test) are:

- Encapsulating resin nr.1. Polyurethane resin (Figure 4.3.) with an electrical comparative tracking index (CTI) of 600V (DIN EN 60112), a dielectric strength of 38 kV/mm (IEC 60243-1, VDE 0303, TI.2), a hardness of 80 Shore A (ISO 868, DIN 53505), a water vapor transmission rate (WVTR) of 3.9 g·mm/(m^2·day) (Standard ASTM F1249-06), a water absorption of 0.3% after 30 days of immersion, a glass transition temperature (Tg) of -4 ºC (by Thermomechanical Analysis, TMA), a tensile strength of 7 N/mm^2 (ISO 527-2), a modulus of elasticity of 20 N/mm^2 (ISO 527-2). This polyurethane is classified as V-0 according to the standard of safety of flammability of plastic materials for parts in devices and appliances testing, UL 94.
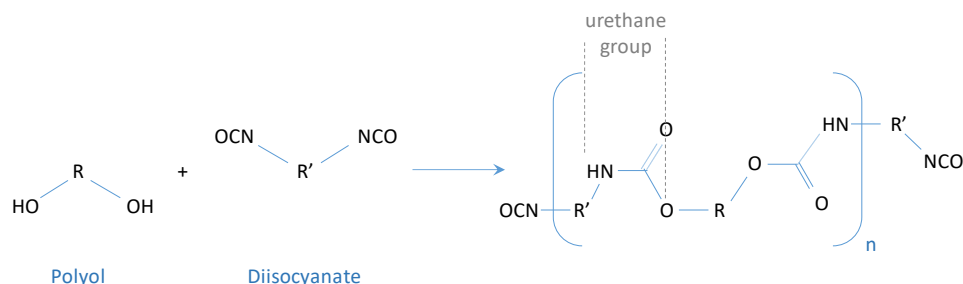
Figure 4.3. Basic reaction scheme for urethane formation.

- Encapsulating resin nr.2. Polyurethane resin based on castor oil (Figures 4.3. and 4.4.) with a dielectric strength of 10 kV/mm (IEC 60243-1, VDE 0303, TI.2), a hardness of 50 Shore A (ISO 868, DIN 53505), a water vapor transmission rate (WVTR) of 28.4 g·mm/(m^2·day) (Standard ASTM F1249-06), a water absorption of 2.3% after 30 days of immersion, a glass transition temperature (Tg) of -20 ºC (by Thermomechanical Analysis, TMA), a tensile strength of 2.1 N/mm^2 (ISO 527-2) and a modulus of elasticity (Young's modulus) of 4 N/mm^2 (ISO 527-2).
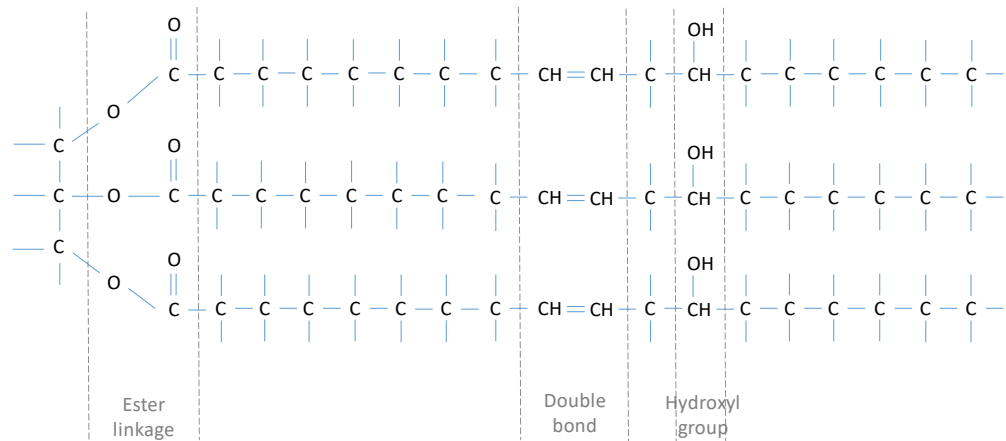
Figure 4.4. Structure of castor oil (main polyol of encapsulating resin nr.2).

- Encapsulating material nr.3. Silicone cross-linked through a chemical reaction with moisture from the environment. The main properties shown by this encapsulating material are a dielectric strength of 15-23 kV/mm (IEC 60243-1, VDE 0303, TI.2), a hardness of 11 Shore A (DIN 53505), a water vapor transmission rate (WVTR) of 82.9 g·mm/(m²·day) (ASTM F1249-06), a glass transition temperature (Tg) higher than -50 ºC (by Dynamic Mechanical Analysis, DMA) and a tensile strength of 0.67 N/mm² (DIN 53504 S2).

4.1.4. Thermoplastics as box

The plastic material of reference injected as box to protect the capacitor was a polybutylene terephthalate (PBT) (Figure 4.5.) without reinforcement of glass fiber with a comparative tracking index (CTI) of 250V (Standard IEC 60112), a thermal expansion coefficient (CTE) of 63 (1/ºC) (ISO 11359), an oxygen transmission rate (OTR) of 0.38 ((l·cm³·mm)/(m²·day)) (ASTM F1249-06), a water vapor transmission rate (WVTR) of 0.2 g·mm/(m²·day) (ASTM F1249-06), a water absorption of 0.17% weight (at 23 ºC and 50% of relative humidity during 23 h) (Standard ISO 62), a glass transition temperature (Tg) of 44ºC (with a ramp-up of 10ºC/min by Differential Scanning Calorimetry, DSC), a tensile strength of 60 N/mm² (ISO 527-2/1A), a modulus of elasticity (Young's modulus) of 3000 N/mm² (ISO 527-2) and a hardness of 79 Shore A (ISO 868, DIN 53505).
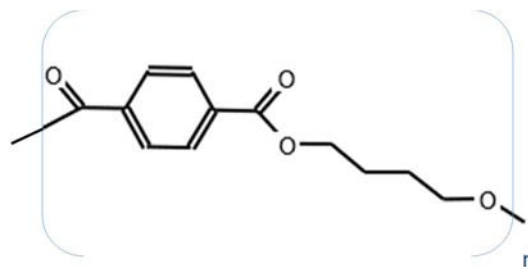
Figure 4.5. Structure of polybutylene terephthalate (PBT).

However, in target 2 (described in section 3) additional thermoplastics were characterized and tested in the MKP wound boxed capacitors to analyze the failure mechanisms on those in function of the selected plastic material.

In addition to the reference, the studied polymer types (not only as material characterization but also in the device under temperature/humidity/bias (THB) test) are:

- Polymer type nr.1. Polyphenylene sulphide (PPS) (Figure 4.6.) with 40% of glass fiber as reinforcement. The injected material shows a comparative tracking index (CTI) of 125V (IEC 60112), a thermal expansion coefficient (CTE) of 27 (1/ºC) (ISO 11359), an oxygen transmission rate (OTR) of 1.9 ((l·cm^3·mm)/(m^2·day)) (ASTM F1249-06), a water vapor transmission rate (WVTR) of 0.2 g·mm/(m^2·day) (ASTM F1249-06), a water absorption of 0.01% weight (at 23 ºC and 50% of relative humidity during 23 h) (Standard ISO 62), a glass transition temperature (Tg) of 105ºC (with a ramp-up of 10ºC/min by Differential Scanning Calorimetry, DSC), a tensile strength of 158 N/mm^2 (5mm/min according to ISO 527-2/1A), a modulus of elasticity (Young's modulus) of 14500 N/mm^2 (ISO 527(1)) and a hardness of 79 Shore A (ISO 868, DIN 53505).
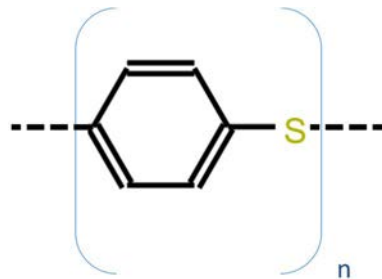
Figure 4.6. Structure of polyphenylene sulphide (PPS).

- Polymer type nr.2. Polycarbonate of Bisphenol A (PC) (Figure 4.7.) without reinforcement of glass fiber. The injected material shows a comparative tracking index (CTI) of 250V (IEC 60112), a thermal expansion coefficient (CTE) of 70 (1/ºC) (ISO 11359), an oxygen transmission rate (OTR) of 84.3 ((l·cm^3·mm)/(m^2·day)) (ASTM F1249-06), a water vapor transmission rate (WVTR) of 1.4 g·mm/(m^2·day) (ASTM F1249-06), a water absorption of 0.10% weight (at 23 ºC and 50% of relative humidity during 23 h) (Standard ISO 62), a glass transition temperature (Tg) of 142ºC (with a ramp-up of 10ºC/min by Differential Scanning Calorimetry, DSC), a tensile strength of 110 N/mm^2 (5mm/min according to ISO 527-(1)), a modulus of elasticity (Young's modulus) of 2330 N/mm^2 (ISO 527(1)) and a hardness of 78 Shore A (ISO 868, DIN 53505).
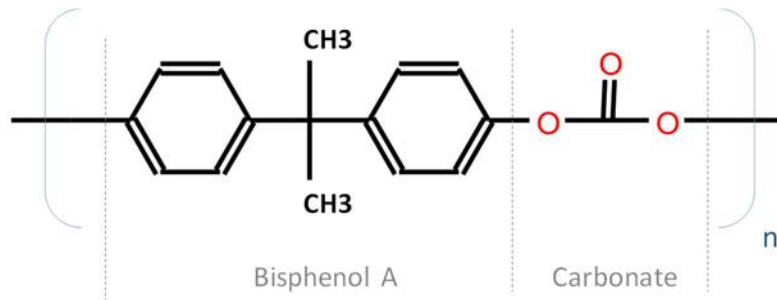
Figure 4.7. Structure of polycarbonate of Bisphenol A (PC).

- Polymer type nr.3. Polypropylene (PP) (*Figure 4.8.)* without reinforcement of glass fiber. The injected material shows a comparative tracking index (CTI) of 250V (IEC 60112), a thermal expansion coefficient (CTE) of 70 (1/ºC) (ISO 11359), a water vapor transmission rate (WVTR) of 0.1 g·mm/(m^2·day) (ASTM F1249-06), a glass transition temperature (Tg) of -18ºC (with a ramp-up of 10ºC/min by Differential Scanning Calorimetry, DSC), a tensile strength of 110 N/mm^2 (5mm/min according to ISO 527-(1)), a modulus of elasticity (Young's modulus) of 2330 N/mm^2 (ISO 527(1)) and a hardness of 77 Shore A (ISO 868, DIN 53505).
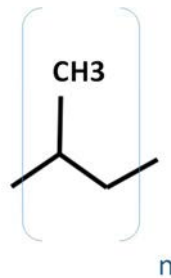
Figure 4.8. Structure of polypropylene (PP).

It is important to remark the fact that the study of thermoplastics injected as boxes purposes to analyze the behavior of different polymer types without the influence of a reinforcement; however, due to process feasibility the PPS was required to be injected with a minimum percentage of 40% of glass fiber. This is the reason to be the PPS the only polymer characterized with a reinforcement whilst the others are not reinforced.

4.1.5. Sprayed metal (schoop)

The metallization of reference sprayed onto the lateral side of the winding before being encapsulated with the epoxy resin was firstly 100% of zinc and a second layer of an alloy composed by tin and copper according to DIN EN 29453 (3 % in weight of copper).

However, in target 4 (described in section 3) additional alloys were characterized as material sheets and also tested in naked windings and MKP wound boxed capacitors to analyze the failure mechanisms according to the schoop composition and morphology characterized.

Thus, the material characterization and operational test on the devices were carried out in the following sprayed metallizations as schoop:

- 100% zinc (Zn)
- tin-copper (3% in weight of copper) (SnCu)
- zinc-aluminum (15% in weight of aluminum) (ZnAl)

In addition to the chemical composition of the schoop, different combinations of single layer or more than one were studied. Figure 4.9. illustrates the cases of a single layer and the combination of two layers as schoop. This figure is not scaled; it is only a scheme to highlight the element under study (sprayed schoop).
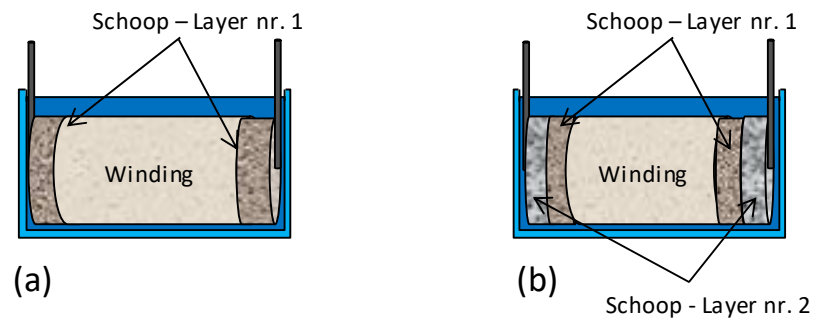
Figure 4.9. Scheme of configuration of schoop with a single layer (a) or two combined (b) (not scaled).

The used spray method for every composition was electric arc and the process parameters were the standard ones defined confidentially by TDK Electronics. All the schoops are in the thickness frame between 0.2 ~ 0.5 mm. The established comparative between different compositions and combinations of number of layers were defined with the same final thickness to ensure that the differences of performance observed during the material characterizations and tests were not associated to the thickness variable but to the composition and/or the number of interphases.

For the material characterization, sheets of sprayed metal were produced with the same conditions than the windings.

4.1.6. Surface treatments

During operation, as described in Section 1, the MKP wound box capacitors are submitted to thermal stress due to rapid changes of temperature, leading to a mechanical loss of adhesion between the box and the encapsulating resin that might be necessary to compensate with an

additional chemical adhesion during the curing process. Several techniques of functionalization of surfaces might be used. In target 5, different plasmas (under vacuum and atmospheric plasmas) and Corona treatments were studied and the materials of interest characterized before selecting the one to apply to the final devices to be tested. The main selected surface treatments were the application of:

❖ Low-pressure microwave plasma with oxygen, considering additionally economic and environmental aspects. The gas reaction mechanisms involve the interaction of neutral and charged plasma-created species, including free radicals, ions of either polarity, electrons and photons. These interactions create unstable short-life species on the polymeric surface that act as reactive centers against the encapsulating resin to produce strong interactions [42-43]. The oxygen as gas to generate the plasma has been found to be energetic enough to modify the surface energy of the treated surfaces and a non-destructive functionalization of polymeric surfaces [44-52]. A reduction in the contact angle with the polar solvent and an improvement on the surface energy is pursued with this treatment to increase the adhesion of the interface between the treated surface and the casting resin.

The low-pressure microwave plasma system used for the treatment is Plasma System 400 PVA TePla. Microwaves of 2.45GHz are applied through a window in the wall of the vacuum chamber producing a largely extended plasma there. The process chamber is made of aluminum with inner dimensions of (400mm x 400mm x 400mm). A mass flow rate of 50cm^3/min. of oxygen with 99.998% of purity is used for creating the plasma. The base pressure of the vacuum system is 5.2Pa, whilst the process pressure reached inside the chamber during the surface treatment is 13Pa. The microwave generator is an adjustable magnetron air-cooled operating at a frequency of 2.45 GHz and a power input of 150 W. The program requires a minimum of 20 min to carry out the treatment, then this system only allows to select multiples of 20 min. as treatment time.

❖ Atmospheric plasma. Different atmospheric plasma systems were studied but finally the atmospheric plasma system selected is Openair® Rotation jet RD1004 and plasma generator FG5001 by Plasmatreat GmbH (Figure 4.10). The treatment is made by a potential-free plasma flume that exits the nozzle at an angle, this involves that part is not exposed to high voltage, therefore, both plastics and metal can be effectively treated with the same system. The jet rotates, then the plasma is applied uniformly in the sample surface. The plasma is generated by an atmospheric pressure high-voltage discharge (1kW) in the jet's reaction chamber, creating a discharge that leaves the jet nozzle at high velocity onto the surface of the material to be treated. The working gas is oil free and water free compressed air (2.5 m^3/h) and the jet rotation is higher than 2800 rpm. The rotation jet working frequency is 23 kHz, as the output frequency of the generator unit [53-54]. Different designs of experiment (DOE) were carried out to define the process conditions, being the speed of the support with the sample and the distance sample

/plasma, the two studied variables. In every TDK Electronics' factory, all the machines for producing film DC caps works with a speed between 0.5-1.8 m/min, thus the speed of the plasma treatment was defined at 2m/min to not be a limitation on the production. As result of the conducted DOEs, a distance sample/plasma between 6-10 mm was defined to get the scope of a surface free energy of 75 ± 10 mN/m (by contact angle with polar and no-polar solvent) with the defined speed.

Figure 4.10. General set-up of atmospheric plasma by Plasmatreat GmbH (left) and detail of the Openair® Rotation jet RD1004 (right)

The surface treatments are applied to two different types of materials:

- Polymeric materials. To the internal faces of the plastic boxes to study the adhesion in the interface encapsulating resin/box.
- Conductive materials. To two different metallic samples with the same chemical composition:
    - Smooth plates
    - Rough sprayed material (schoop) as sheets and also in the windings with the welded wires.

Finally, the effectiveness of the any surface treatment in the plastic film capacitors is checked by operational tests under AC voltage, 85% of relative humidity and 85 ºC during 500 or 1000 hours compared to film capacitors without plasma treatment and standard process of production [55-56].

4.2. METHODS

4.2.1. N$_2$ adsorption-desorption at -196ºC

Gas adsorption measurements are widely used for determining the surface area and pore size distribution of a variety of different solid materials. The measurement of adsorption at the gas/solid interface also forms an essential part of many fundamental and applied investigations of the nature and behavior of solid surfaces.

 The intermolecular forces involved in physisorption are of the same kind as those responsible for the imperfection of real gases and the condensation of vapors. In addition to the attractive dispersion forces

and the short range repulsive forces, specific molecular interactions (e.g. polarization, field-dipole, field gradient-quadrupole) usually occurs as a result of particular geometric and electronic properties of the adsorbent and adsorptive.

It is convenient to regard the interfacial layer as comprising two regions: the surface layer of the adsorbent and the adsorption space in which enrichment of the adsorptive can occur. The material in the adsorbed state is known as the adsorbate, as distinct from the adsorptive, i.e. the substance in the fluid phase which is capable of being adsorbed.

When the molecules of the adsorptive penetrate the surface layer and enter the structure of the bulk solid, the term absorption is used. It is sometimes difficult, impossible or irrelevant to distinguish between adsorption and absorption: it is then convenient to use the wider term sorption which embraces both phenomena and to use the derived terms sorbent, sorbate and sorptive.

The term adsorption may also be used to denote the process in which adsorptive molecules are transferred to, and accumulate in, the interfacial layer. Its counterpart, desorption, denotes the converse process, in which the amount adsorbed decreases.

The relation, at constant temperature, between the amount adsorbed and the equilibrium pressure of the gas is known as the adsorption isotherm.

Many adsorbents of high surface area are porous and with such materials it is often useful to distinguish between the external and internal surface. The external surface is usually regarded as the envelope surrounding the discrete particles or agglomerates, but is difficult to define precisely because solid surfaces are rarely smooth on an atomic scale. A suggested convention is that the external surface be taken to include all the prominences and also the surface of those cracks which are wider than they are deep; the internal surface then comprises the walls of all cracks, pores and cavities which are deeper than they are wide and which are accessible to the adsorptive. In practice, the demarcation is likely to depend on the   methods of assessment and the nature of the pore size distribution. Because the accessibility of pores may depend on the size and shape of the gas molecules, the area of, and the volume enclosed by, the internal surface as determined by gas adsorption may depend on the dimensions of the adsorptive molecules (molecular sieve effect) [5].

In the context of physisorption, pores are classified according to their sizes [17].

(i)   pores with widths exceeding about 50 nm (0.05 μm) are called macropores;

(ii)   pores of widths between 2 nm and 50 nm are called mesopores;

(iii)   pores with widths not exceeding about 2 nm are called micropores.

These limits are to some extent arbitrary since the pore filling mechanisms are dependent on the pore shape and are influenced by the properties of the adsorptive and by the adsorbent-adsorbate interactions. The whole of the accessible volume present in micropores may be regarded as adsorption space and the

process which then occurs is micropore filling, as distinct from surface coverage which takes place on the walls of open macropores or mesopores. Micropore filling may be regarded as a primary physisorption process on the other hand; physisorption in mesopores takes place in two more or less distinct stages (monolayer-multilayer adsorption and capillary condensation).

Most solids of high surface area are to some extent porous. The *texture* of such materials is defined by the detailed geometry of the void and pore space. Porosity, ε, is a concept related to texture and refers to the pore space in a material. An *open pore* is a cavity or channel communicating with the surface of a particle or grain, as opposed to a closed pore. *Void* is the space or interstice between particles or grains. In the context of adsorption and fluid penetration *particle porosity* is the ratio of the volume of open pores to the total volume of the particle. It should be noted that this definition places the emphasis on the accessibility of pore space to the adsorptive.

Porosity is defined as the "fraction of the bulk volume of the porous sample that is occupied by pore or void space" [4]. This definition implies that a pore is the void space in the porous media, however, in natural reservoirs space is always occupied and never "void". According to the Schlumberger Oilfield Glossary [5] Gas adsorption is a well-established tool for the characterization of the texture of porous solids, specifically to the determination of surface area and porosity. Isotherms were measured by means of a Micromeritics ASAP 2420. After nitrogen adsorption, samples were submitted to a cleaning treatment. For that purpose, samples were outgassed at 200 ºC for 10 hours under a pressure of 1.33×10^{-2} Pa. In order to reach the temperature of -196ºC, the specimen holder was thermostatically controlled with a liquid nitrogen containing Dewar. Adsorption-desorption nitrogen isotherms were built from volume data of adsorbed nitrogen at different relative pressures.

Figure 4.11. Micromeritics ASAP 2420.

The most common way of determining the surface area of a solid is to find the monolayer value from the Brunauer, Emmet and Teller equation (1938) Equation 3.1 [17]. This equation considers the solid

surface as a distribution of adsorption sites in equilibrium with the adsorbate (N_2), where the velocity of the condensation of molecules over vacancy sites is the same than the evaporation velocity of the molecules in the occupied sites.

$$\frac{P}{V(P_0 - P)} = \frac{1}{V_m \cdot C} + \frac{C - 1}{V_m \cdot C} \cdot \frac{P}{P_0}$$

(Equation 3.1)

P_0 corresponds to the vapor saturation pressure of the adsorbed gas, V_m is the adsorbate volume (N_2) per gram necessary to cover the solid with a monolayer, V is the adsorbed gas volume per gram of solid for a pressure P and C is the BET constant related to the adsorption heat.

This equation is lineal in the range of relative pressures $0.005 < P/P_0 < 0.35$. V_m and C are calculated from the slope and intercept values. Once the monolayer volume is determined the specific surface BET (S_{BET}) is obtained by the equation 3.2 :

$$S_{BET} = \frac{V_m \cdot N \cdot A}{V_0}$$

(Equation 3.2)

Where N is the Avogadro number, A is the transversal section of nitrogen (16.2Å) and V_0 is the molar volume.

The study of the pore size distribution has been evaluated by the Barret, Johner and Halenda method (BJH) applied to the desorption branch.

4.2.2. Contact Angle Measurements

A higher lifetime will be presented by a metallized film capacitor operating under harsh humid environment if a good adhesion in every interface in the device is ensured. Then, the involved polymers require that they adhere well to the other substrate. Adhesion is a manifestation of the attractive forces that exist between all atoms and which fall into three broad categories: primary (chemical), quasi-chemical (hydrogen bond) and secondary (van der Waals). It is generally agreed that attraction due only to secondary forces and hydrogen-bonding is sufficient to produce adhesive joints between polymers of strength equal to that of the polymers themselves without the need for strong chemical bonds. Since these forces reduce as the inverse sixth power of the distance between molecules, it is apparent that surfaces to be adhered must come into intimate, wetting contact [33].

To examine the wetting and surface energy characteristics of the plasma treated and non-treated surfaces, static contact angle measurements with polar (water, H_2O) and non-polar solvents

(diiodomethane, CH_2I_2) were conducted in normal atmospheric conditions at room temperature ($20\pm2°C$) together with the Department of Material Science and Engineering of the Universitat Politècnica de Catalunya (UPC) under the supervision of Prof. José María Manero.

An OCA15plus (Dataphysics) goniometer equipped with a video software SCA20 (Dataphysics) was used. The contribution of polar (γ_s^p) and dispersive (γ_s^d) components on the total surface free energy (γ_s), were determined using Owens-Wendt-Rabel and Kaelbe (OWRK) method (Equations 3.3 and 3.4).

$$\gamma_s = \gamma_s^d + \gamma_s^p \qquad \text{(Equation 3.3)}$$

$$\gamma_L (1+ \cos \theta) = 2 ((\gamma_L^d \, \gamma_s^d)^{1/2} + (\gamma_L^p \, \gamma_s^p)^{1/2}) \qquad \text{(Equation 3.4)}$$

where γ_s for water solvent is 72.8 mN/m (51.0 and 21.8 mN/m, γ_s^p and γ_s^d, respectively) and for diiodomethane solvent γ_s is 50.8 mN/m (0 and 50.8 mN/m for γ_s^p and γ_s^d, respectively) [31, 32]. The registers of the static contact angles were carried out immediately after placing 3µl drops on the sample at a drop deposition rate of 1µl/s with a dosing needle Hamilton 500µl. The contact angle measurement is associated to a systematic error of $\pm$ 0.5°. At least 5 drops were averaged on 5 new surfaces for every measurement on internal face of a lateral wall of the box (Scheme 4.1.).
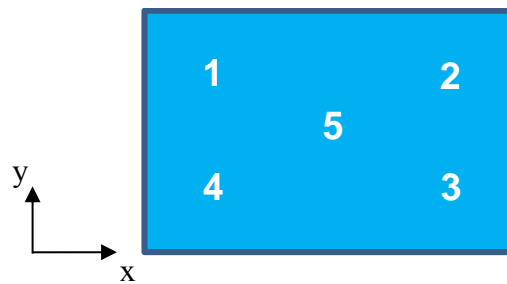
Scheme 4.1. Mapping scheme of drop deposition for contact angle measurements

4.2.3. Electrochemical Impedance Spectroscopy (EIS)

Impedance measurements in the sprayed metals, used as schoopage in the windings, were conducted with the purpose of studying the anodic behaviour of the different selected metals, to obtain information on the active-passive behaviour (dissolution, passivation, passivity) and to obtain practical results related to the dielectric properties of the metal oxides created in the surface of them.

Due to the fact that the processes under consideration are electrochemical, it is possible to analyse them using electrical methods, based on Faraday's law which relates the change in mass per unit area to the current flow. This approach involves relatively short measuring time, high accuracy and the possibility of monitoring continuously. However, the system under study has to be perturbed from its normal state by an external signal, which inevitably changes the properties of the system. In this study, the perturbation is caused by an ac signal.

As the applied potential is a sinusoid ($\Delta E \cdot \sin (\omega \cdot t)$) then the subsequent current will also be sinusoidal,

with a value $\Delta i \cdot \sin (\omega t + \varphi)$. Harmonics of this current (2ω, 3ω… etc.) will also flow. The relationship between the applied potential and the current flow is known as the impedance, which is analogous to the resistance-current-potential relationship of a dc circuit. The impedance (Z) has a magnitude ($\Delta E/\Delta i$) and phase (φ) and is thus a vector quantity.

However, if a sinusoidal potential is applied across a pure resistance of magnitude R, then the magnitude of the impedance Z = R and the phase φ = 0 for all frequencies. This is shown on a plot of the real (a) and imaginary (jb) components as a point on the real axis (Figure 4.12) overleaf [25-30].
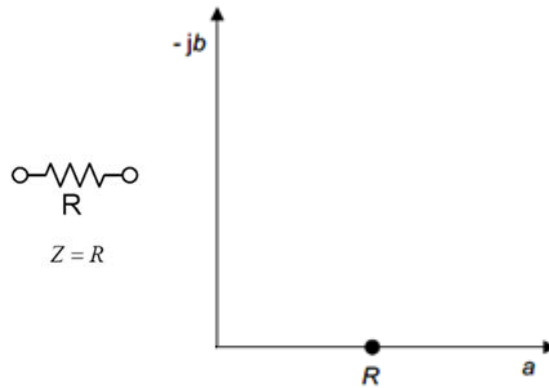
Figure 4.12. Complex plane impedance spectrum - resistance.

If the sinusoid is applied across a pure capacitance, the impedance is then dependent on the frequency, according to the relationship Z = $1/\omega C$ and the phase angle is 90°. As the frequency increases the magnitude of the impedance decreases, as illustrated in Figure 4.13.

The result of combining these two basic circuit components, in series or parallel, can be easily deduced for a series resistance and capacitance and a parallel resistance and capacitance, with two simple examples being depicted in Figure 4.14 and Figure 4.15.
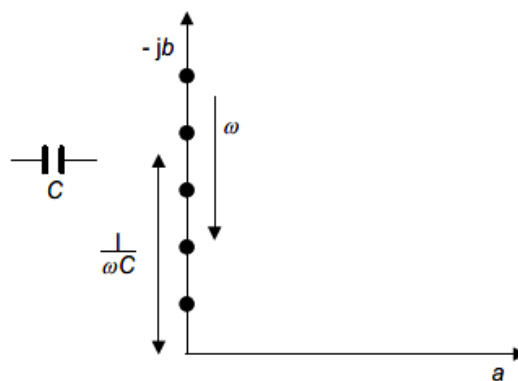
Figure 4.13. Complex plane impedance spectrum - capacitance.
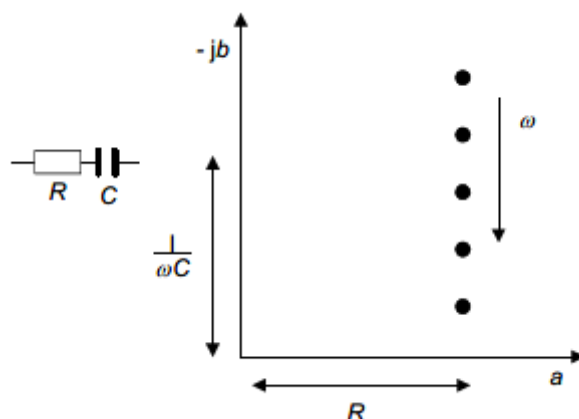
Figure 4.14. Complex plane impedance spectrum. Series resistance and capacitance.
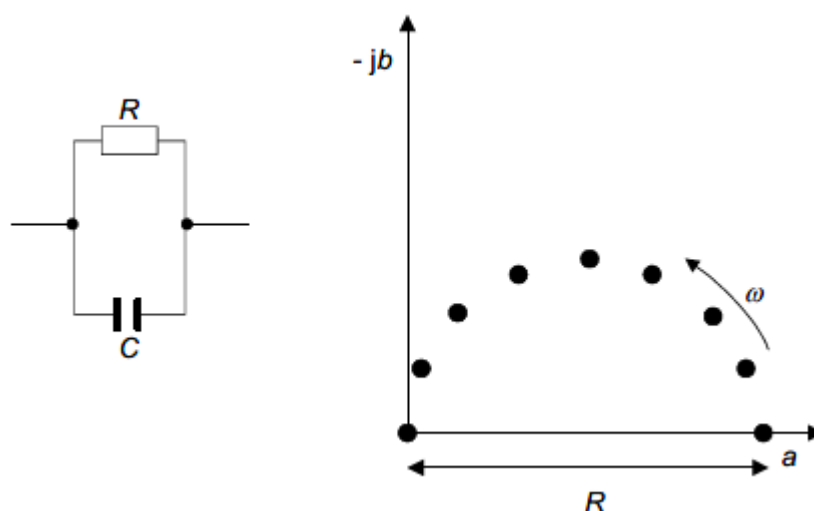
Figure 4.15. Complex plane impedance spectrum. Parallel resistance and capacitance.

An electrochemical cell can be represented by a network of resistors and capacitors, known as an equivalent circuit. From an impedance spectrum, (plotted in the real/imaginary plane, or as gain and phase versus frequency) it is possible to deduce the equivalent circuit and determine the significance of the different components.

The measurements of electrochemical impedance spectroscopy (EIS) were conducted in the laboratories of the National Center of Metallurgic Research (CENIM-CSIC as Spanish acronyms) in an equipment potentiostat/galvanostat Autolab PGSTAT302N and coupled to the FRA32N module, both manufactured by Metrohm/EcoChemie. Figure 4.16 shows the instrumentation used to perform the EIS measurements.
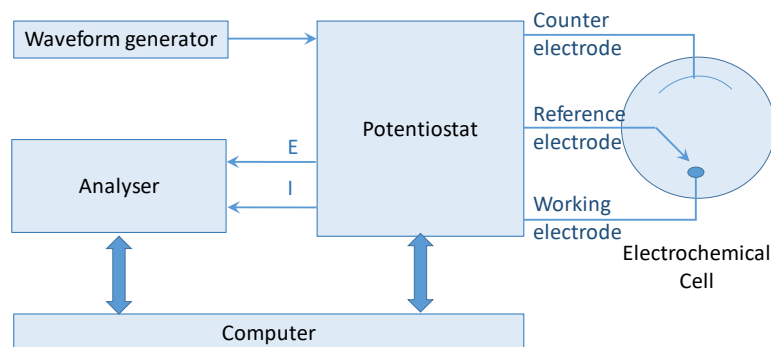
Figure 4.16. A block diagram of the EIS instrumentation.

The used electrolytic cell is a three-electrode configuration (Figure 4.17) to be able of determining the relationship between the current on the one hand and the voltage that is required to drive the reaction at the working electrode. Measurement of the potential between the working and reference electrodes allows the change in potential of the working electrode needed to create current to flow:

I.- A reference electrode of Ag/AgCl saturated in KCl (RE), used to measure the interface characteristics.

II.- A counter electrode of platinum (CE), connected to the working electrode.

III.- A working electrode (WE), being the schoopage samples/electrolyte interface at which the reaction occurs .
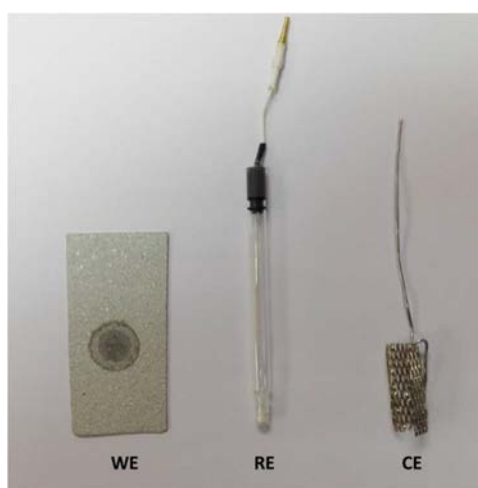
Figure 4.17. Set-up of electrolytic cell and the used three electrodes.

The electrochemical cell is located inside a Faraday cage (for very sensitive measurements on very low or very high impedance) to avoid external electromagnetic interferences and cross-talk between cables.

The scanned frequency ranges for the impedance measurements are between 10^5 Hz and 10^{-2} Hz, registering 71 values of impedance. To get shorter test times and to avoid the irreversible polarization of the samples during the measurements, at the lowest frequencies (10 mHz-1mHz) only 5 impedance values were registered instead of 10. The amplitude of the sinusoidal signal of the applied potential was ±10mV overlapped to the open circuit potential (OCP), to ensure that the answer signal is lineal and at the same time is not aging the sample during the measurement. Under these conditions, the EIS technique is considered a non-destructive test.

The impedance measurements (EIS) were done in–situ during the immersion test in an aqueous solution of NaCl 0.6M. The measurement protocol to apply consists in three stages:

1. The OCP is registered (Ecorr) during three minutes, this time is usually enough to get the stabilization of the corrosion potential of the samples.

2. The impedance spectrum is registered.

3. The samples are in repose stage in immersion in the electrolyte and the same measurement protocol is applied when the defined immersion time is reached.

The defined immersion times were:

- 0h

- 1 or 1.5h (in function of intrinsic characteristic on the samples to stabilise the measurements)

- 3h

- 24h

The electrolyte selected was an aqueous solution of NaCl 0.6M, same concentration than sea water, to accelerate the corrosion in 24h of immersion test.

The program ZView developed by Derek Johnson and commercialized by Scribner Associates Inc. (USA) based in the use of equivalent circuits and calculation routines was used for the interpretation of the impedance diagrams (Bode & Nyquist) and also for the simulation and result fitting based on complex nonlinear least square (CNLS) analysis result.

4.2.4. Focused Ion Beam Scanning Electron Microscopy (FIB-SEM) and Energy Dispersive Spectroscopy (EDS)

Electrons, used in scanning electron microscopes (SEM) and transmission electron microscopes (TEM), are not the only charged particles that can be accelerated and focused using electric and magnetic fields.

The lightest ion has almost 2000 times the mass of an electron and heavier ions can be another 250 times as massive. In a SEM, the relatively low-mass electrons interact with a sample non-destructively to generate secondary electrons which, when collected, provide high quality image resolution down to the sub-nanometer range. A focused ion beam (FIB) instrument is almost identical to a SEM, but uses a beam of ions rather than electrons, as the schematic diagram of a FIB instrument shows (Figure 4.18) [19].
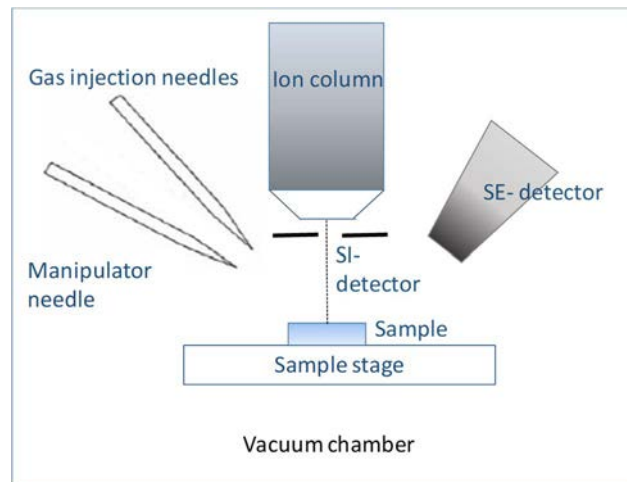
Figure 4.18. Schematic diagram of a FIB instrument.

When energetic ions hit the surface of the solid sample, these lose energy, being gained by the electrons as well as the atoms of the solid. The main physical effects of incident ions on the substrate are: sputtering of neutral and ionized substrate atoms (this effect eases substrate milling), electron emission (this enables imaging, but can additionally charge the sample), displacement of atoms in the solid (induced damage) and emission of phonons (heating). Chemical interactions comprise the breaking of chemical bonds, consequently dissociating molecules (effect promoted during deposition). The FIB can directly modify or "mill" the specimen surface, via the sputtering process, and this milling can be controlled with nanometer precision. By carefully controlling the energy and intensity of the ion beam, it is possible to perform very precise nano-machining to produce minute components or to remove unwanted material. In addition, ion beam assisted chemical vapor deposition can be used to deposit material with a level of precision similar to FIB milling. A small quantity of a specifically selected precursor gas is injected into the vicinity of the beam, where it is decomposed by the beam, depositing the nonvolatile decomposition products on the specimen surface while the volatile products are extracted by the vacuum system [18-23].
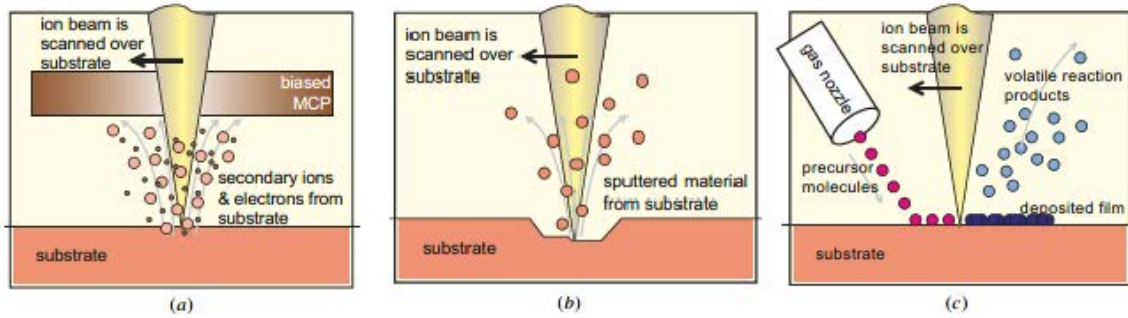
Figure 4.19. Principle of FIB (a) imaging, (b) milling and (c) deposition [21].

As pictured in Figure 4.19 (a), during FIB imaging the finely focused ion beam is raster scanned over a substrate, and secondary particles (ions, electros and neutral atoms) are created in the sample. As they quit the substrate, the electrons or ions are collected in a high performance Ion Conversion and Electron (ICE) detector.

Using a high ion current beam, the removal of sample material is obtained, involving consequently a physical sputtering of substrate, as pictured in Figure 4.19 (b). By scanning the beam over the sample, a random shape may be etched. In addition, FIB enables the localized maskless deposition of materials (both metal and insulator ones). The principle is chemical vapour deposition (CVD), and the process is illustrated in Figure 4.19 (c). Precursor gases are sprayed into the surface by a fine nozzle to be adsorbed. Then, the exciting ion beam decomposes the adsorbed precursor gases and the volatile reaction products desorb from the surface and are removed by the vacuum system, whilst the desired reaction products remain fixed on the surface as a thin film [21].

In any case, FIB becomes even more powerful when it is combined with a SEM. In the Dual beam instrument from FEI company used in this study, the microscope model Helios Nanolab 650, the SEM and the FIB column are combined in one system. The electron beam and the ion beam are positioned at 52° tilt compared to each other. *Figure 4.20.* illustrates the set-up in function of the region of interest characterized on this thesis.

a) Situation where the region of interest (red) is the surface or the sample edge, imaging is started immediately evaluating the secondary electrons with the SEM column.

b) When the region of interest is the bulk, a lot of material needs to be removed before the electron beam can access the whole surface to be imaged. Even more material needs to be removed to avoid shadow effects, because secondary electrons emitted close to a trench wall can be absorbed and will never reach the detector. Then the study is conducted in the FIB cross section but also evaluating the secondary electrons with the SEM column as Figure 4.20.b) shows.
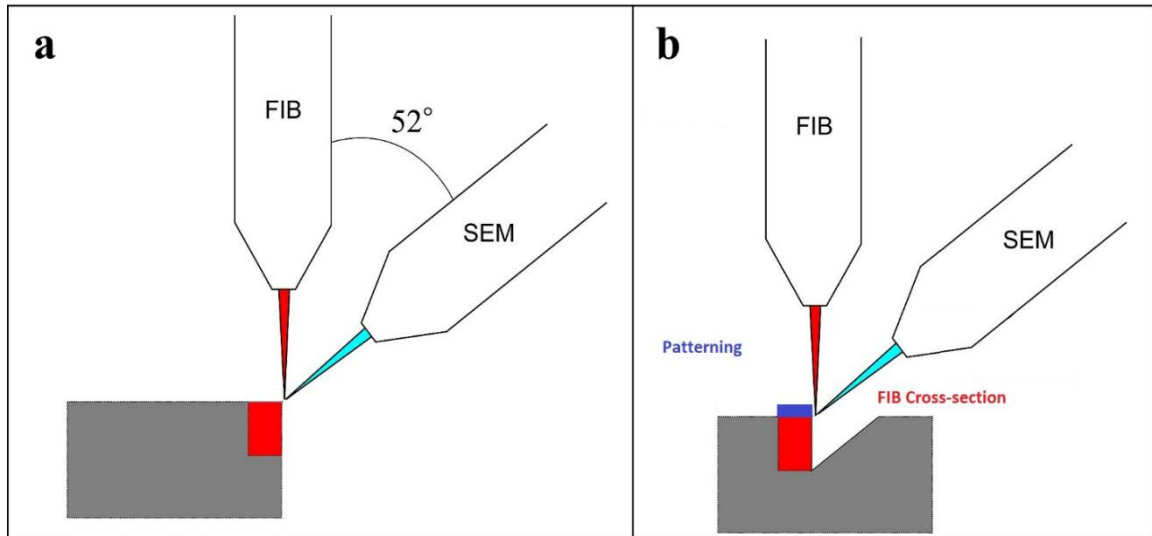
Figure 4.20. FIB-SEM scheme.

FIB-SEM characterizations of this thesis were performed in the Service of Dual Microscopy FESEM & FIB, part of the Central Services for Research of the University of Málaga and located in the Bioinnovation Center in the Unit of Nanotechnology. Helios Nanolab 650 is a unit with Dual Microscope from FEI Company [18]. The SEM column (Elstar XHR immersion lens FESEM column) has resolution of 0.8nm at 15kV and 0.9 nm at 1 kV and it bears an integrated monochromator (UC) and beam deceleration. It delivers sub-nanometer resolution across the whole 1-30 kV range. The FIB column (Tomahawk ion column (2 kV - 30 KV, 65 nA)) is differentially vacuum-pumped at the lowest part, allowing a well-defined beam profile to hit the sample surface. The equipment has got five gas injectors for nanodeposition and the local etching of certain materials too. Besides, the equipment has electrical microprobes and nanoidentation, EDX and EBSD+CBD detections and STEM detection.

For characterizing the elemental composition of the samples during the FIB-SEM analyses of this thesis, the technique of Energy Dispersive Spectroscopy (EDS) was used. The used detectors were, Oxford SDD (Silicon Drift Detector) X-ray detector [22] and AZtec EBSD (Electron Backscatter Diffraction) detector. The technique exploits the fact that an X-ray is created when an orbiting electron is displaced by an electron of the microscope beam (Figure 4.21) [22]. Analysis of the X-ray energy, a fundamental characteristic of an element, then leads to the identification of the element. A material is characterized at a single point by a value showing the ratios of elements, or, with an array of points over the substrate by the denominated elemental map that shows the individual elemental concentrations as a series of colour-coded images [22, 24].
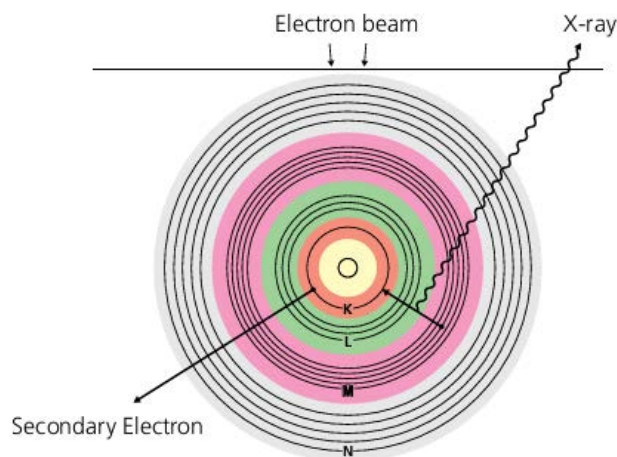
Figure 4.21. Generation of X-rays by electron bombardment [22].

4.2.5. X-ray Photoelectron Spectroscopy (XPS)

X-ray photoelectron spectroscopy is one of the most widely used analytical surface techniques. This technique is characterized for its high surface sensibility, allowing it to be applied to a wide range of study fields. This spectroscopy is based, as all the spectroscopies are, on the interaction between matter and photons. And in this particular case, the photoelectric effect is the physic principle applied [3]. When a sample is irradiated with photons of greater energy than the binding energy of the electrons of the atoms, electrons emerge from the sample with a kinetic energy which is equal to the excess of the incident photon energy. Kinetic energy is measured by means of the hemispheric detector as a function of the photon energy, the binding energy of the electron and the working function of the spectrometer Φ_{espec} which in turn can be approximated to a constant for each device and its value has to be periodically demonstrated. Therefore, kinetic energy can be expressed by the following equation:

$$E_c = \ h\nu - E_B - \Phi_{espec} \ \text{(Equation 4.1.)}$$

factor Φ_{espec} represents the working function of the spectrometer and E_B is the binding energy which is the ionization energy of the electron in its energetic level. A typical XPS spectrum shows the number of electrons accounts versus the binding energy of the inner levels of the atoms present in the solid [3].

Every element gives a unique and characteristic spectrum, in a way that kinetic energies measurements provide an elemental analysis, since any modification in E_B will be reflected in the Ec. This technique is able to analyze all the elements of the Periodic Table of elements excepting hydrogen and helium. Spectral peaks from a mixture of different components correspond, approximately, to the sum of the single peaks of each element in a way that elements on the surface of the sample can be identified. Detailed analysis of the photoelectron spectra reveals the correlation between the kinetic energy and the chemical state of the element and its compounds. This means that in some way there is a charge transfer through the chemical bound with the vicinity atom, provoking a variation of the observed kinetic energy.

Therefore, a qualitative analysis of the test sample can be carried out where we can have information of the present elements, oxidation state and even the coordination environment of the atom. Quantitative analysis is also able through the measurement of the area of the photoelectron peaks.
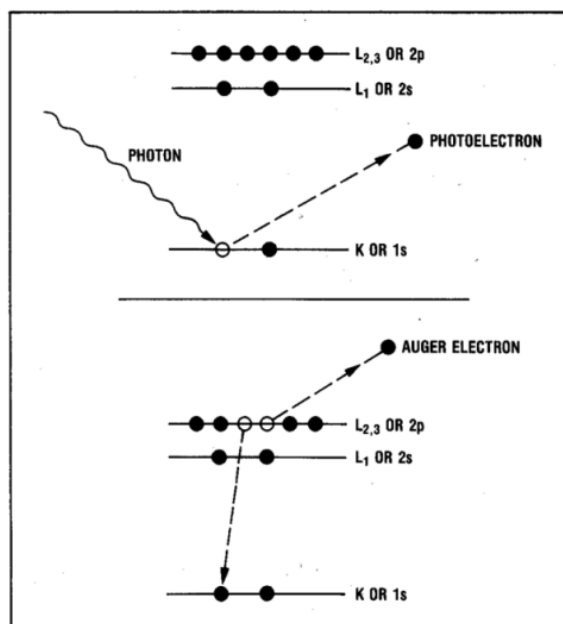
Figure 4.22. Scheme of photoelectron and auger electron emissions [2]

XPS technique allows the study of the surface because although X-ray radiation penetrates inside the matter in the order of 1-10 μm, the free mean path of photoelectrons is very little, between 0.5 and 4 nm. Therefore, photoelectrons from the sample come exclusively from its very external surface.

In order to determine the modifications produced on the outermost surface of the studied materials, XPS analyses were conducted ex-situ with a PHI ESCA 5701 spectrometer using a non-monochromatic Mg Kα radiation (1253.6 eV, 300 W and 15 kV) at a pressure of $5 \cdot 10^{-9}$ torr in the analysis chamber. The instrument is equipped with a hemisphere analyzer model PHI 10-360. Survey spectra to identify the elements on the surface were acquired in the range of 0-1100 eV and multiregion scans were registered on all significant photoelectron lines in the survey spectra (C 1s, O 1s, Si 2p, S 2p, Br 3d, F 1s, Na 1s and N 1s) [2]. High resolution spectra were recorded with constant pass energy of 29.35 eV. The spot size was of 720 μm diameter. The sputtering of the substrate was conducted with an ion gun of 4kV of argon ions and a sputtering area of (4x4mm).The atomic concentrations were calculated after a Shirley type background subtraction and calibrating the binding energies of all photoelectron lines with the C 1s photopeak position at 284.8 eV for C-C/C-H species of adventitious carbon.

4.2.6. Roughness measurement by Contact Stylus Profilometry

For controlling the function and reliability of precision components and the processes used to manufacture them, an accurate characterization of surface texture is critical. The American National

Standards Institute's B46.1 specification defines surface texture as the representative or random deviation from the normal surface that forms the three dimensional topography of a surface [6].

Roughness and waviness may create during manufacturing, and each process can produce different texture. Waviness, the more widely spaced repetitive deviations, may usually be associated to individual machine processes or to external environmental factors, such as vibration, chatter, heat treatment, or warping strains.

Roughness, the finer, is more frequently result of chemical or mechanical polishing, grinding or finishing processes.

In addition to roughness and waviness, surface texture may exhibit directionality. The predominant direction of surface irregularities is referred to as lay. Lathe turning, milling, drilling and grinding typically will produce surfaces with remarkable lay. Defects are also considered a component of surface texture.

Surface texture is not a measurable quantity; a unique "texture" value to every different surface cannot be assigned. However, it is possible to measure some of the intrinsic characteristics, or parameters, of surface texture. For this purpose, the Contact Stylus Veeco Dektak 150 Surface Profiler was used for characterizing the metal sprayed samples before any surface treatment (Figure 4.23.).

Figure 4.23. Contact Stylus Veeco Dektak 150 Surface Profiler

An area of 1mm x 1mm per sample was analysed twice using 500 lines in every area at a stylus speed of 20 μm/s per line, with a lateral resolution of 2μm and a vertical resolution of 0.067 μm/point. The selected stylus tip was terminated in a 45º cone with an end radius of 0.7 μm. This submicron stylus provides excellent resolution for roughness measurements [7, 9]. The used equipment is available in the Service of Optical, Morphological and Mechanical Characterization (part of the Central Services for

Research of the University of Málaga (UMA)) and placed in the Supercomputing and Bioinnovation Center.

The more frequent parameter worldwide standardized is the arithmetic average roughness height, or Roughness Average, Ra. It is defined as the arithmetic mean of the departures of the profile from the mean line. An approximation of average roughness (Ra) is obtained by adding the Y values without regard to sign and dividing the sum by the number of samples taken.

Ra is used to detect general variations in overall profile height. A change in Ra usually involves a new variation in the process. It may be a change in the tool, the coolant, the material, or any other machine related factor. However, Ra cannot detect differences in spacing and its distribution, or the presence or absence of infrequently occurring high peaks and deep valleys.

Rq (or also known as RMS) is the rootmean-square average of the departures of the roughness profile from the mean line. Rq has statistical significance because it represents the standard deviation of the profile heights and it is used in the more complex computation of skewness, the measure of the symmetry of a profile about the mean line.

Rt is defined as the sum total of the maximum height of the highest point of roughness above the mean line, Rp, and the maximum depth or the lowest point of roughness below the mean line, Rv [8, 10].

Figure 4.24. provides descriptions of those roughness parameters. These figures are showing that the scans are divided into five consecutive and equal portions representing the waviness filter cut-off length.
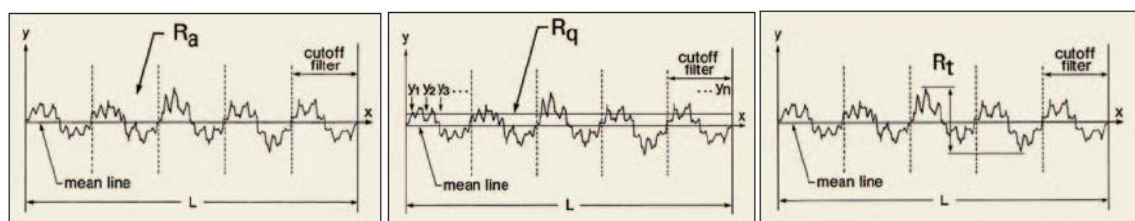
Figure 4.24. Description of Ra, Rq and Rt roughness parameters within the assessment length (L) [8].

4.2.7. Roughness measurement by Stylus Perthometer

The roughness of the surfaces before and after the application of the plasma treatment was measured in the internal faces of the capacitor boxes with a contact-type surface roughness instrument. A perthometer Hommel-Etamic T8000 by Jenoptik was used with the software EVOVIS 1.42.0.3 for this determination due to be available in TDK Electronics Components S.A.U. laboratory [40]. The measuring conditions following the standard EN ISO 4287 were an evaluation length (λn) of 2.5 mm in traversing length of 15 mm with a speed of 0.50 mm/s and a cut-off (λc) of 2.5 mm.

This contact-type method was used to measure the roughness by lines when the characterization of the surface of a material treated with plasma was required, due to the fact that the effects of the plasma treatment start to expire during the first week. However, every material characterization included in this

study has been performed exactly at the same time than the metallized film capacitors were encapsulated. This was done with the purpose of correlating properly the Temperature/Humidity/Bias test results on the devices with representative results on the material characterizations.
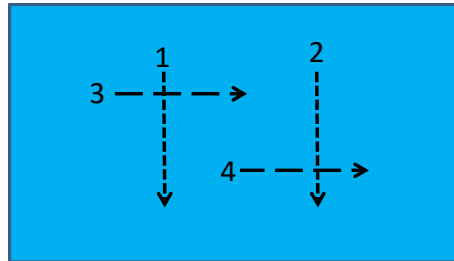
Figure 4.25. Mapping scheme of roughness measurements by Perthometer Hommel-Etamic W10.

The Perthometer Hommel-Etamic T8000 was used to characterized the roughness in-situ just after the plasma application. This equipment does not allow to scan a surface. The detector tip was equipped with a stylus tip, which traced four lines per sample on the internal face of a lateral wall of the box (Figure 4.25) with a measurement speed of 0.50 mm/s, a measuring range of 150 μm and a resolution of 6nm. The selected stylus tip was made of diamond with an end radius of 2μm and 90º. The measured roughness in the four lines were averaged to approach the roughness of the surface of every material. This is the reason to include different roughness parameters, to check the validity of this approach in all of them by means of a low standard deviation of the averaged values of the four lines per material.

The arithmetic mean roughness in the evaluation length, Ra, does not differentiate between peaks and valleys (Figure 4.26) and has therefore a relatively weak information character that is complemented by the total height of profile in the evaluation length, Rt, the highest peak, Rp and the deepest valley, Rv. Then these four roughness parameters were determined [41].
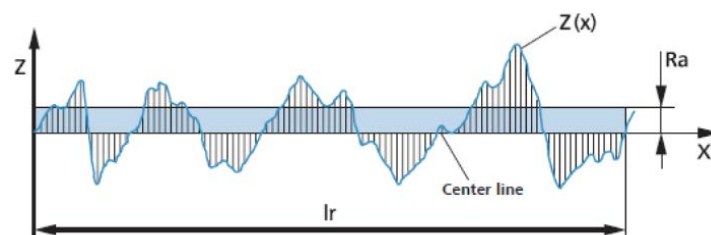
Figure 4.26. Arithmetical mean roughness, Ra, according to ISO 4287 [41].

4.2.8. Water Vapor Transmission Rate (WVTR)

With the aim of knowing the potential protection against humidity, the water vapor transmission rate (WVTR) of a wide spectrum of materials with a key role in the metallized film capacitors; epoxies, polyurethanes, silicones and metal sprayed samples, has been characterized in AIMPLAS Plastic Technology Centre facilities by means of a diffusion cell apparatus according to ASTM F1249-13 [1, 12]. The used equipment was a PERMATRAN-W MG 3/33 manufactured by MOCON Inc.

Flat thin sheet samples are clamped into the test cell. Test cells are divided into two chambers separated by the sample material. The inner chamber is filled with nitrogen as carrier gas, and the outer chamber with water vapor as test gas. Molecule of water, delivered to the outer chamber by the test gas, diffuse through the sample to the inside chamber and are conveyed to the sensor by the carrier gas. The computer monitors the increase in water vapor concentration in the carrier gas, being this value the water vapor transmission rate [16].

The used test conditions for determining the vapor transmission were 38.0 ± 0.5ºC and $90 \pm 3\%$ of relative humidity (%RH) in a nitrogen flow of 10.0 ± 1.0 ml/min according with the chamber schemed (Figure 4.27). The relative humidity of the test gas is generated by the frequency modulation method (no need for salts to select humidity) and controlled by a pressure method. The barometric compensation is not applied to the results. The WVTR and thickness of four specimens per sample are measured to be averaged.

An effective circular area of 50 cm^2 was exposed to permeation. When a smaller testing area is used, fewer molecules permeate through this reduced testing area and fewer molecules will reach the sensor. This will influence the original sensitivity of the instrument, which has been defined with a standard testing area of 50 cm^2. Therefore, this full size of 50 cm^2 of testing area is the one used always that the material allows it in terms of surface flatness/curvature.

In the specific material studies where this characterization is conducted with a 5 cm^2 circular exposed area, this will be indicated, and all the materials included in the same comparison will be analyzed under the same test conditions [11].
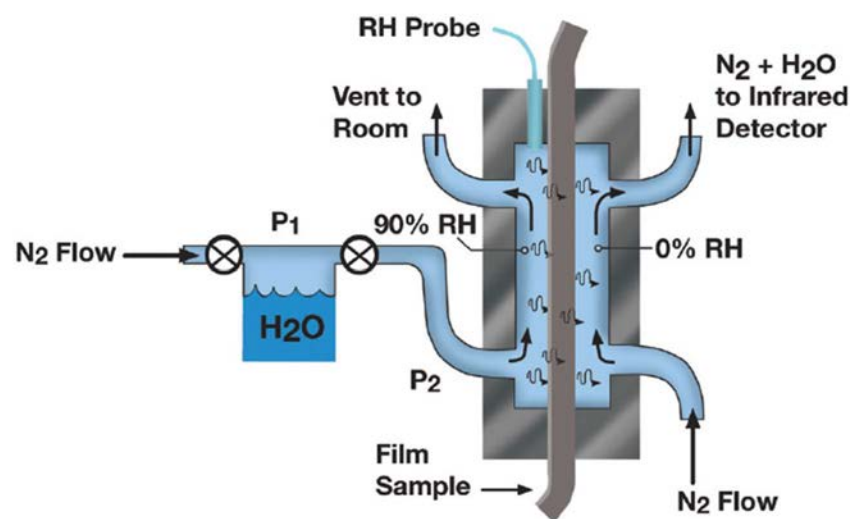
Figure 4.27. Schematic of a water vapour transmission rate test [12].

4.2.9. Oxygen Gas Transmission Rate (O$_2$GTR)

The rate of transmission of oxygen gas (O$_2$GTR), at steady state, through different materials has been determined in AIMPLAS Plastic Technology Centre facilities by means of a diffusion cell apparatus using a coulometric detector according to ASTM F1927-14 [14, 17]. The used device was OX-TRAN Model 2/21 manufactured by MOCON Inc.

Flat thin sheet samples are clamped into the diffusion cell, which is then purged of residual oxygen using an oxygen-free carrier gas. The carrier gas is routed to the sensor until a stable zero has been stablished. Pure (99.9%) oxygen is then introduced into the outside chamber of the diffusion cell. Molecules of oxygen diffusing through the material to the inside chamber are conveyed to the sensor by the carrier gas.

The test conditions used for determining the oxygen gas transmission rate were 23.0 ± 0.5ºC, $50 \pm 3\%$ of relative humidity in oxygen and $50 \pm 3\%$ of relative humidity in a nitrogen flow of $10.0 + 1.0$ ml/min according with the chamber schemed (*Figure 4.28.*).

The OTR and thickness of two specimens per sample were measured to be averaged.

An effective circular area of 5 cm^2 was exposed to permeation. The samples were oriented in the diffusion cell with the coarse side in contact with the permeant gas.
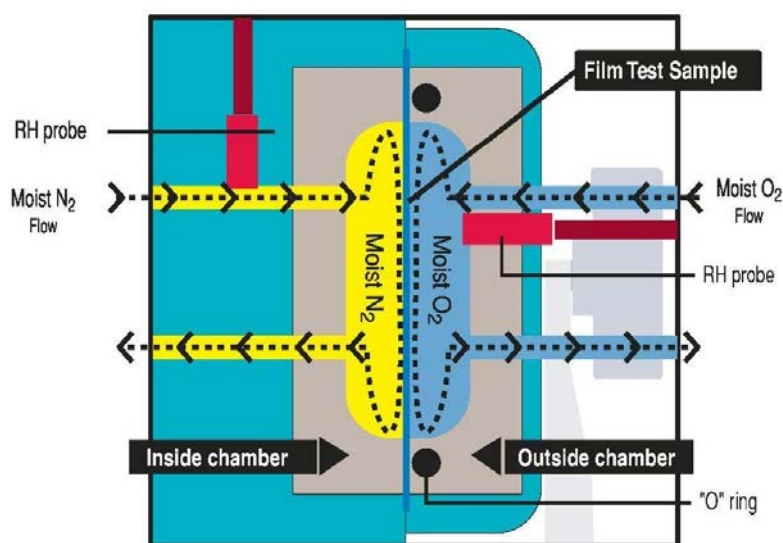
Figure 4.28. Side view of the diagram of an oxygen transmission rate (OTR) test cell [15].

4.2.10. Fourier Transformed Infrared Spectroscopy (FTIR)

Fourier Transformed Infrared Spectroscopy (FTIR) was used to study the changes of the functional groups of the polymeric materials before and after submitting the samples to aging programs and also to study the effects of the plasma application. FTIR Spectroscopy is a molecular spectroscopy which is used to characterize both organic and inorganic evidence. The sample is irradiated with infrared

radiation, when the frequency of this infrared radiation matches the natural frequency of the bond, the amplitude of the vibration increases, and the infrared is absorbed. The output of an infrared spectrophotometer is a chart.

FTIR is the preferred method of infrared spectroscopy because it overcomes the limitations encountered with dispersive instruments by using an interferometer. The interferometer produces a unique type of signal which has all the infrared frequencies "encoded" into it. The signal can be measured very quickly, usually in the order of one second or so [37-39].

The FTIR spectra were recorded in the Material Laboratory of Central R&D in TDK Electronics Components, S.A.U. by using an ALPHA FT-IR Spectrometer (Bruker Optik GmbH) at room temperature covering the wavenumber range of mid-IR region, 4000-400 cm^{-1}, 40 scans were averaged with a resolution of 4cm^{-1} and a diamond prism. A background reading was taken before collecting spectra from the samples and was subtracted from the sample one.

4.2.11. Thermo-Gravimetric Analysis (TGA)

Thermo-Gravimetric Analysis (TGA) is a technique in which the mass of a substance is measured as a function of temperature and/or time whilst the sample is submitted to controlled temperature schedule. The components of TGA instrument is schemed in Figure 4.29. The TGA analysis provides information about temperatures at which the degradation of a material occurs and the content of organic and inorganic components in the sample (ash content). It consists of a high-precision balance with a platinum crucible loaded with the sample. The crucible is located in a small electrically heated furnace with a thermocouple that accurately measures the temperature and a computer that control the instrument. The characterization is carried out by increasing the temperature gradually and plotting weight against temperature [34-35].
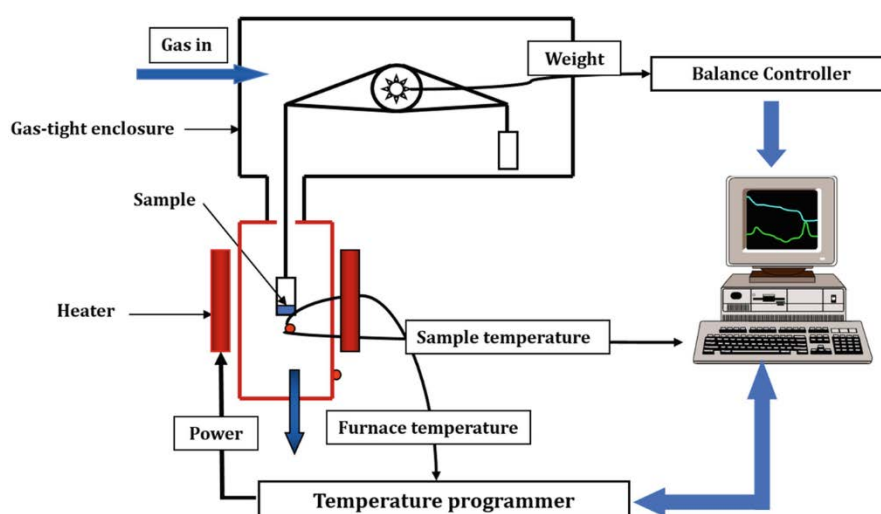
Figure 4.29. Diagram of the set-up of the thermo-gravimetric analysis [36].

The thermal decomposition of the encapsulating resins and the thermoplastics injected as boxes was determined using a Discovery TGA550 (TA Instruments) placed in the Material Laboratory of Central R&D in TDK Electronics Components, S.A.U. [36] By means of the TGA curves the changes in the polymer structures submitted to thermal/humid aging programs and the evolution of the polymer structures (between soft and hard segments) were studied.

The analyses were carried out using a purge gas of nitrogen. Nitrogen and dried air were used as testing gases. The samples use to have a weight of 15-20 mg. The applied thermal program to every sample was always the same:

1. Thermal equilibrium at 30ºC

2. Heating from 30ºC to 800ºC with a heating rate of 10ºC/min in inert atmosphere (nitrogen with a flow of 50ml/min).

3. A change in the atmosphere from a testing gas of nitrogen to dried air.

4. An isotherm at 800ºC with dried air during 10 minutes to ensure the total combustion of the organic part of the sample.

4.2.12. Differential Scanning Calorimetry (DSC)

Differential scanning calorimetry (DSC) is a thermal technique in which the difference between the heat flows from the sample and reference sides of a sensor is measured as a function of temperature or time. Differences in heat flow arise when a sample absorbs or releases heat due to thermal effects such as melting, crystallization, chemical reactions, polymorphic transitions, vaporization and many other processes. Specific heat capacities and changes in heat capacity, for example, during a glass transition, can also be determined from the difference in heat flow.

This method uses individual heaters to maintain identical temperatures for the sample and the reference. The differential power needed to maintain both sample and reference is recorded as a function of temperature. Figure 4.30 depicts an idealized DSC thermogram.

In this thesis, DSC studies were done in two different types of materials:

a) In thermoplastics injected as boxes. The aim was to confirm that the material was correctly processed reaching the optimum glass transition temperature of the material and its complete crystallizations. Therefore, if the material shrinks (failure) as boxes after the functional stress test on the capacitors, it can be discarded any wrong processing condition.

b) Elastomers as encapsulating resins. DSC was used as complementary technique to thermo-gravimetric analysis (TGA). By DSC were determined the glass transitions, melting and crystallization processes below room temperature to confirm the correct processing conditions and to be completed the curing (cross-linking) of the resins.
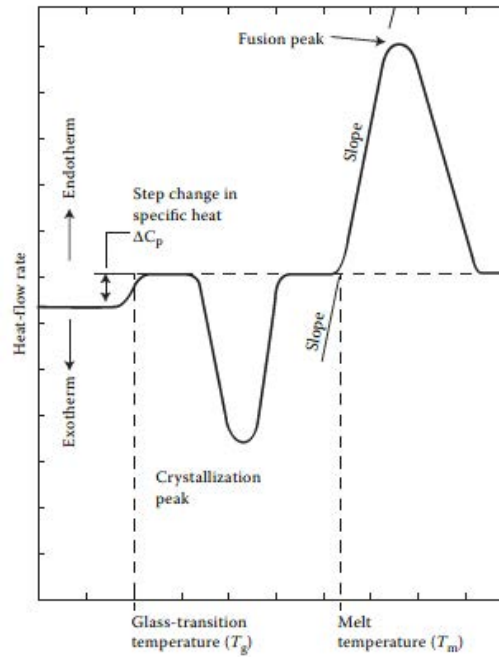
Figure 4.30. Idealized DSC thermogram of a semicrystalline polymer.

DSC curves were carried out in the Material Laboratory of Central R&D in TDK Electronics Components, S.A.U. by using a Mettler Toledo DSC1 calorimeter and the software STARe. The approximate weight of sample characterized for every material was 5 mg. The curves were determined in aluminum crucibles of 40ul using an empty crucible as reference. The operation temperature range was from -30ºC to 800ºC using a heating rate of 10ºC/min in inert atmosphere, a nitrogen flow of 50ml/min.

4.3.   Operational tests on DC film capacitors and naked windings

4.3.1. Temperature-Humidity Bias Test (THB) at 85ºC/85%RH/305Vac

The ability to self-healing the selected metallized film dielectric assures a safe failure mode in AC filtering applications, where to the fundamental frequency are frequently or occasionally added peak voltages and electrical noise. The self-healing result is a minor loss of capacitance, then recovering the initial capacitor electrical properties.

The selected dielectric, polypropylene, is the best in terms of self-healing. X and Y RFI (Radio Frequency Interference) capacitors, as it is the case of study, are designed to optimize the self-healing performance. However, to design focused in self-healing may make these types of MKP wound box capacitors more sensitive than others to loss the capacitance under the exposure of a harsh environment.

In general, X-capacitors are mounted in parallel with the power line, for filtering electromagnetic interference, from both the grid power and the equipment, and also protecting the device from voltage peaks. In general, for this application are used capacitors with large nominal tolerance (even $\pm$ 20%).

Recently for X capacitors, the capacitance stability and a low tolerance have become a key feature due to a substantial development of applications in series to the power line, where the capacitor itself plays the role of feeding AC voltage to the circuit, by a capacitive divider.

This necessity promoted the introduction of the temperature/humidity/bias (THB) as qualification test for X capacitors. THB test is conducted during 1000h at 85ºC and 85% relative humidity applying usually 240Vac for X2 capacitors. The pass criteria of performance is to get a drop of capacitance no larger than 10%.

Other humidity requirement might consist of slight variations in the temperature and relative humidity combination of the just mentioned test. Table 4.1. shows the absolute water content (g/m^3) for the most usual combination of temperature and relative humidity:

Table 4.1. Absolute water content for different temperature/relative humidity conditions.

Temperature (ºC)	Temperature (K)	Relative Humidity (%R.H.)	Water content (g/m^3)	Water content with respect to 85ºC/85%R.H. (%)
40	313	93	48	16%
60	333	85	111	37%
60	333	95	123	41%
70	343	70	138	46%
85	358	85	294	100%

In this table can be observed that the absolute water content of the 85ºC/85%R.H. condition is 6 times higher than the found under 40ºC and 93%R.H., that it is the more frequently specified in the international standard of the X2 capacitors. These standard do not use to cover all the requirements for real applications for this reason and also because is missing the requirement of applying a V_{AC} waveform during the humidity test.

THB is an accelerated endurance test and, hence, stresses the components more than real operation.

In the real application both stresses are present, a V_{AC} and 85ºC/85%R.H. To test like this increases substantially the magnitude of the environmental stress on the devices, because voltage and humidity are combined.

Seven film capacitors per group of sample are tested under the THB test in this thesis under the most exigent conditions. The film capacitors are loaded with 305Vac at 50Hz using a Chroma 6460 Serie AC source. The climatic conditions at 85 ºC and 85 R.H.% are produced by a climatic chamber Climats EXCAL 2223- HA controlled by Spirale 3 system with a temperature and humidity regulation stability of +/- 0.1 °C and +/- 1 R.H.%, respectively. The capacitance and the dissipation factor (tan δ) of the metallized film capacitors are measured. For the selected type of capacitors, MKP wound box capacitor, the generic standards specify same measuring conditions for dissipation factor as for capacitance (IEC

60068-1). 1kHz is the standard measuring frequency but in addition to this, the dissipation factor was measured also at 10 kHz. The found losses at 1kHz are associated with the dielectric (i.e. the energy invested to polarize the dielectric in two possible directions for successive half-cycles of the AC voltage). However, at 10 kHz the series component tan δ_S determines mainly the losses, then it is associated to the sum of the contacts as the wires, schoop and electrode metallization. Those electrical properties were measured every 100h of test at ambient conditions, being compared with the initial measured values. These electrical measurements were conducted using a Danbridge CLR Tester CT-30 with an accuracy of 0.05%.

4.3.2. Robustness of terminations. Test Ue$_2$ – Pull-off test.

MKP wound box capacitors might be submitted to mechanical stress during the device production and handling, as it was described in paragraph 1.2.7.1. For the study of different sprayed schoop materials (target nr. 4 defined in Section 3) the robustness of the wire welding onto every schoop composition is tested by Test Ue$_2$ – Pull-off test according to IEC 60068-2-21[57] (*Table 1.10*).
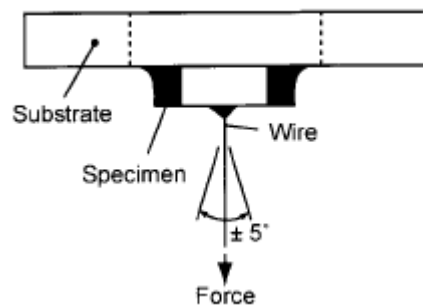
Figure 4.31. Force test Ue2 – pull-off [57].

Figure 4.32. Set-up of mechanical test (tensile) on terminals with dynamometer model 9180 (Burster).

The strength of the solder weakens with time, then this will influence the test results. The test shall be performed after 24h ± 6h of time between welding and testing. A suitable pulling tool is attached to the center of the specimen by clamping or by a wire fastened perpendicularly to the top of the sample mounted on its substrate.

Once the sample is firmly held, a pulling force of 10N is applied gradually at a constant rate. The maximum force is reached within 5 s and is kept constant for 10 s ± 1 s and the force is applied along an axis within 5º to the normal (Figure 4.31).

For this test, five naked windings per schoop variable are tested and averaged. It is used the digital dynamometer model 9180 (Burster) with a measurement accuracy of 0.1% of full scale (F.S.) that it is available in TDK Electronics S.A.U. factory (Málaga, Spain) (Figure 4.32). In function of the lead space (LS) and the wire diameter is selected the tool for the measurement, being the capacitor terminals introduced in the specific spaces indicated for this purpose.

4.3.3. Impulse voltage test

The impulse voltage test is specified by IEC/EN 60384-14, clause 4.13. [58]. This standard defines the application of a minimum of 3 up to maximum 24 impulses of the same polarity to each capacitor and a time between impulses higher than 10 seconds. Nevertheless, for the study of schoops (section 3, target 4), more exigent conditions are applied to compare the different variables. Three capacitors per variant are evaluated and 30 impulses for every intensity level is applied with a time between impulses of 5 s. The ambient conditions are a temperature of 20ºC and an approximated relative humidity of 47%. The test is initiated at 20 A per meter of electrode until reaching 60 A/m with a ramp-up of 5 A/m between intensity levels. The applied waveform for every current impulse level is illustrated in Figure 4.33.

Figure 4.33. Applied waveforms for each current impulse level.

4.4. References

[1] Stevens, M., *Permeation and its impact on Packaging*, MOCON, Inc. Minneapolis, MN USA.

[2] Moulder, J.F., Stickle, W.F., Sobol, P.E. *Handbook of X-ray Photoelectron Spectroscopy*, (1992).

[3] Faraldos, M. and C. Goberna, *Técnicas de análisis y caracterización de materiales.* Consejo Superior de Investigaciones Científicas, (2002).

[4] Dullien, F.A. *Porous media: fluid transport and pore structure* (2nd Ed). Academic Press., (1991).

[5] Sing, K. S. W., Everett, D. H. , Haul, R. A. W. , Moscou, L., Pierotti, R. A. , Rouquerol, J., Siemieniewska, T. (IUPAC, Physical Chemistry Division, Commission on colloid and surface chemistry including catalysis) *Reporting physisorption data for gas/solid systems with Special Reference to the Determination of Surface Area and Porosity.* Pure & Appl. Chem., Vol. 57, No.4 (1985), 603-619.

[6] American Society of Mechanical Engineers. *ANSI B46.1. Surface Texture (Surface Roughness Waviess and Lay*), (2002).

[7] Zecchino, M. *Dektak Stylus Capabilities. How to choose the correct stylus for any application.* Bruker Corporation, (2010).

[8] Chi, T., Ballinger T., Olds, R. and Zecchino M. *Surface texture analysis using Dektak stylus profilers*. Bruker Corporation, (2010).

[9] Veeco Instruments Inc. *Dektak 150 with 200mm wafer support*. Specification B509, Rev A4, (2009).

[10] International Organization for Standardization. *ISO/DIS 4287/1, Surface roughness. Terminology. Part 1: Surface and its parameters*. First edition, (1984).

[11] MOCON Inc. *Reducing the test area of a barrier film for permeation analysis.* Technical Bulletin. TB.PP.5003. Version 1.0. (January 5th, 2018)

[12] MOCON Inc. *ASTM E96 vs. F1249. Which provides more accurate test results?* White Paper WP.PPS.3000 Version 1.0 (May 16th, 2017)

[13] ASTM F1249 – 13. *Standard Test Method for Water Vapor Transmission Rate Through Plastic Film and Sheeting Using a Modulated Infrared Sensor*.

[14] ASTM F1927 – 14. *Standard Test Method for Determination of Oxygen Gas Transmission Rate, Permeability and Permeance at Controlled Relative Humidity Through Barrier Materials Using a Coulometric Detector*.

[15] MOCON Inc. *Specification OX-TRAN Model 2/21*. OX2/2104025M (2002)

[16] MOCON Inc. *Specification PERMATRAN-W® Model 3/33*. Brochure Code 1011A (2010)

[17] Thommes, M., Kaneko, K., Neimark, A. V., Olivier, J.P., Rodríguez-Reinoso, F., Rouquerol, J. and Sing F. S. W. (IUPAC, Physical Chemistry Division, Commission on colloid and surface chemistry including catalysis) *Physisorption of gases, with special reference to the evaluation of surface area and pore size distribution (IUPAC Technical Report)*. Pure & Appl. Chem. (2015) 87(9-10): 1051–1069

[18] FEI Company. *Product Data Helios NanoLab^{TM} 650*. DS0070 01 (2012)

[19] Giannuzzi, L. A. and Stevie, F. A. Introduction to Focused Ion Beams. Springer Verlag (2005)

[20] Martín Gago, J.A. *Capítulo 19. La microscopía para el estudio de materiales y láminas delgadas*, in *Láminas delgadas y recubrimientos: preparación, propiedades y aplicaciones*, Albella, J.M. (Editor). Editorial CSIC. (2012) pp. 519-540.

[21] Reyntjens, S. and Puers, R. *A review of focused ion beam applications in microsystem technology*. Journal of Micromechanics and Microengineering, 11 (2001) 287-300.

[22] OXFORD Instruments Plc.. *Product Datasheet Silicon Drift Detector (SDD) Explained*. Document Reference OINA/SDDExplained/0112 (2012) https://nano.oxinst.com/product/eds-for-sem-and-fib

[23] Tseng, A. A. *Recent developments in micromilling using focused ion beam technology. Journal of Micromechanics and Microengineering*, 14 (2004) R5-R34.

[24] Friel, J. J. and Lyman, C. E. *X-ray Mapping in Electron-Beam Instruments*. Microscopy and Microanalysis 12 (2006) 2-25

[25] Cogger, N. D. and Evans, N. J. *An introduction to Electrochemical Impedance Measurement*. Technical Report No. 6 Solartron Analytical, Part No.: BTR006 (May 1999)

[26] Gabrielli, C. Identification of electrochemical processes by frequency response analysis. Technical report No. 004/83, Solatron Analytical (March 1998)

[27] Gamry Instruments. *Application Note. Basic of Electrochemical Impedance Spectroscopy*, Rev. 5 (2007)

[28] Princeton Applied Research. Application Note AC-1. Basics of Electrochemical Impedance Spectroscopy.

[29] Amand, S., Musiani, M., Orazem, M. E., Pébère, N., Tribollet, B. and Vivier, V. *Constant-phase-elemet behaviour caused by inhomogeneous water uptake in anti-corrosion coatings*. Electrochimica Acta 87 (2013) 693-700

[30] Gui, F. and Kelly, R. G. A study of performance of corrosion prevention compounds on AA2024-T3 with electrochemical impedance spectroscopy. Electrochimica Acta 51 (2006) 1797-1805

[31] W.R.Good. *A comparison of contact angle interpretations*. Journal of Colloid and Interface Science. 44(19 (1973) 63-71.

[32] D.Y. Kwok; A.W. Neumann. *Contact angle measurement and contact angle interpretation.* Advances in Colloid and Interface Science 81 (1999) 167-249.

[33] Owens, D. K. and Wendt, R. C. *Estimation of the Surface Free Energy of Polymers.* Journal of Applied Polymer Science, Vol. 13 (1969) pp. 1741-1747.

[34] Bottom, R. *Thermogravimetric Analysis, in Principles and Applications of Thermal Analysis.* Ed. P. Gabbott, Blackwell Publishing Ltd., Oxford, UK. (2008).

[35] Hatakeyama, T., Quinn, F. X. *Thermal Analysis: fundamentals and applications to polymer science.* 2nd Edition. John Willey & Sons Ltd. ISBN 0-471-98362-4 (1999).

[36] TA Instruments. *High performance TGA systems. TGA 550 Specification.* Brochure nr. L90036.001 (2018)

[37] Griffiths, P. R. and Haseth, J. A. *Fourier Transformed Infrared Spectroscopy.* Wiley-Interscience 2nd Edition, (2007) 1-18.

[38] Koptsov, A. H. and Zhizhin, G. N. *Handbook of Fourier Transform Raman and Infrared Spectra of Polymers.* Physical Sciences Data 45, Elsevier. ISBN 0-444-82620-3 (Vol. 45) (1998).

[39] Socrates, G. Infrared and Raman Characteristic Group Frequencies. Tables and Charts. 3rd Edition. John Wiley & Sons, Ltd. ISBN 0-470-09307-2 (2004) 1-6.

[40] JENOPTIK. *Waveline. Roughness and contour metrology.* Technical Data Hommel-Etamic 1007 2148 (2017) 52-54.

[41] ACCRETECH-TOKYO SEIMITSU. *Surface Texture. Contour Measuring Instruments. Chapter "Explanation of Surface Characteristics".* 230-237.

[42] Pastor-Blas, M.M., Martín-Martínez, J.M. and Dillard, J.G. *Surface characterization of synthetic vulcanized rubber treated with oxygen plasma.* Surf. Interface Anal. 26 (1998) 385.

[43] Inagaki, K. *Plasma surface modification and plasma polymerization. Interaction between plasma and polymeric materials.* Lancaster:Technomic Publishing. 2 (1996) 22-28.

[44] Liu, D., Chen, P., Chen, M. and Liu, Z. *Improved interfacial adhesion in PBO fiber/bismaleimide composite with oxygen plasma plus aging and humid resistance properties.* Materials Science and Engineering A 532 (2012) 78-83.

[45] Lawrence, J. *Identification of the principal elements governing the wettability characteristics of ordinary Portland cement following high power diode laser surface treatment.* Materials Science and Engineering A 356 (2003) 162-172.

[46] Maheshwari, N., Kottantharayil, A., Kumar, M. and Mukherji, S. *Long term hydrophilic coating on poly (dimethylsiloxane) substrates for microfluid applications.* Applied Surface Science 257 (2019) 451-457.

[47] Liston, E.M. *Plasma treatment for improved bonding: a review*. J. Adhes., 30 (1989) 199-218.

[48] Liston, E.M., Martinu, L. and Wertheimer, M. R. *Plasma surface modification of polymers for improved adhesion: a critical review.* J. Adhes. Sci. and Techn. 7 Issue 10 (1993) 1091-1127

[49] Moreno-Couranjou, M., Choquet, P., Guillot, J., Frache, G. and Audinot, J.N. *Effect of Low-pressure Microwave Plasma Discharges on the Surface of Vulcanized Rubbers Before Bonding with a Silicone Sheet. Plasma Process.* Polym. 7 Issue 12 (2010) 963-976.

[50] Kurdi, J., Ardelean, H., Marcus, P., Jonnard, P. and Arefi-Khonsari, F. *Adhesion properties of aluminium-metallized/ammonia plasma-treated polypropylene Spectroscopic analysis (XPS, EXES) of the aluminium/polypropylene interface.* Applied Surface Science 189 (2002) 119-128.

[51] Moreno-Couranjou, M. M., Choquet, P., Guillot, J. and Migeon, H.N. *Surface Modification of Natural Vulcanized Rubbers by Atmospheric Dielectric Barrier Discharges Plasma Treatments*. Plasma Process. Polym. 6, Issue S1 (2009) 397-400

[52] Borges, J.N., Belmonte, T., Guillot, J., Duday, D., Moreno-Couranjou, M., Choquet, P. and Migeon, H.N. *Functionalization of Copper Surfaces by Plasma Treatments to Improve Adhesion of Epoxy Resins.* Plasma Process. Polym. 6 Issue S1 (2009) 490-495.

[53] Plasmatreat GmbH. *Data Sheet DSDE03_12 RD 1004. Plasma Jet RD 1004* (Dec 2013)

[54] Plasmatreat GmbH. *Data Sheet DSDE51_10 FG5001. Plasma generator FG 5001* (Dec 2013)

[55] Wang, H., Nielsen, D.A. and Blaabjerg, F. *Degradation testing and failure analysis of DC film capacitors under high humidity conditions.* Microelectronics Reliability (2015)

[56] Michelazzi, M., Boni, E., Montanari, D., Barbieri, L., Chow, T., Matero, E., Sartini, S. and Bergamaschi, F. *RFI X2 Capacitors for High Humidity Environment*, CARTS International (2014)

[57] IEC 60068-2-21:2006. *International Standard. Ed. 6.0. Environmental testing – Part 2-21: Tests-Test U: Robustness of terminations and integral mounting devices.* ISBN 978-2-88912-734-4 (June 2006)

[58] IEC 60384-14:2005(E). *International Standard. Fixed capacitors for use in electronic equipment. Part 14: Sectional specification: Fixed capacitors for electromagnetic interference suppression and connection to the supply mains.* 3rd Edition. ISBN 2-8318-8078-5 (July 2005)

[59] UL Standard 94, *Tests for Flammability of plastic materials for parts in devices and appliances. 6th Edition.* (March 2013)

5. RESULTS AND DISCUSSION

5.1. ABSTRACT

This chapter focuses on the development of the study of different metallic materials electrically sprayed onto the lateral side of the winding, denominated schoop, before being encapsulated (Target 4 described in Chapter 3).

All the studies and results elaborated during targets 2, 3, 5 and 6 are not developed in this chapter because these researches are the relevant arguments and experimental evidences to support the international published patent under the International Publication Number WO 2019/141388 A1 (*Annex A*) where Azahara Albéndiz is the main inventor.

As a result of these studies, new design rules were defined internally at TDK Electronics Group to design MKP wound box capacitors to operate under extreme humidity conditions. These internal design rules include the material selection for the box and for the encapsulating resins, if a combination of more than one resin should be considered, the minimum distances of resin surrounding the winding element to ensure a lower humidity permeation, the mechanical design of the box, if a surface treatment should be applied to improve the bonding of determined interfaces and/or the design of the wires to ensure the lead space, and at the same time, fulfill the minimum distance between the winding element and the plastic case among others.

In the study of the sprayed schoop (Target 4) that is developed in this chapter, when operational tests are conducted on the DC capacitors, they are manufactured in compliance with all these defined design rules and compiled in the international patent (Annex A).

Furthermore, with the purpose of evidencing some of the results found during the research of this thesis, the following publications are annexed to this manuscript:

- ❖ Annex A. International published patent, IP Nr. WO 2019/141388 A1.
- ❖ Annex B. Paper. Albéndiz García, A., Rodríguez-Castellón, E. and Peláez Millas, D. *Surface modification of thermoplastics by low-pressure microwave O_2 plasma treatment for enhancement of the adhesion of the interface box/encapsulating resin and the influence on film capacitors operating under extreme humidity conditions.* Applied Surface Science 513 (2020) 145764
- ❖ Annex C. Contributions on international congresses, seminars and/or workshops.
  - ▪ Annex C.1. Oral contribution (investigation, validation, writing and presentation) in the European Polymer Congress EPF celebrated in Dresden (Germany) in June 2015 under the code NANO-P-146 and titled as *Encapsulation of film capacitors for power electronics. Study and characterization of adhesion between polymeric materials*.
  - ▪ Annex C.2. Poster contribution (investigation, validation, writing and exposition) in the European Polymer Congress EPF celebrated in Dresden (Germany) in June 2015 under the code NANO-P-147 and titled as *Characterization of transport properties of oxygen and water vapor in polymers for the encapsulation of metallized film capacitors as protection against humidity*.

- Annex C.3. Oral contribution (investigation, validation, writing and presentation) in the 16th European Conference on Applications of Surface and Interface Analysis (ECASIA'15) celebrated in Granada (Spain) in September 2015 under the code oral session O7-W-R4-SFWET1 and titled as *Improvement of performance by a low-pressure microwave O₂ plasma treatment in the interface of polymeric encapsulation of film capacitors for power electronics.*

- Annex C.4. Oral contribution (investigation, validation, writing and presentation) in the European Center for Power Electronics e.V. (ECPE) Workshop "*Humidity and condensation in Power Electronics Systems – Degradation mechanisms and lifetime modelling*" celebrated in Bremen (Germany) in June 2019. The oral session is titled as *Studies on metal spray metallization as humidity barrier in film capacitors*.

- Annex C.5. Oral contribution (investigation, validation and writing) in the CELCORR (Technical University of Denmark) Seminar '*Climatic reliability of Electronics: Global challenges and perspectives*' celebrated in Lyngby (Denmark) during March 2020 under the title *Studies on sprayed metal (schoopage) as humidity barrier in film capacitor.*

All these publications are the result of the investigation of, at least, one target of the present thesis. Figure 5.1. illustrates the results of what target are contributing in what publication and vice versa; in the results of what studies are based the annexed published works.
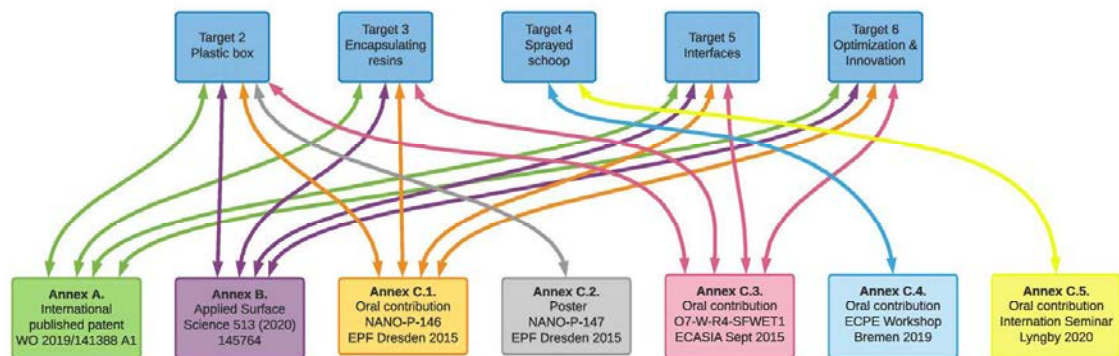
Figure 5.1. Connections between thesis targets and annexed result publications.

In the study of the metal sprayed schoop as humidity barrier in the metallized film capacitors, three different types of samples were analyzed:

- Metal sprayed as sheets (Figure 5.2.). These samples are processed with the same technique and under the same conditions as the windings and/or capacitors and with the same thickness defined for the selected type of MKP wound box capacitor. The width and length of the sheets are not relevant, they do not influence the properties to be characterized and/or the correlation to be established with the operational test of the devices. In this sample type, all the material characterizations are carried out as schemed in Figure 5.5.

Figure 5.2. Example of schoop sprayed as sheets.

▪ Naked windings (Figure 5.3.). Operational tests on the winding elements without the encapsulation and the plastic box were conducted to analyze the performance without influence of the resin, the plastic box and/or the improvements already defined internally as design rules. By means of the naked windings, the differences in performance can be better correlated with the aging mechanisms of the variable under study (different schoop types) and with the results observed in the material characterization over the metal sprayed sheets.
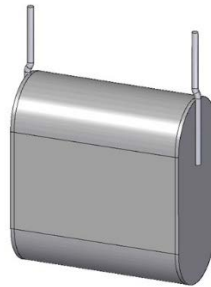
Figure 5.3. Naked winding of the selected type of DC capacitor.

▪ DC capacitors (Figure 5.4.). For the study of the performance of the MKP wound boxed capacitors with different schoops, a humidity resistant X2 EMI suppressor capacitor of 6 μF ($\pm$ 10%) of capacitance, 305 V_{AC} of voltage, parallel wire leads of 1 mm of diameter which are lead-free tinned, in a 2-pin version and a lead spacing of 37.5 mm is selected (described in Section 4.1.1.).
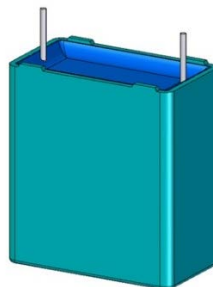
Figure 5.4. DC capacitor selected for the study.

Furthermore, the schoop study comprises the characterization and testing of the following compositions and configurations of number of schoops:

- Single layer: 100% zinc (Zn)
- Single layer: tin-copper (3% in weight of copper) (SnCu3)
- Single layer: zinc-aluminium (15% in weight of aluminium) (ZnAl)
- Two combined layers: a first layer of 100% zinc and a second layer of tin-copper (3% in weight of copper) (Zn + SnCu3) (Figure 4.9. (b)).

Figure 5.5. shows the sprayed compositions in naked windings and DC capacitors, whilst also illustrates the characterization technique applied to every composition sprayed in a material sheet.

100%Zn, SnCu3 and ZnAl are characterized by all the enumerated techniques as single layers; while the sample with combined layers Zn+SnCu3 is only characterized as material by water vapour transmission rate (WVTR) because this is the unique property that is not characterized by the single layers. On the other hand, 100%Zn and ZnAl as single layers; and Zn+SnCu3 as combined configuration are evaluated in naked windings and DC caps. All of them are analysed before and after being aged during 1100h at 85ºC and 85%R.H. as material and their performance in the devices.
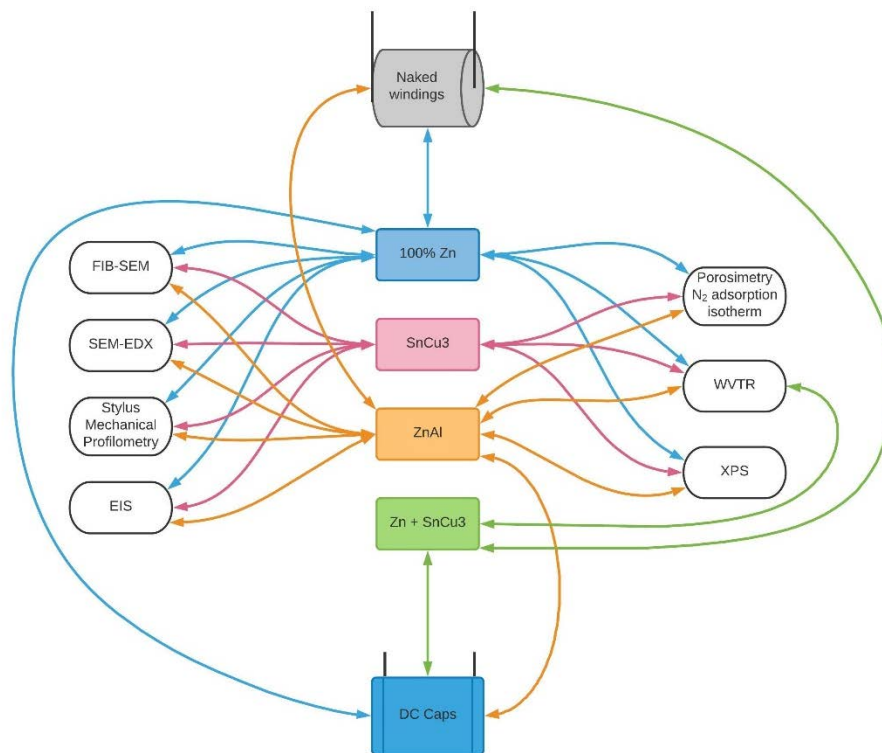
Figure 5.5. Schoop compositions vs sample type and materials characterizations.

The characterization results detailed below were obtained by means of different techniques to understand the material individual behavior and its performance in the film capacitor ensemble. Figure

5.6. shows a diagram organizing all the applied characterization techniques and tests as a function of the schoop sample type.

The naked windings are tested for: (i) the robustness of the wires by the pull-off test and (ii) the temperature humidity bias (THB) test. Whilst DC capacitors were submitted to: (i) THB test (85ºC/85%RH/305V$_{rms}$) without intermediate thermal cycles, (ii) THB test (85ºC/85%RH/305V$_{rms}$) with intermediate thermal cycles as additional stress, (iii) after the THB tests the failures are analyzed and every schoop variant is observed by optical microscopy to confirm that the sprayed schoop thickness is the defined one and different thicknesses are not influencing the observations done in the THB performance; and (iv) impulse voltage test on new pieces.
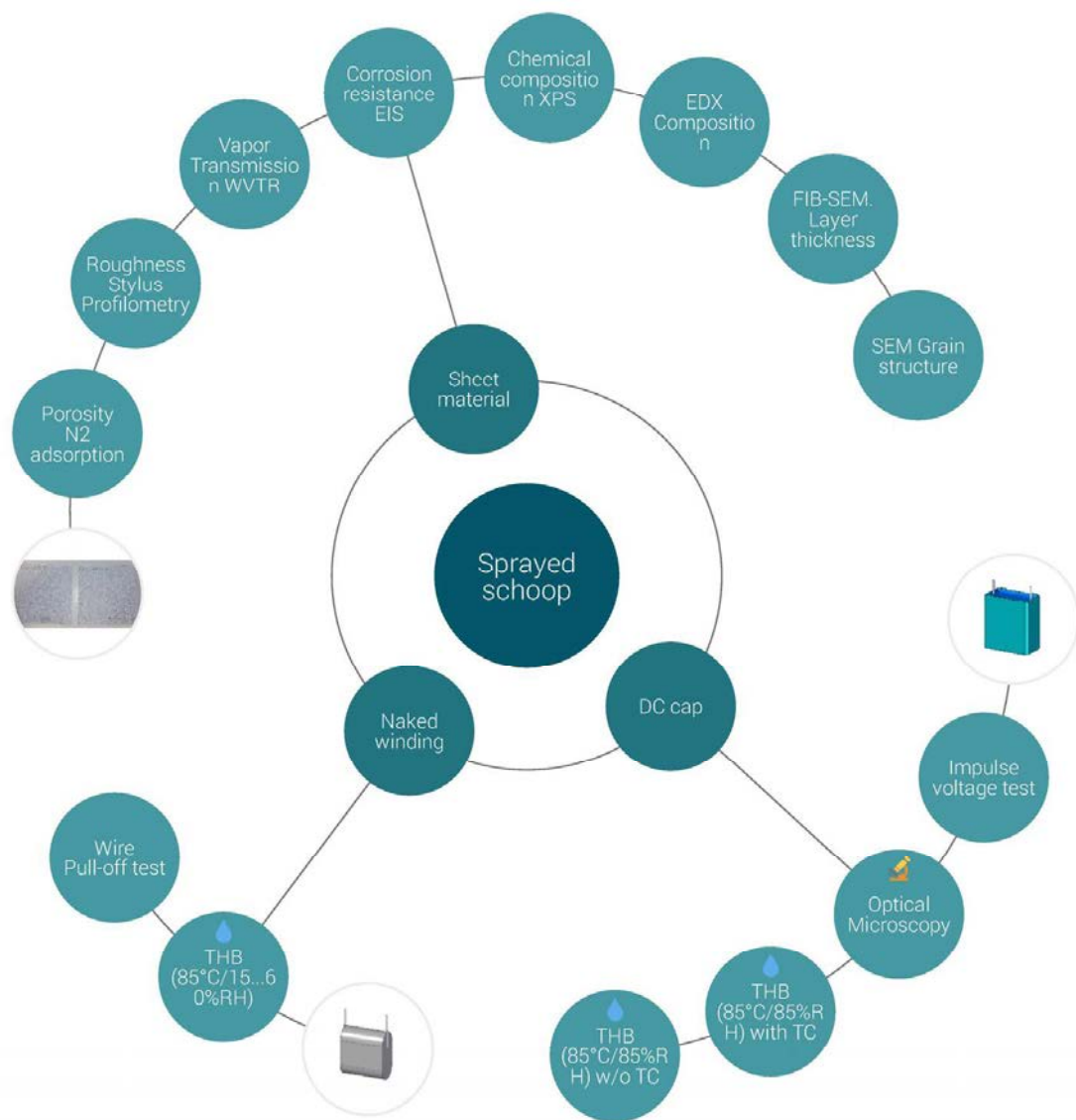
Figure 5.6. Applied techniques and tests to each sample type for the schoop study.

5.2. CHARACTERIZATION RESULTS

5.2.1. Textural properties by N_2 adsorption-desorption isotherms at -196ºC

The textural properties of the schoop are evaluated by N_2 adsorption/desorption isotherms at -196ºC and the corresponding results are compiled in Table 5.1. The determined values are:

- surface area according to the Brunauer-Emmet-Teller method (S_{BET}),
- pore diameter ranges according to the non-local-density functional theory (NLDFT),
- total volume in pores according to NLDFT, and
- total area in pores according to NLDFT.

NLDFT was selected as the most reliable approach to pore size analysis over the complete range of nanopore, micropore and mesopore due to be able to describe the distribution of absorbed molecules in pores on a molecular level and thus provide detailed information about the local fluid structure near the absorbent surface [1].

The samples were characterized before and after being aged during 1100h at 85ºC and 85%R.H. As observed in *Table 5.1.*, significant decreases in S_{BET} and also in the total area and volume in pores by DFT are observed in all the evaluated schoops after the aging program. The porosity of the samples is due to the interparticle space among the sprayed grains so it is expected that after the aging under extreme conditions of temperature and humidity some oxides are created thus these pore properties endure a reduction.

Related to the comparison between compositions, ZnAl15 and SnCu3 show similar total volume and area by DFT and S_{BET}, before and after being aged; whilst 100% Zn presents a higher S_{BET} and DFT pore sizes before the aging program.

In every case, the pore diameter range is equivalent between compositions and show a reduction of the maximum from approximately 20nm to 2nm of maximum pore diameter.

Table 5.1. Textural properties of evaluated schoops before and after being aged.

Schoop sample	BET	Pore size		DFT Pore size	
	Surface Area (m²/g)	Adsorption average pore width (4V/A by BET) (Å)	Pore diameter range (Å)	Total Volume in Pores (cm³/g)	Total Area in Pores (m²/g)
Zn – non aged	1.36	43.6	25 - 2340	0.0018	0.5
Zn - aged	0.39	60.3	25 - 234	0.0005	0.2
ZnAl15 - non aged	0.84	41.3	25 - 2340	0.0009	0.3
ZnAl15 - aged	0.18	60.5	25 - 234	0.0002	0.1
SnCu3 - non aged	0.81	41.2	25 - 2340	0.0009	0.3
SnCu3 - aged	0.30	35.4	25 - 253	0.0002	0.1

In Figure 5.7. are plotted the incremental pore volumes against the determined pore width for the schoop samples, before and after aging, by NLDFT method. Before the degradation program, the three schoops present equivalent pore size and distribution in a very wide range between 25 Å to 2300 Å. Pure zinc is the variant with double total adsorbed volume in pores compared to ZnAl15 and SnCu3; regardless, all of them show very low volumes and surfaces. After the aging, the three schoops reduce the incremental pore volume and narrow the pore size distribution to the mesoporous range, being the pore width distributed between 25 Å and 200 Å.
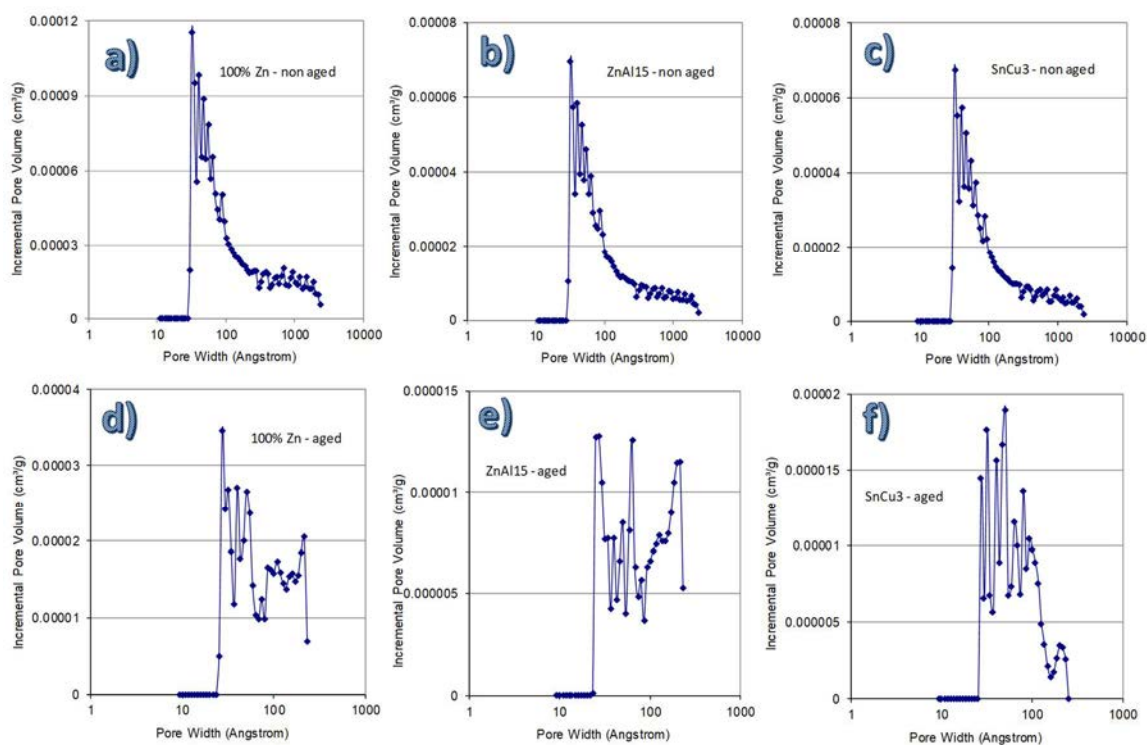
Figure 5.7. Incremental pore volume vs pore width of schoop before aging: a) 100%Zn, b) ZnAl15 and c) SnCu3; and after aging: d) 100%Zn, e) ZnAl15 and f) SnCu3.

The pertinent N_2 adsorption-desorption isotherms at -196 ºC are shown in *Figure 5.8*. All isotherms before aging are of type III, the monolayer formation is not identified (there is no point B); the adsorbent-adsorbate interactions are relatively weak, characteristic of nonporous or macroporous solids. The amount adsorbed remains finite at the saturation pressure ($P/P_0 =1$).

Regarding the N_2 isotherms after the aging of the schoops, relevant differences can be observed in comparison with these without being aged.

In the case of pure Zn, the aged sample shows an evolution of the physisorption isotherm to type II, appearing a very low relative pressure a poor distinctive point B with a slight gradual curvature as indication of a significant amount of overlap of monolayer coverage and the inception of multilayer adsorption. This reversible type isotherm is also characteristic of nonporous or macroporous adsorbents.

It is also remarkable that appears a slight hysteresis loop located in the multilayer range of N_2 physisorption isotherm. This is generally associated with capillary condensation [1-3]. According to the hysteresis loop shape this can be classified as type H3, this can be observed if the pore network consists of macropores which are not completely filled with pore condensate [1].

ZnAl15 presents very similar evolution of the N_2 isotherm to type II after the aging than the schoop of pure zinc, poorly it can be a point B distinguished and a narrow hysteresis loop of type H3 in the multilayer range ($P/P_0 > 0.8$).
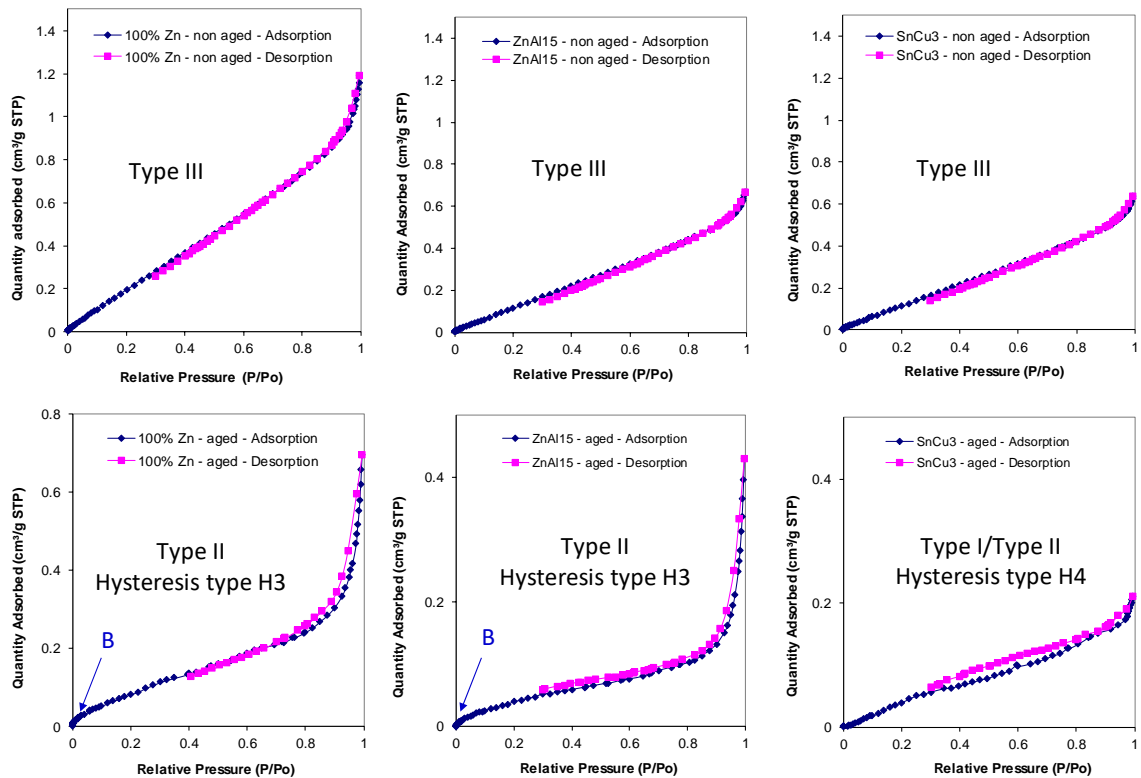
Figure 5.8. N_2 adsorption/desorption isotherms at -196ºC of schoop samples before and after aging.

However, in the case of SnCu3 schoop, after the aging process, there is a change in the pore structure, presenting a hysteresis loop of type H4. The adsorption branch is a combination of types I and II and the more evident assimilation at low relative pressure typically is associated with the filling of micropores.

5.2.2. Roughness measurement by Contact Stylus Profilometry

The roughness of the schoops without being submitted to the aging program is determined by Contact Stylus Profilometry, obtaining Ra, Rq and Rt (defined in *Figure 4.24*). The obtained values are shown

in the diagram of *Figure 5.9*. Negligible differences are observed in the three roughness parameters between schoops made of 100% Zn, ZnAl15 and SnCu3.
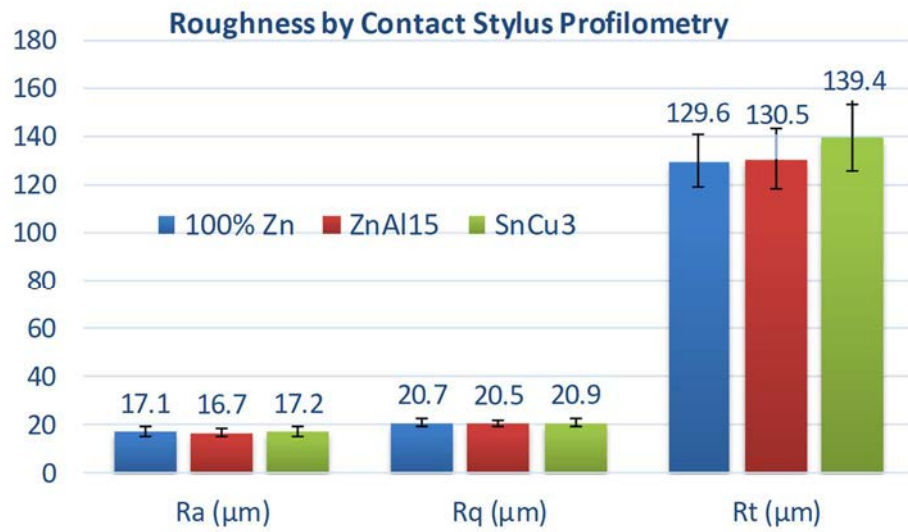
Figure 5.9. Schoop roughness measurements by Contact Stylus Profilometry.

In Figure 5.10. is illustrated the 3-D dimensional surface for every schoop sample with dimensions of 1mm x 1mm.
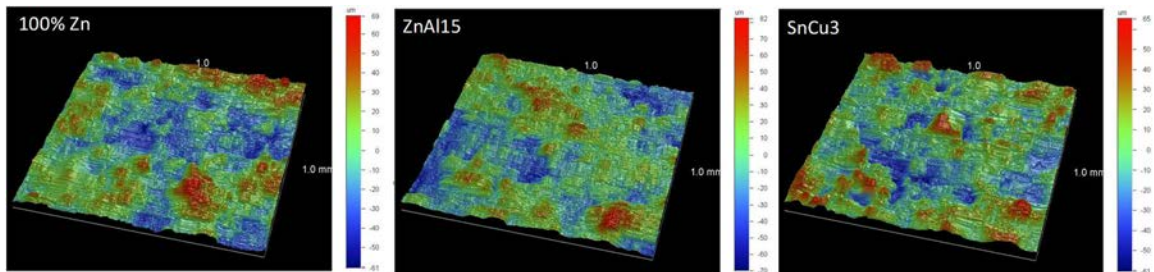
Figure 5.10. 3-D images of roughness measurements by Contact Stylus Profilometry.

5.2.3.   Water Vapor Transmission Rate (WVTR)

WVTR analysis was performed to sprayed schoop samples in order to approach the understanding of the material moisture permeation. A section of 5 cm^2 was evaluated in every specimen.

The same schoop sheets were characterized before and after the application of the aging program during 1100h at 85ºC and 85%R.H. In Figure 5.11. are shown the measurement results. SnCu3 alloy is showing significantly lower moisture transmission rate through its structure, permeating the variant Zn + SnCu3 one order of magnitude less than 100% Zn or ZnAl metallizations. Due to the lack of flatness and the onset of cracks during the aging program in the schoops made of ZnAl15 and Zn + SnCu3, it was not

possible to determine the WVTR to these variants after the degradation plan. In any case, the schoops made of 100% Zn and only SnCu3 show a reduction of the moisture transmission rate, of two orders of magnitude in the case of pure zinc. These results are in agreement with the results found on the porosity characterization after aging the samples. Figure 5.12. shows the appearance of the schoop sheets before applying the aging and after it.
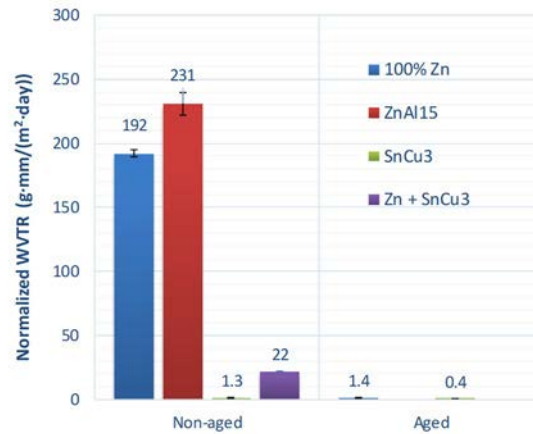
Figure 5.11. Normalized WVTR measurements of schoop before and after aging.

Figure 5.12. Schoop sheets before (left) and after (right) the aging application.

5.2.4. Electrochemical Impedance Spectroscopy (EIS)

The objective of characterizing by EIS was modelling the impedance diagram by equivalent circuits and to perform the simulation and result fitting based on complex nonlinear least square (CNLS) analysis result.

One intrinsic difficulty of EIS technique is that occasionally several equivalent circuits can lead to similar solutions, leading to wrong interpretations. Four criteria were established to overcome this key constraint and to validate the obtained results:

(i) to evaluate the setting curves of the equivalent circuit to select the best approach to the experimental impedance diagram obtained in the laboratory.

(ii) to analyse if the electrical elements of the equivalent circuit show a right physical meaning.

(iii) to evaluate if errors of every individual calculation of the equivalent circuit element are justifiable.

(iv) to select the equivalent circuit that (fulfilling the criteria 1 to 3) is leading to a very low value of the statistic parameter denominated chi-squared (X^2), where the variance and the lowest weighted sum of squares are considered.

Consequently, with those four criteria, the most probable equivalent circuits obtained for every schoop alloy for four different immersion times, 0h, 1/1.5h, 3h and 24h of immersion in electrolyte 0.6M of NaCl are compiled in Tables 5.2., 5.3., 5.4. and 5.5, respectively.

In addition to the equivalent circuits are compiled the values of:

- $|Z|$ ($\Omega \cdot cm^2$), impedance module value at the characteristic frequency of every immersion time ($|Z|_{100mHz}$, at 100mHz for 0h and $|Z|_{10mHz}$, at 10 mHz for immersion times 1/1.5h, 3h and 24h).

- $\sum R$ ($\Omega \cdot cm^2$), the value of the total resistance of the electrical equivalent circuit that is the sum of the individual resistances compiled in every case in Tables 5.2.-5.5.

- Every element of the equivalent circuit fitted for every schoop and immersion time. The used program ZView works without dimensions or units. The codification of every element is:

  - Capacitors in EIS experiments often do not behave ideally. Instead they act like a constant phase element (CPE) as defined below. The impedance of a CPE has the form:

    $$Z = (1/Y_0)/(jw)^{\alpha}$$

    When this equation describes a capacitor, the constant $Y_0 = C$ (the capacitance) and the exponent $\alpha = 1$(CPE-P = 1). For a constant phase element, the exponent will be $\alpha < 1$ (CPE-P<1). The "double-layer capacitor" on real cells often behaves like a CPE instead of like a capacitor. Several theories have been proposed to account for the non-ideal behaviour of the double layer, but none has been universally accepted. In most cases, you can safely treat as an empirical constant and not worry about its physical basis. If CPE-P is equal to 0.5 will show a system with corrosion controlled by diffusion.

  - R1, is the resistance associated to the charge transference. This is related directly to the corrosion velocity.

  - R2, is the resistance associated to the passive layer that it can be created spontaneously in the schoop specimen. If R2 is very low, this will involve very porous passive layers and/or very thin, where no additional barrier to corrosion between electrolyte and metallic substrate in the base of the porous will be applied.

The obtained equivalent circuits, simulation results and fitting are suitable; all of them fulfilled the four criteria previously described. Therefore, those equivalent circuits can be considered reliable models of impedance answer of every schoop under corrosion with an electrolyte media of NaCl 0.6M, not only due to the mathematic fitting but also is in line with the found values of the elements of the equivalent circuits because are presenting a physical meaning in line with the Bode and Nyquist diagrams (Annex D) as the literature defines [4-10].

Table 5.2. Equivalent circuits at 0h of immersion. Impedance module values at 100 mHz and total sum of the electrical resistances values of the equivalent circuits for every schoop variant.
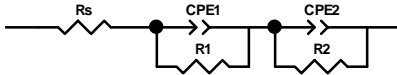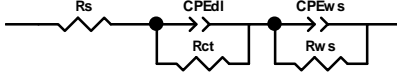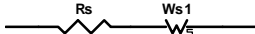
Schoop variant	0 hours of immersion		Equivalent circuit
	$|Z|_{100mHz}$ (Ω cm²)	$\sum R$ (Ω cm²)	
ZnAl15	199	366	 Element — Freedom — Value — Error — Error % Rs — Free(±) — 18.45 — 0.56773 — 3.0771 CPE1-T — Free(±) — 0.00049467 — 4.5404E-05 — 9.1786 CPE1-P — Free(±) — 0.64194 — 0.038124 — 5.9389 R1 — Free(±) — 85.55 — 17.011 — 19.884 CPE2-T — Free(±) — 0.007837 — 0.0010202 — 13.018 CPE2-P — Free(±) — 0.45514 — 0.091601 — 20.126 R2 — Free(±) — 262.2 — 248.64 — 94.828 Chi-Squared: 0.001497 Weighted Sum of Squares: 0.14221
100% Zn	139	426	 Element — Freedom — Value — Error — Error % Rs — Free(±) — 31.16 — 0.14157 — 0.45433 CPEdl-T — Free(±) — 0.00069921 — 3.6571E-05 — 5.2303 CPEdl-P — Free(±) — 0.78204 — 0.015595 — 1.9941 Rct — Free(±) — 41.65 — 1.5553 — 3.7342 CPEws-T — Free(±) — 0.014107 — 0.00051243 — 3.6325 CPEws-P — Free(±) — 0.38963 — 0.0084788 — 2.1761 Rws — Free(±) — 353.5 — 46.832 — 13.248 Chi-Squared: 0.00075386 Weighted Sum of Squares: 0.089709
SnCu3	1012	1324	 Element — Freedom — Value — Error — Error % Rs — Free(±) — 24.71 — 0.52351 — 2.1186 Ws1-R — Free(±) — 1299 — 21.641 — 1.666 Ws1-T — Free(±) — 2.722 — 0.13627 — 5.0062 Ws1-P — Free(±) — 0.46537 — 0.0039163 — 0.84155 Chi-Squared: 0.0087532 Weighted Sum of Squares: 1.0329

Table 5.3. Equivalent circuits at 1/1.5h of immersion. Impedance module values at 10 mHz and total sum of the electrical resistances values of the equivalent circuits for every schoop variant.
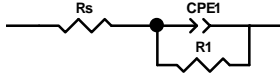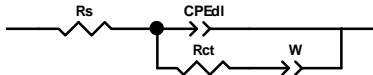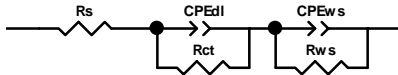
Schoop variant	1.0 – 1.5 hours of immersion		Equivalent circuit
	$|Z|_{10mHz}$ (Ω cm²)	Σ R (Ω cm²)	
ZnAl15	339	506	**Rs — CPE1 / R1** Element — Freedom — Value — Error — Error % Rs — Free(±) — 20.43 — 0.15682 — 0.7676 CPE1-T — Free(±) — 0.0052722 — 5.3174E-05 — 1.0086 CPE1-P — Free(±) — 0.50145 — 0.0037078 — 0.73942 R1 — Free(±) — 485.4 — 10.79 — 2.2229 Chi-Squared: 0.0015769 Weighted Sum of Squares: 0.16399
100% Zn	275	117	**Rs — CPEdl / Rct — W** Element — Freedom — Value — Error — Error % Rs — Free(±) — 32.02 — 0.089301 — 0.27889 CPEdl-T — Free(±) — 0.00067118 — 2.4255E-05 — 3.6138 CPEdl-P — Free(±) — 0.6965 — 0.0061022 — 0.87612 Rct — Free(±) — 84.5 — 2.1055 — 2.4917 W-T — Free(±) — 0.016065 — 0.00041424 — 2.5785 W-P — Free(±) — 0.37245 — 0.0069296 — 1.8605 Chi-Squared: 0.00055546 Weighted Sum of Squares: 0.067767
SnCu3	1839	3042	**Rs — CPEdl / Rct — CPEws / Rws** Element — Freedom — Value — Error — Error % Rs — Free(±) — 28.73 — 0.10703 — 0.37254 CPEdl-T — Free(±) — 0.0073145 — 0.0010455 — 14.294 CPEdl-P — Free(±) — 0.9788 — 0.048409 — 4.9457 Rct — Free(±) — 299.9 — 59.044 — 19.688 CPEws-T — Free(±) — 0.0013711 — 3.8791E-05 — 2.8292 CPEws-P — Free(±) — 0.51694 — 0.00432 — 0.83569 Rws — Free(±) — 2713 — 102.83 — 3.7903 Chi-Squared: 0.00071401 Weighted Sum of Squares: 0.096392

Table 5.4. Equivalent circuits at 3h of immersion. Impedance module values at 10 mHz and total sum of the electrical resistances values of the equivalent circuits for every schoop variant.
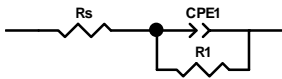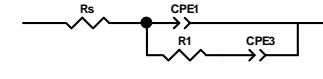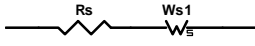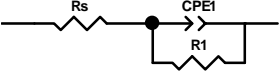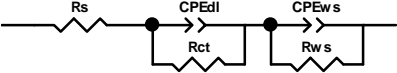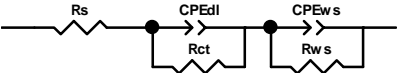
Schoop variant	3 hours of immersion		Equivalent circuit
	$|Z|_{10mHz}$ (Ω cm^2)	$\sum R$ (Ω cm^2)	
ZnAl15	563	938	Element / Freedom / Value / Error / Error % Rs / Free(±) / 19.5 / 0.074626 / 0.3827 CPE1-T / Free(±) / 0.0042481 / 2.441E-05 / 0.57461 CPE1-P / Free(±) / 0.52811 / 0.0020126 / 0.38109 R1 / Free(±) / 918.8 / 15.713 / 1.7102 Chi-Squared: 0.0010096 Weighted Sum of Squares: 0.12318
100% Zn	378	167	Element / Freedom / Value / Error / Error % Rs / Free(±) / 32.22 / 0.089901 / 0.27902 CPE1-T / Free(±) / 0.00054105 / 1.2849E-05 / 2.3748 CPE1-P / Free(±) / 0.73677 / 0.0044688 / 0.60654 R1 / Free(±) / 135.2 / 1.804 / 1.3343 CPE3-T / Free(±) / 0.015804 / 0.00032034 / 2.027 CPE3-P / Free(±) / 0.49205 / 0.0065155 / 1.3242 Chi-Squared: 0.00060526 Weighted Sum of Squares: 0.072632
SnCu3	2428	2803	Element / Freedom / Value / Error / Error % Rs / Free(±) / 27.41 / 0.28745 / 1.0487 Ws1-R / Free(±) / 2776 / 50.719 / 1.8271 Ws1-T / Free(±) / 17.01 / 0.65554 / 3.8539 Ws1-P / Free(±) / 0.49306 / 0.0021327 / 0.43254 Chi-Squared: 0.0038201 Weighted Sum of Squares: 0.46605

120

Table 5.5. Equivalent circuits at 24h of immersion. Impedance module values at 10 mHz and total sum of the electrical resistances values of the equivalent circuits for every schoop variant.

Schoop variant	24 hours of immersion		Equivalent circuit
	$|Z|_{10mHz}$ (Ω cm²)	$\sum R$ (Ω cm²)	
ZnAl15	1542	4719	Rs — CPE1 / R1 Element — Freedom — Value — Error — Error % Rs — Free(±) — 18.61 — 0.051779 — 0.27823 CPE1-T — Free(±) — 0.001666 — 5.3847E-06 — 0.32321 CPE1-P — Free(±) — 0.45984 — 0.00080604 — 0.17529 R1 — Free(±) — 4700 — 88.691 — 1.887 Chi-Squared: 0.00029248 Weighted Sum of Squares: 0.040362
100% Zn	702	1758	Rs — CPEdl / Rct — CPEws / Rws Element — Freedom — Value — Error — Error % Rs — Free(±) — 34.83 — 0.10503 — 0.30155 CPEdl-T — Free(±) — 0.0005853 — 7.8183E-06 — 1.3358 CPEdl-P — Free(±) — 0.69707 — 0.0094331 — 1.3533 Rct — Free(±) — 328.2 — 15.796 — 4.8129 CPEws-T — Free(±) — 0.010288 — 0.001057 — 10.274 CPEws-P — Free(±) — 0.58224 — 0.041977 — 7.2096 Rws — Free(±) — 1395 — 361.37 — 25.905 Chi-Squared: 0.00087566 Weighted Sum of Squares: 0.11821
SnCu3	2341	3761	Rs — CPEdl / Rct — CPEws / Rws Element — Freedom — Value — Error — Error % Rs — Free(±) — 29.37 — 0.043758 — 0.14899 CPEdl-T — Free(±) — 0.00069558 — 7.6555E-06 — 1.1006 CPEdl-P — Free(±) — 0.599 — 0.0019772 — 0.33008 Rct — Free(±) — 116.4 — 1.2438 — 1.0686 CPEws-T — Free(±) — 0.0016177 — 3.399E-06 — 0.21011 CPEws-P — Free(±) — 0.68749 — 0.0014281 — 0.20773 Rws — Free(±) — 3615 — 17.752 — 0.49107 Chi-Squared: 2.9371E-05 Weighted Sum of Squares: 0.0033777

If the sum of resistances is substantially different than the impedance module at the characteristic frequency is a signal of |Z| is not representative of the corrosion resistance of schoops in the electrolyte media, but the response of the material at the complete frequency spectra should be done to get a suitable information.

5.2.4.1.   Ranking of schoops according to corrosion resistance

For establishing a ranking of resistance to corrosion under an aqueous solution of NaCl 0,6M (sea water concentration) of schoops, two different criteria are usually applied in literature (Section 2):

A) **Criteria 1.** To compare impedance module values at the characteristic frequency, being this frequency as low as possible with stable measurements: 100 mHz for immersion time 0h and 10 mHz for longer immersion times (1/1,5h, 3h & 24h).

Advantage: Quick measurement at one specific frequency.

Disadvantage: Unknown response of the material at higher frequencies and corrosion processes kinetically controlling the corrosion.

B) **Criteria 2.** Classification based on the sum of resistances of the electrical equivalent circuit, $\sum$R. This equivalent circuit was simulated and fitted based on complex nonlinear least square (CNLS) analysis result. The total resistance in every case is summarized in Tables 5.2.-5.5.

Advantage: Response of the material at the complete frequency spectra and possibility to define the process kinetically controlling the corrosion for every case.

Disadvantage: Measurements take much more time than criteria 1.

The rankings established after 1/1.5h and 3h of immersion times are equivalent between criteria.

However, as Table 5.6. shows, after 24h of immersion in an aqueous solution of NaCl 0.6M, no equivalent classifications of resistance to corrosion were found on every criterion, Ranking 7 vs. Ranking 8. Criterion A is classifying the schoops only based on one frequency answer (at 10mHz). Then, ranking 7 is only based on one singular point from the complete impedance diagram. Thus ranking 8 is considered the most suitable classification and more representative to the corrosion resistance of winding schoops under long exposure times with harsh humid environment.

$$ZnAl15 \quad >> \quad SnCu3 \quad >> \quad 100\%Zn$$

Table 5.6. Schoop ranking according to the immersion time and the selected criteria.

Immersion time	Classification criteria	Parameter compared	Corrosion resistance	Ranking nr.
0 h	Criteria 1	$\|Z\|_{100mHz}$ (Ω cm^2)	SnCu3 >> ZnAl15> Zn	Ranking 1
	Criteria 2	$\sum$R (Ω cm^2)	SnCu3 >> Zn > ZnAl15	Ranking 2
1/1.5h	Criteria 1	$\|Z\|_{10mHz}$ (Ω cm^2)	SnCu3 >> ZnAl15 > Zn	Ranking 3
	Criteria 2	$\sum$R (Ω cm^2)	SnCu3 >> ZnAl15 > Zn	Ranking 4
3 h	Criteria 1	$\|Z\|_{10mHz}$ (Ω cm^2)	SnCu3 >> ZnAl15 >> Zn	Ranking 5
	Criteria 2	$\sum$R (Ω cm^2)	SnCu3 >> ZnAl15 >> Zn	Ranking 6
24 h	Criteria 1	$\|Z\|_{10mHz}$ (Ω cm^2)	SnCu3 >> ZnAl15 >> Zn	Ranking 7
	Criteria 2	$\sum$R (Ω cm^2)	ZnAl15 >> SnCu3 >> Zn	Ranking 8

5.2.4.2. <u>Corrosion mechanisms</u>

The found values for the elements of the mooted equivalent circuits and the shape of the registered impedance curves (Bode & Nyquist diagrams in Annex D) are suggesting that schoop corrosion can be kinetically controlled by different processes in function of the immersion time in the aqueous solution of NaCl 0.6M, as Table 5.7. summaries:

Table 5.7. Corrosion mechanisms in function of immersion time in aqueous solution of NaCl 0.6M.

Schoop variant	Control of corrosion process / Corrosion mechanisms			
	0 hours of immersion	1/1.5 hours of immersion	3 hours of immersion	24 hours of immersion
ZnAl15	Combined control (Activation + diffusion)	Control by diffusion	Control by diffusion	Control by diffusion
Zn	Combined control (Activation + diffusion)	Combined control (Activation + diffusion)	Combined control (Activation + diffusion)	Combined control (Activation + diffusion)
SnCu3	Control by diffusion	Combined control (Activation + diffusion)	Control by diffusion	Combined control (Activation + diffusion)

If impedance curves (Bode diagrams in Annex D) are showing more than one well defined maximun point is related to a behaviour of an electrode submitted to a corrosion process controlled by a combined process of activation and diffusion. The semicircle at high frequencies (Nyquist diagrams in Annex D) is associated to a corrosion process controlled by activation.

The evolution of Bode and Nyquist diagrams are suggesting that the corrosion process during the immersion test undergoes different stages, as Table 5.7. summaries.

Impedance measurements since 90 min. of immersion are showing that schoops made of ZnAl15 are mainly controlled by diffusion of electrolyte. This behaviour suggests that this schoop composition will present the highest resistance to corrosion because additionally it is the unique variant that it is not showing transference of charge during the exposure to an electrolyte. Nevertheless, impedance measurements also reveal that schoop made of ZnAl15 was not passivated during immersion test.

In addition, by EIS can be determined if the corrosion products after immersion test are applying a barrier effect in every type of schoop. The increasing of total resistance value that is impeding the transit of the applied electrical signal can be reasonably related with a rise of electrode corrosion resistance. Thus, comparing the results found after 90min vs. 24h of immersion, it can be concluded that corrosion products of schoops made of ZnAl15 are applying an additional barrier effect.

5.2.5. Scanning Electron Microscopy (SEM) with Focused Ion beam (FIB) & Energy Dispersive X-Ray Spectroscopy (EDS or EDX)

SEM analyses of the studied schoops were carried out to characterize the surface and also the natural oxidized layer onto the surface by means of the cross-section of the samples created by FIB. The evaluation of microstructure is crucial for understanding the properties found on the different schoops. The determinations done in function of the used detectors are:

- by ETD (Everhart-Thornley Detector) and TLD (Through Lens Detector) detectors on mode Secondary Electron and Backscattering Electron images: (i) the surface contaminants, (ii) the surface homogeneity and textures of the schoop, (iii) the macro-porosity and (iv) the thickness of natural oxidized layer in the schoop,

- by Retractable detector CBS: backscattering electron image: (i) chemical and topographical information as grain distribution in the schoop surface,

- EDS image mapping from Oxford SDD detector: distribution of oxidation in schoop (in surface and in the cross-section),

- EDS semi-quantification and linescan analysis: (i) chemical composition of oxidized layer and (ii) surface chemical composition.

The color codification applied in the EDS analyses (image mapping and/or linescan analysis) is:

- oxygen, O: yellow (code 60)

- zinc, Zn: pink (code 300)

- carbon, C: dark blue (code 240)

- copper, Cu: light blue (code 197)

- platinum, Pt: green (code 120)

- aluminum, Al: turquoise (code 180)

- tin, Sn: red (code 0)

5.2.5.1. <u>Schoop 100%Zn</u>

For the observation of the natural oxidation layer and the bulk of the schoop, the FIB cross-section (FIB-CS) was imaged by a TLD detector on mode Secondary Electron (SE) as shown in Figure 5.13.
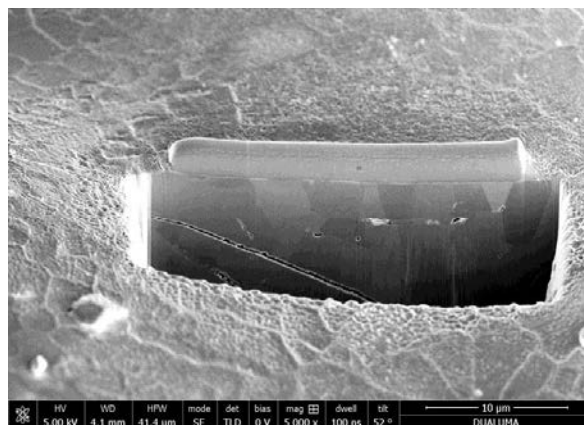
Figure 5.13. Schoop 100% Zn FIB-CS, elevation view (Scale: x5000)

The grain boundaries in the cross-section were clearly distinguished, whilst no porosity was observed in the schoop bulk. In addition, no cracks from the surface to the inner of the schoop were appreciated.

However, several internally aging mechanisms were observed. Mechanical fatigue, due to detected internal cracks and cavities between grain boundaries, and delamination of the oxidized layer (Figure 5.14.). The inception of a second crack by joining cavities was also observed in *Figure Y1* under the crack already created.
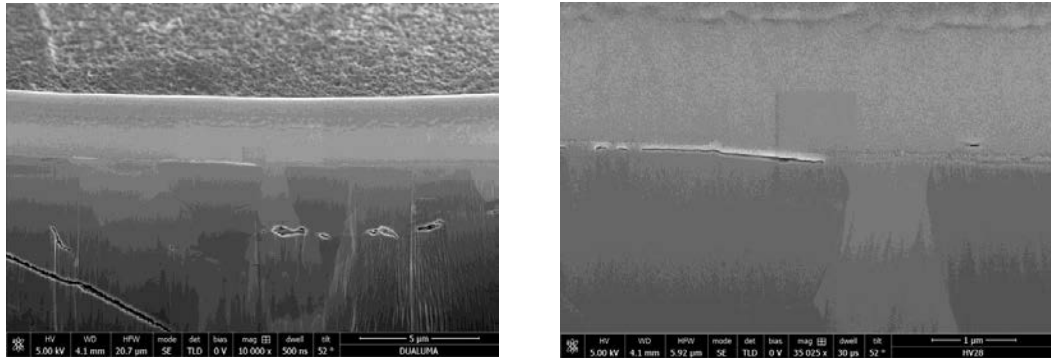
Figure 5.14. FIB-CS. Aging mechanisms in Zn schoop. Mechanical fatigue (left) and delamination (right).

A homogeneous thickness in the natural oxidized layer in 100%Zn schoop was determined, obtaining a measured average value of 69.6 nm ($\pm$ 1.2nm), Figure 5.15.
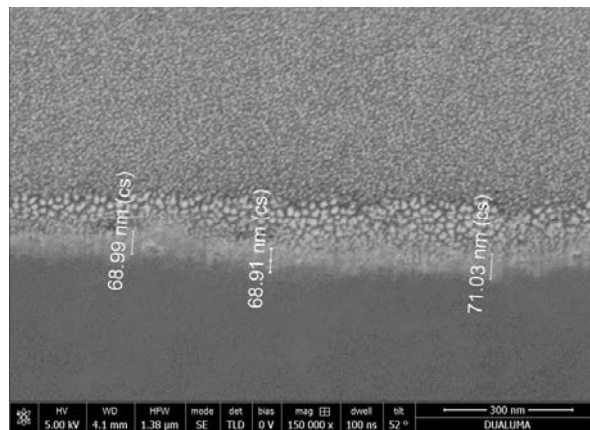
Figure 5.15. Schoop 100%Zn FIB-CS. Oxidized layer thickness (Scale: x15000)

The grained layers observed in Figure 5.15. onto the oxidized zinc layer are related to the platinum pattern deposited (with carbon) twice, first with electrons and second with gallium ions. This is the reason to evidence a change in platinum coating structures.

The distribution of oxidation in the schoop was characterized in the cross-section by an EDS image mapping from the SDD detector. This distribution is observed in Figure 5.16.
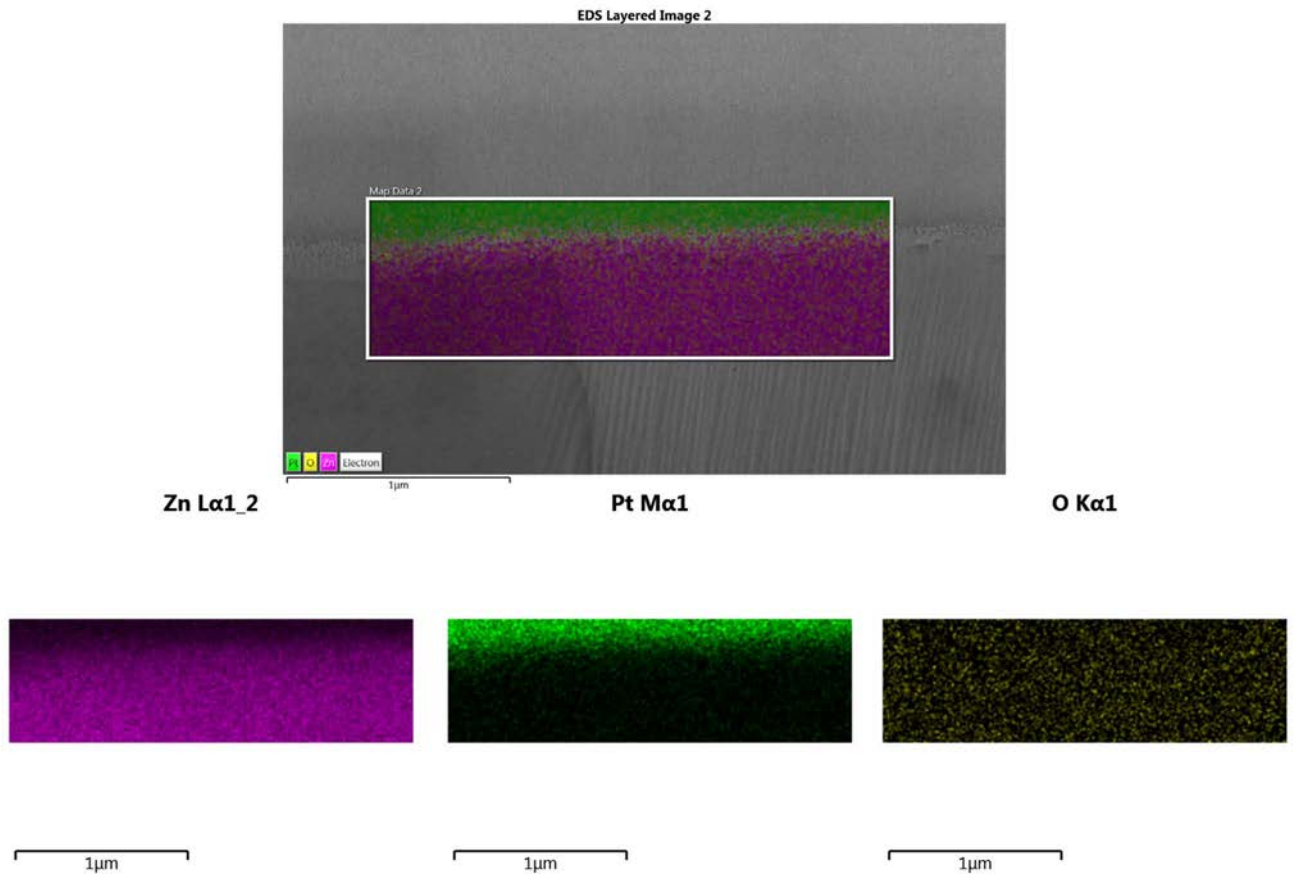
Figure 5.16. EDS image mapping of schoop 100%Zn FIB-CS and Zn, Pt and O individual mappings.

The natural oxidation in the Zn schoop is homogeneously distributed on the surface but also in the grains (bulk). Figure 5.16. shows the EDS mapping of the concentration for the oxidation in surface. Nevertheless, an additional EDS analysis was performed by a linescan analysis of the main elements (C, Zn, O and Pt) to confirm the thickness of the oxidized layer already determined in Figure 5.15. Figure 5.17 (left) shows the drawn line for determining the EDS semi-quantification from point 0 (inside the schoop) to point 1 (inside the platinum pattern).
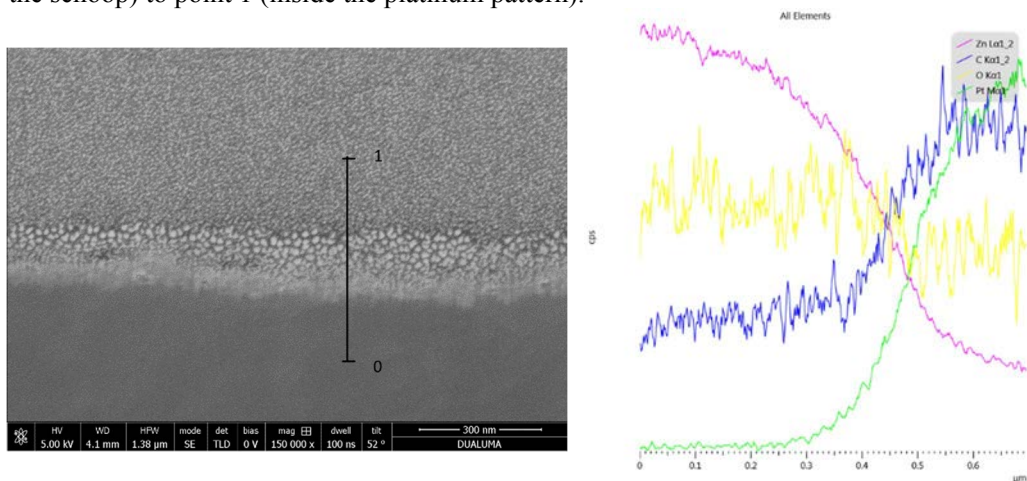
Figure 5.17. FIB-CS SEM of Zn schoop with drawn linescan (left) and EDS scanned lines in the oxidized layer (right).

This is a semi-quantitative chemical analysis due to be a relative quantification between elements. No absolute values are determined, coordinate axis represents counts per second in the individual elements spectrum, however, Figure 5.17. (right) is no dimensional and combines all the spectra.

The EDS scanned lines from point 0 to point 1 evidence the interface schoop/platinum pattern by the fall in the zinc signal in favor of the platinum and carbon one.

A natural oxidized zinc layer of 70 nm thickness is confirmed by the linescan analysis.

The base line in the oxygen signal shows a negligible variation of this element between the bulk schoop and the surface, suggesting a low oxidation grade of the sample in the bulk and also in the oxidized layer on surface.
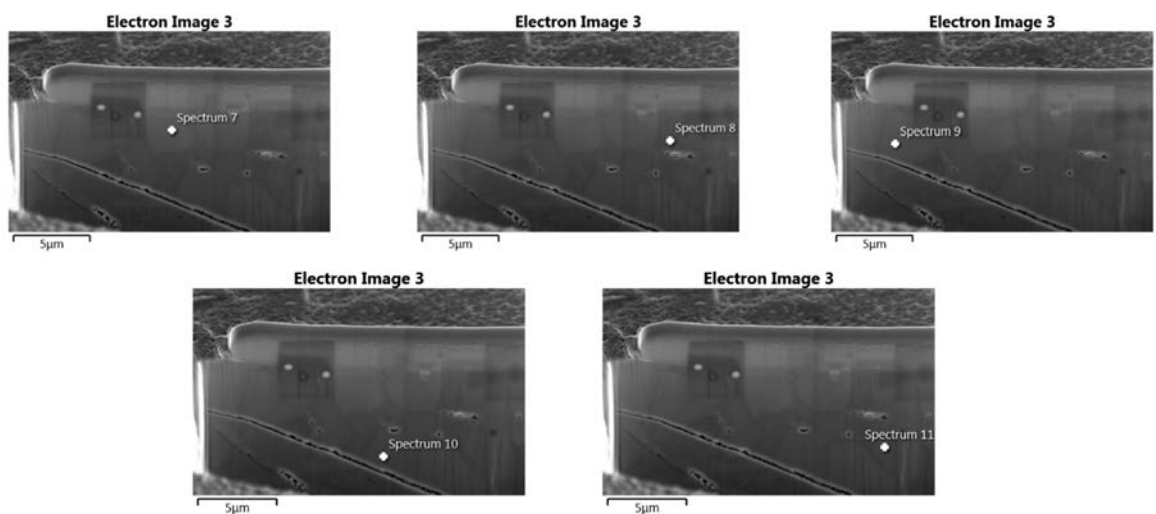
Figure 5.18. Selected points in FIB-CS of Zn schoop for EDS bulk analysis

A quantitative chemical characterization of the schoop grains in the FIB-CS was done by EDS point analyses. Several points were selected to quantify the elements in the bulk (Figure 5.18.). Table 5.8. compiles the EDS results in every nominated point.

- Spectrum 7. Point in the middle of a grain distant of a cavity or a crack.
- Spectrum 8. Point near to an intergranular cavity.
- Spectrum 9. Point in the middle of a grain but near to a crack.
- Spectrum 10. Point in the middle of a grain but near to a crack.
- Spectrum 11. Point in the middle of a grain distant of a cavity or a crack.

Table 5.8. Grain chemical composition in FIB-CS of Zn schoop by EDS bulk analysis (atomic %).

Spectrum Label	C	O	Zn	Total
Spectrum 7	2.63	2.69	94.67	100.00
Spectrum 8	4.07	2.20	93.73	100.00
Spectrum 9	2.70	3.34	93.96	100.00
Spectrum 10	2.03	2.32	95.65	100.00
Spectrum 11	2.26	1.98	95.76	100.00

A homogeneous chemical composition between grains in pure zinc schoop is observed, whilst negligible differences are found in the characterized points.

The chemical characterization on the surface was analyzed at the selected points shown in Figure 5.19.

Spectrum 5 maps the selected point in the oxidized layer (surface), whilst *Spectrum 6* analyzed the chemical composition in the middle of a grain near the surface and to a delamination effect.
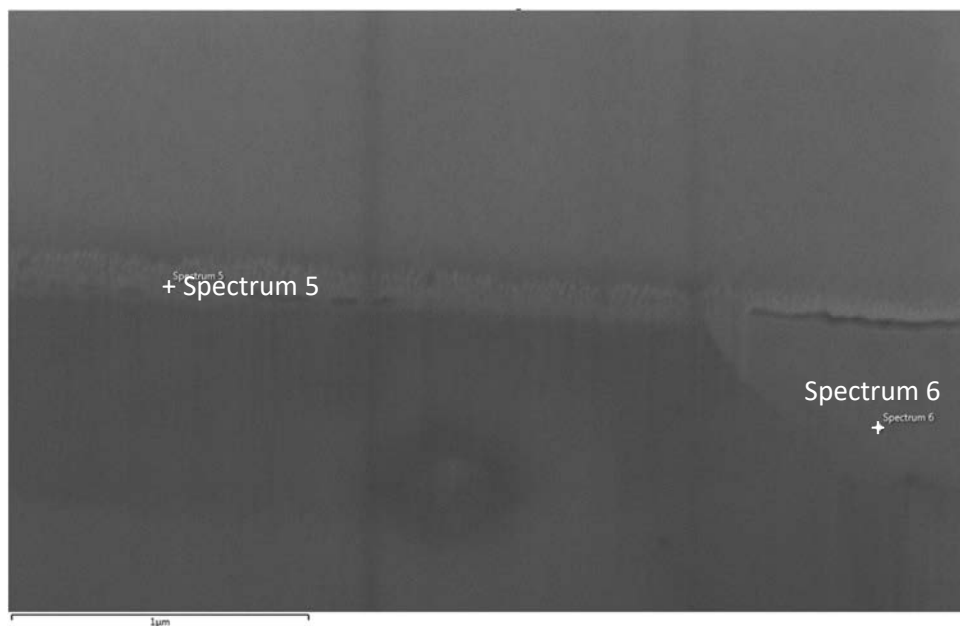

Figure 5.19. Selected points in FIB-CS of Zn schoop for EDS surface analysis

Table 5.9. Grain chemical composition in FIB-CS of Zn schoop by EDS surface analysis (atomic %)

Spectrum Label	C	O	Zn	Pt	Total
Spectrum 5	6.90	4.06	85.53	3.51	100.00
Spectrum 6	3.69	2.59	93.71		100.00

The EDS analysis of the oxidized layer (*Spectrum 5*) in the FIB-CS shows the platinum presence related to the pattern and a higher carbon and oxygen contents than in the center of a surface grain, related with the contaminants present on the surface (Table 5.9.). The result found in *Spectrum 6* is representative of the chemical composition found on the bulk in the analyses of Figure 5.18. and Table 5.8.

In general, from the FIB-CS it may be concluded that the natural oxidation of a schoop made of 100% zinc is not undermining the chemical and morphological properties of this material.

In addition to the chemical characterization by EDS in the FIB-CS, the distinction between oxidation states in oxygen and zinc elements in the bulk were studied by X-ray Photoelectron Spectroscopy (XPS).

Furthermore, the surface of pure zinc schoop was imaged by ETD (Everhart-Thornley Detector in Secondary Electron mode (Figure 5.20, left) and also by Retractable detector CBS (Backscattering electron image) (Figure 5.20, right) to characterize the chemical and topographical information.

The SEM images show a surface with a particle morphology representative of a spray process at low atomizing gas pressure and a low standoff distance. The particles during the process acquired velocity enough to get a high deformation when impacting the surface and thus create a surface with a lower roughness than that created with particles at slower velocities. [11]

No porosity was observed by FIB-CS analysis, thus the observed irregularities on the surface may be related to the roughness conferred by the melted grains during the spray process (Figure 5.20. left). Studies related to the surface roughness were additionally performed by contact stylus profilometry.

Due to the thin layer of natural oxidized zinc, by CBS image was able to be observed the grain boundaries well defined (Figure 5.20. right).
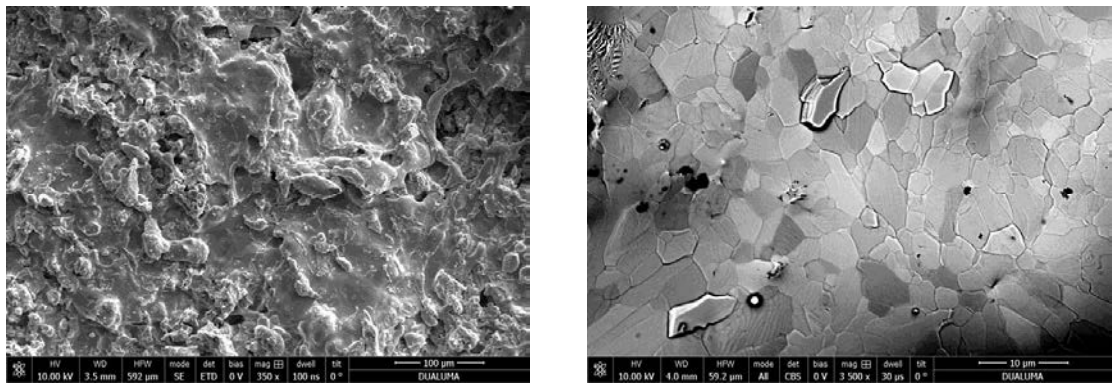
Figure 5.20. Zn schoop surface imaged by SE (left, scale x350) and by CBS (right, scale x3500)

The average metal grain size and its distribution are calculated by the image treatment with an internal software of TDK (AIM Grain Analysis) and Fiji ImageJ software. Figure 5.21. shows the grain numeration of one of the analyzed micrographs, the shown in Figure 5.20 right.

The grain size distribution in 100% Zn schoop has been achieved using Heywood distribution. A range of particle diameter of 1- 4 µm and an average Heywood diameter of 2.5 ± 1.0 um have been determined. In addition, an area distribution between 1-15 μm^2 is determined as reported in Figure 5.22. Furthermore, the Heywood circularity (HC) factor is shown in Figure 5.22 (right), the closer the shape of the particle is to a disk, the closer the HC is to 1.
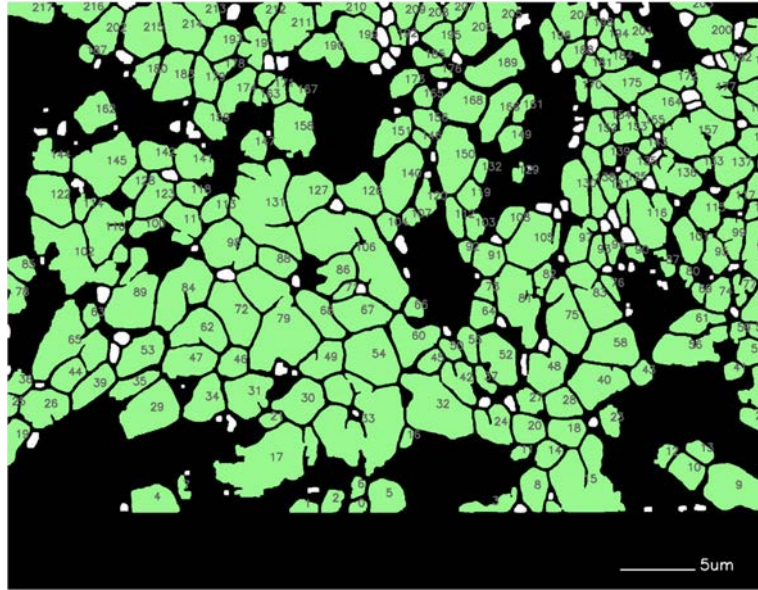
Figure 5.21. Grain numeration of Zn schoop surface for determining the grain size and its distribution.
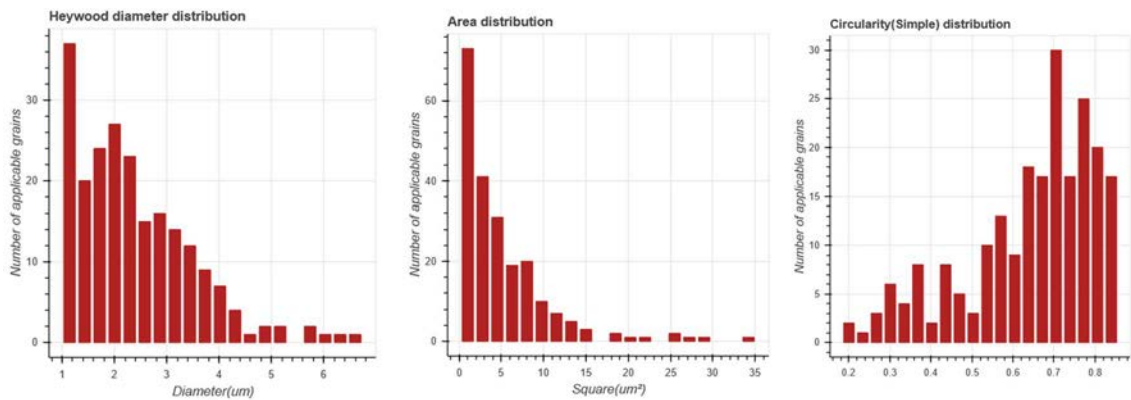

Figure 5.22. Grain analysis of 100% Zn schoop on surface (AIM software).

The intergranular area percentage shown on the surface by the evaluated sample of 100% Zn schoop reached the 9%.

Furthermore, the grain size was determined by using the single phase linear intercept method. 20 straight lines were drawn to measure the number of grains. An average grain diameter of 1.9 ± 0.4 μm was calculated (Figure 5.23.).
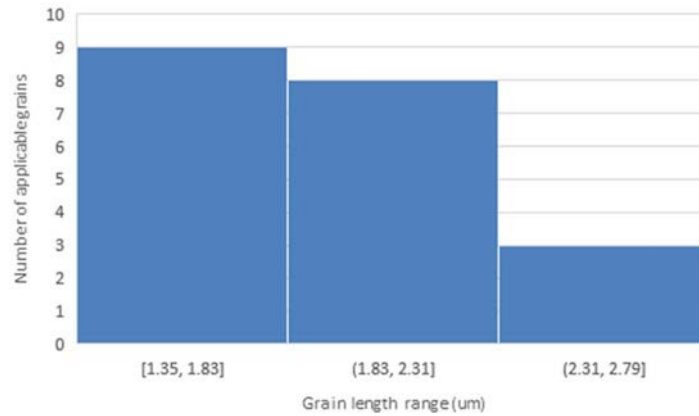
Figure 5.23. Grain size distribution of 100% Zn schoop on surface (Intercept method).

In addition to topographical information, the distribution of oxidation and contamination in the schoop surface was characterized by-EDS image mapping from the SDD detector. This distribution is observed in a schoop made of 100% Zn in *Figure 5.24*, using the color codification previously defined.
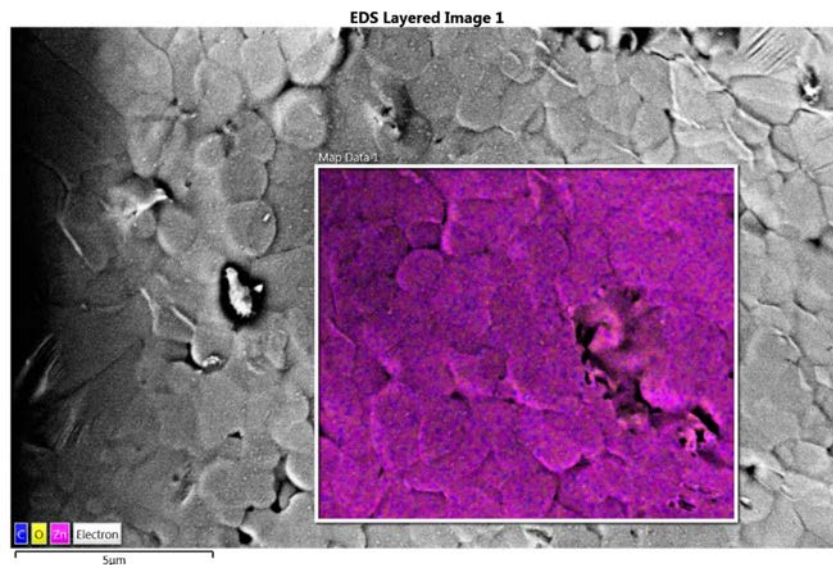
Figure 5.24. Mapping of Zn schoop surface imaged by SE (x10000)

The chemical composition of the surface is very homogeneous. All the found elements are well distributed. The homogeneous distribution of the oxygen signal may show that the oxygen presence is not related to oxides located at the edge of the grain or surface cavities. XPS analysis will characterize this point.

The atomic percentages found for every element on the mapped area are compiled in Table 5.10.

Table 5.10. Chemical composition in the surface of Zn schoop by EDX analysis (atomic %)

Statistics	C	O	Zn
Average	4.49	6.89	88.63
Standard Deviation	0.41	3.30	3.47

This chemical composition is in agreement with the results found in the previous analysis in the FIB-CS (Tables 5.8 and 5.9.).

5.2.5.2. <u>Schoop ZnAl15</u>

The superficial oxidation layer and bulk of schoop made of ZnAl15 were studied in the FIB-cross section imaged by an ETD detector on mode Secondary Electron (SE) as shown in *Figure 5.25*.
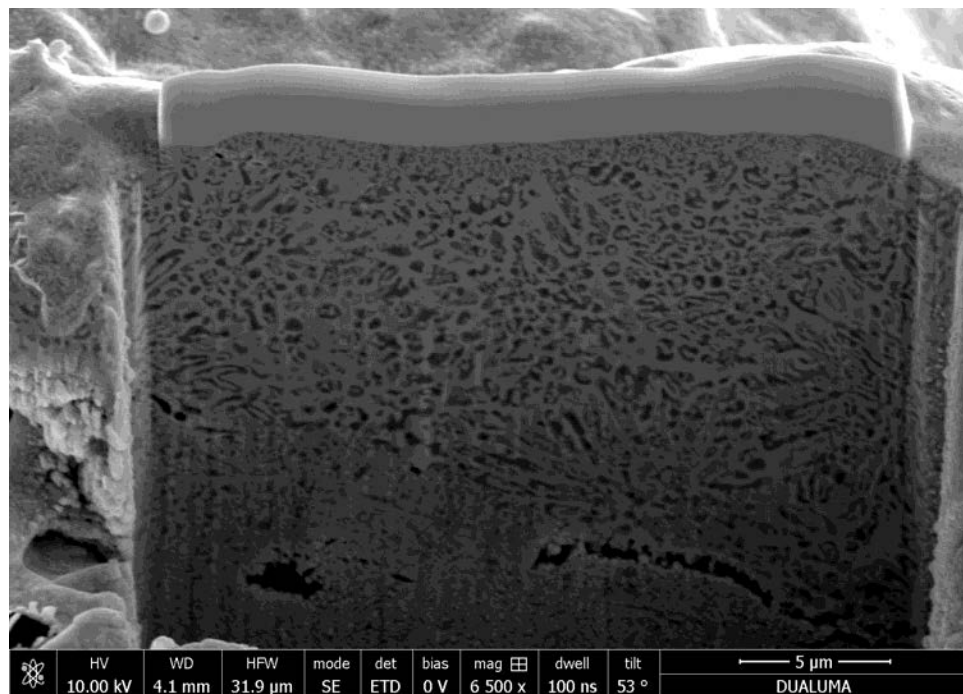
Figure 5.25. Schoop ZnAl FIB-CS, elevation view (Scale: x6500)

A homogeneous structure in the FIB cross section of the schoop can be observed, where a grey linked structure and some darker areas can be distinguished. If these dark areas are pores and cavities or the right integration of the 15% of aluminum inside the zinc structure will be clarified later by EDX analysis. No delamination in the schoop surface was appreciated.

On the other hand, as aging mechanisms were observed internal cracks and some cavities between grain boundaries due to mechanical fatigue.

The natural oxidation of a schoop made of 85% zinc and 15% aluminum presented a relevant morphological change in the size of the structure in surface. The superficial layer shows the same morphology than the bulk but with smaller size (Figure 5.26.). Additionally, a clear interface between

this superficial layer and the inner structure is shown in Figure 5.27, being this interface a perfect area to be unstuck both surfaces and being located cavities or creating a crack.
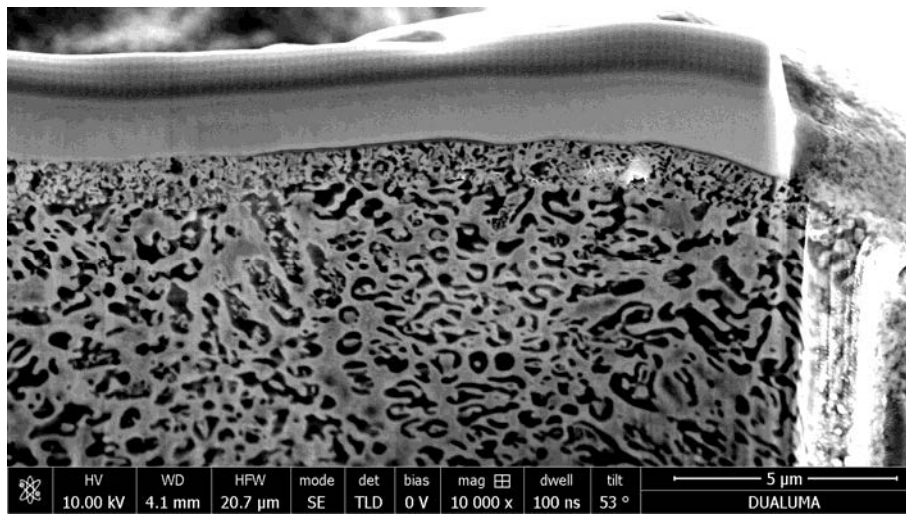
Figure 5.26. FIB-CS. Aging mechanisms in ZnAl schoop at time 0 of THB test. Mechanical fatigue (left) and delamination (right).
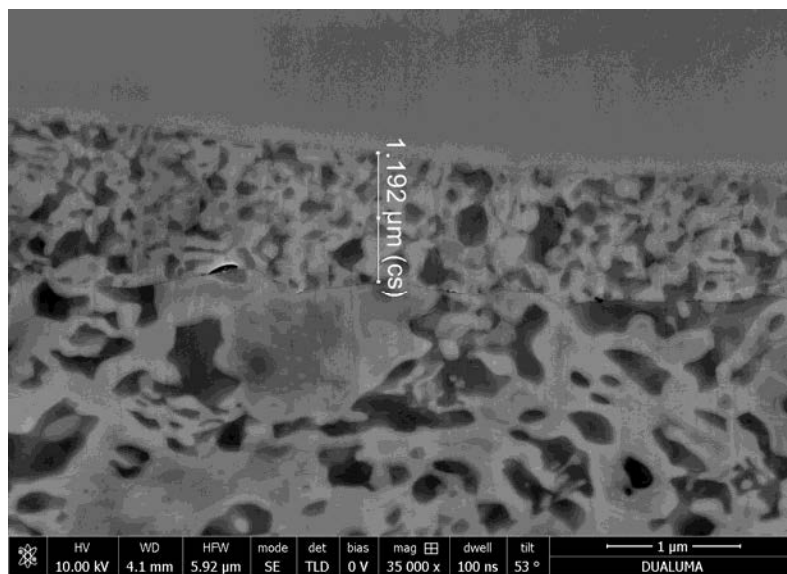

Figure 5.27. Schoop ZnAl FIB-CS. Superficial layer thickness (Scale: x35000)

This layer shows a homogeneous thickness in ZnAl schoop surface, an averaged value of 1.2 ± 0.02 μm thickness was measured (Figure 5.27).

The distribution of contaminants and oxidation in the schoop surface was characterized in the FIB-CS by an EDS image mapping from SDD detector (Figure 5.28). With this mapping will be additionally confirmed if the dark areas are cavities or not.
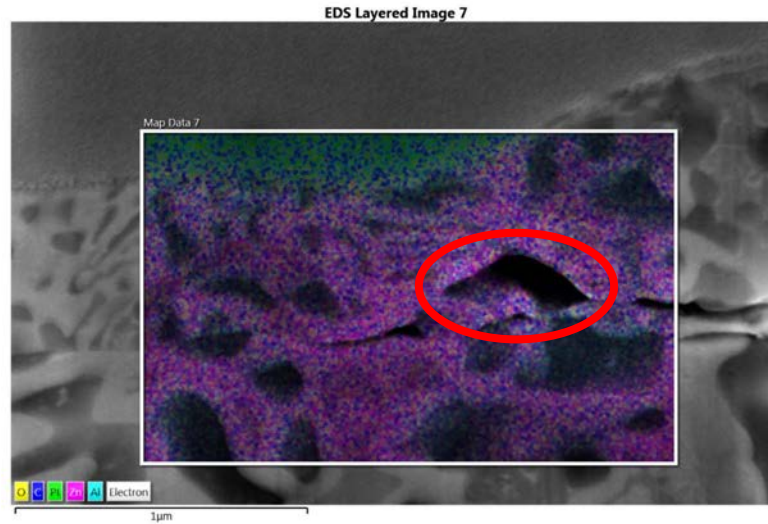
Figure 5.28. EDS image mapping of schoop ZnAl FIB-CS
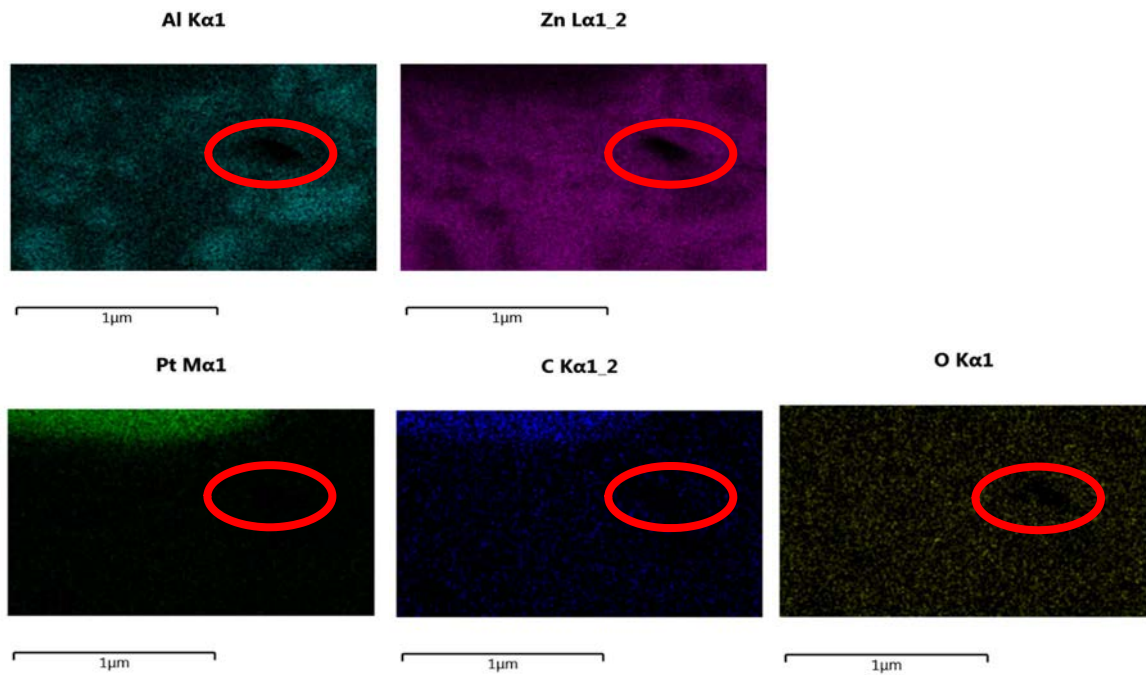
Figure 5.29. EDS image mapping by elements FIB-CS of schoop ZnAl15

The EDS image mapping confirms that the main structure shown in the FIB-CS is made of zinc and that the dark areas are not pores or cavities, but solid areas of aluminum homogeneously integrated inside the zinc structure.

Only one cavity is observed in the SEM image (encircle in red in Figures 5.28. and 5.29) and this is located in the interface between the superficial layer and the internal structure.

The oxygen is homogeneously distributed on surface but also in the structure (bulk) of the schoop ZnAl15 (Figure 5.29.). A higher concentration of oxygen in the surface is not observed.

An additional EDS analysis was performed by a linescan analysis of the main elements (carbon (C), zinc (Zn), aluminum (Al), oxygen (O) and platinum (Pt)) to confirm the thickness of the superficial layer already characterized in *Figure 5.27*. *Figure 5.30.* shows the drawn line (upper SEM image) where the EDS semi-quantification was determined from left (inside the platinum pattern) to right (inside the schoop). This is a semi-quantitative chemical analysis due to be a relative quantification between elements. No absolute values are determined, coordinate axis represents counts per second in the individual elements spectrum, but this chart combining all is no dimensional.
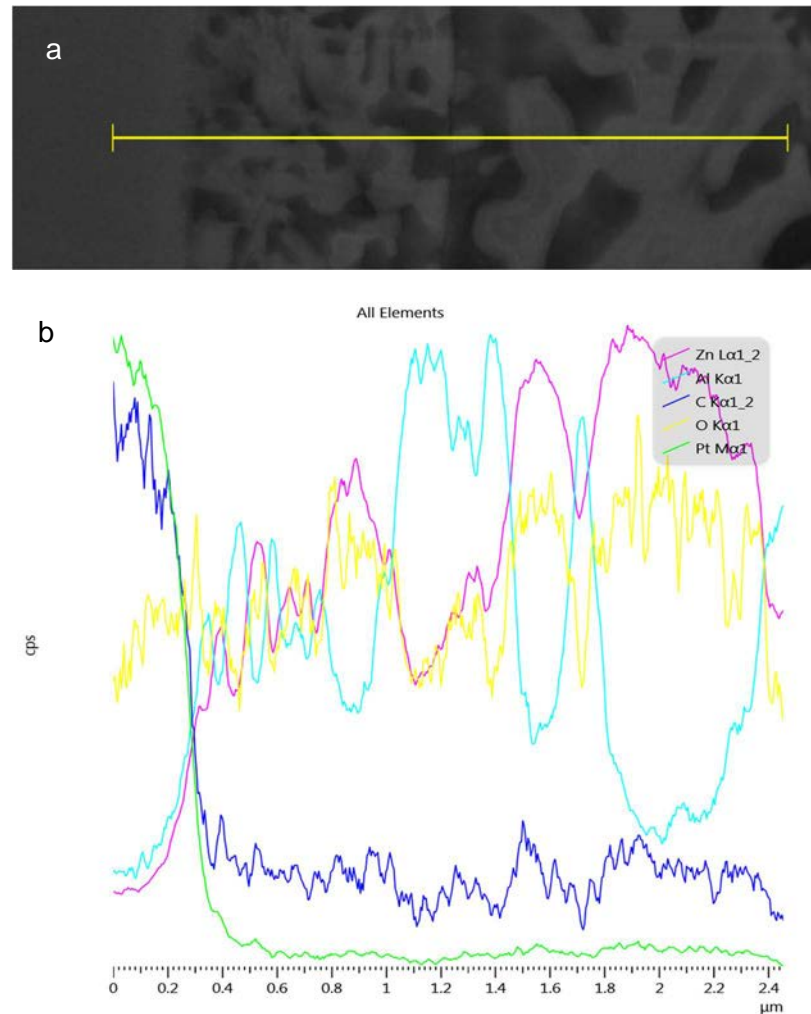
Figure 5.30. FIB-CS SEM of ZnAl15 schoop with linescan drawn (a). EDS scanned lines in the oxidized layer(b).

The EDS scanned lines from left to right evidence the interface platinum pattern/schoop by the fall in the platinum and carbon signals in favor of the zinc and aluminum ones.

A superficial layer of 0.9 μm thickness is measured by the linescan analysis in a different position than in Figure 5.27. and both are in agreement.

This EDS scanline analysis confirms additionally that the dark areas are aluminum particles integrated in the zinc surface. It can be observed the increase and decrease of aluminum signal when the analysis is detecting the composition of dark areas in the drawn line.

Furthermore, it is evidenced that the oxygen signal evolution goes together the zinc signal variations. This suggests that the oxygen is mainly bonded to the zinc. The detailed study of how is bonded the oxygen to the elements and the different contributions of binding energies in each element will be studied by XPS in the following paragraph.

A semi-quantitative chemical characterization of the schoop grains in the FIB-CS was done by EDS point analyses. Figure 5.31. shows the selected points for determining the semi-quantification of the elements in the bulk. And *Table Y4* compiles the EDS results in every point:

- Spectra 14: grain of zinc, centered point,

- Spectra 15: grain of zinc, edge, and

- Spectra 16: grain of aluminum, centered point.
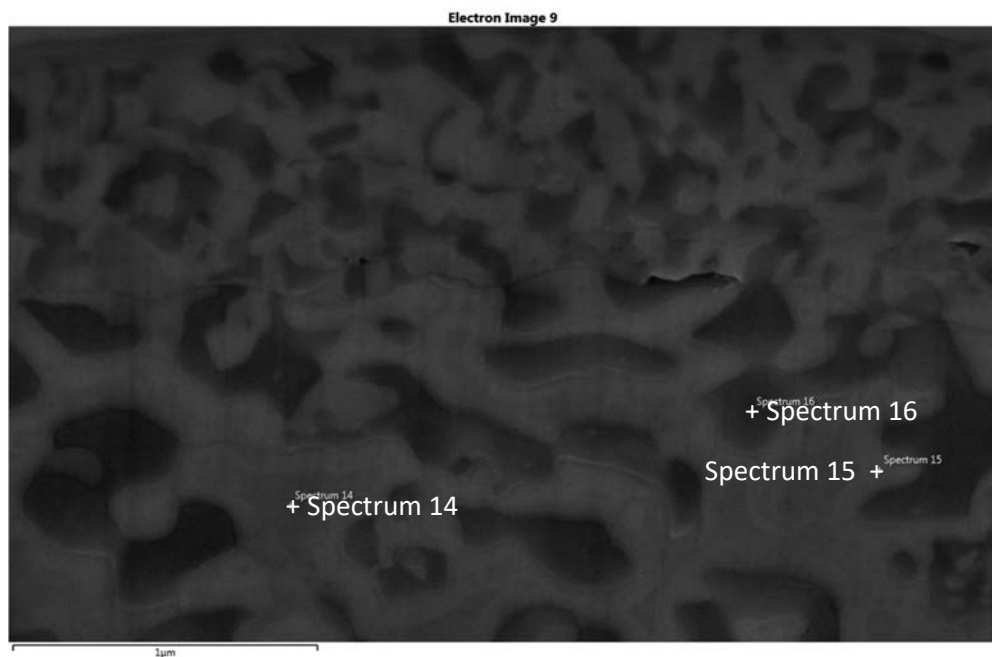
Figure 5.31. Selected points in FIB-CS of ZnAl15 schoop for EDX bulk analysis

Table 5.11. Grain chemical composition in FIB-CS (Figure 5.31) of ZnAl schoop by EDX analysis (atomic %)

Spectrum Label	C	O	Al	Zn	Total
Spectrum 14	2.92	3.05	8.61	85.42	100.00
Spectrum 15	3.02	3.03	18.79	75.16	100.00
Spectrum 16	1.87	1.86	40.17	56.11	100.00

The chemical composition shows overlapping between zinc and aluminum in the edges of the aluminum grains as Spectrum 15 shows. However, a higher content in oxygen in the grain boundaries was not observed, same oxygen contents in Spectrum 14 and 15. On the contrary, the oxygen content in aluminum grain (Spectrum 16) is reduced approximately 1% atomic due to the fall in zinc content.

The surface of ZnAl schoop was imaged by ETD (Everhart-Thornley Detector on mode Secondary Electron (*Figure 5.32., left*) and also by Retractable detector CBS (Backscattering electron image) (*Figure 5.32, right*) to characterized the chemical and topographical information.

A low presence of bores was observed by FIB-CS analysis. The complexity to distinguish pores/cavities from aluminum dark areas was evidenced by FIB-CS analysis.

The SEM images show a surface with a particle morphology representative of a spray process at low atomizing gas pressure and a low standoff distance (Figure 5.32.-left). The particles during the process have acquired velocity enough to get a high deformation upon impact to the surface and thus create a surface with a lower roughness than the one created with particles at slower velocities. [1]. Nevertheless, Mechanical Profilometry will perform surface roughness studies further.
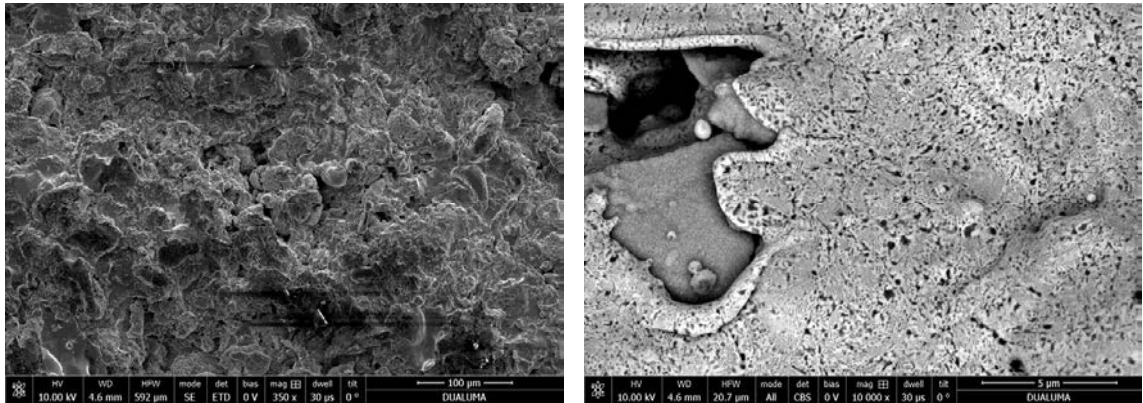
Figure 5.32. ZnAl schoop surface imaged by SE with ETD detector (left, scale x350) and by CBS (right, scale x10000)
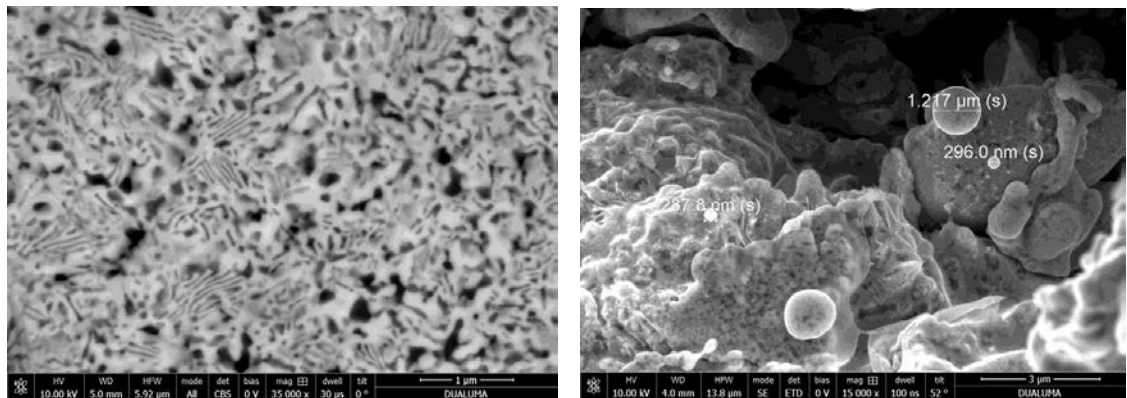
Figure 5.33. ZnAl schoop surface imaged by CBS (left, scale x35000) and by SE ETD detector (right, scale x15000)

The surface was recorded with secondary electron (SE) and backscatter electron detectors (CBS). Figure 5.33.-left show different regions as lamellae and islands that are originally formed during the eutectic reaction. The structure is not perfectly lamellar, but contain substantial rod shaped constituents appearing as islands, this is characteristic for Zn-Al alloys with Al contents higher than 7 wt.% [24]. SEM micrographs suggest that the formed nanostructure framework with lamellae and islands most likely corresponds to α-Al/β-Zn- eutectoid (Figure 5.34.). Aluminium particles exhibiting a spheroidal shape are observed in Figures 5.32-right and Figure 5.33-right, due to the combined effect of a high surface tension [18] and poor wetting angle in contact with zinc [19, 20].
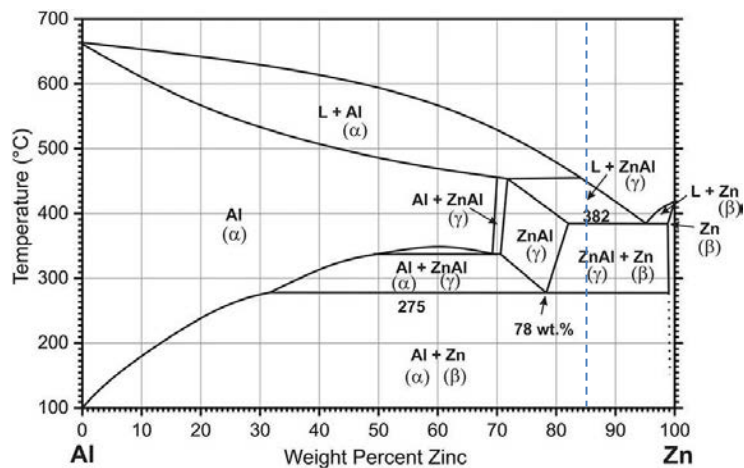
Figure 5.34. Phase diagram of binary Zn-Al alloy [21-23].

In addition to the topographical information, the distribution of oxidation and contamination in the schoop surface was characterized by an EDS image mapping from SDD detector (Figure 5.35).

The chemical composition in the surface is homogeneously distributed. The oxygen signal shows slight concentration of this element in the edge of the superficial peaks.

XPS analyses will confirm the accurate composition by distinguishing oxidation states of every element.
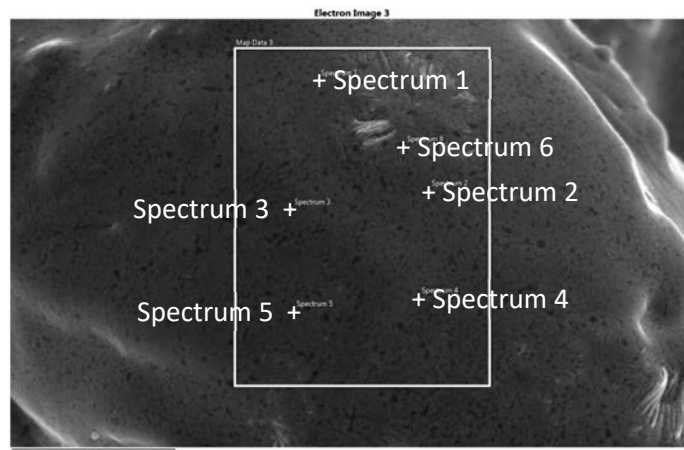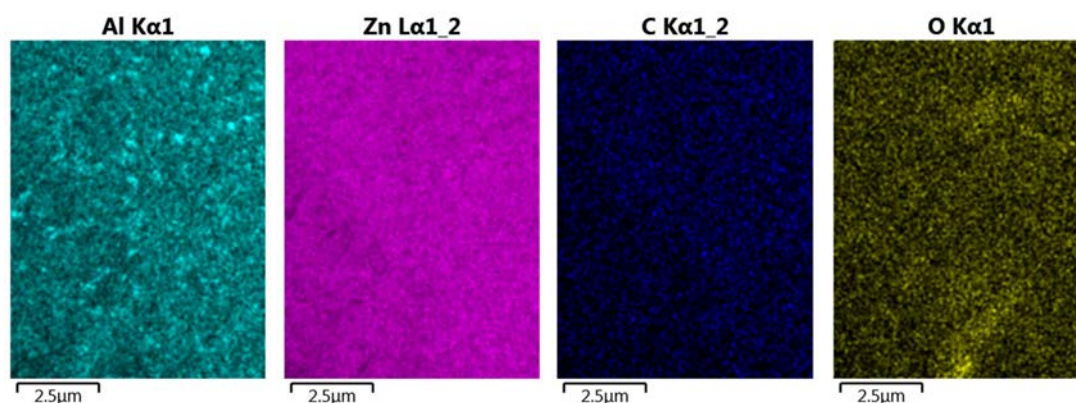
Figure 5.35. Mapping of ZnAl schoop surface imaged by SE (Map Data 3)

The atomic percentages found for every element on the selected points in *Figure 5.35* are compiled in *Table 5.12*.

Table 5.12. Chemical composition in the surface of Zn schoop by EDX analysis (atomic %)

Spectrum Label	C	O	Al	Zn	Total
Spectrum 1	8.81	1.52	23.94	65.73	100.00
Spectrum 2	6.39	1.19	30.87	61.55	100.00
Spectrum 3	5.72	2.17	29.00	63.11	100.00
Spectrum 4	7.90	3.60	21.30	67.20	100.00
Spectrum 5	8.20	2.46	26.42	62.91	100.00
Spectrum 6	5.18	0.83	48.07	45.91	100.00

Statistics	C	O	Al	Zn
Max	8.81	3.60	48.07	67.20
Min	5.18	0.83	21.30	45.91
Average	7.03	1.96	29.93	61.07
Standard Deviation	1.47	1.01	9.52	7.70

This chemical composition is in agreement with the results found in the previous analysis in the FIB-CS.

5.2.5.3. Schoop SnCu3

FIB polishing was used in SnCu3 schoop to obtain high quality cross-sections which revealed clear boundaries between the droplets (Figure 5.36). Typical trapped air pockets between copper droplets of different sizes are appreciated in Figures 5.36 & 5.37-a. In Fig. 5.37 (b&d) the characteristic copper condensate formed as small circular droplets is observed [17]. This topography suggests that the condensation of these copper spheres took place according to the mechanism V$\rightarrow$ L ($\rightarrow$ S), in which the liquid state is retained during the deposition and the crystallization took place during consequent cooling of the substrate [13-16].

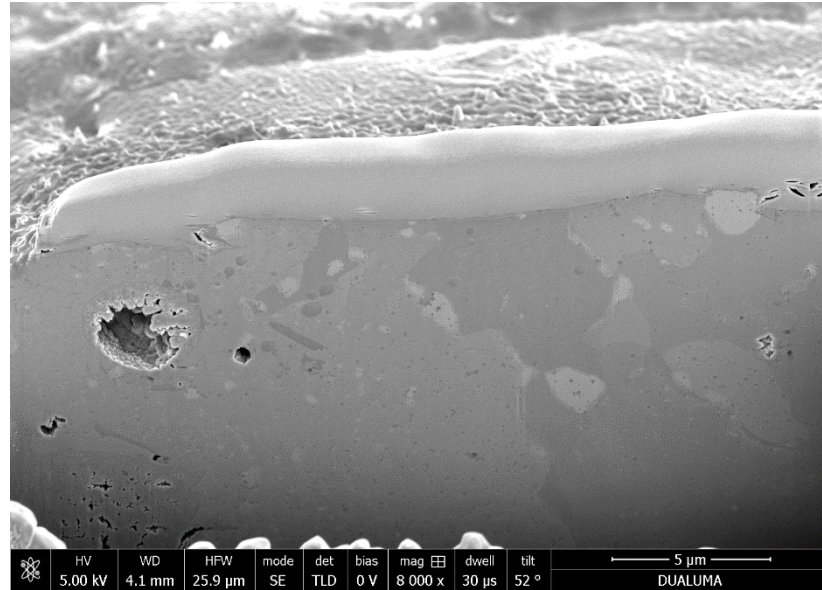No delamination between droplets or intergranular cracks on the FIB-CS were observed.

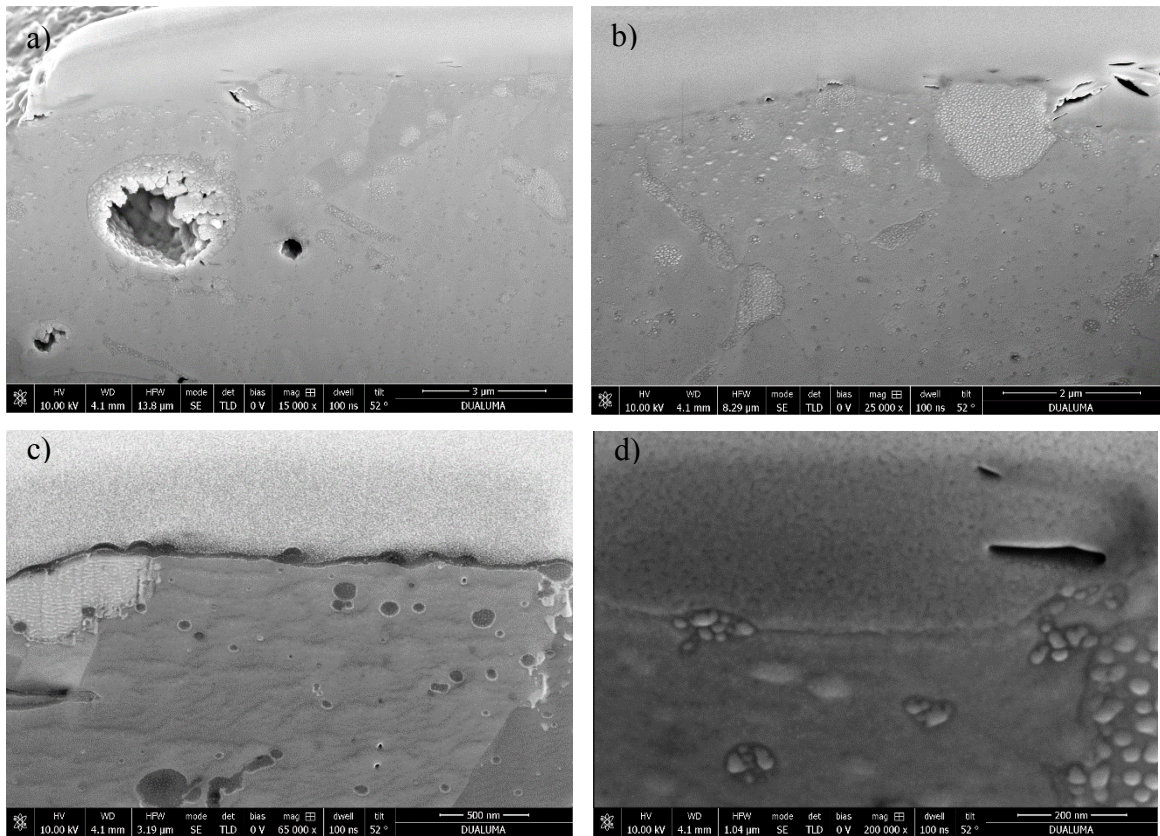Figure 5.36. Schoop SnCu3 FIB-CS, TLD detector on SE mode, elevation view (Scale: x8000)

Figure 5.37. Schoop SnCu3 FIB-CS, different sites, elevation views (Scales: a) x15000, b) x25000, c) x65000 and d) x200000).

The distribution of the copper in the tin matrix and the oxidation in the schoop surface was characterized in the FIB-CS by EDS mappings from SDD detector (Figure 5.38). A higher concentration of oxygen is found inside the copper void (Figure 5.38a)) and in the surface (Figure 5.38c).
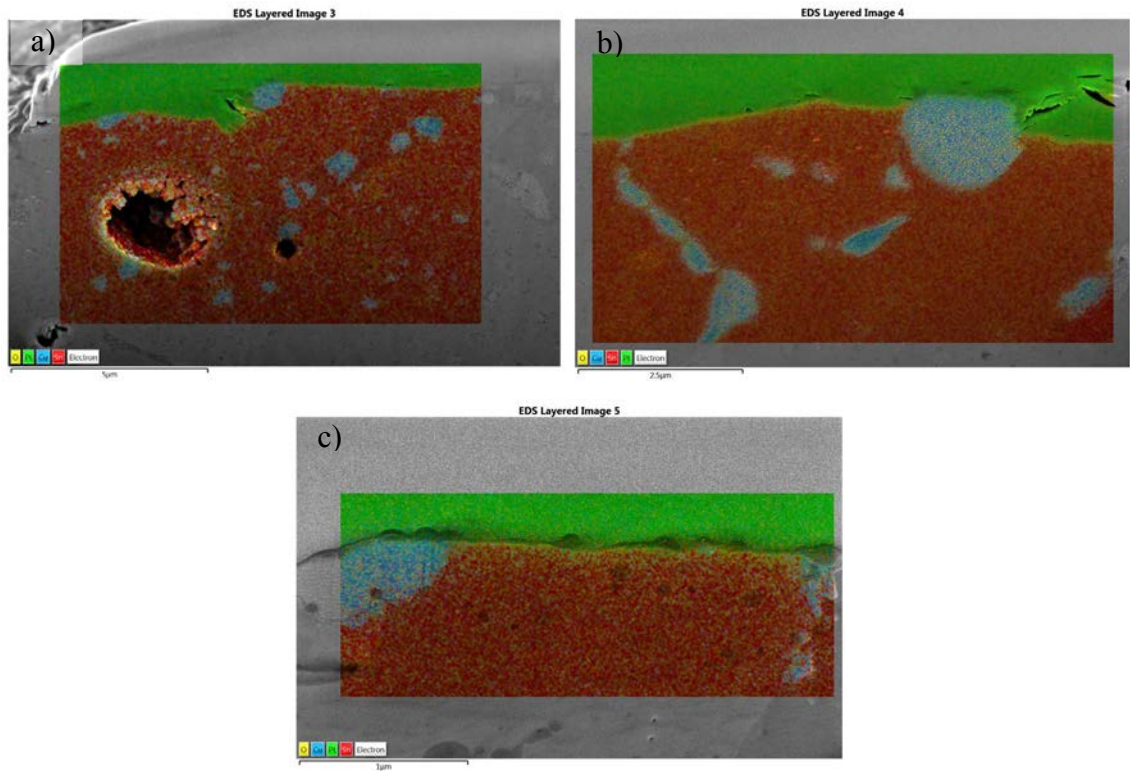
Figure 5.38. EDX mapping of a) Figure 5.37-a, b) Figure 5.37-b and c) Figure 5.37-c. Color codification: O (yellow), Cu (light blue), Pt (green) and Sn (red).

An EDX analysis by points was conducted in the site imaged in Figure 5.37-a.
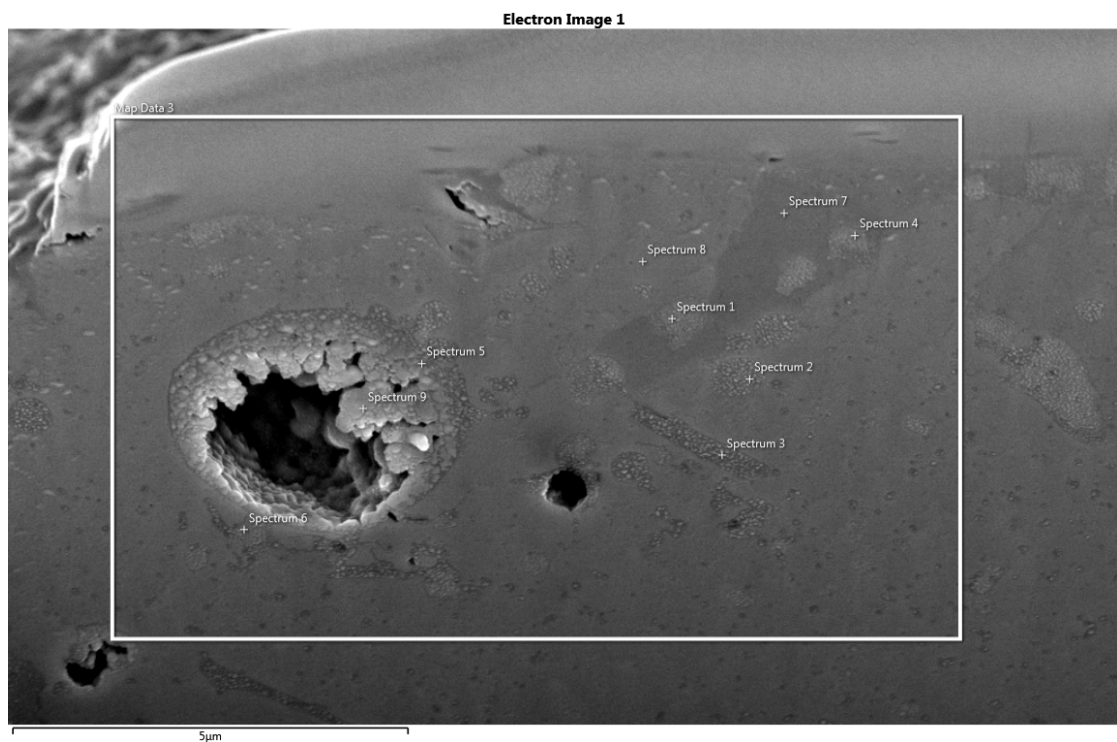
Figure 5.39. Selected points in FIB-CS of SnCu3 schoop for EDX bulk analysis

141

Table 5.13. Grain chemical composition in FIB-CS of SnCu3 schoop by EDS bulk analysis (atomic %).

Spectrum Label	O	Cu	Sn	Total
Spectrum 1	1.43	25.36	73.21	100.00
Spectrum 2	8.53	1.40	90.07	100.00
Spectrum 3	7.96	1.37	90.67	100.00
Spectrum 4	2.93	30.13	66.94	100.00
Spectrum 5	8.00	8.11	83.89	100.00
Spectrum 6	4.47	38.07	57.46	100.00
Spectrum 7	1.22		98.78	100.00
Spectrum 8	1.31		98.69	100.00
Spectrum 9	4.67	10.66	84.67	100.00

According to the phase diagram (Figure 5.40 [25-27]), below 350 ºC the stable intermetallic phases are Cu_6Sn_5 and Cu_3Sn phases [29-30]. Sn-3% Cu is an hypereutectic system and the main phases are β-Sn and Cu_6Sn_5 at room temperature. The eutectic reaction of L→ β-Sn + η-Cu_6Sn_5 occurs at 227ºC. With the further cooling, the transformation of the Cu_6Sn_5 phase takes place from the hexagonal η-Cu_6Sn_5 to a monoclinic polymorph η'-Cu_6Sn_5 at 186ºC [29-30].
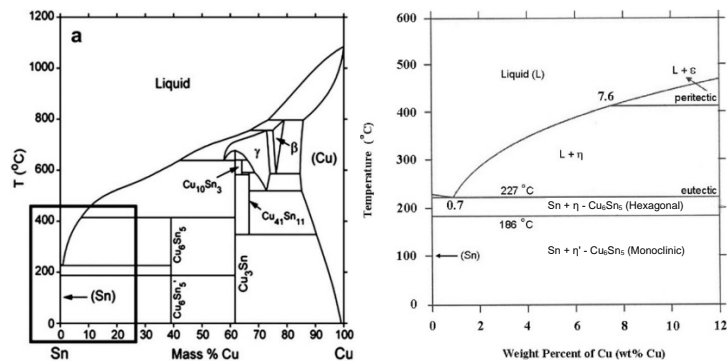
Figure 5.40. a) Phase diagram of Sn-Cu [25, 26]. b) Magnification of the Sn-rich corner of a) [adaptation of 26, 27]

The SnCu3 schoop surface was imaged by ETD (Everhart-Thornley Detector) on mode Secondary Electron (Figure 5.41a), by Retractable detector CBS (Backscattering electron image) (Figure 5.41b) and mapped by EDX (Figure 5.41c) to characterize the topographical and chemical information, respectively.

Figure 5.41a shows the surface topography with the characteristic splash of the sprayed metal drops. Figure 5.41b and c shows the microstructure of the SnCu3 schoop. The matrix contained Sn-rich phases and fine eutectic Sn-Cu phases are present between the β-Sn grains. Furthermore, Cu_6Sn_5 particles distribute evenly in the matrix. A higher presence of Cu_6Sn_5 is reported according to Cu content is increased [25, 33], playing the Cu a refining role on the β-Sn.
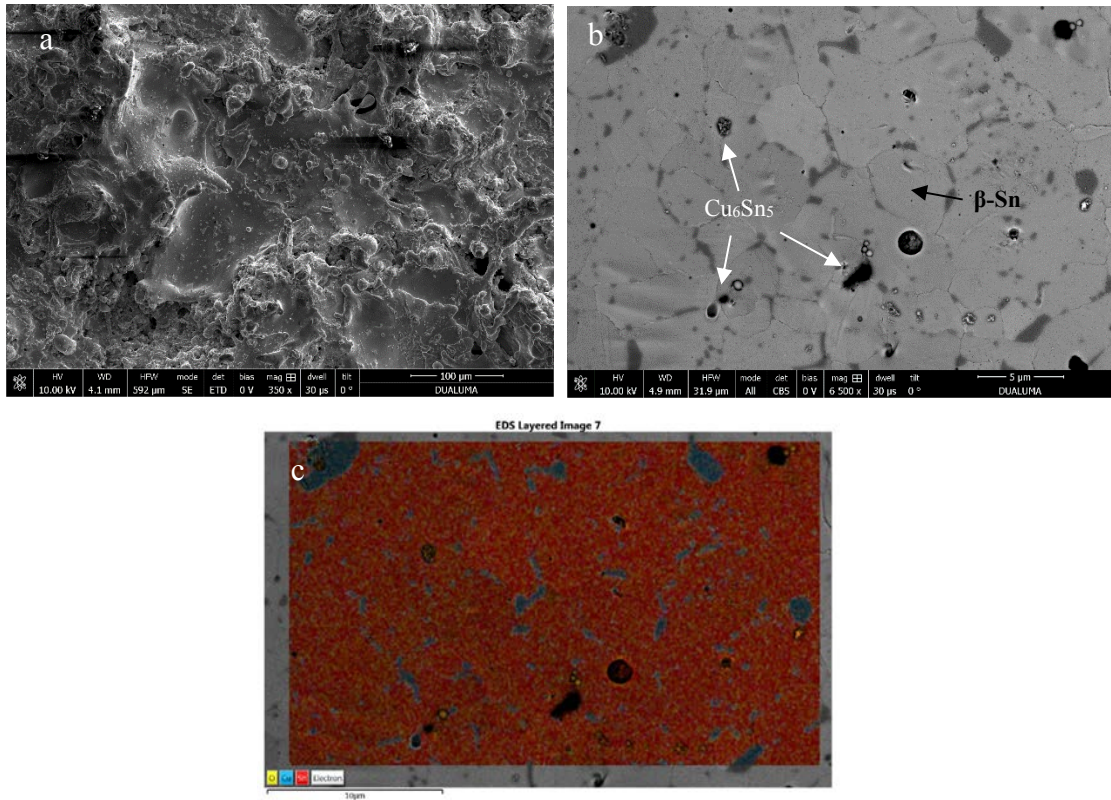
Figure 5.41. SEM image of SnCu3 schoop surface by ETD detector (left, scale x350) and by CBS (right, scale x6500). Color codification: O (yellow), Cu (light blue) and Sn (red).

5.2.6. X-ray photoelectron spectroscopy (XPS)

XPS was conducted to determine the chemical composition of the exposed oxidized layer (due to natural oxidizing ambient) on surface of the schoop samples as well as the underlay composition. In addition, the chemical state of the main constituent elements is determined for every schoop variant.

Figure 5.2.6.1. presents the XPS core level C 1s, O 1s and Zn 2p3 spectra recorded on the surface of schoop made of 100% Zn and after being sputtered during 14 min with an ion gun of 4kV of argon ions and an sputtering area of (4x4mm).

The high resolution C 1s core level spectrum on surface can be fitted with three peaks, associated to the CH$_2$-CH$_2$ bonds (B.E.: 284.7 $\pm$ 0.1 eV), the C-O bonds (B.E.: 286.4 $\pm$ 0.1 eV) and the C=O bonds (carboxyl groups, B.E.: 288.7 $\pm$ 0.1 eV). These peaks can be explained by the XPS was conducted to determine the chemical composition of the exposed oxidized layer (due to natural oxidizing ambient) on the surface of the schoop samples as well as the underlay composition. In addition, the chemical state of the main constituent elements is studied for every schoop variant.

Figure 5.2.6.1. presents the XPS core level C 1s, O 1s and Zn 2$p_{3/2}$ spectra recorded on the surface of schoop made of 100% Zn and after being sputtered during 14 min with an ion gun of 4kV of argon ions and an sputtering area of (4x4mm).

The high resolution C $1s$ core level spectrum can be fitted with three contributions, associated to the CH_2-CH_2 bonds (B.E.: 284.7 $\pm$ 0.1 eV), the C-O bonds (B.E.: 286.4 $\pm$ 0.1 eV) and the O-C=O bonds (carboxylate groups, B.E.: 288.7 $\pm$ 0.1 eV). These peaks can be explained by the presence on the surface of a low quantity of organic contaminations on the metallic samples exposed to ambient air. This explanation is supported by the fact that after 14 min of sputtering, all contributions disappeared.

The O $1s$ envelope obtained from the surface was fitted with two components, the O-1 component, located at 530.1 $\pm$ 0.1 eV, corresponds to lattice oxygen in zinc oxide. The O-2 component located at 531.8 $\pm$ 0.1 eV is attributed to -OH bonds due to Zn-OH bonds or to absorbed H_2O molecules on the films. This component is not observed after 14 min of Ar$^+$ sputtering. All these values are similar to the values reported by others [48-50]. Atomic concentration of O $1s$ is reduced from 22.7% to 4.1% after 14 min of Ar$^+$ sputtering (*Table 5.2.6.1.*).

The differentiation of chemical state by XPS on the basis of Zn $2p_{3/2}$ can be very difficult due to the small binding energy shifts between Zn^0, ZnO, $Zn(OH)_2$, $ZnCO_3$, and $Zn_5(OH)_6(CO_3)_2$. The Zn $2p_{3/2}$ peak was fitted with only one component located at 1021.5 $\pm$ 0.1 eV and a FWHM of 1.97 and a 74% Gauss fitting that is attributed in literature to zinc bonded to oxygen in zinc oxide, as well as, peak width may broaden if more than one Zn species are present. However, after the sputtering, the component is registered at 1021.7 $\pm$ 0.1 eV but a narrower peak with a FWHM of 1.54 and a 54% Gauss fitting, being this reported to be associated to zinc hydroxide [48-50, 54, 56, 57, 59, 60, 61]. The O/Zn atomic ratio was obtained from the ratio between the normalized areas of the O-1 and Zn $2p_{3/2}$ contribution (Tables 5.2.6.1. and 5.2.6.4.). On the surface was found to be around 1.61, whilst sputtering the surface with Ar$^+$ for 14 min was determined 0.04.

Table 5.2.6.1. Chemical composition (in atomic concentration %) determined by XPS for 100% Zn on surface and after sputtering 14 min with Ar$^+$.

Schoop sample	C $1s$	O $1s$	Zn $2p_{3/2}$
100% Zn - surface	69.3 $\pm$ 3.5	22.7 $\pm$ 1.1	8.0 $\pm$ 0.4
100% Zn - after 14 min. Ar$^+$	2.4 $\pm$ 0.1	4.1 $\pm$ 0.2	93.5 $\pm$ 4.7

Table 5.2.6.2. Chemical composition (in atomic concentration %) determined by XPS for ZnAl15 on surface and after sputtering 14 min with Ar$^+$.

Schoop sample	C $1s$	O $1s$	Al $2p$	Zn $2p_{3/2}$
ZnAl15 - surface	39.2 $\pm$ 1.9	39.3 $\pm$ 1.9	17.8 $\pm$ 0.9	3.7 $\pm$ 0.2
ZnAl15- after 14 min. Ar$^+$	0.0 $\pm$ 0.0	14.9 $\pm$ 0.7	24.9 $\pm$ 1.2	60.2 $\pm$ 3.0

Table 5.2.6.3. Chemical composition (in atomic concentration %) determined by XPS for SnCu3 on surface and after sputtering 14 min with Ar⁺.

Schoop sample	C 1*s*	O 1*s*	Sn 3*d*5	Cu 2*p*
SnCu3 - surface	39.4 ± 2.1	36.9 ± 1.9	21.6 ± 1.2	2.1 ± 0.1
SnCu3- after 14 min. Ar⁺	4.1 ± 0.3	5.0 ± 0.3	80.2 ± 4.1	10.7 ± 0.7
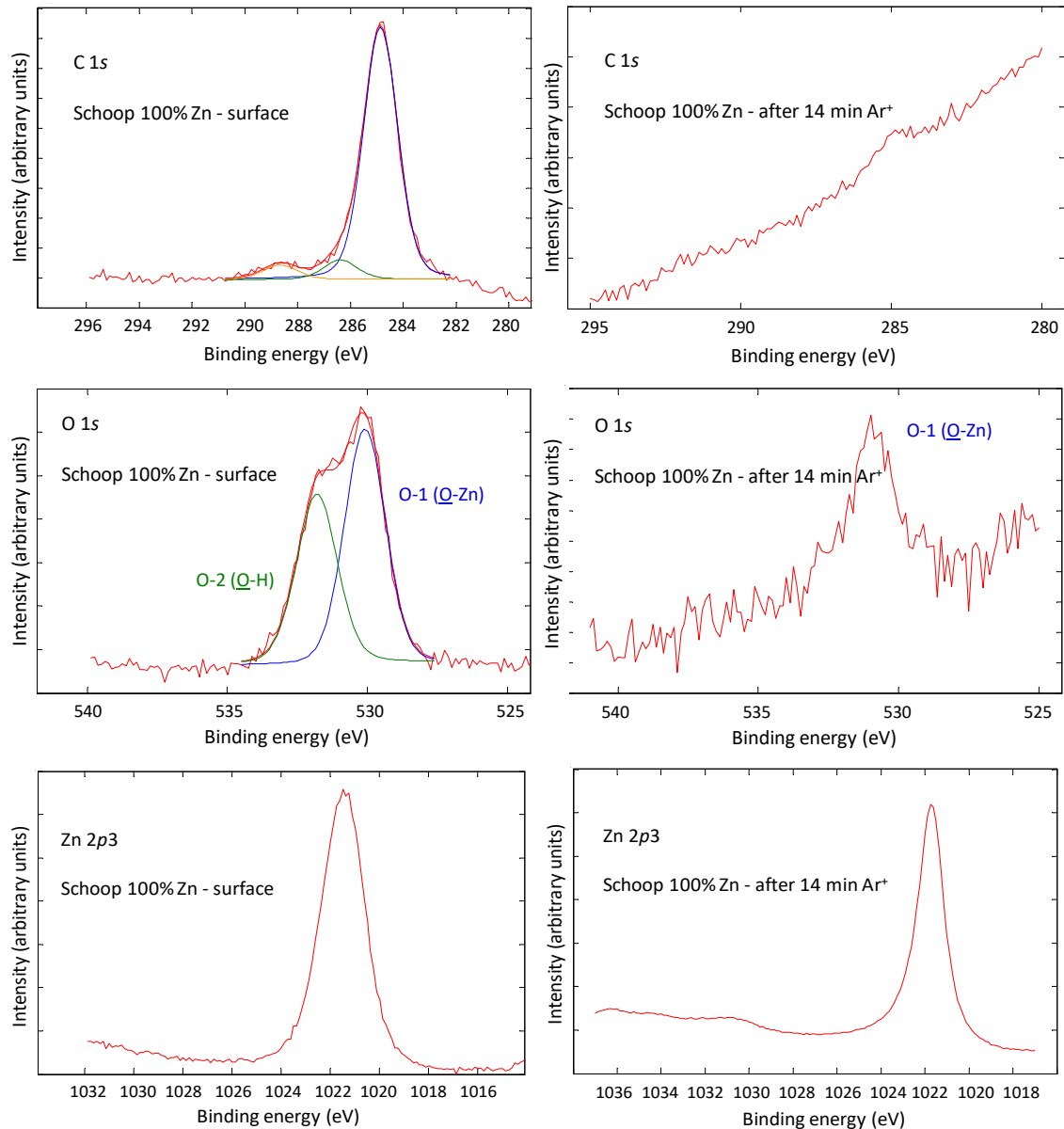
Figure 5.2.6.1. C 1*s*, O 1*s* and Zn 2*p*₃/₂ core level spectra for schoop of pure Zn on surface and after 14 min of sputtering with Ar⁺ 4kV.

Table 5.2.6.4. Binding energy (B.E.) and FWHM for the O1s peaks for 100% Zn schoop on surface and after sputtering 14 min with Ar$^+$.

Film Sample	Region: O1s Bands	Proportion of area (%)	Position (eV) Corrected B.E.	FWHM (eV)	% Gauss	Chi Squared
100% Zn schoop_Surface	O-1	56.9	530.09	1.71	89	2.28
100% Zn schoop_Surface	O-2	43.1	531.80	1.71	80	
100% Zn schoop_after 14min Ar+	O-1	100.0	530.67	1.71	88	3.05

Figure 5.2.6.2. illustrates the XPS core level C 1*s*, O 1*s*, Zn 2*p*3/2 and Al 2*p* spectra recorded on the surface of schoop made of ZnAl15 and after being sputtered during 14 min with an ion gun of 4kV of argon ions.

The high resolution C 1*s* core level spectrum can be fitted with three contributions associated to the CH_2-CH_2 bonds (B.E.: 284.7 $\pm$ 0.1 eV), the C-O bonds (B.E.: 286.2 $\pm$ 0.1 eV) and the O-C=O bonds (carboxylate groups, B.E.: 288.8 $\pm$ 0.1 eV). As shown by the schoop of 100% Zn, these peaks are associated to the presence on the surface of organic contaminants that come from the ambient air, disappearing after the sputtering.

The O 1*s* envelope obtained from the surface was fitted with only one component located at 531.1 $\pm$ 0.1 eV, being this binding energy associated to lattice oxygen of the alumina matrix. After sputtering the substrate for 14 min with 4kV of Ar$^+$, the binding energy is shifted to 532.4 $\pm$ 0.1 eV, being this attributed to hydroxyl groups (like AlOOH or Al(OH)$_3$ species) embedded in the zinc oxide [37-44, 48, 51]. Atomic concentration of O 1*s* is reduced from 39.3% to 14.9% after 14 min of Ar$^+$ sputtering (*Table 5.2.6.2.*). This high content in oxygen still after blasting suggests that the sputtering rate on schoop made of ZnAl15 was lower than expected due to the studied structure by FIB-SEM or that 14 min. is not time enough to completely remove the oxidized superficial layer.

The Zn 2*p*3/2 peak was fitted with only one component located at 1021.7 $\pm$ 0.1 eV attributed to zinc bonded to oxygen in zinc oxide in both cases, before and after being sputtered 14 min the substrate.

The Al 2*p* core level can be decomposed in two components. On the surface, Band 1 at 71.5 $\pm$ 0.1 eV is associated to metallic aluminium and Band 2 at 74.0 $\pm$ 0.1 eV is attributed to aluminum hydroxides. After sputtering, Band 1 shifted to 73.0 $\pm$ 0.1 eV being assigned to the Al 2p of metallic aluminium and Band 2 at 75.4 $\pm$ 0.1 eV is associated to aluminium oxide (*Table 5.2.6.5.*)[37-44, 48, 51].
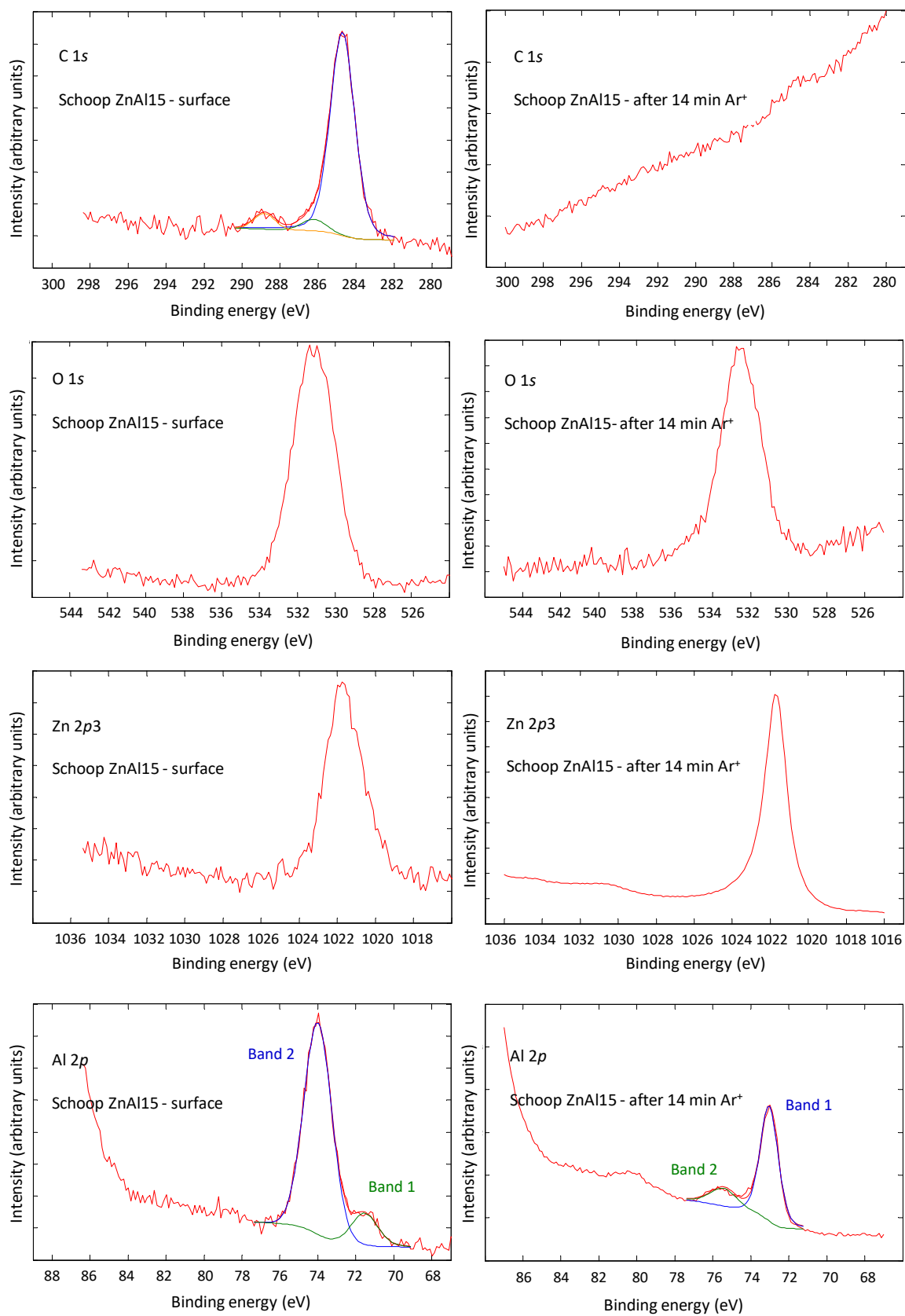
Figure 5.2.6.2. C 1*s*, O 1*s*, Zn 2*p*$_{3/2}$ and Al 2*p* core level spectra for ZnAl15 schoop on surface and after 14 min of sputtering with Ar$^+$ 4kV.

Table 5.2.6.5. Binding energy (B.E.) and FWHM for the Al 2*p* peaks for ZnAl15 schoop on surface and after sputtering 14 min with Ar⁺ (4kV).

Film Sample	Region: Al2*p* Bands	Proportion of area (%)	Position (eV) Corrected B.E.	FWHM (eV)	% Gauss	Chi Squared
ZnAl15 schoop_Surface	Band 1	13.5	71.53	1.65	82	0.91
ZnAl15schoop_Surface	Band 2	86.5	74.00	1.74	99	
ZnAl15 schoop_after 14min Ar+	Band 1	79.6	73.03	1.13	75	7.29
ZnAl15 schoop_after 14min Ar+	Band 2	20.4	75.43	1.70	70	

Figure 5.2.6.3. illustrates the high resolution XPS spectra of C 1*s*, O 1*s*, Sn 3$d_{5/2}$ and Cu 2*p* in the surface of schoop made of SnCu3 and after being sputtered during 14 min with an ion gun of 4kV of argon ions.

The high resolution C 1*s* core level spectrum for time 0 (on surface) is attributed to carbon of contamination, as explained for the schoops made of 100% Zn and ZnAl15.

The O 1*s* envelope is asymmetric, suggesting the presence of multi-component oxygen species. It can be resolved by using a curve fitting with two components, the O-1 component located at 531.2 $\pm$ 0.1 eV, being this binding energy associated to lattice O atoms linked to tin; and O-2 at 533.1 $\pm$ 0.1 eV is attributed to hydroxyl species or O-H bonds due to absorbed H_2O molecules or oxygen on the films, this component is not observed after 14 min of Ar⁺ sputtering (Table 5.2.6.6.). These data are close to the reported values on literature [51-55]. Atomic concentration of O 1*s* is reduced from 36.9% to 5.0% after 14 min of Ar⁺ sputtering (*Table 5.2.6.3.*).

The Sn 3*d* core level spectrum showed spin-orbit doublet peaks in two components. On surface. the Sn^{2+} fit component shows the doublet peak at 486.4 $\pm$ 0.1 eV (Sn^{2+} 3$d_{5/2}$) and at 494.9 $\pm$ 0.1 eV (Sn^{2+} 3$d_{3/2}$). Whilst the Sn^{4+} fit component peaks are located at 488.5 $\pm$ 0.1 eV (Sn^{4+} 3$d_{5/2}$) and at 496.8 $\pm$ 0.1 eV (Sn^{4+} 3$d_{3/2}$). After sputtering for 14 min., the Sn 3d core level spectrum revealed that the chemical state of Sn is mainly 0 and contains a small proportion of Sn2+ (see Figure 5.2.6.3. c). Every peak is attributed to the metallic component (Sn^0 fit) located at 484.9 $\pm$ 0.1 eV (Sn^0 3$d_{5/2}$) and at 493.5 $\pm$ 0.1 eV (Sn^0 3$d_{3/2}$). Whilst the Sn^{2+} fit component shifted slightly the doublet peak at 486.3 $\pm$ 0.1 eV (Sn^{2+} 3$d_{5/2}$) and at 495.1 $\pm$ 0.1 eV (Sn^{2+} 3$d_{3/2}$). [52, 53].

The Cu 2p envelop was not detected on the surface. However, after 14 min of sputtering at 4kV with argon ions, the Cu 2p$_{3/2}$ and Cu 2p$_{1/2}$ core levels were registered at 933.2 $\pm$ 0.1 eV and 952.8 $\pm$ 0.1 eV, respectively, which are close to the values found on literature for Cu 2p in CuO [54, 55].
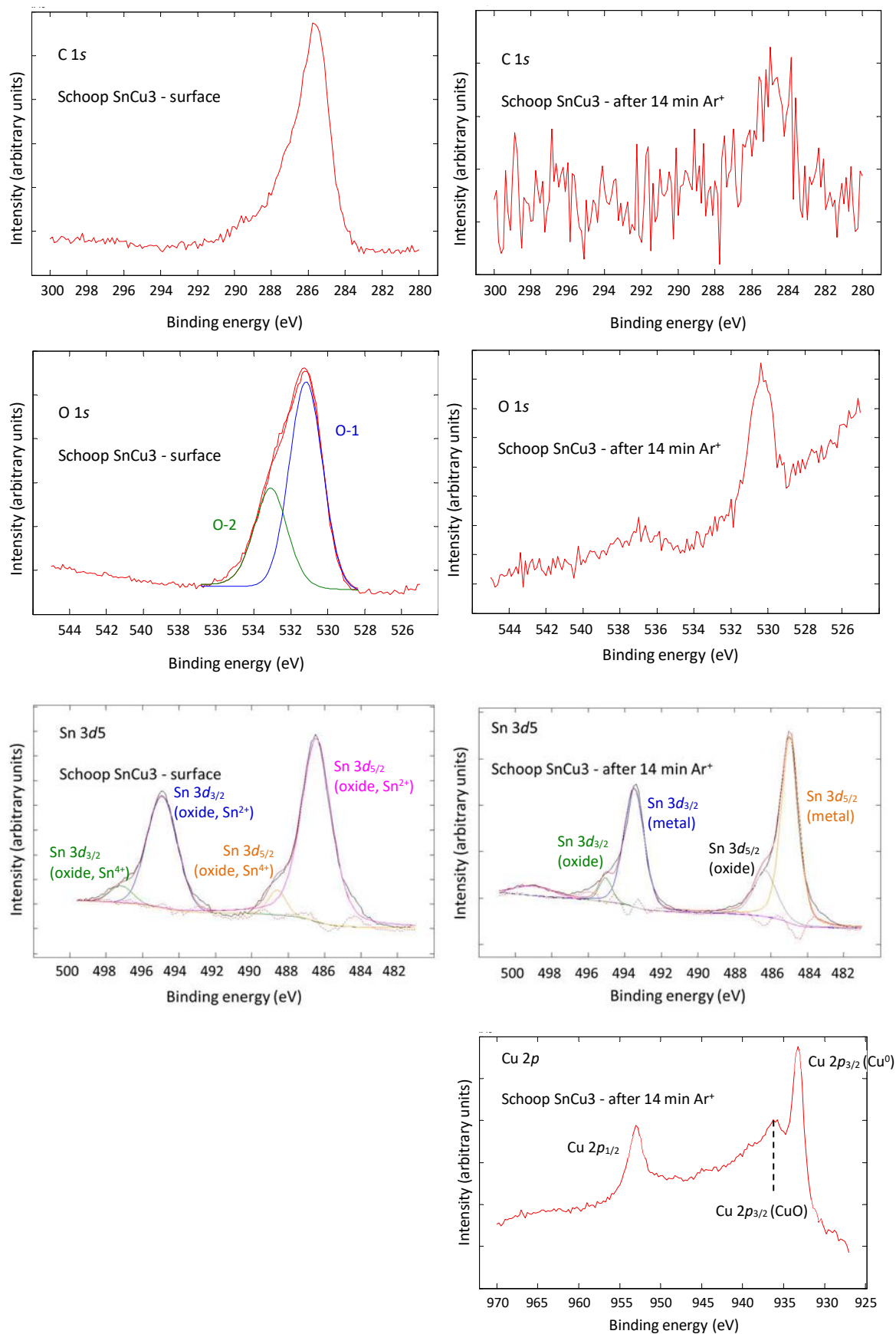
Figure 5.2.6.3. C 1*s*, O 1*s*, Sn 3*d*5 and Cu 2*p* core level spectra for SnCu3 schoop before and after 14 min of sputtering with Ar⁺ 4kV.

Table 5.2.6.6. Binding energy (B.E.) and FWHM for the O1s peaks for SnCu3 schoop on surface and after sputtering 14 min with Ar+.

Film Sample	Region: O1s Bands	Proportion of area (%)	Position (eV) Corrected B.E.	FWHM (eV)	% Gauss	Chi Squared
SnCu3 schoop_Surface	O-1	65.7	531.18	2.11	100	8.49
SnCu3 schoop_Surface	O-2	34.3	533.09	2.11	80	
SnCu3 schoop_after 14min Ar+	O-1	100.0	530.67	2.11	83	9.71

X-ray photoelectron spectroscopy depth profile analysis was conducted in the C 1*s*, O 1*s* and Zn 2*p*$_{3/2}$ regions for the substrate made of 100% zinc (Figure 5.2.6.4.). It was found that after sputtering its surface during 1min. the O 1*s* component associated to hydroxyl groups was disappeared, whilst after 2 min. the signal related to C 1*s* was also removed.

Therefore, the superficial layer with contamination is completely removed after 2min. in the schoop made of pure zinc.
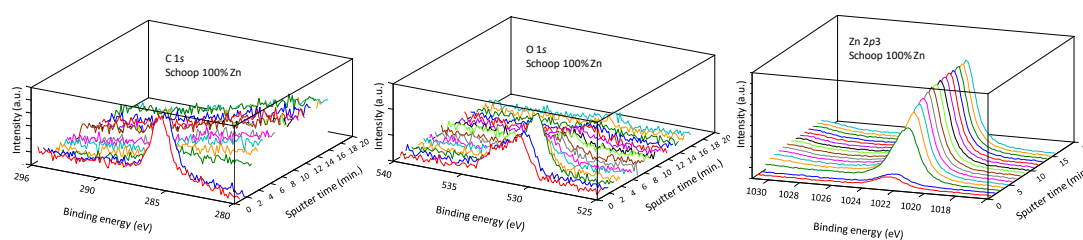
Figure 5.2.6.4. Depth profiles for C 1*s*, O 1*s* and Zn 2*p*3 (from left to right) core level spectra for pure zinc schoop (Ar+ 4kV).

XPS depth profile analysis (*Figure 5.2.6.5.*) was conducted in the C 1*s*, O 1*s*, Zn 2*p*$_{3/2}$ and Al 2*p* regions for the substrate made of ZnAl15, obtaining that after sputtering the schoop surface during 1min. disappeared the O 1*s* component associated to hydroxyl groups and every peak related to C 1*s*. After 2min. of sputtering appears the Al 2*p* component related to the oxidation state (0) and after 8 min. disappears the Al 2*p* contribution at high binding energy.
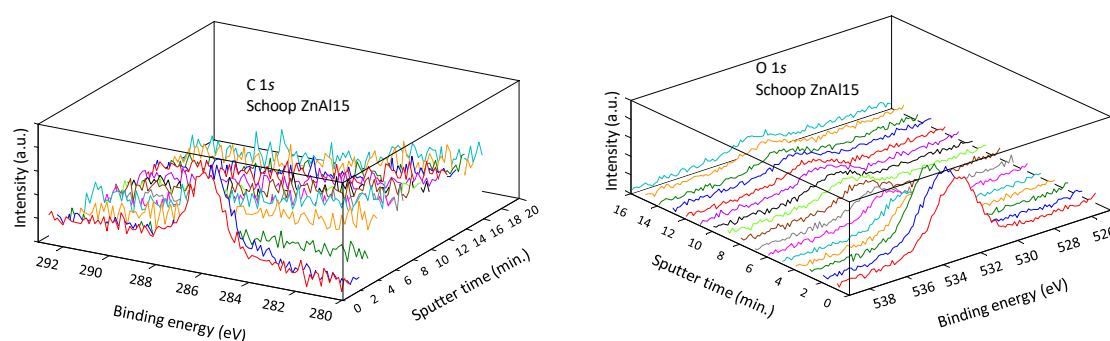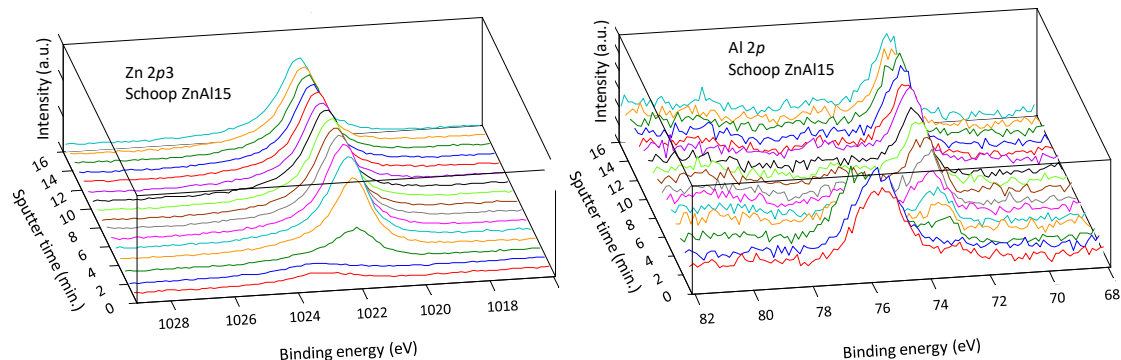
Figure 5.2.6.5. Depth profiles for C 1*s*, O 1*s*, Zn 2*p*3 and Al 2*p* core level spectra for ZnAl15 schoop (Ar$^+$ 4kV).

XPS depth profile analysis was conducted in the C 1*s*, O 1*s*, Cu 2*p* and Sn 3*d* regions for the schoop made of SnCu3 (*Figure 5.2.6.6.*), finding that after sputtering the schoop surface during 1min. disappeared the O 1*s* component associated to hydroxyl groups and every peak related to C 1*s*. And additionally after 1 min of Ar$^+$ sputtering appeared the Cu 2*p* signal and the Sn 3*d* component related to the oxidation state 0.
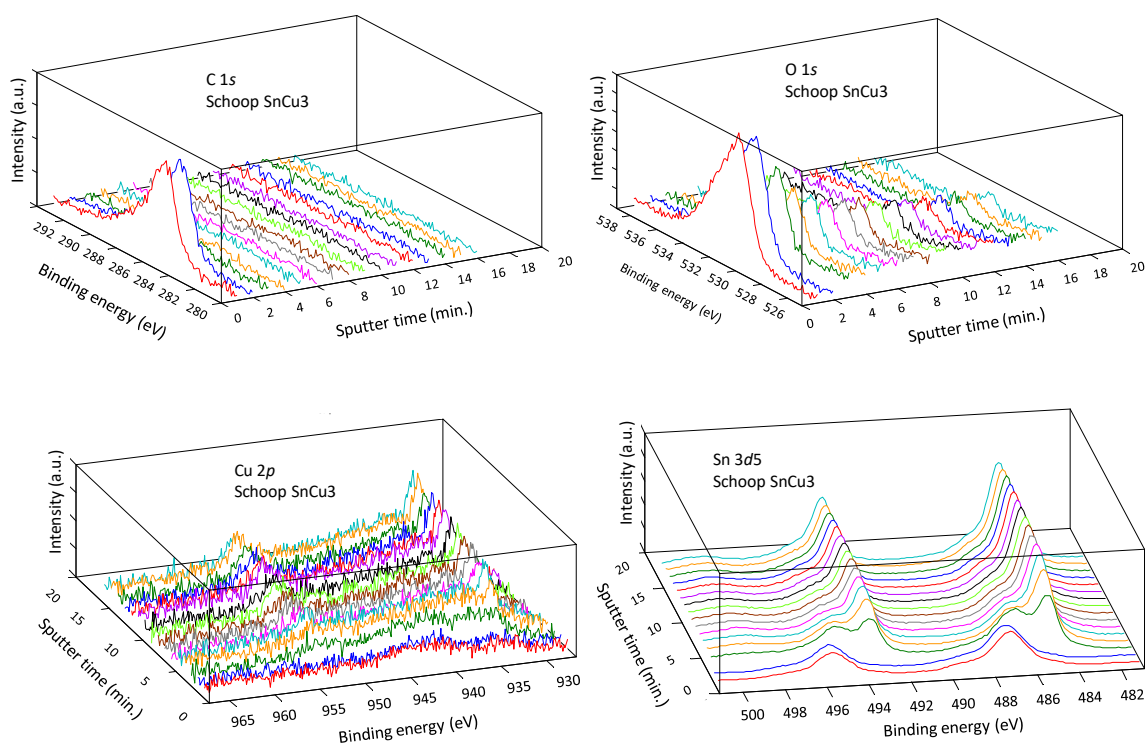
Figure 5.2.6.6. Depth profiles for C 1*s*, O 1*s*, Sn 3*d*5 and Cu 2*p* core level spectra for SnCu3 schoop (Ar$^+$ 4kV).

5.2.7. Naked winding. Wire pull-off test

The robustness of the wire welding onto every schoop variant is evaluated according to the conditions described in section 4.3.2. Figure 5.2.7.1. plots the maximum supported tensile force per schoop composition. Each value is the average of the measurements obtained for five windings in each metallization composition.
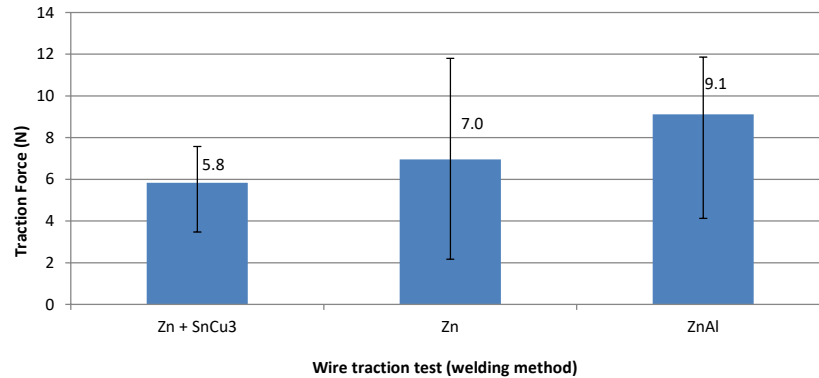
Figure 5.2.7.1. Results of pull-off test (robustness of wires).

Every schoop variant evidences a high dispersion in the found traction forces, being the schoop made of zinc in the first layer and SnCu3 in the second sprayed layer the variant showing lower dispersion. However, this variant offers the lowest robustness in the pull-off test. The schoop made of a single layer of ZnAl is the most robust in comparison.

The strength of the weld weakens over time, and this is influencing the test results. This shows how important it is during the production process to encapsulate the naked winding in the defined time. On the other hand, this is evidencing that all the evaluations conducted on naked winding are under much worse conditions than the encapsulated capacitors fulfilling all the process times.

5.2.8. Naked winding. THB test (85ºC/15…60%R.H./305Vrms)

The temperature/humidity/bias test is applied on the winding elements without the encapsulation and the plastic box to analyze the performance without influence of the resin, the plastic box and/or the improvements already defined internally as design rules (naked winding).

Five windings per variant are subjected to the THB test for 2168h at 305Vac, 85ºC and with a starting relative humidity of 15% and a final of 60%R.H. gradually increased in five steps as defined in Table 5.2.8.1. among the other test conditions, including the equivalent absolute humidity. Approximately every 100-150h the test is interrupted to make the electrical measurements of the devices. *Figure 5.2.8.2.* plots the average drop of capacitance presented by the naked windings with the exposed different schoop compositions: 100% zinc, ZnAl (15 wt% of aluminium) and Zn + SnCu3 (3 wt% of copper). The error bars represent the standard deviation of the measurements made.

There is not a pass criterion of naked winding performance after running this accelerating test. The objective is a destructive test to make a direct comparison between variants under the harshest warm

humid biased conditions but being able to analyze after failure the piece for understanding the failure mechanism. Figure 5.2.8.1. shows the set-up mounting of the naked windings on the PCBs inside the climatic chamber.

All the windings with schoop of Zn + SnCu3 failed after 385h of test (85ºC/14%R.H./305V$_{rms}$) because of de-welding of their wires from the components. This is in line with the found results on the robustness evaluation of the wire in the pull-off test (Figure 5.2.7.1.).

Therefore, five new fresh windings of this variant replaced the failed ones. Figure 5.2.8.2. to Figure 5.2.8.4. plot the performance of new fresh windings. Those figures do not plot the performance of the failed ones.
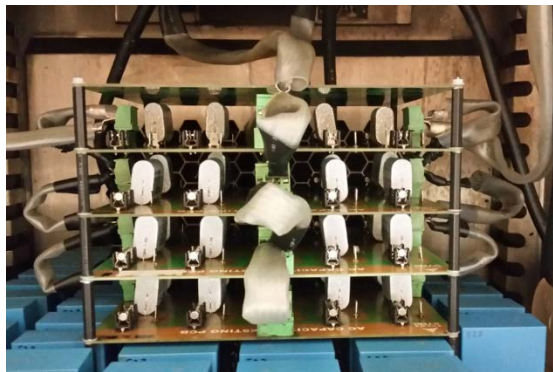
Figure 5.2.8.1. Set-up of THB inside climatic chamber with naked windings mounted on PCBs.
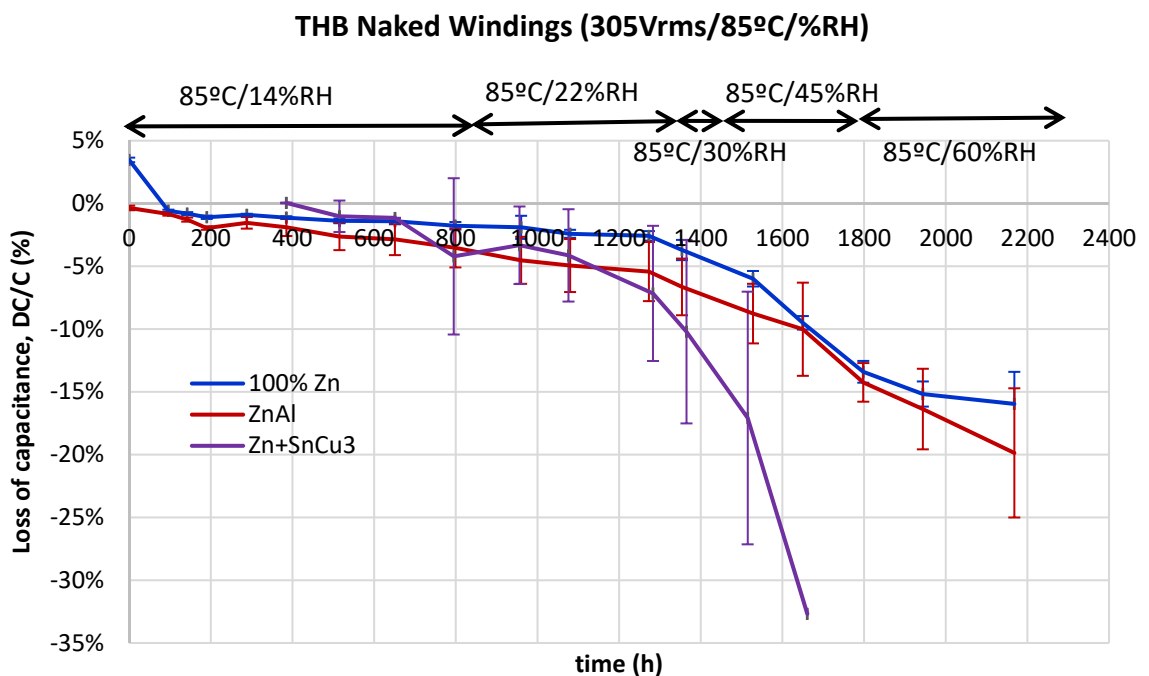
Figure 5.2.8.2. Drop of capacitance of windings in THB (305Vac/85ºC/15…60%R.H.) test.

Despite the replacement, schoop of Zn + SnCu3 shows the highest drop of capacitance when the winding is exposed directly without encapsulation, reaching a -32.7% after 1274h of testing (the test starts at

385h for this schoop variant) whilst others variants do not loss more than -10% of capacitance with 385h more of testing (Figure 5.2.8.2.).

In terms of capacitance loss, the schoops of ZnAl and 100% Zn perform in a similar way, reaching all the elements a -15% DC/C after 1800h of THB testing with windings without encapsulation and a reasonable dispersion of the measurements.
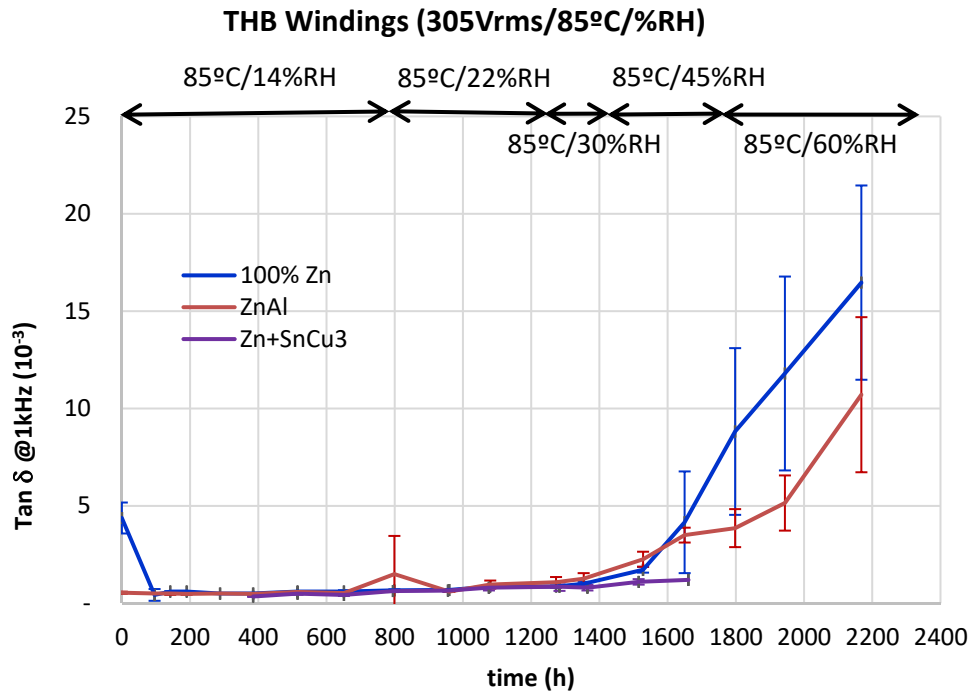
Figure 5.2.8.3. Loss factor at 1kHz of windings in THB (305Vac/85ºC/15…60%R.H.) test.

As for the losses, those soared after 1500h of THB test (at 85ºC/45%R.H./305 V_{ac}) in windings with schoop of 100% Zn and ZnAl. Both launch, losses associated with the dielectric (at 1kHz) as well as those measured at 10 kHz and related to the contacts (wires, schoop, electrode metallization…) (Figures 5.2.8.3. and 5.2.8.4.). An increase in the dispersion of the measurements is also observed since this test time, especially in the elements with a schoop of 100% Zn, indeed, at the end of the THB test two out of five of the windings failed due to melting with the self-heating caused by the losses (Table 5.2.8.1.). This explain the final loss factor reduction at 10 kHz in 100%Zn variant, where the two windings with bad contacts are not included in the average. The final loss factor at 1kHz shows that losses related to dielectric continue with same rising trend.

THB Naked Windings (85ºC/%RH)
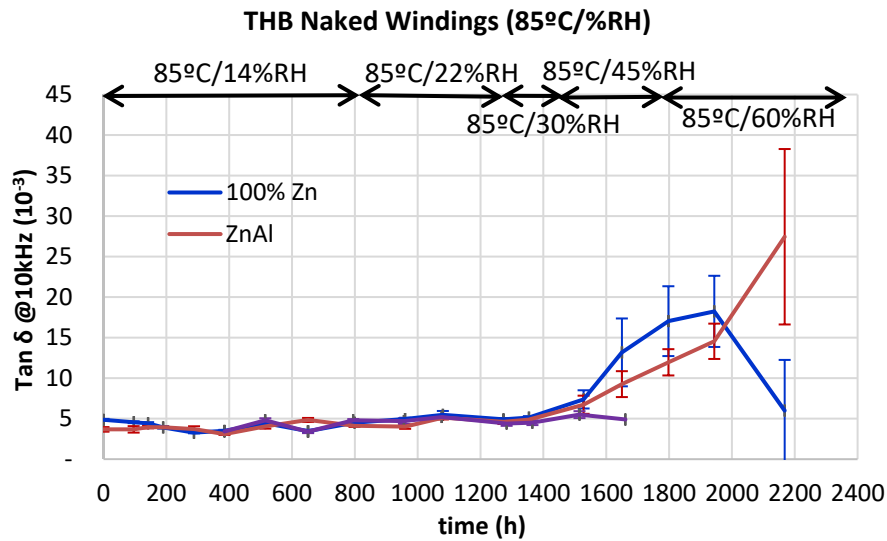
Figure 5.2.8.4. Loss factor at 10kHz of windings in THB (305Vac/85ºC/15…60%R.H.) test.

The windings made of ZnAl failed at the end of the test, but related to the desoldering of the wires from the schoop. However, the breakage of the wires (properly welded to the schoop) cause the failure of all windings with schoop made of Zn + SnCu3 (Figure 5.2.8.5. and Table 5.2.8.1.).

Figure 5.2.8.5. Appearance of winding failure causes: (a) broken wire, (b) desoldering of wire and c) melted windings.

Table 5.2.8.1. Naked winding failure tracking during THB (305Vac/85ºC/15…60%R.H.) test.

Time (h)	T (ºC)	%RH	Absolute Humidity (g H_2O/m^3 air)	Voltage (V_{rms})	REG.248 ZnAl	REG. 247 100% Zn	REG. 275 Zn + SnCu3
0	85	14	48.5	305			
96	85	14	48.5	305			
142	85	14	48.5	305			
190	85	14	48.5	305			
288	85	14	48.5	305			1/5F [1]
385	85	14	48.5	305			5/5F [1]
515	85	14	48.5	305			
651	85	14	48.5	305			1/5F [3]
799	85	14	48.5	305			1/5F [3]
960	85	22	76.2	305			1/5F [3]
1080	85	22	76.2	305			1/5F [3]
1273	85	22	76.2	305			3/5F [3]
1354	85	30	103.9	305			3/5F [3]
1528	85	45	155.9	305			3/5F [3]
1650	85	45	155.9	305			4/5F [3]
1798	85	60	207.8	305			5/5F [3]
1944	85	60	207.8	305	1/5F [1]		
2168	85	60	207.8	305	1/5F [1]	2/5F [2]	

Note: Failure causes:
[1] Desoldering of wires
[2] Melted winding
[3] Broken wire

5.2.9.   DC capacitor. Optical Microscopy

Five DC capacitors per analysis group are visual and dimensionally evaluated by optical microscopy to check that the devices to submit to operational tests are produced rightly according to the defined design rules (Table 5.2.9.1. and *Annex A. International published patent, IP Nr. WO 2019/141388 A1*).

Table 5.2.9.1. Defined dimensions for different schoops on DC capacitors.

Schoop type (1st layer + 2nd layer)	Zn	Zn + SnCu3	ZnAl
Composition	**100% Zn**	**100%Zn + (3% Cu + 97% Sn)**	**15%Al + 85%Zn**
Total thickness (mm)	(0.5~0.65)	(0.5~0.7)	(0.5~0.8)

For this purpose, the DC capacitors were transversally cut and then polished the cross-section for their observation and analysis by the optical microscopy in reflection mode. The thicknesses of the schoop in both winding sides and of the encapsulating resin surrounding the winding (resin 1) in both sides were measured (Table 5.2.9.2.). A minimum of 10 thickness measurements were taken per evaluated winding schoop. All the thicknesses compliant the defined ranges, except one out of five evaluated capacitors with Zn + SnCu3 schoop that showed significantly thinner resin thickness surrounding the winding.

Furthermore, it was conducted a visual inspection of the key interfaces in the capacitor through which the humidity can find a path to reach the internal electrode:

- interface between the resin top closing layer (resin 2) and the resin used as encapsulation that surrounds the winding (resin 1),
- interface between resin 1 and the schoop (Figure 5.2.9.1),
- interface between resin 1 and the top side of the winding (Figure 5.2.9.1), and
- interface between resin 1 and the bottom side of the winding.

Table 5.2.9.2. Visual and dimensional inspection of DC caps by optical microscopy.

Schoop composition	THICKNESS (um)				INTERFACES			
	Schoop left side	Schoop right side	Resin 1 left side	Resin 1 right side	Resin 2/ Resin 1	Resin 1/ schoop	Resin 1/ winding top	Resin 1/ winding bottom
Zn	500-650	550-630	980-1050	1000-1750	↑↑	↑↑	↑	↑↑
ZnAl	580-650	650-700	980-1400	800-1500	↑↑	↑↑	↑↑	↑↑
Zn + SnCu3	550-650	550-700	300-1200	300-1400	↑↑	↑↑	↑↑	↑↑

Note:
Resin 1: encapsulating resin surrounding the winding.
Resin 2: closing top layer

↑↑	No bubbles. Interface perfectly joined. Compliant with the humidity design rules.
↑	Some local bubble/cavities/unstuck point between interfaces.
↓	Adhesion between parts of one interface broken.

During the visual inspection it was evaluated the presence of bubbles in the cured resin, if the interfaces are properly adhered and if the thicknesses comply with the humidity design rules. As a result, the analysis is considered right in all the evaluations in compliance with the design and process defined specifications (Table 5.2.9.2 and Figure 5.2.9.1.).
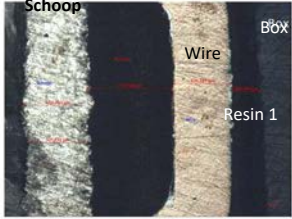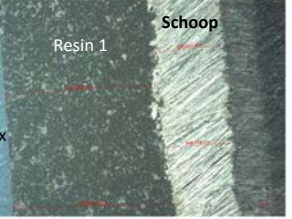
Figure 5.2.9.1. Optical micrographs of polished cross section of DC capacitors.

5.2.10. DC capacitor. Impulse Voltage Test

Three capacitors per schoop variant are evaluated and 30 impulses for every intensity level are applied. Measurements of capacitance and loss factor at 1kHz and 10kHz of frequency are registered before and after the impulses application. Figure 5.2.10.1. shows the found values in the capacitors metallized with Zn (a), Zn+SnCu3 (b) and ZnAl (c) before and after applying the three current pulse steps: 20, 25 and 30 A/m of electrode.
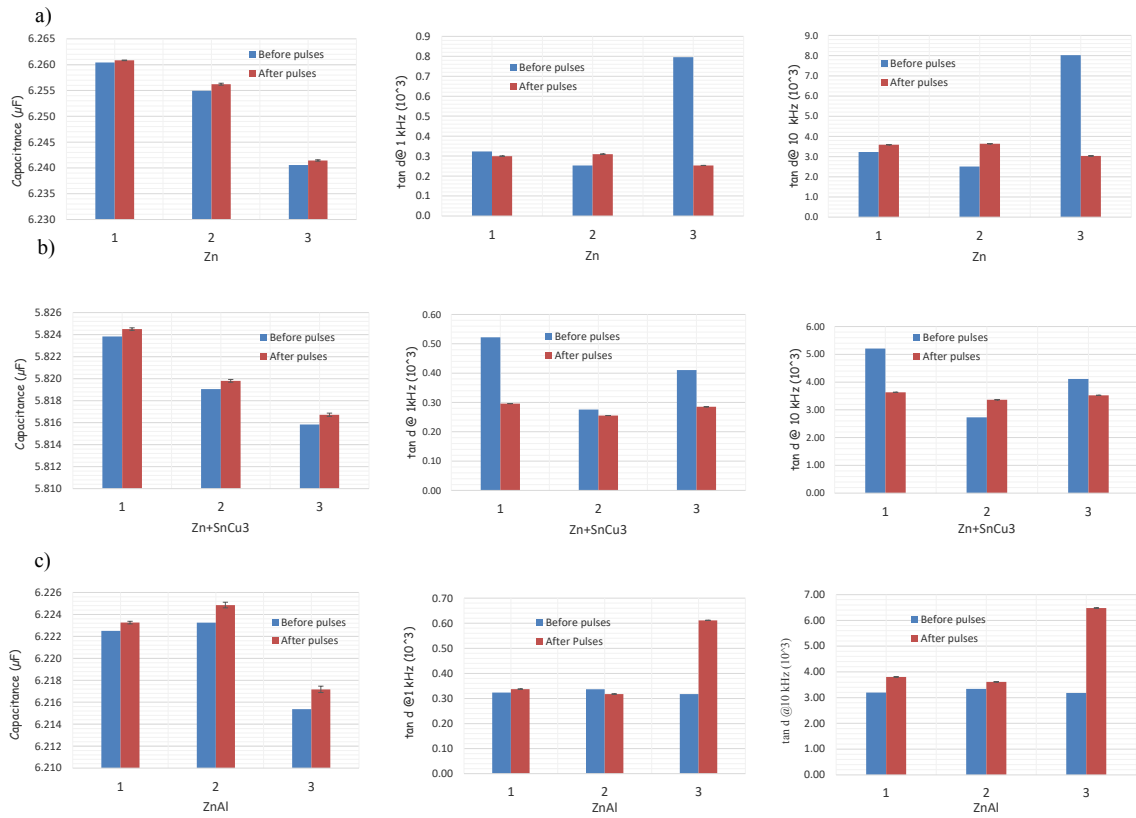
Figure 5.2.10.1. Electrical measurements before and after current pulse (20, 25 & 30 A/m).

High loss factors are measured at 1 and 10 kHz for winding nr. 3 with schoop made of Zn and winding nr. 1 of schoop of Zn+SnCu3 before the application of the current pulses. These are associated with experimental errors due to a wrong contact during the measurement. Being considered unaffected by the current pulses the variant of schoop made of Zn and Zn+SnCu3.

However, the high loss factor measured in winding 3 of schoop made of ZnAl at 1kHz and 10 kHz are related to the pulses applications. The current did not affect to the others two pieces of ZnAl schoop.

The test was repeated in fresh capacitors for higher current, applying three steps of 35, 40 and 45 A/m of electrode, registering intermediate electrical measurements after the application of each individual step (Figure 5.2.10.2).

a)

b)

c)
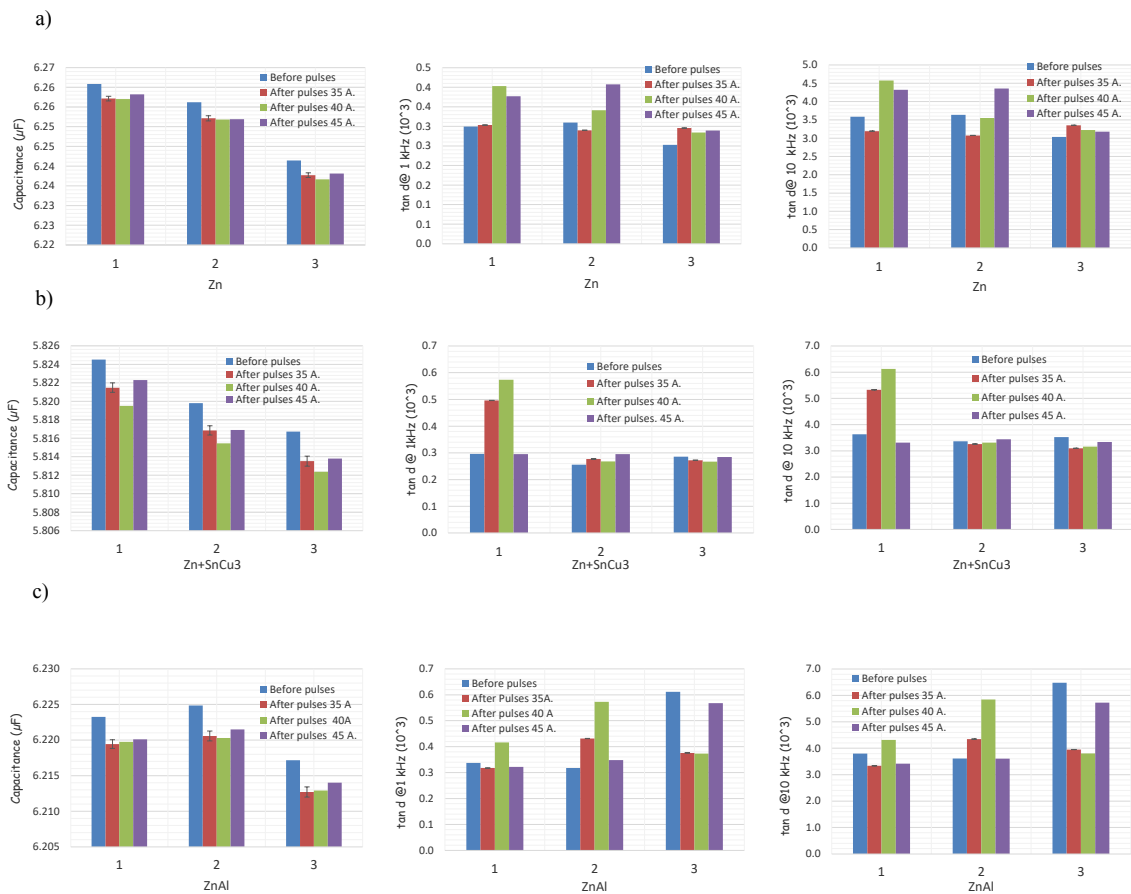
Figure 5.2.10.2. Electrical measurements before and after current pulse (35, 40 & 45 A/m).

The variant of schoop of pure zinc shows an increase in loss factor (at 1 and 10kHz) in piece nr. 2 gradually according to the current increasing of the pulses. But the others two pieces remained unaffected.

The variant of ZnAl also shows the increasing of the losses at 1 and 10 kHz in one winding (nr. 3) after the application of the current impulses at a level of 45 A/m of electrode. However, the others two pieces do not increase their losses.

The best current handle capability is shown by the capacitors made of Zn + SnCu3 schoop where only is shown in winding nr.1 the increasing of the loss factor at 35 and 40 A/m but not at 45 A/m. This behavior suggests that this increase is associated to an experimental error due to a poor contact during the electrical measurement.

All the capacitance values are stable after the current handle.

A third test to confirm results was carried out in fresh capacitors but increasing the current steps to 50, 55 and 60 A/m of electrode. Intermediate measurements between current steps are also done (Figure 5.2.10.3).

a)

b)

c)
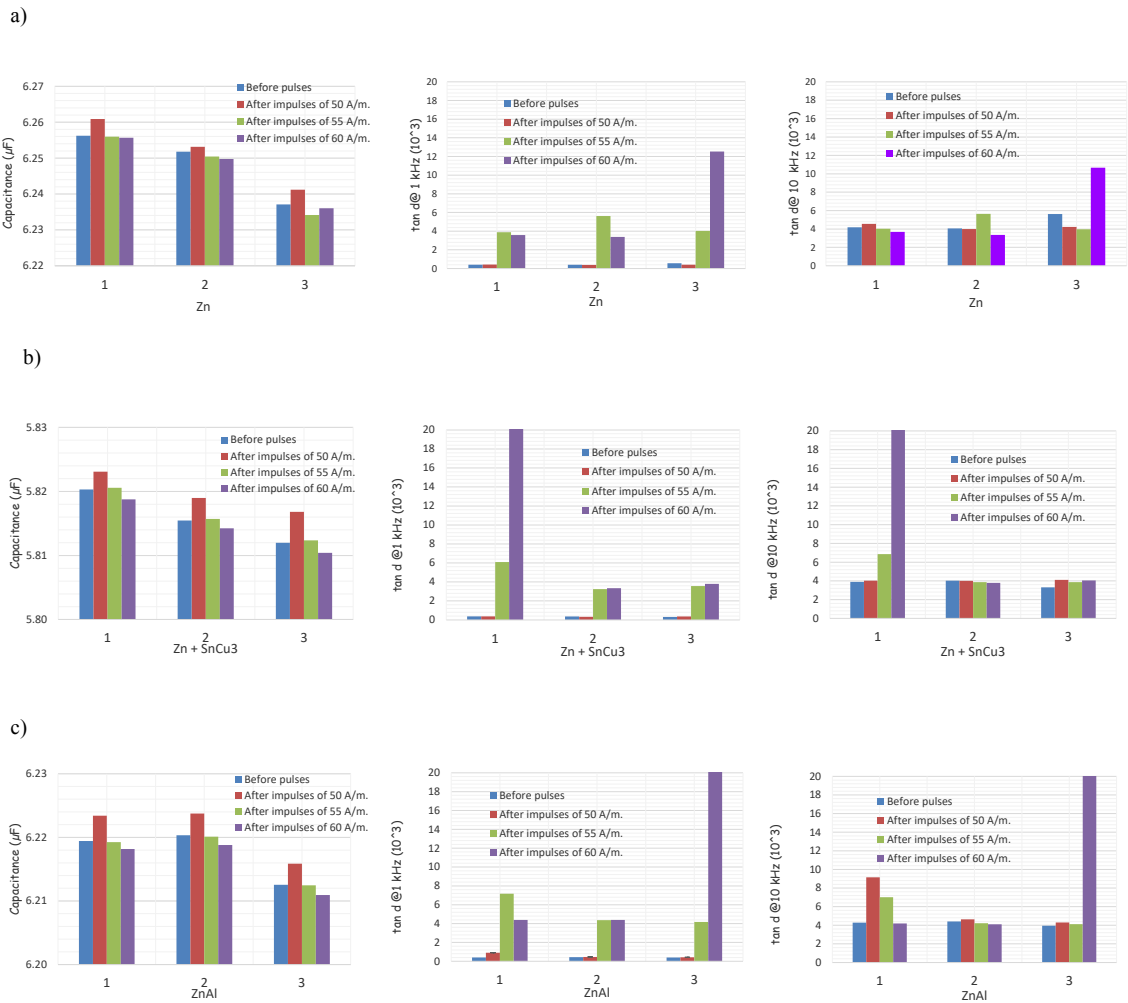
Figure 5.2.10.3. Electrical measurements before and after current pulse (50, 55 & 60 A/m).

DC capacitors made of ZnAl decrease very slightly the capacitance and pure Zn in the schoop keeps stable. However, both compositions show the same current handle capability in terms of loss factor. At 1kHz, the losses are increased since the application of the pulses of 55 A/m of electrode in all the windings. However, at 10 kHz only winding nr.3 shows an increase of the losses due to the impulses applied with 60 A/m of current.

The devices made of a schoop of Zn + SnCu3 show a trend to decrease very slightly the capacitance. At 1kHz the dielectric losses are increased after applying 55 A/m current level in all the windings, but only winding nr.1 is rising its losses with the current at 10kHz (contact resistances) after applying 55 A/m.

5.3. DC capacitor. THB test (85ºC/85%R.H./305Vrms)

Seven DC capacitors per variant are THB tested at 305Vac, 85ºC and 85%R.H. during 1000h. Approximately every 100h the test is interrupted to make the electrical measurements of the devices. *Figure 5.3.1.* plots the average drop of capacitance presented by the film capacitors made of different

schoop compositions: 100% zinc, ZnAl (15 wt% of aluminium) and Zn + SnCu3 (3 wt% of copper). The error bars represent the standard deviation of the done measurements.

The pass criterion of capacitor performance after running this accelerating test is to get a loss of capacitance no larger than 10%. All the evaluated capacitors fulfill this criterion.

The capacitors made of schoops of ZnAl and 100% Zn perform similar, reaching a drop of capacitance of -4.3% in both cases after 1000h of THB test (85ºC/85%R.H./305Vac). However, the devices made of a schoop with two layers, first 100%Zn and a second of SnCu3, remain a stable capacitance during the test with a final loss of -0.9% (1000h).
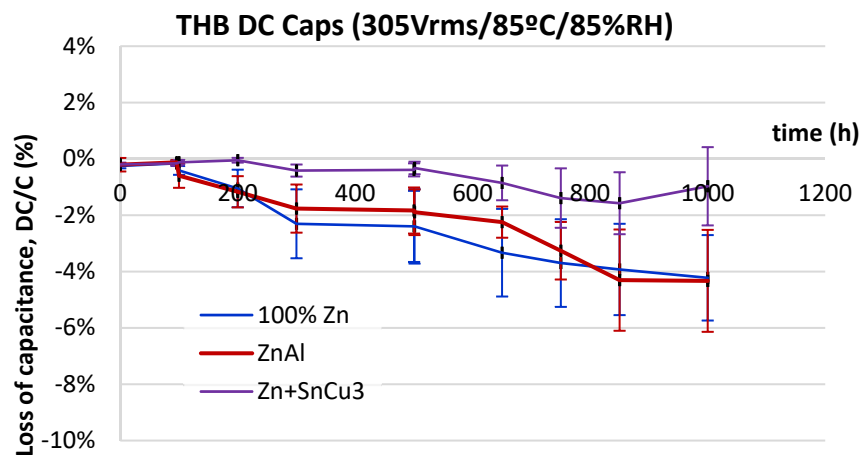
Figure 5.3.1. Drop of capacitance in THB 85ºC/85%R.H./305Vac test.

Related to the evolution of the losses during the THB test, the capacitors with ZnAl schoop increase drastically both losses after 750h of THB test; losses associated to the dielectric (at 1kHz) as well as the measured at 10 kHz and related to the contacts (wires, schoop, electrode metallization…) (Figures 5.3.2. and 5.3.3., respectively). During the last 150h, the dispersion of tan δ soars in the evaluated population of this metallization. At 650h one of the capacitors of ZnAl failed (piece nr. 2 of sample register nr. 248) and is removed from the test due to melting the film with the heat associated to the loss factor souring (Table 5.3.1.).

Pieces with schoops of 100% Zn and Zn + SnCu3 finalize the operational test by tripling the initial loss factor at 1kHz (energy wasted to polarize and repolarize the dielectric in two opposite directions for successive half-cycles of the AC voltage and the ohmic losses) and double it at 10kHz (sum of the contact resistances). One capacitor made of Zn+SnCu3 (piece nr. 5 of sample register nr. 275) is extracted from the test due to failing by losing the contact (the loss factor soars). However, all the capacitors made of 100%Zn passed the test until the 1000h (Table 5.3.1.).
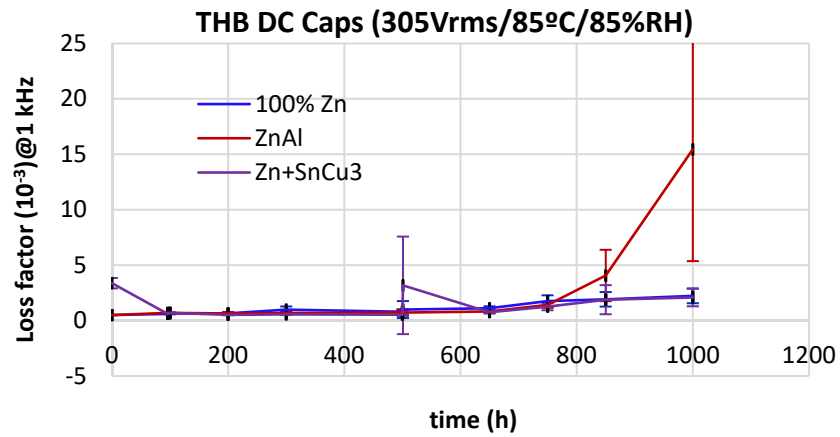
Figure 5.3.2. Loss factor at 1kHz during THB 85ºC/85%R.H./305Vac test.
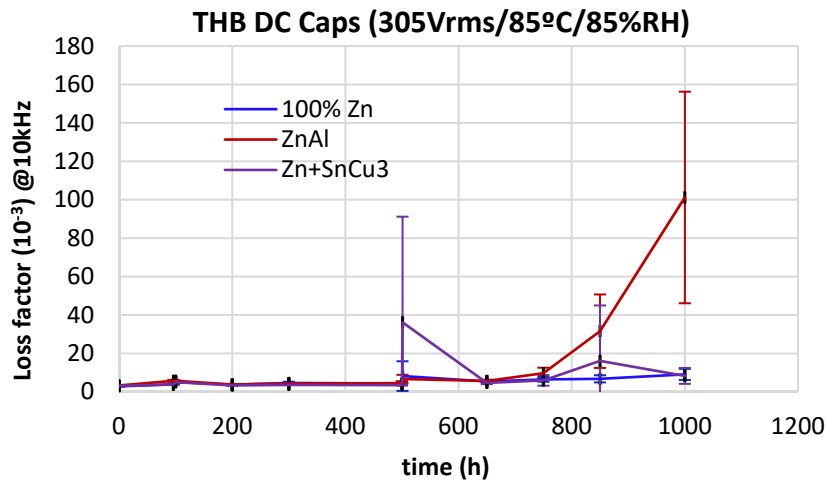
Figure 5.3.3. Loss factor at 10kHz during THB 85ºC/85%R.H./305Vac test.

Table 5.3.1. DC capacitor failure tracking during THB 85ºC/85%R.H./305Vac test.

Time (h)	T (ºC)	%RH	Absolute Humidity (g H2O/m3 air)	Voltage (Vrms)	REG. 247 100% Zn (HDH)	REG.248 ZnAl	REG. 275 Zn + SnCu3
0	85	85	294	305			
100	85	85	294	305			
200	85	85	294	305			
300	85	85	294	305			
500	85	85	294	305			
501	85	85	294	305			
650	85	85	294	305		1/7F	
750	85	85	294	305		1/7F	
850	85	85	294	305		1/7F	1/7F
1000	85	85	294	305		2/7F	1/7F

DC capacitors were mounted in PCB plates during the THB test to avoid the manipulation of wires in every pause for measuring electrically the devices, but at 500h the pieces are demounted to make an intermediate visual inspection of the capacitors (Figure 5.3.4.). The observed rise of the loss factor, and its standard deviation, at 500h in DC capacitors with Zn+SnCu3 schoop is associated with an experimental error due to the lack of contact during the measurement of some pieces of this variant. The

recovery of the values in the following measurements are evidence of this. The averaged losses in this variant increase likewise at 10kHz and 850h failing one piece due to this reason.
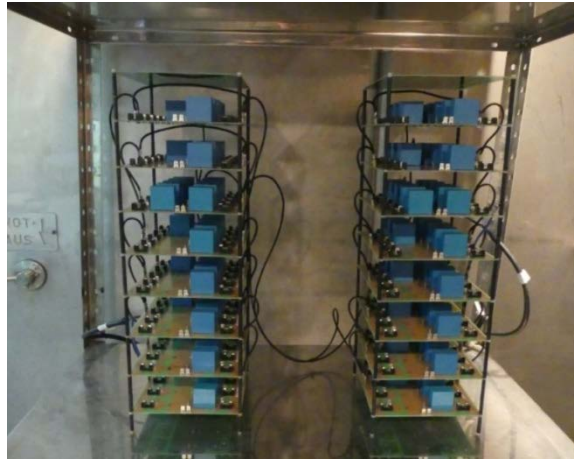
Figure 5.3.4. Set-up of THB inside climatic chamber with DC caps mounted on PCBs.

5.4.   CONCLUSIONS

All the schoops presented equivalent pore size and distribution in the range of 25 Å to 2300 Å before applying any aging program. Pure zinc was the schoop able to adsorb double of total volume in pores compared to ZnAl15 and SnCu3; regardless, all of them showed very low volumes and surfaces (~0.0009-0.0018 cm^3/g by DFT model). After the aging (1100h at 85ºC and 85%R.H.), all the schoops reduced the incremental pore volume and narrow the pore size distribution to the mesoporous range, showing a pore width distribution between 25 Å and 200 Å. However, no differences were observed in surface roughness (Ra, Rq or Rt) between different schoops (without aging program).

SnCu3 schoop showed the lowest WVTR and the Zn + SnCu3 WVTR was lower than the 100%Zn and ZnAl WVTRs one order of magnitude. After aging, the WVTR of 100% Zn and SnCu3 schoop reduced even two orders of magnitude than before aging in the case of 100%Zn. Evolution of WVTR before and after aging was in agreement with the porosity results.

Impedance measurements after 90 min. of immersion were showing that schoops made of ZnAl15 were mainly controlled by diffusion of electrolyte. This behaviour suggested that this schoop composition was presenting the highest resistance to corrosion because additionally it was the unique variant that it was not showing transference of charge during the exposure to an electrolyte. Nevertheless, impedance measurements also revealed that schoop made of ZnAl15 was not passivated during immersion test. Comparing the results found after 90min vs. 24h of immersion, it can be concluded that corrosion products of schoops made of ZnAl15 were applying an additional barrier effect.

The material characterization by EIS of corrosion mechanism and resistances in shorter immersion times (0-3h) was in agreement with the differences of performance found during the THB test on DC capacitors. The components with schoop made of Zn + SnCu3 as 2nd schoop layer showed the highest resistance to corrosion because they perform with a stable capacitance and loss factor at both evaluated frequencies (1 and 10 kHz).

The performance on THB test of the naked windings (that were directly exposing the schoop to the harsh humid ambient without encapsulation) were not so in conformity with the expectations based on the results of corrosion resistance at high immersion time (24h), where Zn + SnCu3 was predicted to perform with higher stability. In any case, no robust wires (impact on the losses) have been evidenced to be adversely affecting to the found results. The strength of the welding weakens with time, and then this was influencing the test results. This is demonstrating how important is during the production process to encapsulate the naked winding in the defined time. Furthermore, there was a big manipulation of these wires during the intermediate measurements during the test and this was mechanically weakening, especially this variant made of a combination of two (thinner) layers than the other two candidates were. In the case of DC capacitors, this was much less influencing due to the mechanical robustness that the encapsulating was providing to the wire welding.

In general, from the FIB-CS it may be concluded that the natural oxidation of a schoop made of 100% zinc was not undermining the chemical and morphological properties of this material. The intergranular area percentage on the surface reached 9%. The lack of metallurgical union between grains on this intergranular area is the explanation to the observed permeation of water vapour or liquids through any schoop in the capacitor.

The natural oxidation of a schoop made of 85% zinc and 15% aluminum presented a relevant morphological change in the size of the structure at the surface. The superficial layer shows the same morphology than the bulk but with smaller size. A low presence of bores was observed in the FIB-CS. The complexity to distinguish pores/cavities from aluminium dark areas was evidenced by FIB-CS analysis. SEM micrographs suggest that the formed nanostructure framework with lamellae and islands most likely corresponds to α-Al/β-Zn- eutectoid.

The FIB-CS of SnCu3 schoop revealed clear boundaries between the droplets. Typical trapped air pockets among copper droplets of different sizes were appreciated but no delamination and neither intergranular cracks.

In respect of XPS characterization study, it was determined that the superficial layer of the three schoops were chemically composed by CH_2-CH_2, the C-O and the O-C=O bonds (carboxylate groups) associated to the presence on the surface of organic contaminants that come from the ambient air, disappearing after the sputtering. Besides, the schoop made of 100% zinc evidenced O-components associated to lattice oxygen in zinc oxide and also to O-H bonds due to hydroxyl groups or from absorbed H_2O molecules on film oxide.

The schoop made of ZnAl15 showed aluminium hydroxides and oxides in the superficial layer. However, 14 min of sputtering with argon ions of 4kV seemed to be not enough to completely remove the oxidized layer may be due to a lower sputtering rate than expected because of the structure shown by this schoop composition; may be due to a thicker superficial layer than in the cases of the schoop made of 100%Zn and SnCu3.

The XPS analysis of the schoop made of SnCu3 registered no signal of Cu 2p region in the surface. Besides, after sputtering it was found values of binding energy for Cu 2p similar to those reported in the literature for CuO. Furthermore, it was recorded the Sn $3d$ core level and two components ($3d_{5/2}$ and $3d_{3/2}$) with spin-orbit doublet peaks were detected and associated in the superficial layer to Sn^{4+} and Sn^{2+}, whilst after sputtering for 14 min. were attributed mainly to Sn^0, but also a small amount to Sn^{2+}. After Ar^+ blasting the surface during 14 min the main composition in the present oxides is predicted to be CuO based on the atomic composition detected where the percentage of Cu $2p$ is 10.7 ± 0.7 at%.

Related the welding robustness, a high dispersion in the traction forces was found, being the schoop made of zinc in the first layer and SnCu3 in the second one the variant showing the lowest dispersion. However, this variant was the most weakened in the pull-off test. The schoop made of a single layer of ZnAl is the most robust in the comparison.

As far as the performance of the naked windings under the THB (85ºC/15…60%R.H.) test, the schoop of Zn + SnCu3 showed the highest drop of capacitance when the winding exposes directly without encapsulation, reaching a -32.7% after 1274h of test whilst others variants did not loss more than -10% of capacitance after additional 385h of testing.

As regards the losses, those soared after 1500h of THB test (at 85ºC/45%R.H./305Vac) in windings with schoop of 100% Zn and ZnAl, both losses launch, losses associated to the dielectric (at 1kHz) as well as the measured at 10 kHz and related to the contacts (wires, schoop, electrode metallization…).

The failure causes during the test of the naked windings were the break of the wires for the variant of Zn + SnCu3, terminal desoldering for ZnAl and dielectric melting due to self-heating for 100%Zn.

For testing the DC capacitors, visual and dimensional analyses by optical microscopy were conducted. All the evaluated properties were in compliance with the design and process defined specifications.

In reference to the Impulse Voltage Test, a stable capacitance after applying even 60A/m to the DC capacitors with different schoop compositions was shown. Devices with Zn + SnCu3 increased both losses at 55 A/m current level, dielectric (1kHz) and the ones related to the contact (10kHz). However, DC capacitors made of pure Zn and ZnAl increased also at 55A/m the dielectric losses but at 60A/m of current the related to the contact losses (10kHz). Showing the contacts of Zn and ZnAl analysed capacitors higher resistance than Zn + SnCu3 ones under current pulses.

Besides the THB (85ºC/85%R.H./305Vrms) on DC capacitors, these with schoop of Zn + SnCu3 remained after 1000h with a high capacitance stability with a final drop of capacitance of -0.9%, compared with the -4.3% DC/C shown by ZnAl and 100% Zn.

Pieces with schoops of 100% Zn and Zn + SnCu3 finalized the operational test by tripling the initial loss factor at 1kHz (energy wasted to polarize and repolarize the dielectric in two opposite directions for successive half-cycles of the AC voltage and ohmic losses) and doubling it at 10kHz (sum of the contact resistances). Related to the capacitors with ZnAl schoop, these increased drastically both losses (at 1 and 10 kHz) after 750h of THB test.

5.5. REFERENCES

[1] Thommes, M., Kaneko, K., Neimark, A. V., Olivier, J.P., Rodríguez-Reinoso, F., Rouquerol, J. and Sing F. S. W. (IUPAC, Physical Chemistry Division, Commission on colloid and surface chemistry including catalysis) *Physisorption of gases, with special reference to the evaluation of surface area and pore size distribution (IUPAC Technical Report)*. Pure & Appl. Chem. (2015) 87(9-10): 1051–1069

[2] Dullien, F. A. L. *Porous media – Fluid transport and pore structure.* Academic Press. 2nd Ed. (1992)

[3] Scheidegger, A. E. *The physics of flow through porous media*. University of Toronto Press. (1974)

[4] Barsoukov, E. and Ross Macdonald, R. *Impedance Spectroscopy: Theory, experiment and aplications*, 3rd Edition, ISN: 978-1-119-07408-3 (May 2018)

[5] Orazen, M. E. and Tribollet, B. Electrochemical Impedance Spectroscopy, 2nd Edition, ISBN: 978-1-118-52739-9 (April 2017)

[6] Lvovich, V. F. *Impedance Spectroscopy: Applications to electrochemical and dielectric phenomena*, ISBN: 978-0-470-62778-5 (July 2012)

[7] Lasia, A. *Electrochemical Impedance Spectroscopy and its Applications*. 1st Edition, Springer-Verlag New York. eBook ISBN: 978-1-4614-8933-7 (2014)

[8] Gamry Instruments. *Application Note. Basics of Electrochemical Impedance Spectroscopy.* Rev. 5 (2007)

[9] Amand, S., Musiani, M., Orazem, M. E. and Pébère, N. *Constant-phase-element behaviour caused by inhomogeneous water uptake in anti-corrosion coatings*. Electrochimica Acta 87 (2013) 693-700

[10] Hirschorn, B., Orazen, M. E., Tribollet, B., Vivier, V., Frateur, I. and Musiani, M. *Determination of effective capacitance and film thickness from constant-phase-element parameters.* Electrochimica Acta 55 (2010) 6218-6227

[11] Johnson, A. L., Hall, A. C., McCloskey, J.F. *Effect of process inputs on coating properties in the twin-wire arc zinc process*. Journal of Thermal Spray Technology, 856, Vol.22(6) (August 2013)

[12] ASTM E112-13. Standard test methods for determining average grain size. ASTM International, West Conshohocken, PA. DOI:10.1520/E0112-13 (2013)

[13] Tzaneva, D., Dobrev, D. and Kanev, M. *Topography and microstructure of Cu-Sn coatings deposited by magnetron sputtering. Thin Solid Films*, 151 (1987) 235-242

[14] Shen, J., Yongchang, L., Han, Y. and Gao, H. *Microstructure and mechanical properties of lead-free Sn-Cu solder composites prepared by rapid directional solidification*. Journal Mater Sci: Mater Electron (2007) 18:1235-1238

[15] Hu, R. Z., Zhang, Y. and Zhu, M. *Microstructure and electrochemical properties of electron-beam deposited Sn-Cu thin film anodes for thin film lithium ion batteries*. Electrochimica Acta 53 (2008) 3377-3385

[16] Mohd Salleh, M.A.A., McDonald, S. and Nogita, K. *Non-metal reinforced lead-free composite solder fabrication methods and its reinforcing effects to the suppression of intermetallic formation: short review*. Applied Mechanics and Materials Vol 421 (2013) 260-266

[17] Gorodesky, N., Sedghani-Cohen, S., Fogel, O., Silber, A., Tkachev, M., Kotler, Z. and Zalevsky, Z. *Improving compactness of 3D Metallic microstructures printed by Laser-Induced forward transfer*. Crystals, 11 (2021) 291

[18] Leitner, M., Leitner, T., Schmon, A., Aziz, K. and Pottlache, G. *Thermophysical Properties of Liquid Aluminum*. Metall. MatER. Trans. A, 48 (2017) 3036–3045

[19] Gatzen, M., Woizeschke, P., Radel, T., Thomy, C. and Vollertsen, F. *Experimental and Numerical Investigation of an Overheated Aluminum Droplet Wetting a Zinc-coated Steel Surface*. Metals, 7 (2017) 535

[20] Gatzen, M., Radel, T., Thomy, C. and Vollertsen, F. *Wetting and solidification characteristics of aluminium on zinc coated steel in laser welding and brazing*. Journal of Materials Processing Technology, 238 (2016) 352-360

[21] Mondolfo, L. F. *Aluminium-Zinc System*, in Aluminum Alloys: Structure and Properties (London; Boston, MA: Butterworth-Heinemann), (1976) 398–413. DOI: 10.1016/B978-0-408-70932-3.50097-8

[22] Goldak, G. R., and Gordon Parr, J. A. *High-temperature x-ray diffractometer study of the zinc-aluminium system in the region 40-75 wt.% Zinc*. J. Inst. Met. 95, (1964) 230–233

[23] Wei, X., Ren, L., Geng, X., Sun, Z., Hu, H. and Nie, X. *Nano-microstructure development and solidification of Zn-6 wt% Al hypereutectic alloy*. Mater. Charact. 147, (2019) 295–302. DOI: 10.1016/j.matchar.2018.11.016

[24] Bluni, S. T., Notis, M. R., and Marder, A. R. *Nucleation characteristics and microstructure in off-eutectic Al-Zn alloys*. Acta Metall. Mater. 43, (1995) 1775–1782. DOI: 10.1016/0956-7151(94)00397-Z

[25] Zhao, M., Zhang, L., Liu, Z.Q., Xiong, M. Y. and Sun, L. *Structure and properties of Sn-Cu lead-free solders in electronics packaging*. Science and Technology of Advanced Materials, Vol. 20, No. 1 (2019) 421-444

[26] Satyanarayan, Prabhu KN. *Reactive wetting, evolution of interfacial and bulk IMCs and their effect on mechanical properties of eutectic Sn-Cu solder alloy*. Adv Colloid Interface Sci. 166 (1) (2011) 87–118

[27] Nogita K. *Stabilisation of Cu6Sn5 by Ni in Sn-0.7Cu-0.05Ni lead-free solder alloys*. Intermetallics. 18(1) (2010)145–149

[28] Sanabria, C. *A new understanding of the heat treatment of Nb-Sn wires*. PhD Dissertation of Florida State University, The Graduate Shool, (April 2017)

[29] Abtew, M. and Selvaduray, G. *Lead-free Solders in Microelectronics*. Materials Science and Engineering, 27 (2000) 95-141

[30] Abd El-Rehim, A. F. and Zahran, H.Y. *Investigation of microstructure and mechanical properties of Sn-xCu solder alloys*. Journal of Alloys and Compounds, 695 (2017) 3666-3673

[31] Nogita, K., Gourlay, C.M., Mcdonald, S.D. et al. *Kinetics of the η- η' transformation in Cu_6Sn_5*. Scr Mater. Vol. 65, No. 10 (2011) 922-925

[32] Zou, H. F. and Zhang, Z. F. *Ductile-to-brittle transition induced by increasing strain rate in Sn-3Cu/Cu joints*. Journal Mater. Res., Vol. 23, No. 6 (Jun 2008) 1614-1617

[33]Hung, F. Y., Lui, T. S., Chen, L. H. and He, N. T. *Resonant characteristics of the microelectronic Sn-Cu solder*. Journal of Alloys and compounds 457 (2008) 171-176

[34] D. R. Baer, M. H. Engelhard, A. S. Lea, P. Nachimuthu, T. C. Droubay, J. Kin, B. Lee, C. Mathews, R. L. Opila, L. V. Saraf, W. F. Stickle, R. M. Wallace, B. S. Wright, "*Comparison of the sputter rates of oxides films relative to the sputter rate of SiO2*", Journal of Vacuum Science and Technology A 28 (5) (2010) pp1060-72, DOI:10.1116/1.3456123.

[35] Peter M.A. Sherwood. *Introduction to studies of aluminum and its compounds by XPS*. Surface Science Spectra, Vol. 5, No. 1 (1998)

[36] M. R. Alexander, G. E. Thompson and G. Beamson. *Characterization of the oxide/hydroxide surface of aluminum using x-ray photoelectron spectroscopy: a procedure for curve fitting the O 1s core level*. Surface and Interface Analysis. 29 (2000) 468-477

[37] S. Thomas and Peter M. A. Sherwood. *Valence band spectra of aluminum oxides, hydroxides, and oxyhydroxides interpreted by Xα calculations*. Analytical Chemistry, Vol. 64, No. 21 (November 1992) 2488-2495

[38] John A. Rotole and Peter M. A. Sherwood. *Bayerite (b-Al(OH)₃) by XPS*. Surface Science Spectra, Vol. 5, Nº. 39 (1998), DOI: 10.1116/1.1247855

[39] John A. Rotole and Peter M. A. Sherwood. *Boehmite (g-AlOOH) by XPS*. Surface Science Spectra, Vol. 5, Nº. 53 (1998), DOI: 10.1116/1.1247857

[40] John A. Rotole and Peter M. A. Sherwood. *Corrundum (a-Al₂O₃) by XPS*. Surface Science Spectra, Vol. 5, Nº. 11 (1998), DOI: 10.1116/1.1247851

[41] John A. Rotole and Peter M. A. Sherwood. *Diaspore (b-AlOOH) by XPS*. Surface Science Spectra, Vol. 5, Nº. 46 (1998), DOI: 10.1116/1.1247856

[42] John A. Rotole and Peter M. A. Sherwood. *Gamma-Alumina (g-Al₂O₃) by XPS*. Surface Science Spectra, Vol. 5, Nº. 18 (1998), DOI: 10.1116/1.1247852

[43] John A. Rotole and Peter M. A. Sherwood. *Gibbsite (a-Al(OH)₃) by XPS*. Surface Science Spectra, Vol. 5, Nº. 25 (1998), DOI: 10.1116/1.1247853

[44] John A. Rotole and Peter M. A. Sherwood. *Nordstrandite (Al(OH)₃) by XPS*. Surface Science Spectra, Vol. 5, Nº. 32 (1998), DOI: 10.1116/1.1247854

[45] B. Singh, R. Hesse and M. R. Linford. *Good Practices for XPS (and other Types of) Peak Fitting. Use Chi Squared, Use the Abbe Criterion, Show the Sum of Fit Components, Show the (Normalized) Residuals, Choose an Appropriate Background, Estimate Fit Parameter Uncertainties, Limit the Number of Fit Parameters, Use Information from Other Techniques, and Use Common Sense*. Vacuum Technology & Coating. (December 2015)

[46] Alexander, M. R., Payan, S. and Duc, T. M. *Interfactial interactions of plasma-polymerized acrylic acid and an oxidized aluminium surface investigated using XPS, FTIR and Poly(acrylic acid) as a model compound*. Surface and Interface Analysis. 26 (June 1998) 961-973

[47] Kharitonov, D. S., Dobryden, I., Sefer, B., Ryl, J., Wrzesinska, A., Makarova, I. V., Bobowska, I., Kurilo, I. I. and Claesson, P. M. *Surface and corrosion properties of AA6063-T5 aluminum alloy in molybdate-containing sodium chloride solutions*. Corrosion Science 171 (2020) 108658, 1-13

[48] Amor, S. B., Jacquet,M., Fioux, P. and Nardin, M. *XPS characterisation of plasma treated and zinc oxide coated PET*. Applied Surface Science 255 (2009) 5052-5061

[49] Futsuhara, M., Yoshioka, K. and Takai, O. *Structural, electrical and optical properties of zinc nitride thin films prepared by reactive rf magnetron sputtering*. Thin Solid Films 322 (1998) 274-281

[50] Mutel, B., Ben Taleb, A., Dessaux, O., Goudmand, P., Gengembre, L. and Grimblot, J. *Characterization of mixed zinc-oxidized zinc thin films deposited by a cold remote nitrogen plasma*. Thin Solid Films 266 (1995) 119-128

[51] Jun Tao. *Surface composition and corrosion behaviour of an Al-Cu alloy.* Chemical Physcs. Université Pierre et Marie Curie – París VI (2016) NNT:2016PA066159

[52] Xia, W., Wang, H., Zeng, X., Han, J., Zhu, J., Zhou, M. and Wu, S. *High-efficiency photocatalytic activity of type II SnO/Sn3O4 heterostructures via interfacial charge transfer*. CrystEngComm, 16 (2014) 6841

[53] Korusenko, P.M., Nesov, S.N., Bolotov, V. V., Povoroznyuk, S.N., Pushkarev, A. I., Ivlev, K.E. and Smirnov, D.A. *Formation of tin-tin oxide core–shell nanoparticles in the composite SnO₂-*

x/nitrogen-doped carbon nanotubes by pulsed ion beam irradiation. Nuclear Instruments and Methods in Physics Research B 394 (2017) 37-43

[54] Xu, D., Fan, D. and Shen, W. *Catalyst-free direct vapor-phase growth of Zn$_{1-x}$Cu$_x$O micro-cross structures and their optical properties*. Nanoscale Research Letters (2013) 8:46

[55] Shuai, M., Liao, L., Lu, H. B., Zhang, L., Li, J. C. and Fu, D. J. *Room temperature ferromagnetism in Cu$^+$ implanted ZnO nanowires.* J. Phys. D: Appl. Phys. 41 (2008) 135010 (5pp)

[56] Winiarski, J., Tylus, W., Winiarska, K., Szcygiel, I. and Szczygiel, B. *XPS and FT-IR Characterization of Selected Synthetic Corrosion Products of Zinc Expected in Neutral Environment Containing Chloride Ions*. Hindawi. Journal of Spectroscopy. Article ID 2079278 (2018) 1-14

[57] Bang, S., Lee, S., Ko, Y., Park, J., Shin, S., Seo, H. and Jeon, H. *Photocurrent detection of chemically tuned hierarchical ZnO nanostructures grown on seed layers formed by atomic layer deposition*.Nanoscale Research Letters, 7:290 (2012) 1-11

[58] Pombo Rodríguez, R. M. H., Paredes, R. S. C., Wido, S. H. and Calixto A. *Comparison of aluminum coatings deposited by flame spry and by electric arc spray*. Surface & Coatings Technology 202 (2007) 172-179

[59] Joshi, N., da Silva, L. F., Shimizu, F. M., Mastelaro, V. R., M'Peko, L.C., Lin, L. and Oliveira Jr, O. N. *UV-assisted chemiresistors made with gold-modified ZnO nanorods to detect ozone gas at room temperature*. Microchim. Acta 186:418 (2019) 1-9

[60] Parthasarathy, S., Nandhini, V. and Jeyaprakash, B. G. *Improved sensing response of photo activated ZnO thin film for hydrogen peroxide detection*. Journal of Colloid and Interface Science 482(2016)81-88

[61] Diler, E., Lescop, B., Rioual, S., Nguyen Vien, G., Thierry, D. and Rouvellou, B. *Initial formation of corrosion products on pure zinc and MgZn2 examinated by XPS*. Corrosion Science 79 (2014) 83-88

6. GENERAL CONCLUSIONS

6. GENERAL CONCLUSIONS

According to the defined targets and also the results obtained and described in chapter 5, it can be concluded:

- As result of these studies, new design rules were defined internally at TDK Electronics Group to design MKP wound box capacitors to operate under extreme humidity conditions (international published patent under the International Publication Number WO 2019/141388 A1 (Annex A9)). All the studies and results elaborated during targets 2, 3, 5 and 6 were not included in this thesis script because these researches are the relevant arguments and experimental evidences to support the international published patent under the International Publication Number WO 2019/141388 A1 (Annex A) where Azahara Albéndiz is the main inventor.

- This thesis script focuses on the development of the study of different metallic materials electrically sprayed onto the lateral side of the winding, denominated schoop (Target 4 described in Chapter 3 and developed in chapter 5). In this study, when operational tests were conducted on the DC capacitors, they were manufactured in compliance with all these defined design rules and compiled in the international patent (Annex A). The performance during the combined temperature humidity bias test (THB at 305Vac, 85ºC and 85%R.H.) revealed that fulfilling the design rules the metallized film capacitors were designed to pass 1000h under the most strict environmental requirements getting a final drop of capacitance no larger than 10% (~4% DC/C in the worst case).

7. ANNEXES

List of Figures and Schemes

Figure 4.33. Applied waveforms for each current impulse level.

Scheme 4.1. Mapping scheme of drop deposition for contact angle measurements.

5.   Results and discussion

List of Tables

List of nomenclatures and abbreviations.

Abbreviation	Meaning
AC	Alternating current
BE	Binding Energy
BET	Brunauer, Emmet and Teller method
BJH	Barret, Johner and Halenda method
BOPP	Biaxially oriented polypropylene
CAGR	Compound Annual Growth Rate
CE	Counter electrode
CELCORR	Centre for Electronic Corrosion
CENIM	Centro Nacional de Investigaciones Metalúrgicas
CNLS	Complex nonlinear least square
CPE	Constant phase element
CSIC	Consejo Superior de Investigaciones Científicas
CTE	Coefficient of thermal expansion
CTI	Comparative tracking index
CVD	Chemical Vapour Deposition
DC	Direct current
DC/C or ΔC/C	Drop of capacitance
DFT	Density-functional theory
DIN	Deutsches Institut für Normung
DOE	Design of experiments
DSC	Differential Scanning Calorimetry
EBSD	Electron BackScattering Diffraction
ECASIA	European Conference on Applications of Surface and Interface Analysis
ECPE	European Center for Power Electronics
EDS or EDX	Energy Dispersive Spectroscopy
EIS	Electrochemical Impedance Spectroscopy
EMI	Electromagnetic interference
EPF	European Polymer Congress
ESR	Equivalent series resistance
ETD	Everhart-Thornley detector
FIB	Focused Ion Beam
FTIR	Fourier Transformed Infrared Spectroscopy

GF	Glass fiber
ICE	Ion conversion and electron
IEC	International Electrotechnical Commission
IP Nr.	International Publication Number
MFC	Metallized film capacitor
MFP	Metal foil and metallized plastic film capacitor based on PET
MFT	Metal foil and metallized plastic film capacitor based on PP
MKN	Metallized plastic film capacitor based on PEN
MKT	Metallized plastic film capacitor based on PET
MKP	Metallized plastic film capacitor based on PP
NLDFT	Non-local-density functional theory
O2	Oxygen
O2GTR	Oxygen gas transmission rate
OCP	Open circuit potential
OWRK	Owens-Wendt-Rabel and Kaelbe method
PBT	Polybutylene terephthalate
PC	Polycarbonate of bisphenol A
PCB	Printed circuit board
PEN	Polyethylene naphthalate
PET	Polyethylene terephthalate
PP	Polypropylene
PPS	Polyphenylene sulphide
PVC	Polyvinyl chloride
RE	Reference electrode
RFI	Radio frequency interference
RH	Relative humidity
R_{iso}	Insulation resistance
RMS	Root mean square
SAW	Surface Acoustic Wave
SE	Secondary electron
SEM	Scanning Electron Microscopy
TLD	Through lens detector
TEM	Transmission Electron Microscopy
TGA	Thermo-Gravimetric Analysis
THB	Temperature Humidity Bias

TMA	Thermomechanical analysis
UMA	Universidad de Málaga
USD	United State Dollar
VCD	Voltage of starting Corona Discharge
WE	Working electrode
WVTR	Water Vapour Transmission Rate
XPS	X-ray Photoelectron Spectroscopy

List of symbols and terms.

Abbreviation	Meaning
a	Real component of impedance
A	Surface of the electrodes
α	Heat transfer coefficient
α_c	Temperature coefficient of the capacitance
β_c	Humidity coefficient of the capacitance
C	Capacitance
C_R	Rated capacitance
δ	Defect angle
ε	Dielectric constant of the dielectric
E	Activation energy
E_B	Binding energy
E_c	Kinetic energy
F or ν	Frequency
f_{res}	Resonance frequency
F	Relative humidity
F_D	Thermal acceleration factor for diffusion (according to Arrhenius' law)
Φ_{espec}	Working function of spectrometer
γ_s	Total surface free energy
γ_s^d	Polar contribution of total surface free energy
γ_s^p	Dispersive contribution of total surface free energy
h	Planck's constant
I	Current
jb	Imaginary component of impedance
Ls	Series inductance
N	Avogadro number
O2	Oxygen
P	Power dissipation
P_0	Vapour saturation pressure
P_{gen}	Power generated in the capacitor
P_{diss}	Power dissipated through the capacitor surface
R	Universal molar constant for gases
ρ	Density

Ra	Arithmetic mean roughness
R_{iso}	Insulation resistance
Rp	Parallel resistance
Rp	Highest peak of roughness profile
Rq	RMS roughness
Rs	Series resistance
Rt	Total height of roughness profile
Rv	Deepest valley of roughness profile
S	Severity
S_{BET}	Surface area according to BET
t	Thickness of the dielectric
T	Temperature
T_g	Glass transition temperature
T_R	Rated temperature
θ	Phase angle
$\tan \delta$	Loss or dissipation factor
$\tan \delta_D$	Parallel component of tan d
$\tan \delta_P$	Dielectric component of tan d
$\tan \delta_S$	Series component of tan d
V	Voltage
V	Volume
V_0	Molar volume
V_{ESR}	Voltage though the equivalent series resistance
V_L	Voltage through the series inductance
V_m	Adsorbate volume
V_R	Rated voltage
X^2	Chi-squared (statistic parameter)
X_c	Capacitive reactance
X_L	Inductive reactance
Z	Impedance

ANNEX A

(54) Title: WOUND CAPACITOR ENCAPSULATED IN HOUSING

FIG 4
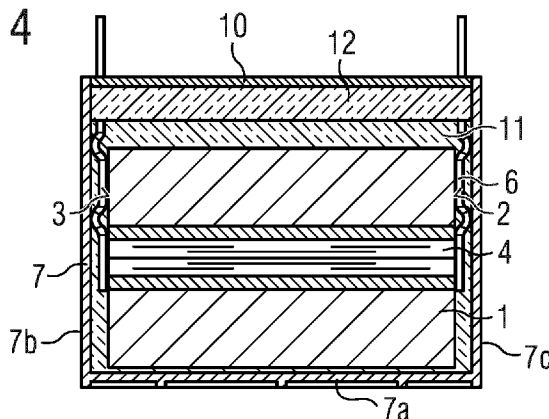
(57) Abstract: The present invention concerns a capacitor comprising a winding element (1), a housing (7) in which the winding
element (1) is arranged, a first insulating material (11) which encapsulates the winding element (1), and a second insulating material
(12) which forms a layer covering the first insulating material (11).

WO 2019/141388 A1

Description

WOUND CAPACITOR ENCAPSULATED IN HOUSING

5   The present invention concerns a capacitor.

A self-healing metallized film capacitor which may be used
for various applications typically consists of a winding
element housed in a plastic or metal housing impregnated with
10   insulating material. The metallized film capacitor is
typically designed to work in ambient environment of -40^{0}C to
a maximum of 125^{0}C. Under the effects of an application
environment, the ambient working conditions and an applied
electric field, the metallized film capacitor suffers from
15   various capacitance loss mechanisms. The capacitance loss
mechanisms are typically due to self-healings resulting in a
loss of metallized electrode area and electrode oxidation.

Eventually, the metallized film capacitor fails due to a high
20   capacitance drift. The failure should normally occur after
the expected end of life of the capacitor. Drift in the
capacitance is typically associated with an increase in the
loss factor.

25   Present day applications demand key components to withstand
higher amount of electrical as well as environmental
stresses. Capacitors are required to operate at higher
ambient temperatures in the presence of high relative
humidity conditions while achieving higher lifetime and
30   reliability for the products.

Capacitance loss mechanisms are accelerated under harsh
environmental working condition. In particular, the presence

of humidity lead to corrosion on the metallized film. The capacitance loss phenomenon affect either an active electrode surface or an electrode edge. In electrochemical corrosion, the series resistance of the capacitor increases over a

5   period of time causing a further increase in loss factor due to de-metallization of the metallized electrode leading to an increase in local hotspot temperatures. Higher ambient temperatures further accelerate this failure mechanism.

10 There is a growing demand for the capacitors capable to withstand high temperatures of 85^{0}C or more, under high relative humidity of 85% or more. As discussed above, under these stringent ambient working conditions, the capacitance loss mechanisms are accelerated. Thus, this situation calls

15 for new design considerations to be adopted in the metallized film capacitor.

Therefore, it is an object of the present invention to provide an improved capacitor which is less likely to suffer

20 from capacitance loss mechanisms under harsh environment conditions.

This object is solved by a capacitor according to claim 1. Preferred embodiments are subject of the dependent claims.

25

A capacitor is provided which comprises a winding element, a housing in which the winding element is arranged, a first insulating material which encapsulates the winding element, and a second insulating material which forms a layer covering

30 the first insulating material.

The capacitance loss mechanisms have been analyzed and it has been found that subjecting a capacitor to high thermal

stresses may intensify the following capacitance loss
mechanisms: Cracks may be generated on the housing surface.
Nano-pores and micro-scopic cracks may develop in the
insulating material, which may allow humidity to enter into
5   the insulating material. There may be non-adhesion between
the insulating material and the housing surface and non-
adhesion between insulating material and electrical
conducting terminals or leads. Further, the insulating
material may be de-laminated from electrical conducting
10   terminals or leads.

By providing a capacitor having two insulating materials, it
is possible to optimize the first insulating material in such
a manner that the above discussed capacitance loss mechanisms
15   which may be intensified under high thermal stress can be
prevented or at least significantly reduced. In particular,
the first insulating material can be optimized to prevent at
least one of the generation of cracks on the housing surface,
the development of nano-pores and micro-scopic cracks in
20   insulating material, the non-adhesion between the insulating
material and the housing surface, the non-adhesion between
insulating material and electrical conducting terminals or
leads and the de-lamination between the insulating material
and electrical conducting terminals or leads. Thermal
25   stresses may result, for example, from natural temperature
changes in an environment or from heat being applied to the
capacitor during a soldering process. The capacitor may be
used in an environment having a high humidity, for example a
relative humidity of 85% or more.
30

Apart from preventing these capacitance loss mechanisms, an
insulating material has to fulfil other requirements in a
capacitor, too. The second insulating material can be

provided to fulfil these requirements, for example providing
a low flammability. As these requirements may be fulfilled by
the second insulating material, the first insulating material
can be chosen without restrictions from the other
requirements. For example, there may not be a need that the
first insulating material has a low flammability, if the low
flammability of the capacitor can be guaranteed by the second
insulating material.

The first insulating material may be a different material
than the second insulating material. The first insulating
material may form a fist layer and the second insulating
material may form a second layer. The layers may not mix with
each other. The second insulating material may have a lower
density than the first insulating material. Thus, the second
layer may float on the first layer.

The first insulating material may completely cover the
winding element. In particular, the outer surface of the
winding element may be completely covered by the first
insulating material. Further, an opening extending through
the winding element may be completely filled with the first
insulating material. The second insulating material may not
be in direct contact to the winding element.

The first insulating material may not provide any direct path
for water vapor to the winding element. Accordingly, in the
first insulating material, no cracks or voids may be formed
and the first insulating material does may not suffer from a
lack of adherence between interfaces. Otherwise, water vapor
could quickly damage the winding element. The second
insulating material may be a barrier against water vapor
diffusion.

The first insulating material may be more flexible than the second insulating material.

The flexibility of an unbranched chain polymer may characterized by its persistence length. The persistence length is a basic mechanical property quantifying the stiffness of a polymer. For example, for pieces of a polymer that are shorter than their respective persistence length, the molecule behaves rather like a flexible elastic rod or beam, while for pieces of a polymer that are much longer than the persistence length, the properties can only be described statistically, like a three-dimensional random walk.

As the first insulating material may be very flexible, it may show a high adhesion. Therefore, the first insulating material adheres to the winding element, to wires and to an inner surface of the housing in such a way that a de-lamination or non-adhesion does not occur between the first insulating material and these elements, even under high thermal stresses and/or high humidity. Thus, no channels or voids may be generated in the first insulating material which could be penetrated easily by humidity. Accordingly, due to its high flexibility, the first insulating material may protect the winding element against the above-discussed capacitance loss mechanisms.

As the second insulating material may not be in direct contact to the winding element, it may not have to have a high flexibility. Voids and channels in the second insulating material do not present a problem as humidity cannot access the winding element through these voids or channels.

- 6 -

The first insulating material may comprises polymer chains,
and the second insulating material comprises polymer chains.
An average length of the polymer chains of the second
insulating material may be shorter than an average length of
5   the polymer chains of the first insulating material. A
shorter average length may result in a lower flexibility.

The second insulating material may have a lower flammability
than the first insulating material. Further, the second
10 insulating material may float on the first insulating
material and, thereby, it may form a sealing on the first
insulating material preventing oxygen from contacting the
first insulating material. Due to the low flammability of the
second insulating material and due to the sealing of the
15 first insulating material, an ignition of the first
insulating material may be prevented. Thus, very low
requirements can be posed to the flammability of the first
insulating material. In particular, a highly flammable
material may be used as a first insulating material. Flexible
20 materials often have a high flammability.

The first insulating material may have a higher adherence
than the second insulating material. The adherence of a
material may describe the tendency of particles of this
25 material to cling to dissimilar particles or surfaces. The
higher adherence of the first insulating material may result
from the first insulating material having a high free surface
energy and a similar polar character than the surface to be
bonded.. The polar character refers to the polarity of the
30 material. Polarity is a separation of electric charge leading
to a molecule or its chemical groups having an electric
dipole or multipole moment. Polarity underlies a number of
physical properties including surface tension.

- 7 -

As the first material may have a high adhesion, it may be connected to the winding element, the inner surface of the housing and to wires without forming any voids or channels even under thermal stress and/or high humidity. Thereby, the first insulating material may prevent the loss of capacitance of the winding element due to humidity affecting the winding element.

The second insulating material may have a higher cross-linking rate than the first insulating material. A cross-link is a bond that links one polymer chain to another. The cross-linking rate indicates a number of bonds between the polymer chains of the respective material. The first insulating material having a lower cross-linking rate than the second insulating material may further contribute to the first insulating material being more flexible than the second insulating material.

The first insulating material may comprise a polyurethane. In particular, the first insulating material may consist of a polyurethane. The second insulating material may comprise a polyurethane or an epoxy resin. In particular, the second insulating material may consist of a polyurethane or an epoxy resin. The polyurethane of the second insulating material may be different from the polyurethane of the first insulating material.

The capacitor may further comprise a wire forming an electrically conducting terminal which is electrically contacted to the winding element, wherein the wire comprises at least one kink.

The kink may help to center the winding element in the
housing such that the winding element does not abut an inner
surface of the housing. The kink may, thereby, ensure that
the winding element is encapsulated in a layer of the first
5   insulating material wherein the thickness of this layer
corresponds to a width of a protrusion formed by the kink.

The at least one kink may be arranged such that it abuts an
end face of the winding element and an inner surface of the
10   housing. Thereby, the kink may ensure that the end face of
the winding element is spaced apart from the inner surface of
the housing at least by a width of the kink.

The wire may comprise at least a second kink. The second kink
15   may be arranged such that the parts of the wire which are
free of the first kink and the second kink do not contact the
inner surface of the housing. Thus, the second kink may
ensure that humidity cannot enter into the capacitor along a
path formed by an abutment of the wire and the inner surface
20   of the housing. The second kink may be covered with the first
insulating material and the second insulating material.

Further, projections may be arranged at an inner surface of
the housing which form a guide for the wire. The projections
25   may help to fix the wire at its position even when the
capacitor is subjected to high thermal stresses.

A rib may be arranged at an inner surface of the housing,
wherein the rib abuts the winding element, wherein the rib is
30   adapted and arranged such that the rib ensures that the
winding element is surrounded by the first insulating
material in a minimum thickness.

A material of the housing may comprise any polymer material which provides an electrical insulation, a high resistance to moisture ingress and withstands high temperatures and thermal stresses. For example, the material of the housing may

5   comprise a polypropylene, a polybutylene terephthalate, a poly(p-phenylene sulfide) (PPS), a polycarbonate or a polyphenylene oxide (PPO). The material of the housing may be reinforced with glass fibres.

10   The capacitor may be designed to withstand temperatures of 85°C under a relative humidity of 85%.

     The capacitor may be a metallized film capacitor.

15   In the following, the invention and preferred embodiments are described with respect to the Figures.

     Figure 1 shows a winding element of a capacitor.

20   Figure 2 shows a capacitor comprising the winding element.

     Figure 3 shows a top view on the capacitor shown in Figure 2.

     Each of Figures 4, 5 and 6 shows a cross-sectional view of
25   the capacitor.

     Figure 7 shows a more detailed view of a part of Figure 5.

     Figure 8 shows a perspective view a wire which forms an
30   electrically conducting terminal.

     Figure 9 shows a schematic view of a part of the wire.

Figures 10 shows perspective view of a housing of the capacitor.

Figure 11 shows a partial view of one compartment of the
5   housing.

Figure 12 shows a cross-sectional view of the compartment.

Figures 13 and 14 show cross-sectional views of a third
10   embodiment of the capacitor.

Figure 1 shows a winding element 1 of a capacitor, in
particular of a metallized film capacitor. The winding
element 1 has a cylindrical shape, in particular a right
15   circular cylinder.

The winding element 1 is formed by a dielectric film which is
metallized on its surface. A dielectric material of the film
is a material in which electrostatic fields can persist for a
20   long time. The dielectric material may include polypropylene
(PP), polyethylene terephthalate (PET) or polyethylene
naphthalate. The winding element forms a parallel plate
capacitor wherein the metallization is separated by the
dielectric material.
25
The winding element 1 has two end faces 2, 3 opposite to each
other. One end face 2 corresponds to a bottom face of the
cylinder which is formed by the winding element 1 and the
other end face 3 corresponds to a top face of the cylinder.
30   The winding element 1 has an opening 4 which extends through
the winding element 1 from one end face 2 to the other end
face 3. The opening 4 is arranged along a symmetry axis of
the cylinder.

Each of the end faces 2, 3 is covered with a metallic contact layer, the so-called schoopage 5. The schoopage 5 allows to electrically contact the metallization of the dielectric
5   film.

The schoopage 5 on each end face 2, 3 is contacted by a wire 6 which forms an electrically conducting terminal. In particular, Figure 1 shows four wires 6, each wire 6 forming
10   an electrically conducting terminal. A voltage can be applied to the winding element 1 via the wires 6. Each wire 6 is fixed to one of the end faces 2, 3 of the winding element 1, e.g. by soldering. In particular, two wires 6 are fixed to the bottom face and two wires 6 are fixed to the top face.
15   The wires 6 are fixed to the end faces 2, 3 in positions that are symmetric to each other. This arrangement of the fixing points of the wires 6 to the end faces 2, 3 helps to centre the winding element 1 inside a housing 7 of the capacitor. In an alternative embodiment, only exactly one wire 6 may be
20   fixed to each end face 2, 3 of the winding element 1.

Each of the wires 6 has two kinks 8, 9, which will be discussed in more detail later.

25   Figure 2 shows a capacitor comprising the winding element 1 in a perspective view. The capacitor further comprises the above-mentioned housing 7. The housing 7 forms a box having a bottom wall 7a and four side walls 7b, 7c, 7d, 7e. The housing 7 forms a cavity in which the winding element 1 is
30   placed. The cavity is boarded by the bottom wall 7a and the side walls 7b, 7c, 7d, 7e. In particular, two of the side walls 7b, 7c are parallel to the end faces 2, 3 of the winding element. These two side walls 7b, 7c are each

directly adjacent to one end face 2, 3 and spaced apart from
the respective end face 2, 3 by a minimum distance. The other
two side walls 7d, 7e are perpendicular to the end faces 2,
3.

5

The housing 7 further comprises a lid 10, which is not shown
in Figure 2. In an alternative embodiment, the housing 7 does
not comprise a lid 10. The lid 10 can be placed such that it
closes the cavity formed by the housing 7. Accordingly, the
10   lid 10 can be arranged opposite to the bottom wall 7a. The
lid 10 has one opening for each of the wires 6 which form the
electrically conducting terminals. Each wire 6 can protrude
out of the cavity formed in the housing 7 through the
corresponding opening in the lid 10. Thereby, the wires 6
15   allow electrically contacting the winding element 1 to a
circuit outside the housing 7.

The housing 7 is designed such that it will provide a high
resistance to moisture ingress and withstand high
20   temperatures. In particular, the material of the housing 7 is
chosen to provide high resistance to humidity and to thermal
stress. The material of the housing 7 may be one of
polypropylene (PP), polybutylene terephthalate (PBT), p-
phenylene sulphide (PPS) or nylon. The material of the
25   housing 7 may be reinforced with glass fibres. Further, a
thickness of the bottom wall 7a, the side walls 7b, 7c, 7d,
7e and the lid 10 is chosen to provide high resistance to
humidity and to thermal stress.

30   The housing 7 is filled with two insulating materials 11, 12,
as will be discussed in more detail later. In Figure 2, only
a second insulating material 12 is visible.

Figure 3 shows a top view on the capacitor shown in Figure 2.
In Figure 3, sections AA, BB and CC are marked. Each of
Figures 4, 5 and 6 shows a cross-sectional view of the
capacitor shown in Figure 3. The cross-sectional view shown

5   in Figure 4 is taken along the section AA. The cross-
sectional view of Figure 5 is taken along the section CC. The
cross-sectional view of Figure 6 is taken along the section
BB.

10   The capacitor comprises a first insulating material 11 and
the second insulating material 12. Each of the first and the
second insulating material 11, 12 forms a separate layers.
The layers do not mix with each other. A volume occupied by
the first insulating material 11 is larger than a volume

15   occupied by the second insulating material 12.

The first insulating material 11 completely encapsulates the
winding element 1. The opening 4 extending from one end face
2 of the winding element 1 to the other end face 3 of the

20   winding element 1 is completely filled with the first
insulating material 11. A height H of the cavity inside the
housing 7 may be defined as the distance from the lowest
point of an inner surface of the bottom wall 7a to the lid
10. The layer formed by the first insulating material 11 has

25   a thickness which corresponds to at least 90% of the height H
of the cavity, preferably to at least 95% of the height H of
the cavity.

The second insulating material 12 is arranged on the first

30   insulating material 11. In particular, in a direction from
the bottom wall 7a of the housing 7 to the lid 10, the second
insulating material 12 is arranged on top of the first
insulating material 11.

Each of the two insulating material 11, 12 is optimized for a different purpose. In particular, the first insulating material 11 is optimized to prevent or at least reduce
5 capacitance loss mechanisms which over the lifetime of the capacitor result in a drift in the capacitance of the winding element 1. The second insulating material 12 is optimized to fulfil other tasks of an insulating material in a metallized film capacitor, in particular to provide a low flammability.
10

In a common capacitor having only one insulating material, different and sometimes contradicting requirements are demanded from the insulating material. As the capacitor has two insulating materials, it is possible to fulfil some
15 requirements by the first insulating material 11 and some requirements by the second insulating material 12, thereby preventing problems from contradicting requirements.

The first insulating material 11 is a polyurethane. The first
20 insulating material 11 is more flexible than the second insulating material 12. Each of the insulating materials 11, 12 comprises polymer chains. The polymer chains of the first insulating material 11 are longer than the polymer chains of the second insulating material 12.
25

The first insulating material 11 has similar polar character than housing 7.. Thereby, it is ensured that the first insulating material 11 shows a good adhesion to an inner surface of the housing 7, to the wires 6 and to the winding
30 element 1. Thus, no voids or channels are formed in the first insulating material 11 or between the first insulating material 11 and one of the inner surface of the housing 7, to the wires 6 and to the winding element 1. Otherwise, there

would be a significant risk that humidity from outside of the
housing 7 accesses the winding element 1 via the voids or
channels and, thereby, would result over a rather short time
in a loss of capacitance of the winding element 1 and,
5   eventually, in a failure of the capacitor.

Moreover, the first insulating material 11 is optimized to
prevent cracks on the inner surface of the housing 7 due to
its low expansion and contraction with temperature changes.
10   The first insulating material 11 is optimized to prevent the
development of nano-pores and microscopic cracks in the first
insulating material 11 as the first insulating material 11 is
very flexible. Thus, the first insulating material 11 is
optimized to prevent or at least reduce capacitance loss
15   mechanisms which may occur at high thermal stresses and/or
high humidity.

The second insulating material 12 may be a polyurethane or an
epoxy resin. The second insulating material 12 is more rigid
20   than the first insulating material 11. The second insulating
material 12 may be exposed to an external environment as it
is formed on the top of a cavity defined by the housing 7.
The second insulating material 12 shows a low flammability.
In particular, the second insulating material 12 has a lower
25   flammability than the first insulating material 11. The
second insulating material 12 is optimized to have a low
flammability and thereby to fulfil requirements regarding the
flammability of the capacitor. As these requirements are
fulfilled by the second insulating material 12, the first
30   insulating material 11 can be optimized for preventing
performance losses due to thermal stress and high humidity.

Figure 7 shows a more detailed view of a part of Figure 5
which is marked in Figure 5 by line X. Figure 8 shows a
perspective view of one of the wires 6 which forms an
electrically conducting terminal. Figure 9 shows a schematic
5 view of a part of the wire 6.

The wire 6 comprises a first kink 8 and a second kink 9. Both
kinks 8, 9 are arranged such that they are inside the housing
7 when the wire 6 is fixed to the end face 2, 3 of the
10 winding element 1.

The wire 6 mostly forms a straight line. Each of the kinks 8,
9 defines a deviation from the straight line. Both kinks 8, 9
point in the same direction, i.e. away from the winding
15 element 1 and towards the inner surface of the housing 7. The
first kink 8 is arranged such that it abuts an inner surface
of the housing 7 and the end face 2, 3 of the winding element
1. The first kink 8 forms a protrusion which protrudes by a
distance D towards the inner surface of the housing 7.
20 Thereby, the first kink 8 ensures that a layer of the first
insulating material 11 having a thickness of D is arranged
between the inner surface of the housing 7 and the end face
2, 3 of the winding element 1. Accordingly, the first kink 8
prevents that the end face 2, 3 of the winding element 1
25 directly contacts the inner surface of the housing 7. The end
face 2, 3 of the winding element 1 is covered by the
schoopage 5 which is very sensitive to humidity. As the first
kink 8 prevents a direct contact of the schoopage 5 and the
housing 7, humidity is prevented from travelling directly
30 from the inner surface of the housing 7 to the schoopage 5.

The second kink 9 is arranged on the wire 6 at such a height
that it is above the winding element 1 and below the second

insulating material 12 in the direction from the bottom wall
7a to the lid 10. Accordingly, the second kink 9 is covered
by the first insulating material 11. The second kink 9
ensures that the remainder of the wire 6 is spaced away from
5   the inner surface of the housing 7 by a distance which is
defined by a length L of a protrusion of the second kink 9.
Accordingly, this space is filled with the first insulating
material 11. The second kink 9 ensures that no air channel is
created between the wires 6 and the inner surface of the
10   housing 7 because the wires 6 and the inner surface of the
housing 7 are separated by a minimum thickness of insulating
material 11, 12..

In the following, the design of the wire 6 is described in
15   more detail with respect to Figures 1, 8 and 9. Only one wire
6 is described in the following. However, each of the wires 6
is designed in the same manner. In the shown embodiment, the
capacitor comprises four wires 6. However, the capacitor may
also comprise another number of wires, for example two wires
20   or six wires.

The wire 6 comprises a first straight section 13, a first
kink 8, a second straight section 14, a second kink 9 and a
third straight section 15. In the each of the straight
25   sections 13, 14, 15, the wire 6 is completely straight, i.e.
free from turns.

The first straight section 13 of the wire 6 is fixed to the
schoopage 5 on the end face 2, 3 of the winding element 1.
30   The first straight section 13 does not extend beyond the end
face 2, 3 of the winding element 1. The first straight
section 13 merges over in the first kink 8.

The first kink 8 is adjacent to the first straight section
13. The first kink 8 is formed by a first bend 16 of the wire
6, a second bend 17 of the wire 6 and a third bend 18 of the
wire 6. The first bend 16 is in a direction away from the
5   winding element 1 and towards the inner surface of the
housing 7. The second bend 17 of the wire 6 is directly
adjacent to the first bend 16. The second bend 17 is directed
towards the winding element 1. The second bend 17 is arranged
at a position furthest away from the winding element 1. The
10   third bend 18 is directly adjacent to the second bend 17 and
is formed such that the first kink 8 merges over to the
second straight section 14. The first kink 8 is formed such
that the distance D from the second straight section 14 to
the inner surface of the housing 7 is identical to the
15   distance from the first straight section 14 to the inner
surface.

The second straight section 14 is dimensioned such that it
extends beyond the end face 2, 3 of the winding element 1.
20   The second straight section 14 is completely arranged inside
the layer of the first insulating material 11. The second
straight section 14 merges over into the second kink 9.

The second kink 9 is completely arranged inside the layer of
25   the first insulating material 11. The second kink 9 is formed
by three bends similar to the first kink 8. The first and the
second bend are formed identical. The third bend of the
second kink 9 is formed at a different position. Thus, the
distance L from the third straight section 15 to the inner
30   surface of the housing 7 is smaller than the distance D from
the second straight section 14 to the inner surface. The
second kink 9 merges over into the third straight section 15.

The third straight section 15 extends through the layer of
the second insulating material 12 and protrudes out of the
housing 7.

5   Figures 10 shows a perspective view of the housing 7 of the
capacitor according to a second embodiment. The housing 7
comprises multiple compartments 19, each compartment 19 being
configured to receive one winding element 1. Figure 10 shows
the housing 7 upside down. It can be seen in Figure 10 that
10   the bottom of each compartment 19 is curved.

Figure 11 shows a partial view of one of the compartments 19
wherein parts of the housing 7 are not. The compartment 19 is
free of a lid. In an alternative embodiment, the compartment
15   19 may additionally comprise a lid 10.

Figure 12 shows a cross-sectional view of the compartment 19
shown in Figure 11.

20   Ribs 20, 21 are arranged on the inner surface of the housing
7.

The bottom wall 7a of the housing is shaped as a halfpipe.
The halfpipe has the radius R. Two ribs 20 are arranged at
25   the bottom wall 7a of the housing 7. At the position of the
ribs 20, the bottom wall 7a has a reduced radius r which is
smaller than the radius R. When the winding element 1 rests
on the ribs 20, the winding element 1 is spaced away from the
remainder of the bottom wall 7a by at least a minimum
30   distance which corresponds to the difference between the
radius R and the radius r.

Further, ribs 21 are arranged at the inner surfaces of the
side walls 7d, 7e of the housing 7 which are perpendicular to
the end faces 2, 3 of the winding element 1. In particular,
three ribs 21 are arranged on the inner surface of one of the
5   side walls 7d, 7e that are perpendicular to the end faces 2,
3 and three ribs 21 are also arranged on the inner surface of
the opposite side wall 7d, 7e.

The ribs 21 on the side walls 7d, 7e abut the winding element
10 1 and, thereby, ensure that the winding element 1 is centred
inside the housing 7. The ribs 21 further ensure that the
winding element 1 is spaced apart from the inner surface of
the housing 7 and does not directly contact the inner
surface. Thus, it is prevented that humidity can access the
15 winding element 1 directly from the housing.

Moreover, on the inner surface of the side faces 7b, 7c which
are arranged adjacent to the end faces 2, 3 of the winding
element 1, two rails 22 are defined by projections of the
20 inner surface. These rails 22 form guiding elements for the
wires 6 which are used as electrically conducting terminals.
The rails 22 help to keep the wires 6 in their respective
position even when thermal stress is applied to the
capacitor. Each rail 22 is formed by two projections 22a, 22b
25 which are arranged to sandwich the corresponding wire
inbetween.

Figures 13 and 14 show cross-sectional views of a third
embodiment of the capacitor. The housing 7 of the capacitor
30 comprises a flat bottom wall 7a. Two ribs 20 are arranged at
the bottom wall 7a. Each of the two ribs 20 protrudes into
the inside of the housing 7. The winding element 1 rests on
the ribs 20. Thus, the winding element 1 is spaced away from

the remainder of the bottom wall 7a by at least a minimum distance which corresponds to a height of the ribs 20.

Figures 13 and 14 show a housing 7 which consists of only one
5   compartment. In an alternative embodiment, the housing 7 may comprise multiple compartments wherein each compartment has a flat bottom wall 7a.

The housing 7 may additionally comprise ribs 21 arranged at
10   the inner surfaces of the side walls 7d, 7e of the housing 7 similar to the second embodiment. The housing 7 may additionally comprise two rails 22 defined by projections of the inner surface similar to the second embodiment. These rails 22 may form guiding elements for the wires 6 which are
15   used as electrically conducting terminals.

Reference numerals

	1	winding element
	2	end face
5	3	end face
	4	opening
	5	schoopage
	6	wire
	7	housing
10	7a	bottom wall
	7b	side wall (parallel to end face)
	7c	side wall (parallel to end face)
	7d	side wall
	7e	side wall
15	8	first kink
	9	second kink
	10	lid
	11	first insulating material
	12	second insulating material
20	13	first straight section
	14	second straight section
	15	third straight section
	16	first bend
	17	second bend
25	18	third bend
	19	compartment
	20	rib
	21	rib
	22	rail
30	22a	projection
	22b	projection
	H	height of cavity

D   protrusion of first kink

L   protrusion of second kink

R   radius of the bottom wall

r   radius of the ribs

5

Claims (We claim)

1.   Capacitor comprising
     a winding element (1),
5   a housing (7) in which the winding element (1) is
     arranged,
     a first insulating material (11) which encapsulates the
     winding element (1), and
     a second insulating material (12) which forms a layer
10   covering the first insulating material (11).

2.   Capacitor according to claim 1,
     wherein the first insulating material (11) is more
     flexible than the second insulating material (12).

15
3.   Capacitor according to one of the preceding claims,
     wherein the first insulating material (11) comprises
     polymer chains, and
     wherein the second insulating material (12) comprises
20   polymer chains, wherein an average length of the polymer
     chains of the second insulating material (12) is shorter
     than an average length of the polymer chains of the
     first insulating material (11).

25   4.   Capacitor according to one of the preceding claims,
     wherein the second insulating material (12) has a lower
     flammability than the first insulating material (11).

5.   Capacitor according to one of the preceding claims,
30   wherein the first insulating material (11) has a higher
     adherence than the second insulating material (12).

6.   Capacitor according to one of the preceding claims,

wherein the second insulating material (12) has a higher cross-linking rate than the first insulating material (11).

5   7.   Capacitor according to one of the preceding claims, wherein the first insulating material (11) comprises a polyurethane, and wherein the second insulating material (12) comprises a polyurethane or an epoxy resin.

10

8.   Capacitor according to one of the preceding claims, further comprising a wire (6) forming an electrically conducting terminal which is electrically contacted to the winding element (1), wherein the wire (6) comprises at least one kink (8, 9).

15

9.   Capacitor according to the preceding claim, wherein the at least one kink (8) is arranged such that it abuts an end face (2, 3) of the winding element (1) and an inner surface of the housing (7).

20

10. Capacitor according to one of claims 8 or 9, wherein the wire (6) comprises at least a second kink (9).

25

11. Capacitor according to the preceding claim, wherein the second kink (9) is arranged such that the parts of the wire (6) which are free of the first kink (8) and the second kink (9) do not contact the inner surface of the housing (7).

30

12. Capacitor according one of claims 8 to 11,

wherein projections (22a, 22b) are arranged at an inner surface of the housing (7) which form a guide for the wire (6).

5 13. Capacitor according one of the preceding claims, wherein a rib (20, 21) is arranged at an inner surface of the housing (7), wherein the rib (20, 21) abuts the winding element (1), wherein the rib (20, 21) is adapted and arranged such
10   that the rib ensures that the winding element (1) is surrounded by the first insulating material (11) in a minimum thickness.

14. Capacitor according one of the preceding claims,
15   wherein a material of the housing (7) comprises a polypropylene, a polybutylene terephthalate, a poly(p-phenylene sulfide), a polycarbonate or a polyphenylene oxide and/or
20   wherein the material of the housing (7) is reinforced with glass fibres.

15. Capacitor according one of the preceding claims, wherein the capacitor is designed to withstand
25   temperatures of 85°C under a relative humidity of 85%.
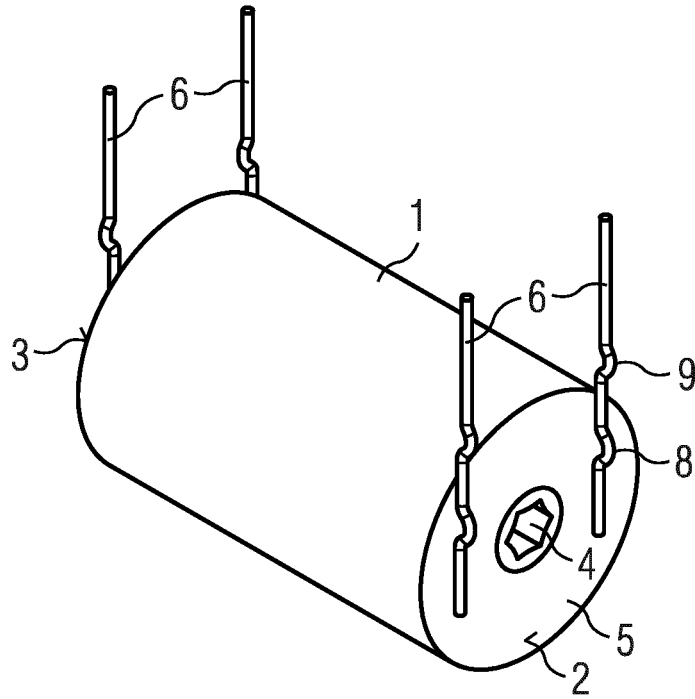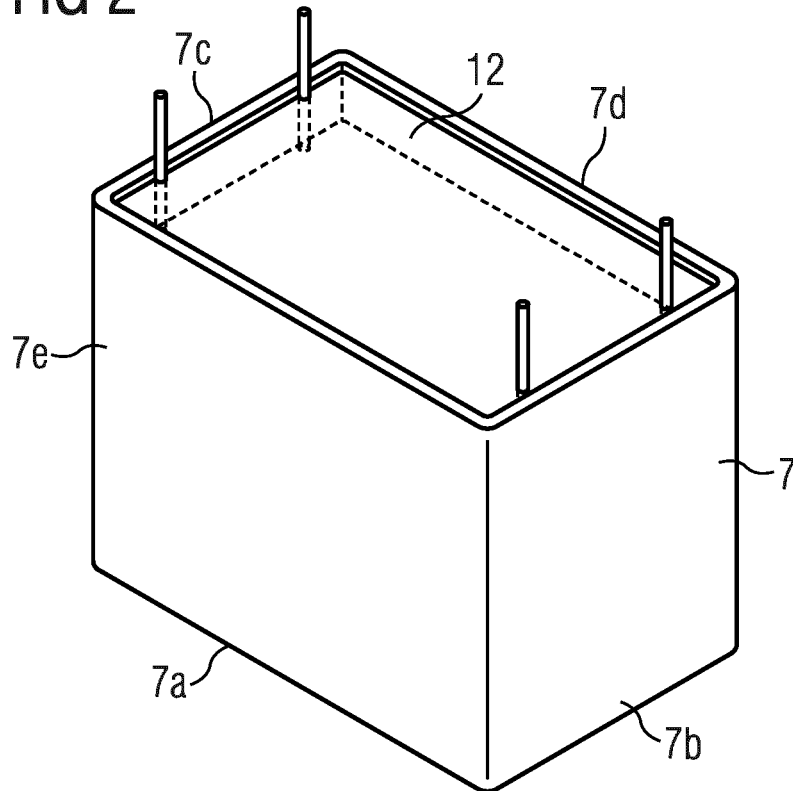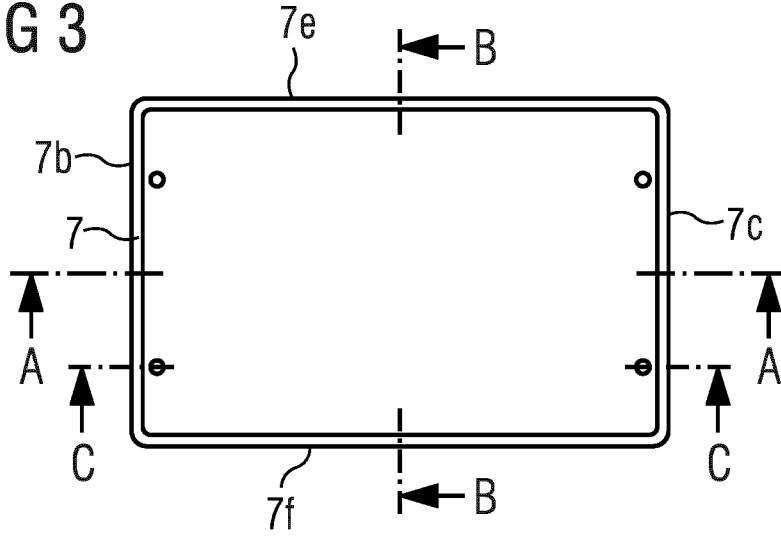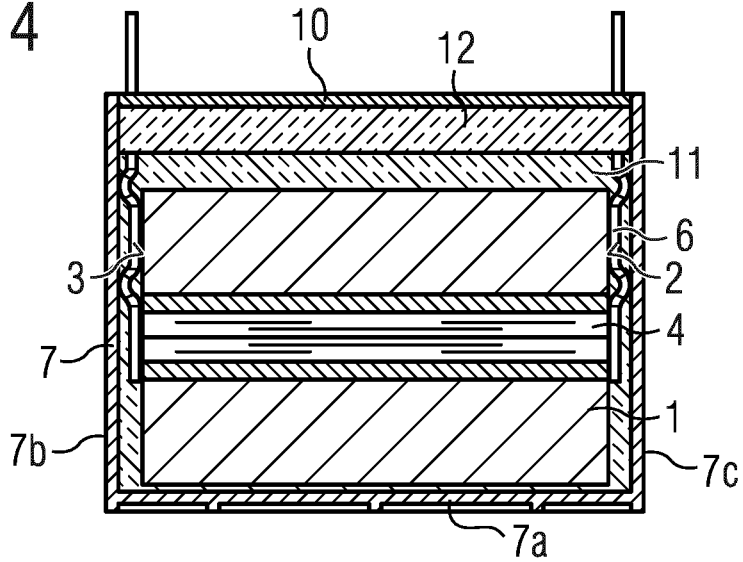
FIG 1

FIG 2

FIG 3

FIG 4

FIG 5
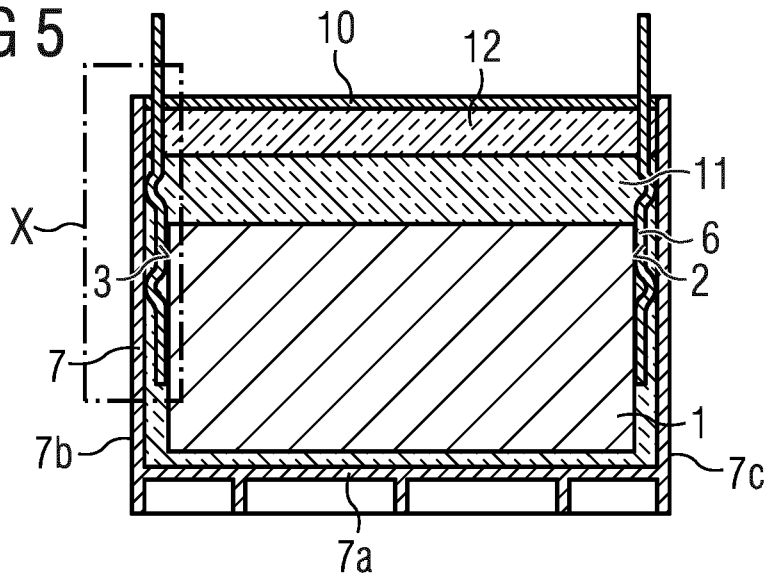
FIG 6
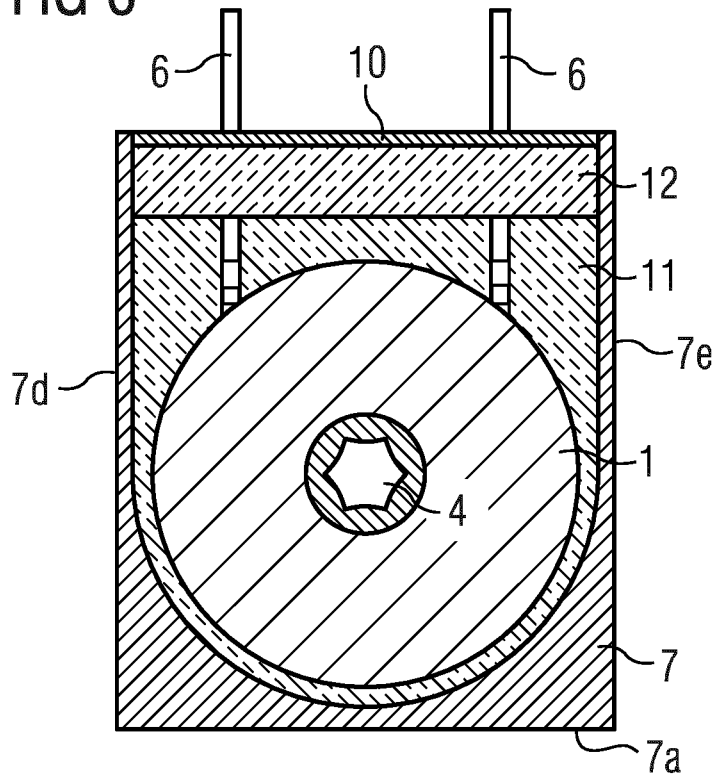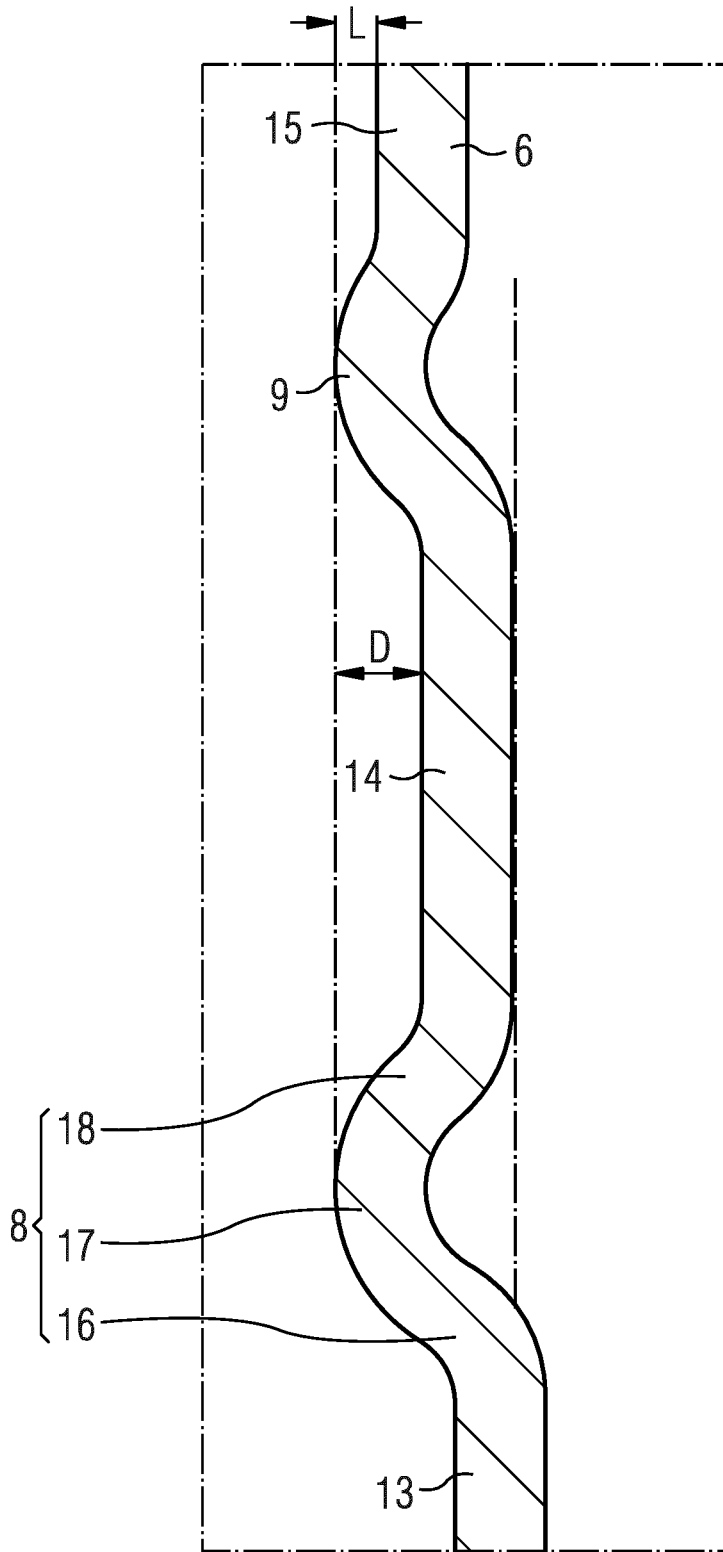

FIG 7
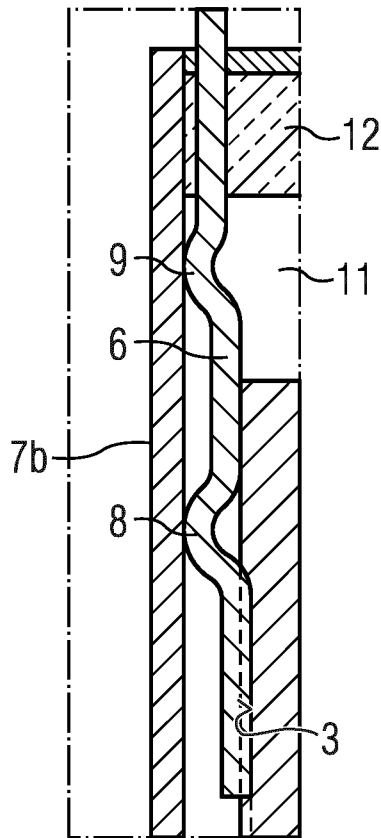
FIG 8
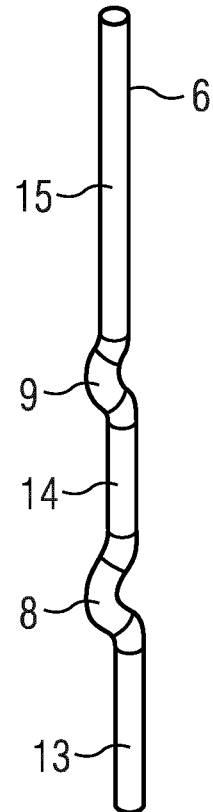
FIG 9

FIG 10
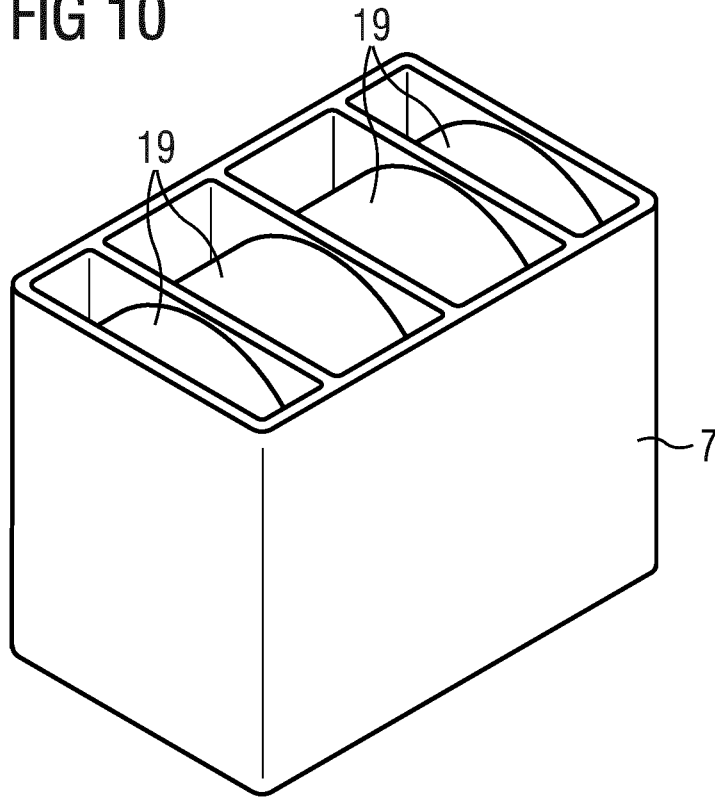
FIG 11

FIG 12

FIG 13

FIG 14

ANNEX B

Full Length Article

Surface modification of thermoplastics by low-pressure microwave O₂ plasma treatment for enhancement of the adhesion of the interface box/ encapsulating resin and the influence on film capacitors operating under extreme humidity conditions

Azahara Albéndiz García[b,*], Enrique Rodríguez-Castellón[a,*], David Peláez Millas[b]

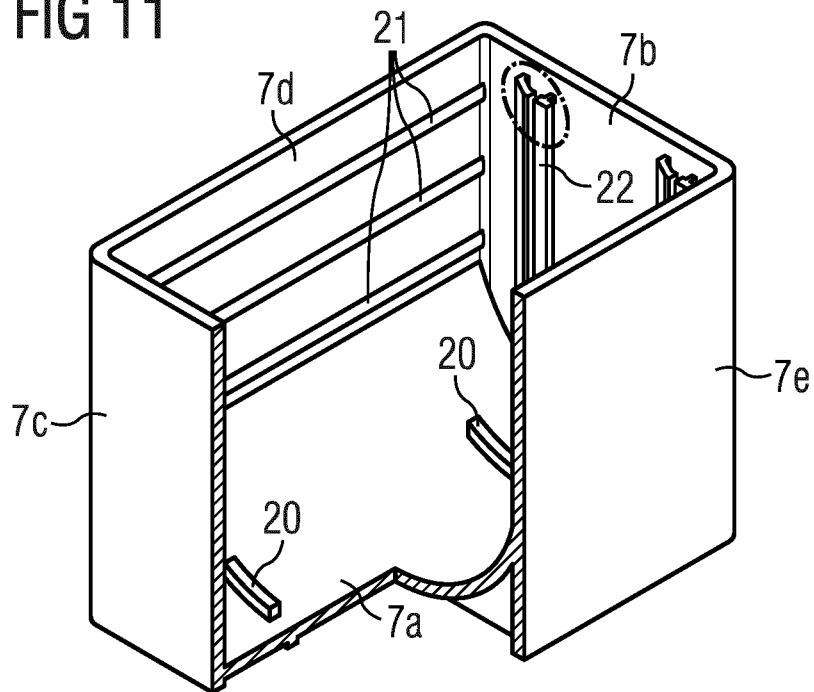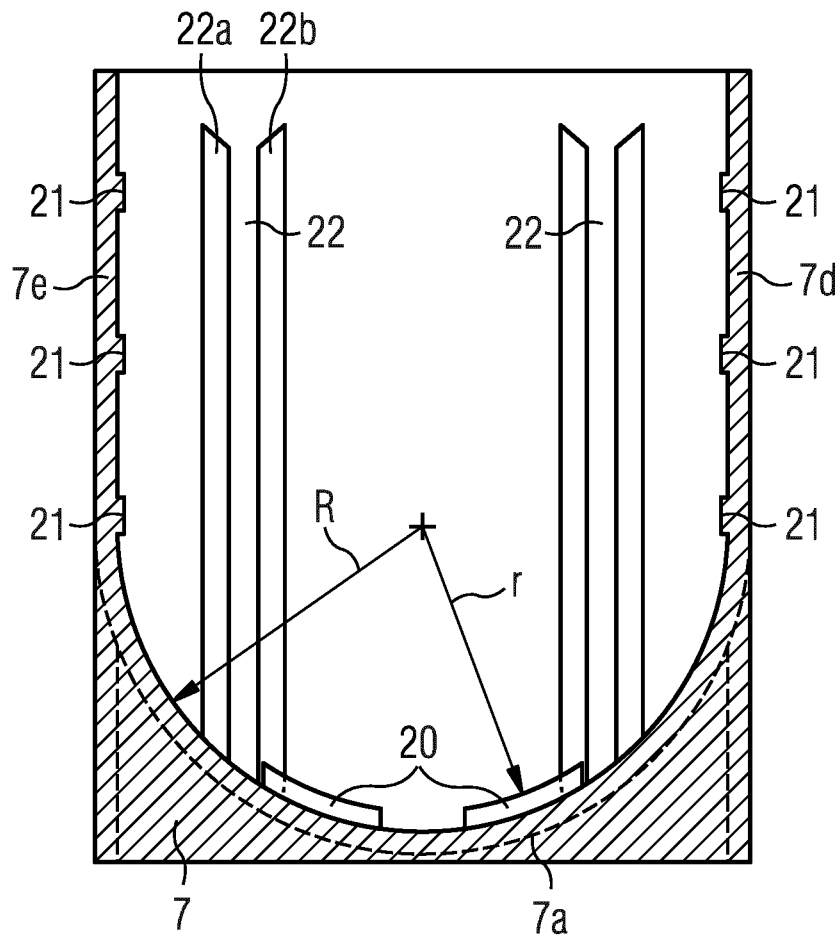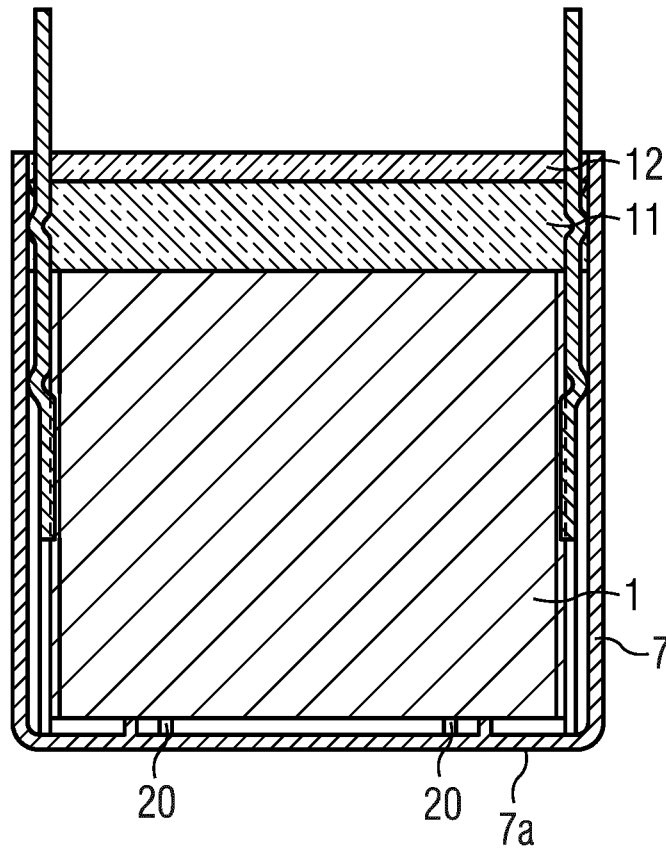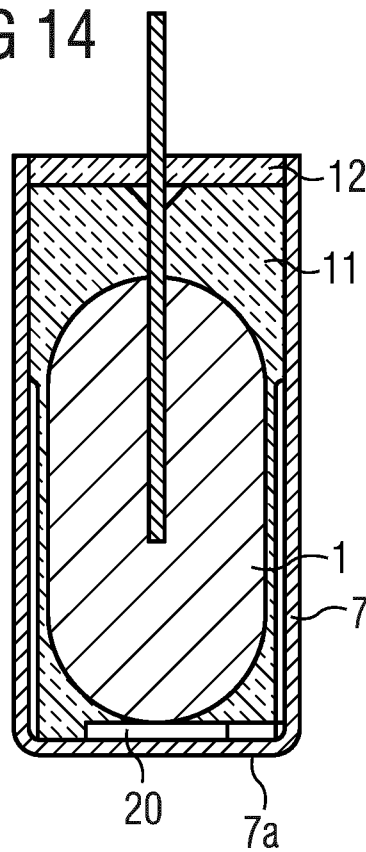[a] Department of Inorganic Chemistry, Faculty of Science, University of Málaga, Málaga 29071, Spain
[b] R&D Department, TDK Electronics Components S.A.U., C/ Severo Ochoa, 66-68, 29590 Málaga, Spain

ABSTRACT

A low-pressure microwave O₂ plasma is applied on the plastic boxes of the metallized film capacitors to strengthen the interfacial adhesion of thermoplastic box/encapsulating resin. The effectiveness of the plasma is reported by analyzing Scanning Electron Microscopy (SEM) micrographs, X-Ray Photoelectron Spectroscopy (XPS) spectra, and contact angle and roughness measurements. An enhancement of the polar character and total free surface energy in both thermoplastics (polybutylene terephthalate (PBT) and polycarbonate (PC)) are determined. Hence, a better wettability of the plastic boxes with the encapsulating epoxy resin is achieved after the plasma application. During the Temperature-Humidity Bias Test (THB), the metallized film capacitors with PC box improves the performance after being plasma treated. Additional capacitor interfaces seem to play a key role in the performance of the device according to the loss of capacitance determined during the THB Test.

1. Introduction

The automotive industry is progressively requesting that film capacitors pass very aggressive tests where the devices are submitted to voltage in an environment of high humidity and high temperature. The electrodes in metallized film capacitors are comprised of very thin layers of metal, usually zinc or aluminum, evaporated onto the surface of a polymeric thin film. Electrochemical corrosion in metallized film capacitors encapsulated with polymeric materials is one of the most common mechanisms of failure due to the direct penetration of water vapor inside the device. A drop in the capacitance of the capacitor is found when the corrosion of the electrode is started [1–3].

All the polymers playing the role of insulating materials undergo a slow degradation due to the submitted conditions. The presence of cavities in the interface between the resin of encapsulation and the plastic box may lead to cracks by the break of bonds, creating paths to the direct penetration of water vapor inside the device. This generates the migration of oxygen and/or moisture to the electrode, initiating the process of corrosion [4].

The polymers used as encapsulate usually are tailored developed to fulfill a good processability, advanced mechanical properties,

dimensional stability, chemical inertness, non-flammable properties, etc. in addition to their function as electrical isolator. Most of the adhesion problems in casting resins are usually related to the additives in the formulation of these epoxy resins, which migrate to the surface once the adhesive joint is established, causing further a lack of adhesion [5–7].

The second polymeric material involved in the interface of the joint is the thermoplastic injected as box. Glass fiber and active ingredients have been incorporated into a wide variety of thermoplastic as polyethylene, polypropylene, polyamides, polyvinyl chloride, etc. [8–11,34,36–37]. In most of the formulations, the use of dispersing and/or coupling agents is required to minimize the dissimilar nature of the highly polar agents and the non-polar ones. Polyolefins are the most attractive thermoplastic components in these composites due to their properties and cost. However, surface functionalization reactions using conventional wet chemistry techniques are not adequate due to the chemical inertness of polyolefins. Plasma technologies are more appropriated for the functionalization of this type of materials due to be dry processes developed in a wide pressure range, altering only the very top layers of the plasma exposed surface and hence leaving the bulk properties of the substrates unchanged, and they are energy efficient

ANNEX C.
Contributions on international congresses, seminars and/or workshops.

epf

DRESDEN 2015

EUROPEAN POLYMER CONGRESS

GDCh

MAKRO MOLEKULARE CHEMIE
Eine Fachgruppe der GDCh

IUPAC
INTERNATIONAL UNION OF
PURE AND APPLIED CHEMISTRY

epf European Polymer Federation

Leibniz-Institut
für Polymerforschung
Dresden e.V.

BOOK OF ABSTRACTS

UNIVERSIDAD DE MALAGA

Dresden Marketing GmbH – A. Üçmer

235

Encapsulation of film capacitors for power electronics. Study and characterization of adhesion between polymeric materials

A. Albéndiz García [a], *D. Peláez Millas* [a], *E. Rodríguez Castellón* [b]

[a] R&D, EPCOS Electronic Components, C/ Severo Ochoa, 66-68, 29590, Málaga, Spain

[b] Department of Inorganic Chemistry, University of Málaga, Spain,

azahara.albendiz@epcos.com

The electrodes in metallized film capacitors are comprised of very thin layers of metal, usually zinc or aluminium, evaporated onto the surface of a polymeric film. Electrochemical corrosion in metallized film capacitors encapsulated with polymeric materials is one of the most common mechanisms of failure due to the direct penetration of water vapor inside the device. A drop in the capacitance of the capacitor is found when the corrosion of the electrode is started [1].

All the polymers playing the role of insulating materials undergo a slow degradation due to the submitted conditions. The presence of cavities in the interface encapsulation-box or the lack of adherence between the encapsulating material and the metallic wires may lead to cracks by the break of bonds, creating paths to the direct penetration of water vapor inside the device. This generates the migration of oxygen and/or moisture to the electrode, initiating the process of corrosion [2].

Progressively, customers are requesting that film capacitors pass very aggressive tests where the devices are submitted to voltage in an environment of high humidity and at high temperature.

During the process of potting the encapsulating resin, to get an adequate adhesion between the polymeric material of the box and the one that is encapsulating the electrode is a fundamental contributor to the lifetime of the film capacitor. Thus voids or lack of adhesion might be minimized when the device is submitted to temperature-humidity accelerations [3].

This study has the aim to characterize different polymers to be injected as boxes and to study if the wettability with the encapsulating resin before this one is cured might be improved with a plasma treatment on the surface. With this purpose, chemical and physical parameters as surface energy, contact angles with polar and non-polar solvents, and composition of the polymeric materials have been characterized by contact angle, SEM-EDX and XPS.

[1] D.F. Taylor, *IEEE Transactions on Electrical Insulation*, **1984**, *19*, 288-293

[2] E. Yildiz, A. Güngor, H. Yildirim, B.M. Baysal, *Macromolecular Materials and Engineering*, **1994**, *219*, Issue 1, 55-66

[3] S.P. Sim, R.W.Lawson, *Reliability Physics Symposium*, **1979**, *17th* Annual, 103-112

Characterization of transport properties of oxygen and water vapor permeation in polymers for the encapsulation of metallized film capacitors as protection against humidity

△ *Albéndiz García* [a], *D. Peláez Millas* [a], *E. Rodríguez Castellón* [b]

[a] R&D, EPCOS Electronic Components, C/ Severo Ochoa, 66-68, 29590, Málaga, Spain

[b] Department of Inorganic Chemistry, University of Málaga, Spain,

azahara.albendiz@epcos.com

The electrodes of metallized film capacitors consist of very thin layers of metal, usually zinc or aluminium, evaporated onto the surface of a polymeric film. The electrochemical corrosion in metallized film capacitors encapsulated with polymeric materials is one of the most common mechanisms of failure. A drop in the capacitance of the capacitor is found when the corrosion of the electrode is initiated [1].

The diffusion of the humidity and/or oxygen through the encapsulation may initiate the process of corrosion if these reach the interface metallization-dielectric [2].

A right selection of the material for the plastic encapsulation in the stage of design is very important to avoid the corrosion due to the migration of ions. A low water vapor transmission rate, WVTR, through the polymer injected as box covering the device and the encapsulation surrounding the electrode is one of the elemental contributors to limit this aging mechanism [3].

The aim of this research is to characterize the transport properties of oxygen and water vapor permeation in different polymers injected as boxes and potted as encapsulation of the electrode and to study their barrier performance in the capacitor operating with AC voltage and submitted to high humidity and high temperature (85%RH and 85ºC).

[1] D.G. Shaw, S.W. Cichanowski, A.Yializis, *IEEE Transactions on Electrical Insulation*, **1981**, EI-16, Issue 5, 399-413

[2] D.S. Peck and C.H. Zierdt, *Reliability Physics Symposium*, **1973**, 11th Annual, 146-152

[3] J. J. Licari, *Coating Materials for Electronic Applications*, **2003**, 65-200

Improvement of performance by a Low-Pressure Microwave O2 Plasma Treatment in the interface of polymeric encapsulation of Film Capacitor for Power Electronics

A. Albéndiz García [1*], D. Peláez Millas [1], E. Rodríguez Castellón [2]

[1] Department of R&D, EPCOS Electronic Components S.A.U.
[2] Department of Inorganic Chemistry, University of Málaga, Spain,
*azahara.albendiz@epcos.com

1. Introduction

Power electronic industry is progressively demanding that film capacitors encapsulated with polymeric materials operate under extremely humid conditions with stable capacitance values. All the polymers endure a slow degradation during the operation accelerated in harsh environments. The presence of voids in the interface between the plastic case and the epoxy resin sealing the electrodes of the metallized film capacitor might initiate paths to the migration of moisture to the electrode, initiating a process of corrosion and hence a drop of capacitance of the capacitor [1]. An improvement in the adhesion on this interface and to minimize consequently the cavities between both polymers before bonding is a fundamental contributor in the lifetime of the metallized film capacitor [2].

Figure 1   Image of a metallized film capacitor encapsulated. A 2-pin version

Before the process of filling the capacitor with the epoxy resin, a Low-Pressure Microwave O_2 Plasma treatment was applied on the polypropylene box to functionalize the surface leaving the bulk properties of the substrate unchanged. Plasma technologies are more appropriated than conventional wet chemistry for the activation of this type of material due to inertness of polyolefins[3-5].

The purposes of this study are first; to characterize the surface energies due to the effect of the oxygen plasma and the differences on the dispersive and polar components; and secondly to analyze the plasma treated polypropylene case by X-Ray Photoelectron Spectroscopy (XPS) to establish the nature of the modifications produced on the outermost surface further bonded with the epoxy resin. Finally, the efficacy of the Low-Pressure Microwave O_2 Plasma on polypropylene

will be studied verifying the performance of metallized film capacitors under a damp heat test with operational conditions of AC voltage, 85% of relative humidity and 85°C during 500h. The evolution of the capacitance of film capacitors with and without plasma treatment will be followed up during the damp heat test.
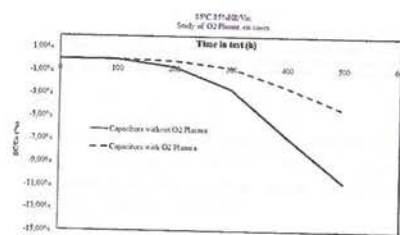

Figure 2   Damp Heat Test 85%RH/85°C/V_{AC}

2. References

[1]   D.F. Taylor, *IEEE Transactions on Electrical Insulation*, **1984**, *19*, 288-293
[2]   S.P. Sim, R.W.Lawson, *Reliability Physics Symposium*, **1979**, *17th* Annual, 103-112
[3]   F. Denes. Trends Polymer Sci. 1997;5(1):23-31
[4]   E.M. Liston. J. Adhes. 1989, 30, 199
[5]   *M.M.* Pastor-Blas, J.M. Martín-Martínez, J.G.Dillard. *Surf.Interface Anal.* 1998, 26, 385

239

Studies on metal spray metallization as humidity barrier in film capacitor

Azahara Albéndiz García [1*], Lucía Cabo[2], David Peláez Millas [3], Enrique Rodríguez Castellón [4]

[1] Department of CAP T R&D BR, TDK Electronics Components S.A.U., Málaga, Spain
[2] Department of CAP T R&D BR, TDK Electronics AG, Munich, Germany
[3] Department of CAP T, TDK Electronics Components S.A.U., Málaga, Spain
[4] Department of Inorganic Chemistry, University of Málaga, Spain,
[*] azahara.albendiz@tdk-electronics.tdk.com

Abstract

Power electronic industry is progressively demanding that film capacitors encapsulated with polymeric materials operate under extremely humid conditions with stable capacitance values. Furthermore, during operation, the devices are submitted to thermal stress due to rapid changes of temperature, leading to a mechanical loss of adhesion between the box and the casting resin and/or between the encapsulating material and the metallic wires. This thermal cycling may also lead to cracks by the break of bonds, creating paths to the direct penetration of water vapor inside the device. This generates the migration of moisture to the winding [1]. The electrodes in metallized film capacitors are comprised of very thin layers of metal, usually zinc or aluminum, evaporated onto the surface of a polymeric film. This metallized film is wound in a winding and contacted by a metal sprayed onto the lateral, usually denominated schoop (*Figure 1*).
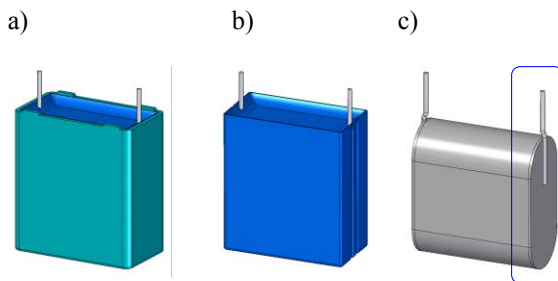
a)   b)   c)

Figure 1. A 2-pin version of a metallized film capacitor encapsulated with resin and box (a), only with resin(b) and a winding with sprayed schoops.

Electrochemical corrosion in metallized film capacitors encapsulated with polymeric materials is one of the most common mechanisms of failure due to the moisture penetration inside the device. A drop in the capacitance and an increasing of the loss factor of the capacitor is found when the corrosion of the electrode is started [1]. The scope of this study is to improve the performance of film capacitor in long endurance test at 85ºC and 85% of relative humidity (%RH) by a good behavior of schoop as additional humidity barrier. For this purpose, two different schoop materials (zinc, Zn, and tin/copper with 3% of copper, SnCu3) were characterized. Porosity by N2 adsorption isotherms, roughness by mechanical profilometry, grain interfaces and distribution by scanning electron microscopy (SEM) (*Figure 2*), water vapor transmission rate (WVTR) and corrosion resistance by electrochemical impedance spectroscopy

(EIS) were determined in the material characterization. Metallized film capacitor sprayed with schoops of those compositions (100%Zn of a defined thickness and a schoop with the same final thickness but in a double layer configuration of Zn and SnCu3) were submitted to the long endurance test at 85ºC, 85%RH and 305 Vrms with intermediate thermal cycles to simulate a representative thermal stress during operation.

A good correspondence between the results on material characterization and the behavior of metallized film capacitor under humidity has been stablished. The failure mechanisms controlling the corrosion process on every metal spray metallization are defined.

Schoop made of Zn with a second layer of SnCu3 shows the best behavior as barrier against humidity according to the results on material characterizations and temperature/humidity/bias test on film capacitors.
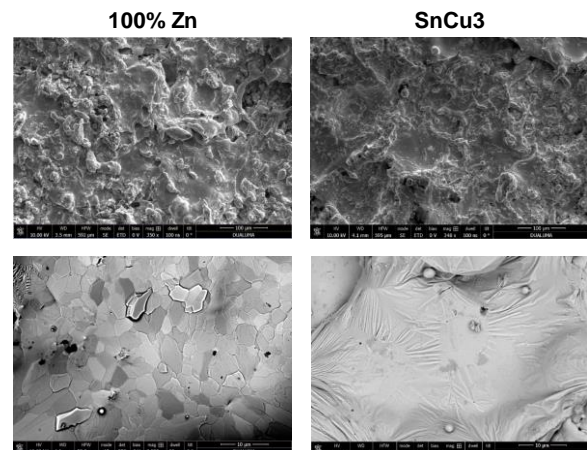
100% Zn   **SnCu3**

Figure 2. SEM Micrographs of 100%Zn schoop (left)& SnCu3 (right)

References

[1] D.F. Taylor, *IEEE Transactions on Electrical Insulation*, **1984**, *19*, 288-293

[2] S.P. Sim, R.W.Lawson, *Reliability Physics Symposium*, **1979**, *17th Annual*, 103-112

[3] R. Brown. *Trans. Device Mater. Reliab*. 6 (2) (2006) 326-333.

[4] Evgenij Barsoukov , J. Ross Macdonald, *Impedance Spectroscopy: Theory, Experiment, and Applications*, 3rd Edition, (May 2018) ISBN: 978-1-119-07408-3, 560 pages

[5] Vadim F. Lvovich ,*Impedance Spectroscopy: Applications to Electrochemical and Dielectric Phenomena* (Jul 2012), ISBN: 978-0-470-62778-5

Studies on sprayed metal (schoopage) as humidity barrier in film capacitor

Azahara Albéndiz García [1*], Lucía Cabo[2], David Peláez Millas [3], Enrique Rodríguez Castellón [4]

[1] Department of CAP T R&D BR, TDK Electronics Components S.A.U., Málaga, Spain
[2] Department of CAP T R&D BR, TDK Electronics AG, Munich, Germany
[3] Department of CAP T, TDK Electronics Components S.A.U., Málaga, Spain
[4] Department of Inorganic Chemistry, University of Málaga, Spain,
[*] azahara.albendiz@tdk-electronics.tdk.com

Abstract

Electrochemical corrosion in metallized film capacitors encapsulated with polymeric materials is one of the most common mechanisms of failure due to the moisture penetration inside the device. A drop in the capacitance and an increasing of the loss factor of the capacitor is found when the corrosion of the electrode is started [1].

The scope of this study is to improve the performance of film capacitor in long endurance test at 85ºC and 85% of relative humidity (%RH) by a good behavior of the metal sprayed onto the lateral of the winding, usually denominated schoop (*Figure 1*), as additional humidity barrier.
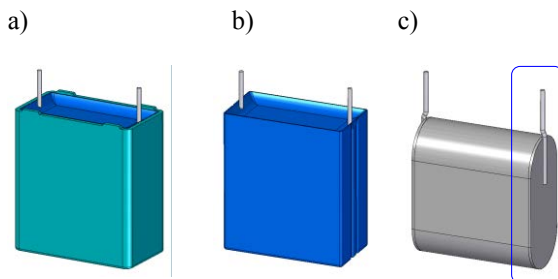
Figure 1. A 2-pin version of a metallized film capacitor encapsulated with resin and box (a), only with resin(b) and a winding with sprayed schoops.

For this purpose, two different schoop materials (zinc, Zn, and tin/copper with 3% of copper, SnCu3) were characterized. Porosity by N2 adsorption isotherms, roughness by mechanical profilemetry, grain interfaces and distribution by scanning electron microscopy (SEM) (*Figure 2*), water vapor transmission rate (WVTR) and corrosion resistance by electrochemical impedance spectroscopy (EIS) were determined in the material characterization.

A good correspondence between the results on material characterization and the behavior of metallized film capacitor under humidity has been stablished. The failure mechanisms controlling the corrosion process on every metal spray metallization are defined.

Schoop made of Zn with a second layer of SnCu3 shows the best behavior as barrier against humidity according to the results on material characterizations and temperature/humidity/bias test on film capacitors.
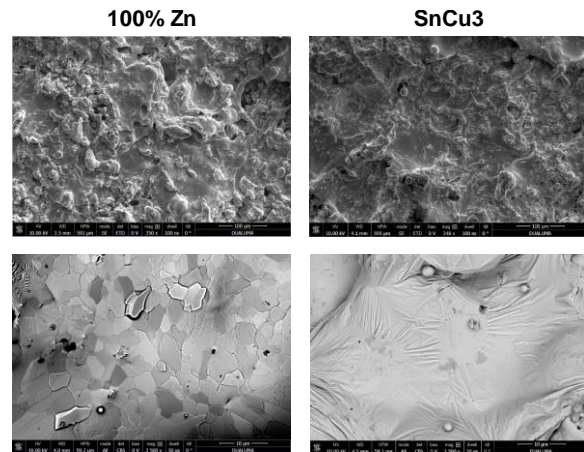
100% Zn **SnCu3**

Figure 2. SEM Micrographs of 100%Zn schoop (left)& SnCu3 (right)

References

[1] D.F. Taylor, *IEEE Transactions on Electrical Insulation*, **1984**, *19*, 288-293

[2] S.P. Sim, R.W.Lawson, *Reliability Physics Symposium*, **1979**, *17th Annual*, 103-112

[3] R. Brown. *Trans. Device Mater. Reliab*. 6 (2) (2006) 326-333.

[4] Evgenij Barsoukov , J. Ross Macdonald, *Impedance Spectroscopy: Theory, Experiment, and Applications*, 3rd Edition, (May 2018) ISBN: 978-1-119-07408-3, 560 pages

[5] Vadim F. Lvovich ,*Impedance Spectroscopy: Applications to Electrochemical and Dielectric Phenomena* (Jul 2012), ISBN: 978-0-470-62778-5

Oral Title: Studies on sprayed metal as humidity barrier in film capacitor

Brief summary: Electrochemical corrosion in metallized film capacitors is one of the most common mechanisms of failure due to the moisture. To improve the performance of film capacitor by a good behavior of the sprayed metal (schoop) as additional humidity barrier will be investigated by material characterizations (SEM, WVTR, EIS, etc.) and Temperature Humidity and Bias tests on film capacitors.

2

ANNEX D.
Impedance diagrams (EIS)

Comparison of impedance (EIS) diagrams of schoops at fixed immersion times

Immersion time zero, 0h (reference)

In Figure 7.1., the impedance (EIS) diagrams of schoop samples at the beginning of the immersion test are compared. These diagrams are part of a wider study were the thesis is enclosed. The schoop samples are codified as follows:

- Al 100%. Sprayed schoop in a single layer made of 100% aluminium.

- SnCu3. One of the thesis samples. Sprayed schoop with a single layer made of tin (97% weight) and copper (3% weight)

- SnZn50. Sprayed schoop in a single layer made of tin and zinc at 50% weight.

- Zn. One of the thesis samples. Sprayed schoop in a single layer made of 100% zinc.

- ZnAl15. One of the thesis samples. Sprayed schoop in a single layer made of 15% aluminium in weight.

The Bode's diagrams should be compared to frequencies higher than 100 mHz because for lowers values not all the schoop samples were stable during the measurements. The noises appreciated in the impedance diagrams of schoop made of 100%Al and SnZn50 at the lowest frequencies at the beginning of the test are due to the samples are not reaching a stable equilibrium potential.

However, at 100 mHz or higher frequencies, a meaningful information can be obtained due to the measurements in this range are very quick and a comparison can be established:

- At 100 mHz the impedance module of 100%Al and SnCu3 is one order of magnitude higher than the shown by 100%Zn, SnZn50 and/or ZnAl15.

- In concordance with Bode diagrams, to be able to observe the complete Nyquist plot in schoops made of 100%Al and SnCu3, to use a scale of one order of magnitude higher than the other schoops was required.
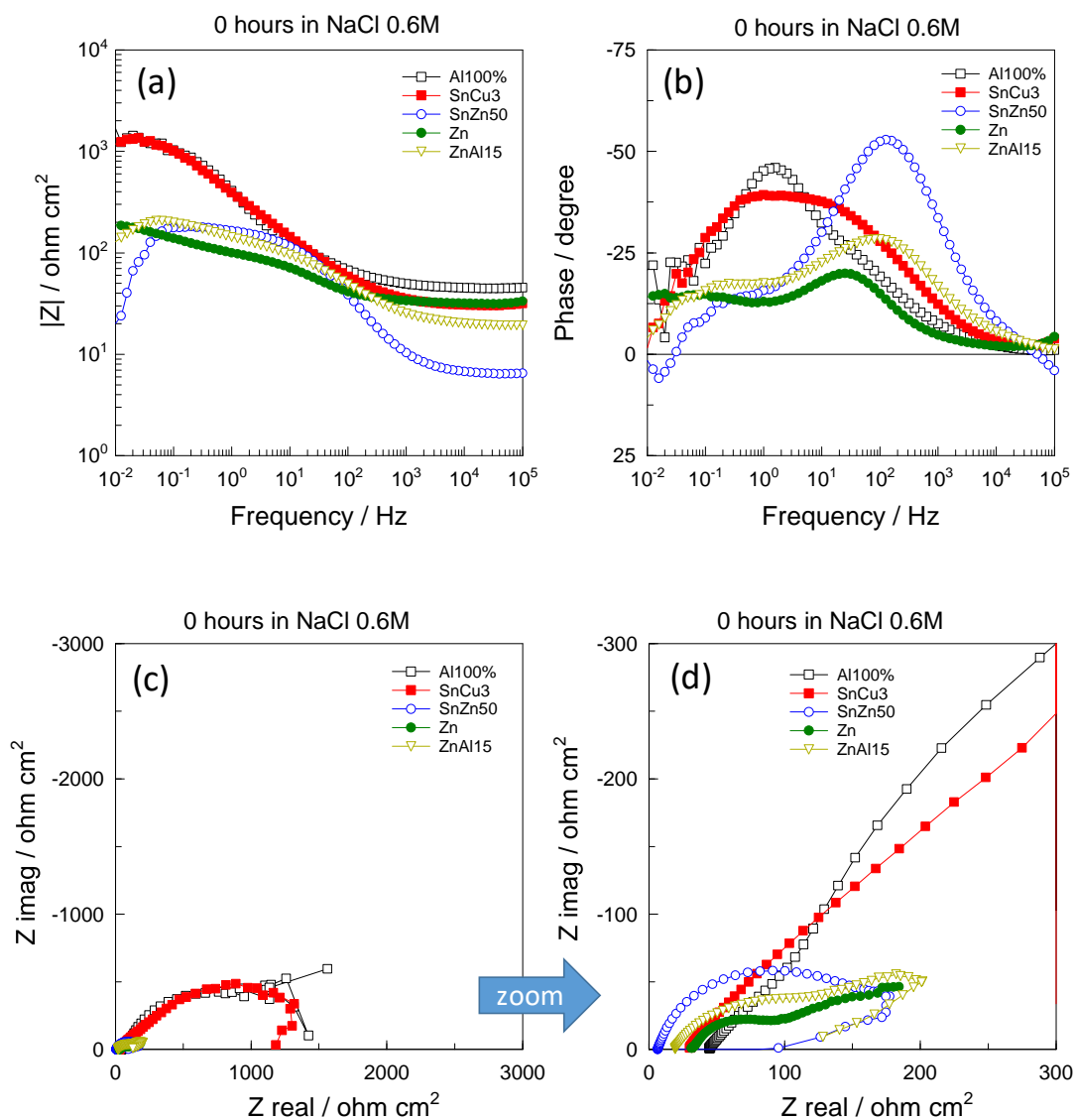
Figure 7.1.Comparison of Bode's and Nyquist's diagrams obtained for every schoop at time 0h of immersion in NaCl 0,6M.

Frequency domain of the Nyquist's diagrams: 100 kHz-10mHz.

Immersion time 1h/1.5h (aqueous electrolyte NaCl 0.6M)

In Figure 7.2., the impedance (EIS) diagrams of the five schoop samples after 1h (SnCu3 and 100%Zn) and 1.5h (Al100%, ZnAl15 and SnZn50) of immersion are compared.

This difference in immersion time is due to be for every case the minimum time required for registering the complete impedance spectrum in the defined frequency scan (10^5 Hz and 10^{-2} Hz). The schoop made of 100%Al was only possible to be measured after 90min of immersion due to the intrinsic properties of the material. Nevertheless, the samples compared after 1h of immersion showed very stable behaviour between 1h and 2h of inmersion. This is the reason to be considered a good approach this comparison although all the samples were not measured at the same immersion time.

.
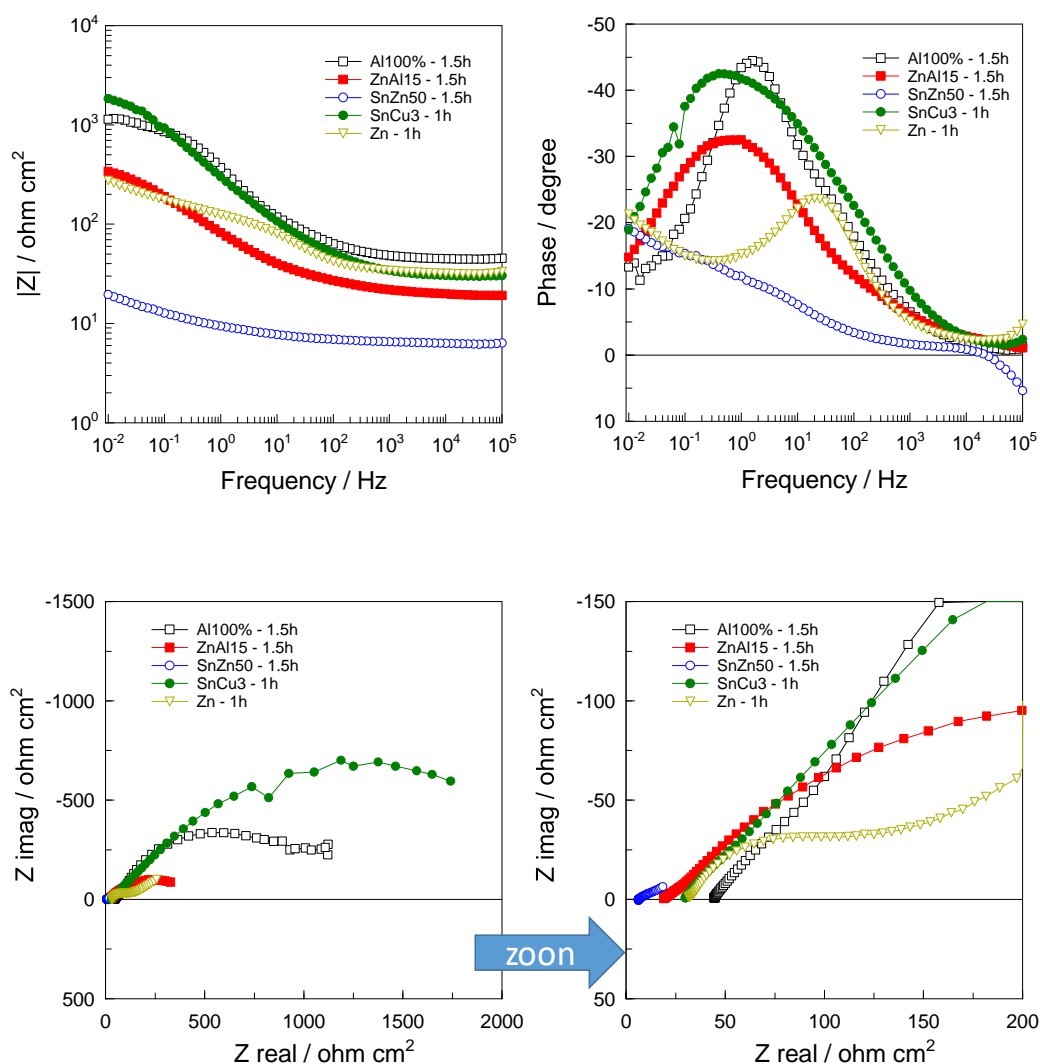
Figure 7.2. Comparison of Bode's and Nyquist's diagrams obtained for every schoop at time 1h (SnCu3 & 100%Zn) and 1,5h (Al100%, ZnAl15 & SnZn50) of immersion in NaCl 0,6M.

Frequency domain of the Nyquist's diagrams: 100 kHz-1 mHz.

The 100%Al schoop presents low grain compactness; this is not allowing the retention of the electrolyte in the electrochemical cell and being kept in only one face. The electrolyte is diffusing quickly over the schoop sample, filtering the electrolyte to the back side of the sample before reaching 3h of immersion.

After 60-90 min of immersion, the impedance module of schoop made of 100%Al and SnCu3 are one order of magnitude higher than ZnAl15 and 100%Zn and two orders of magnitude higher than SnZn50. Nyquist diagrams show same result. This is showing that corrosion resistances of 100%Al and SnCu3 at short inmersion times are much higher than the one presented by the other schoops. SnZn50 is the weakest schoop sensitive to be corroded at short immersion periods.

Immersion time 3h (aqueous electrolyte NaCl 0.6M)

In Figure 7.3., the impedance (EIS) diagrams of four of the five schoop samples after 3h of immersion are compared, due to the described intrinsic limitations of schoop made of 100% Al.

After 3h of immersion, the schoop made of SnCu3 showed the highest impedance module at low frequency (10 mHz), this is one order of magnitude higher than schoop made of 100%Zn and ZnAl15, presenting those alloys additionally an impedance module one order of magnitude higher than SnZn50.

With the visual inspection of these curves, a classification for short periods of immersion can be established, being SnCu3 the most stable alloy and SnZn50 the most sensitive to suffer corrosion.
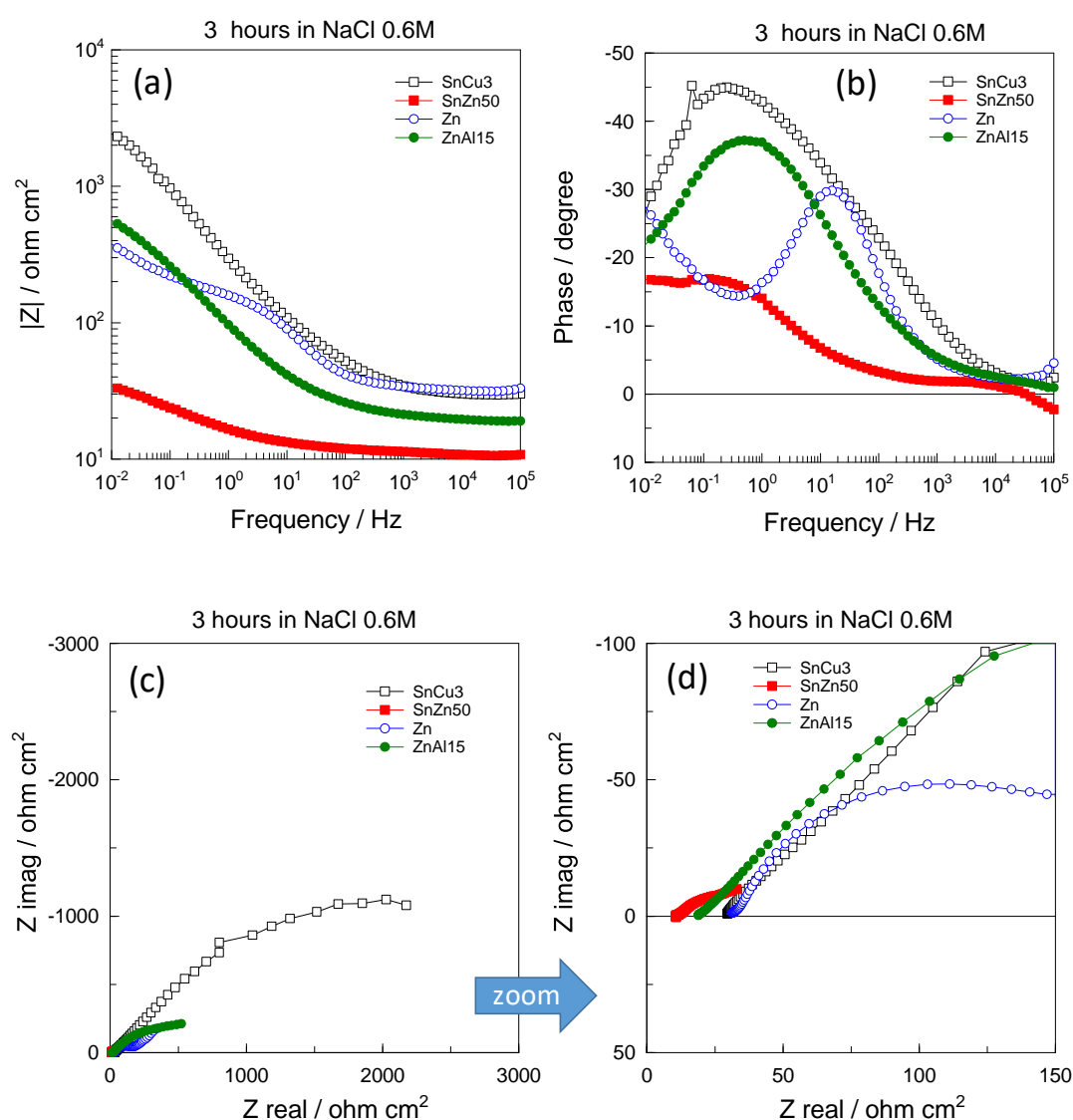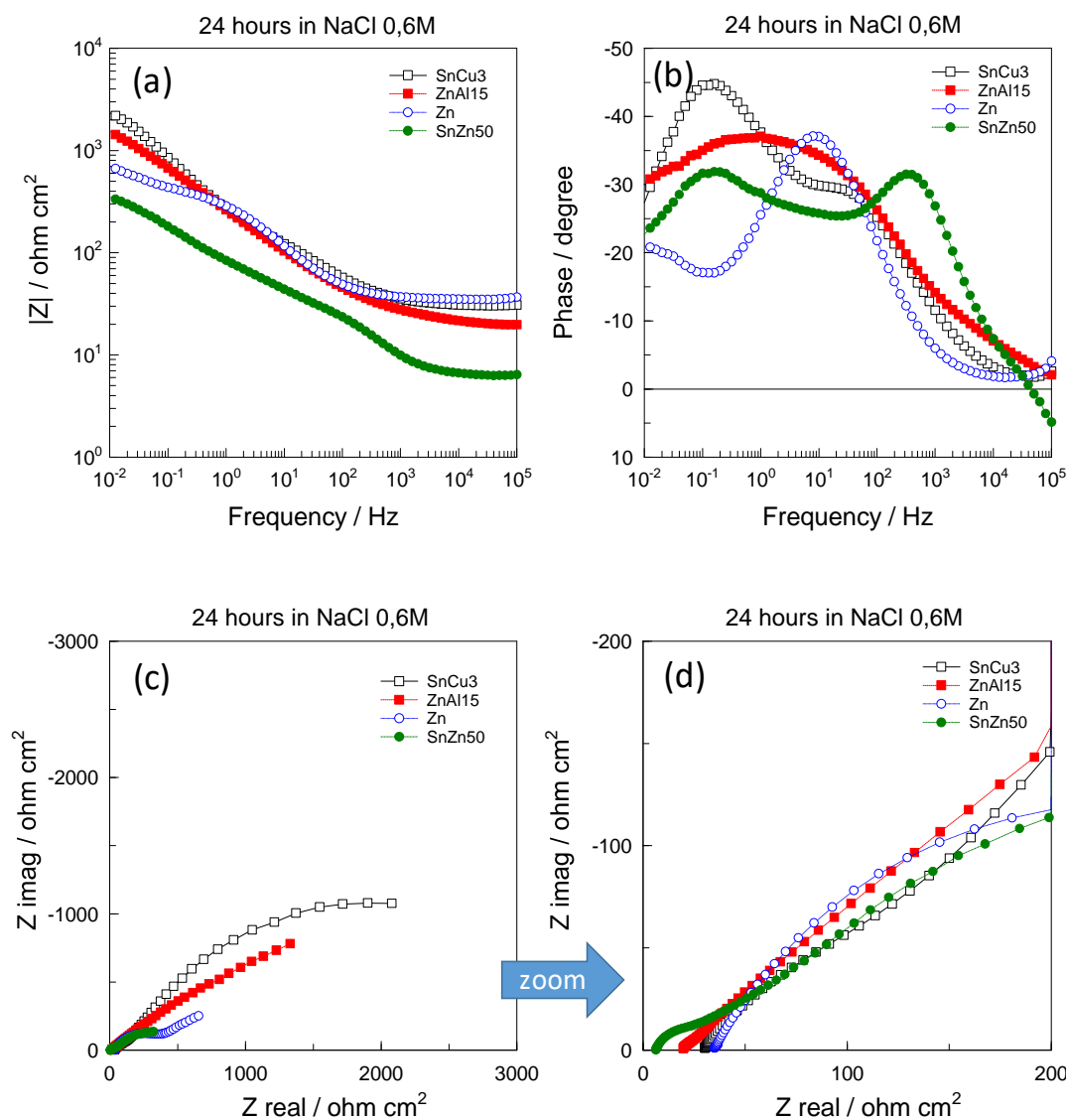

Figure 7.3. Comparison of Bode's and Nyquist's diagrams obtained for every schoop at time 3h of immersion in NaCl 0.6M.

Frequency domain of the Nyquist's diagrams: 100 kHz-10 mHz.

Immersion time 24h (aqueous electrolyte NaCl 0.6M)

In Figure 7.4., the impedance (EIS) diagrams of four of the five schoop samples after 24h of immersion are compared, due to the described intrinsic limitations of schoop made of 100% Al.

In Bode's diagrams plotted in Figure 4 can be observed that SnCu3 and ZnAl15 schoops present a impedance module one order of magnitude higher than the schoop made of SnZn50 in all the scanned frequency domain, being the schoop made of 100%Zn in an intermediate situation. This is associated to a higher corrosion resistance by ZnAl15 and SnCu3 schoops after 24h of immersion in electrolyte NaCl 0,6M.

Figure 7.4.Comparison of Bode's and Nyquist's diagrams obtained for 4/5 schoops at time 24h of immersion in NaCl 0.6M.

Frequency domain of the Nyquist's diagrams: 100 kHz-10mHz.

Figure 7.5. shows an interesting observation, the impedance values achieved by ZnAl15 after 24h of immersion are much higher than the ones presented after short immersion periods.

Qualitatively it can be analyzed that:

- For long immersion times. Schoops made of ZnAl15, 100% Zn and SnZn50 increase slightly the corrosion resistance with the immersion time; however, this is significantly greater in ZnAl15 schoop. (Annexes 1, 4 &5).

- SnCu3 schoop is the variant with highest stability during all the tested immersion period.(Annex 2)

- Bell-shaped curves observed in Bode's diagrams with two well defined maximum points (as in SnZn50, SnCu30 or 100% Zn schoops after 24h of immersion) or a sweeping curve are showing a corrosion with several electrochemical processes.(Figure 7.1.).
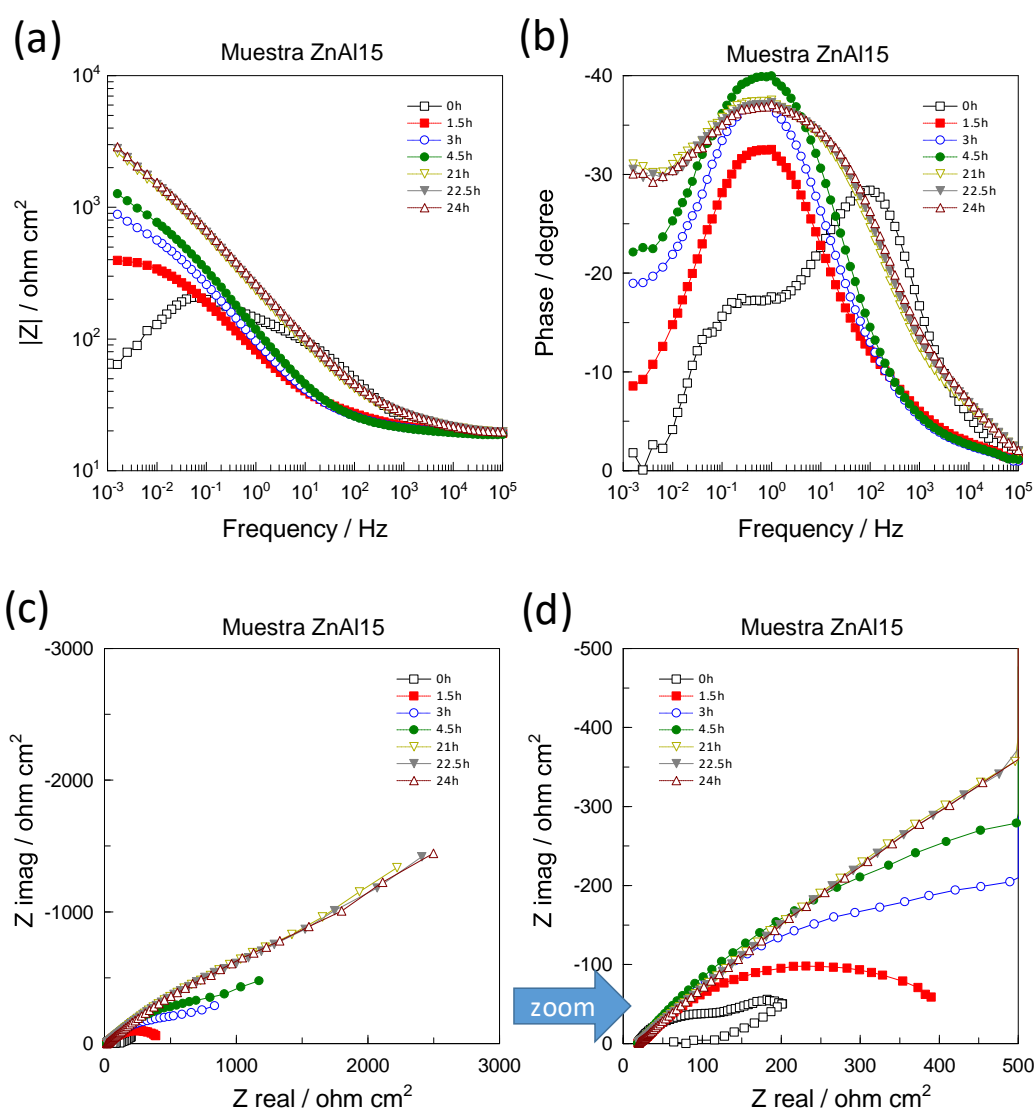
Figure 7.5. Evolution of Bode and Nyquist diagrams during immersion tests of ZnAl15 schoop sample. Electrolyte: NaCl 0.6M

100% Zinc schoop
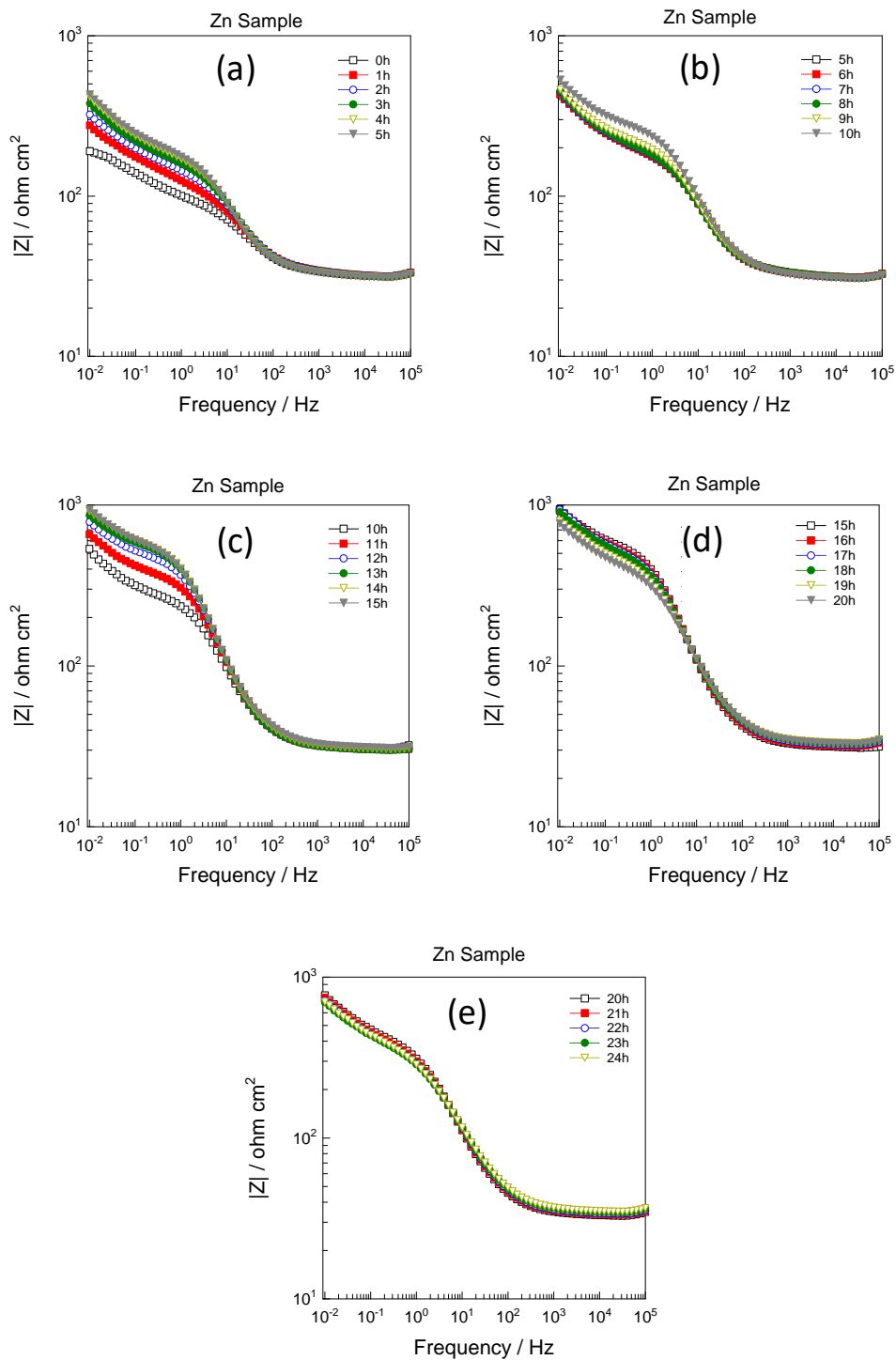
Bode diagram. Impedance module vs frequency during 24h of immersion in aqueous solution of NaCl 0,6M.
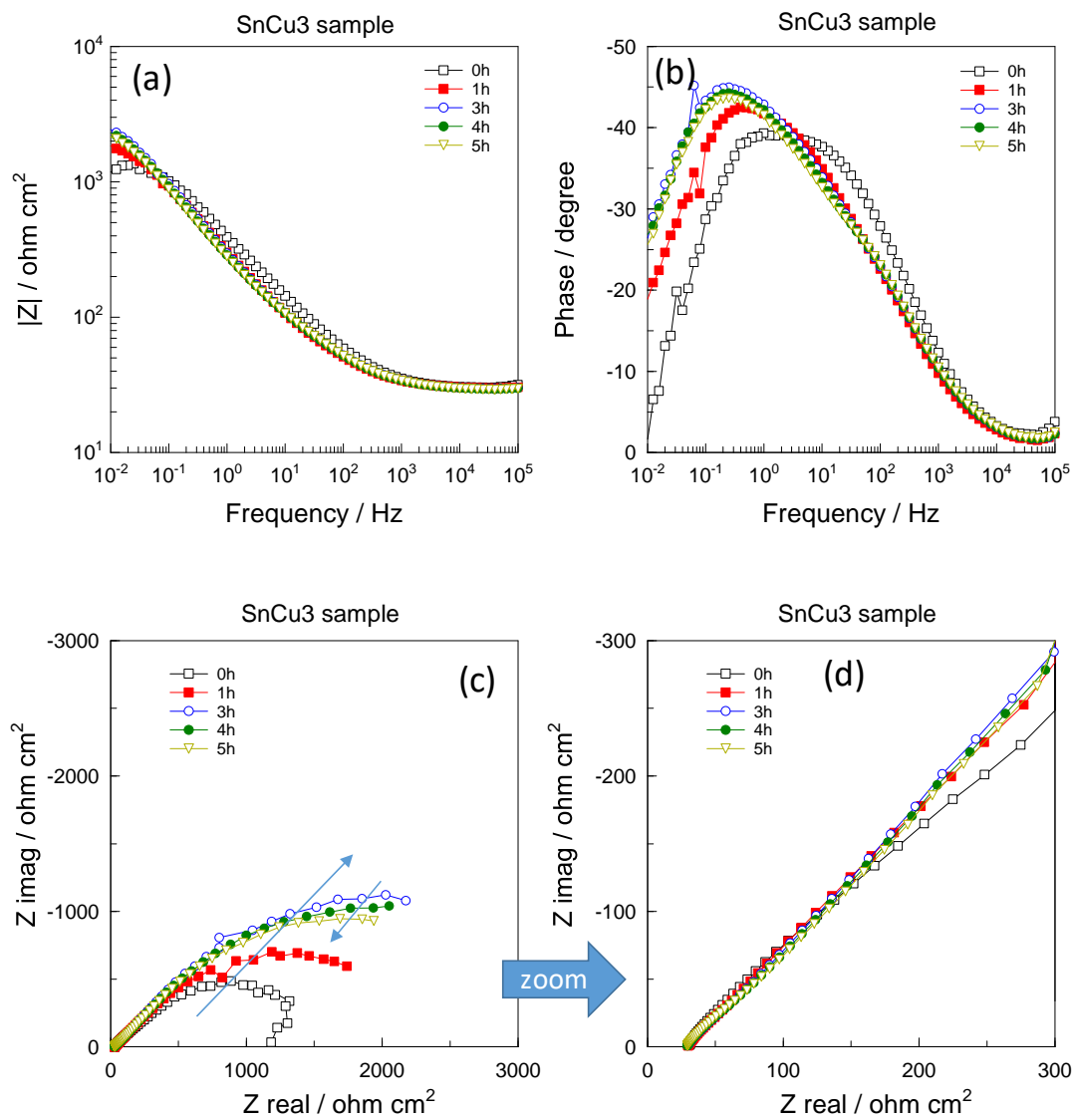
.
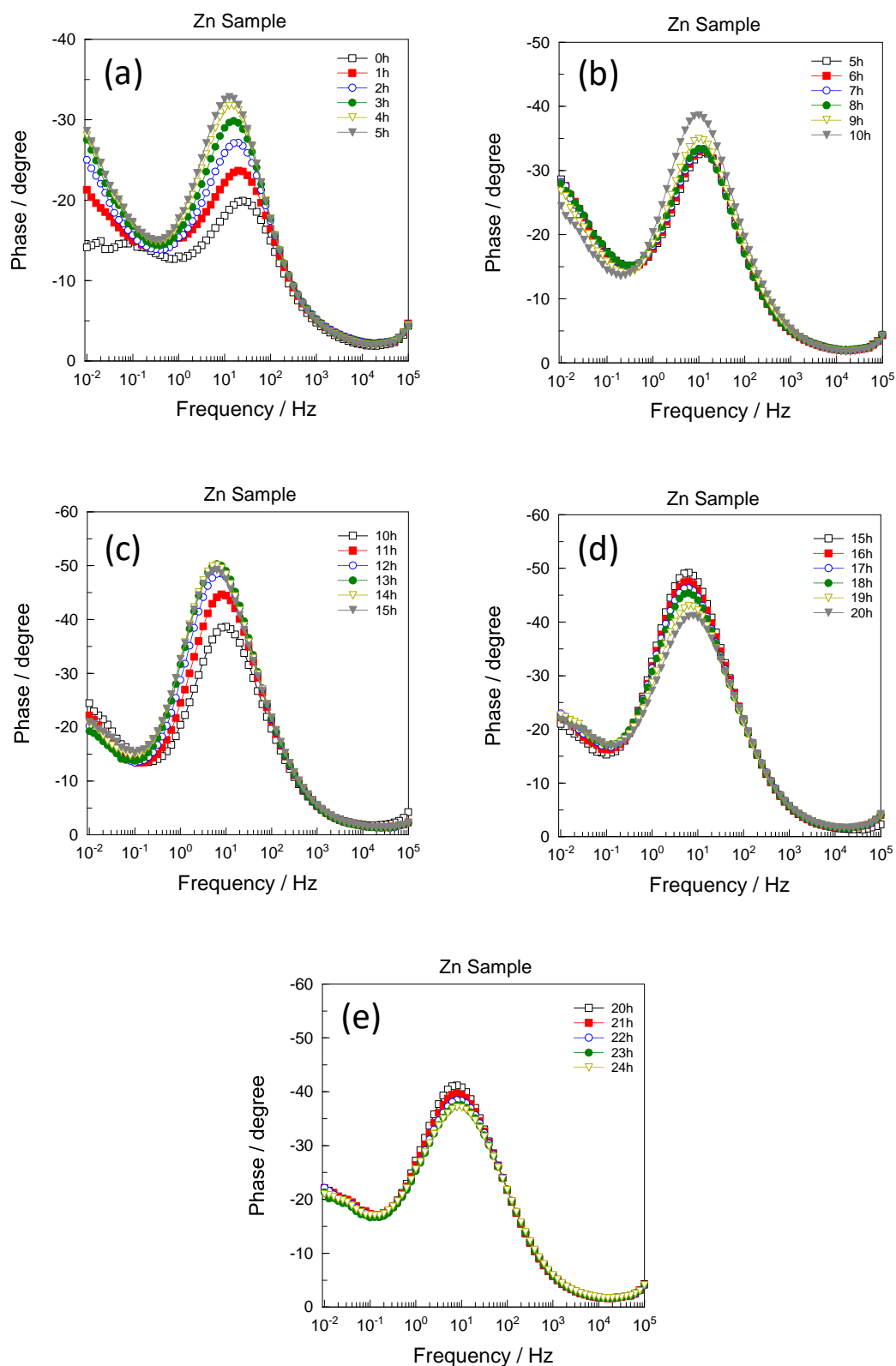
Bode diagram. Phase angle vs frequency during 24h of immersion in aqueous solution of NaCl 0,6M.
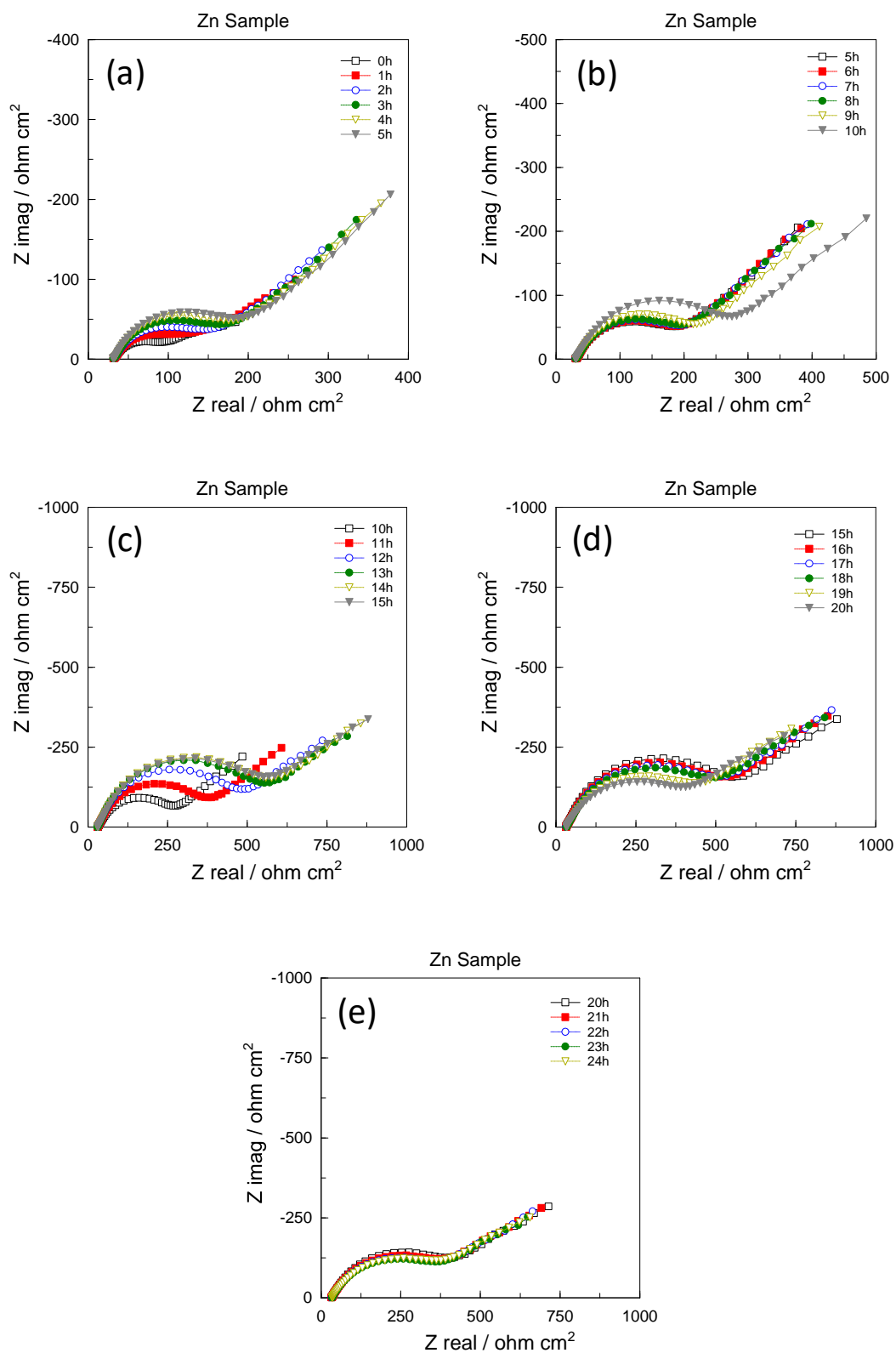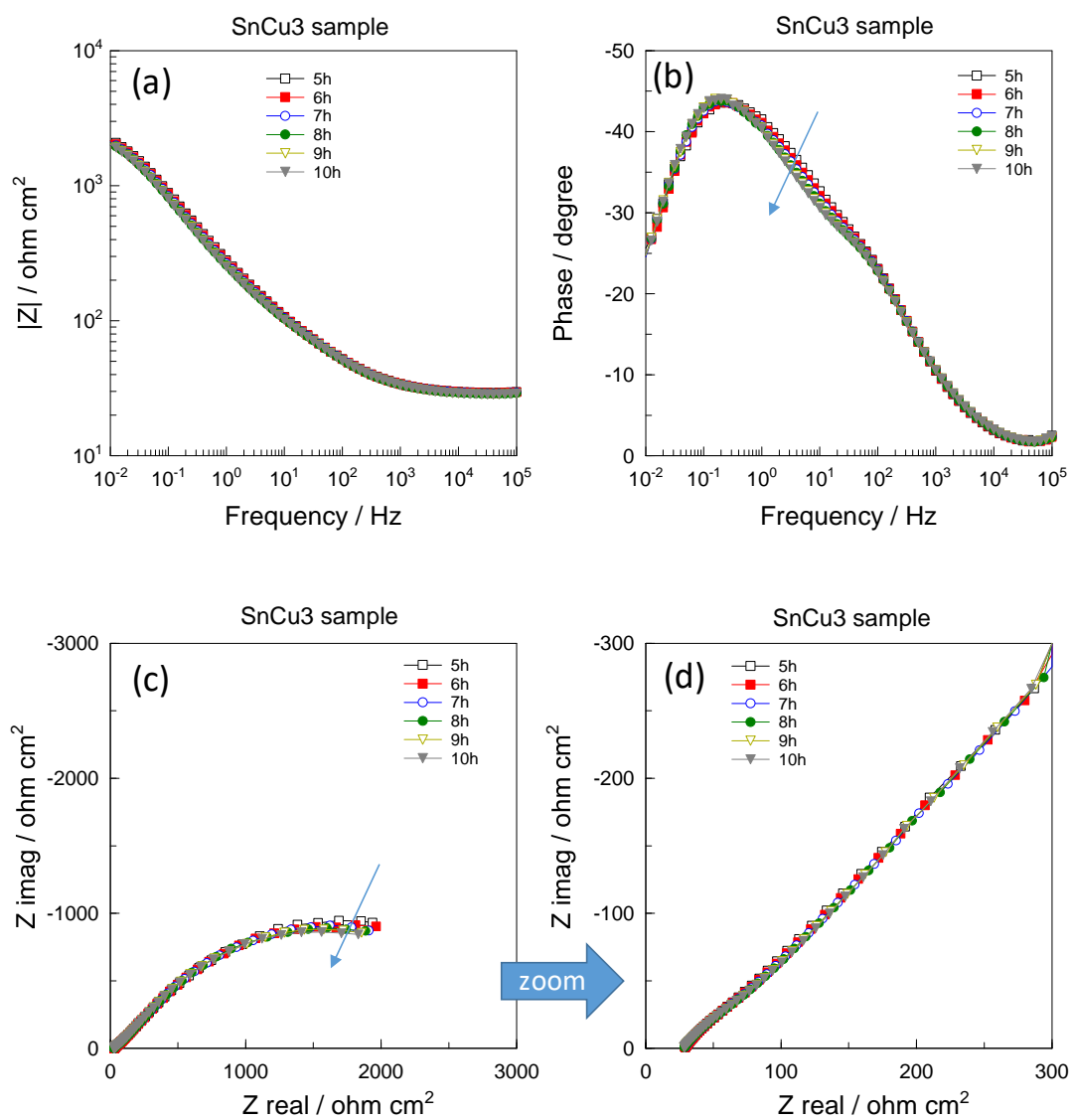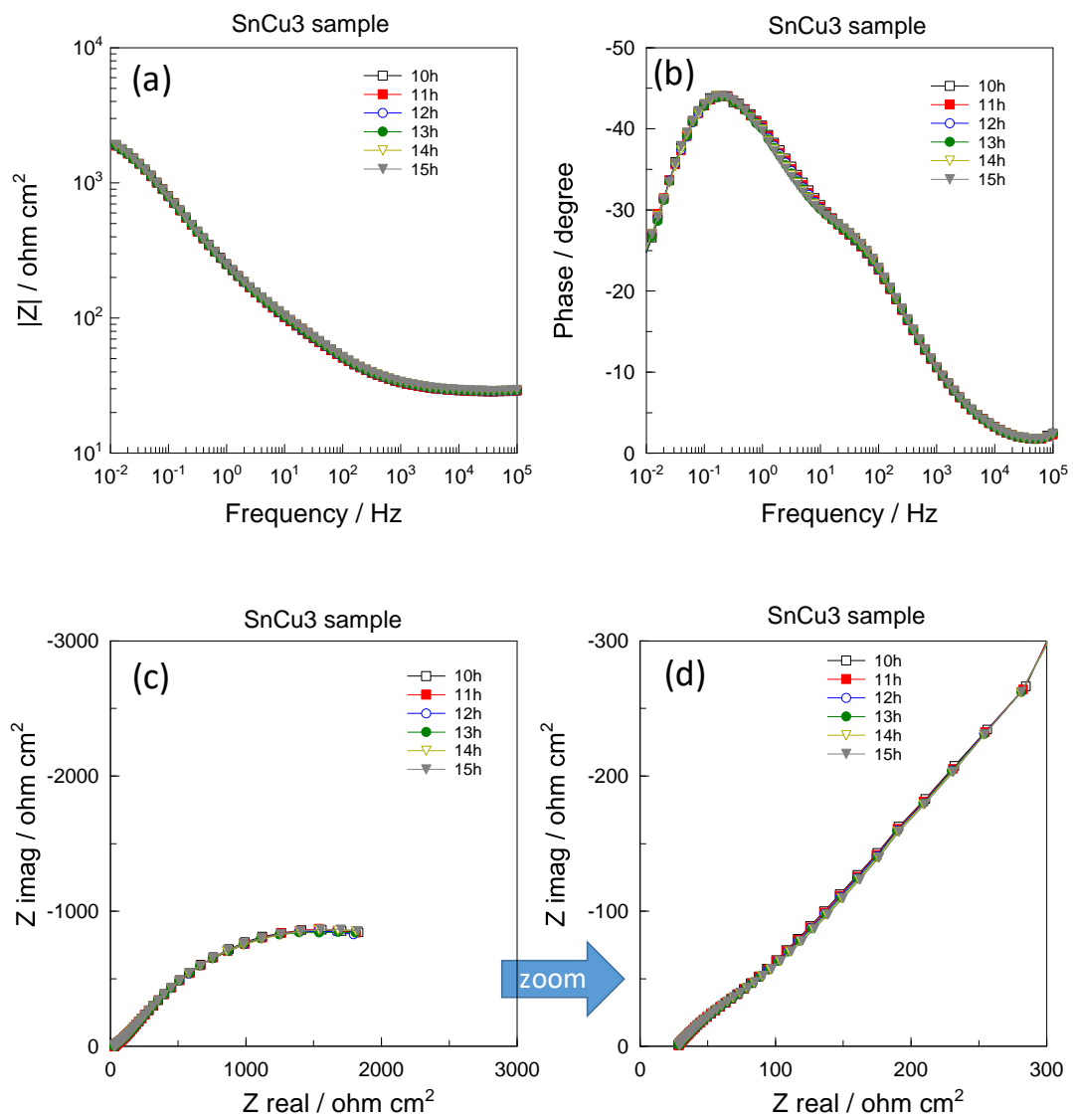
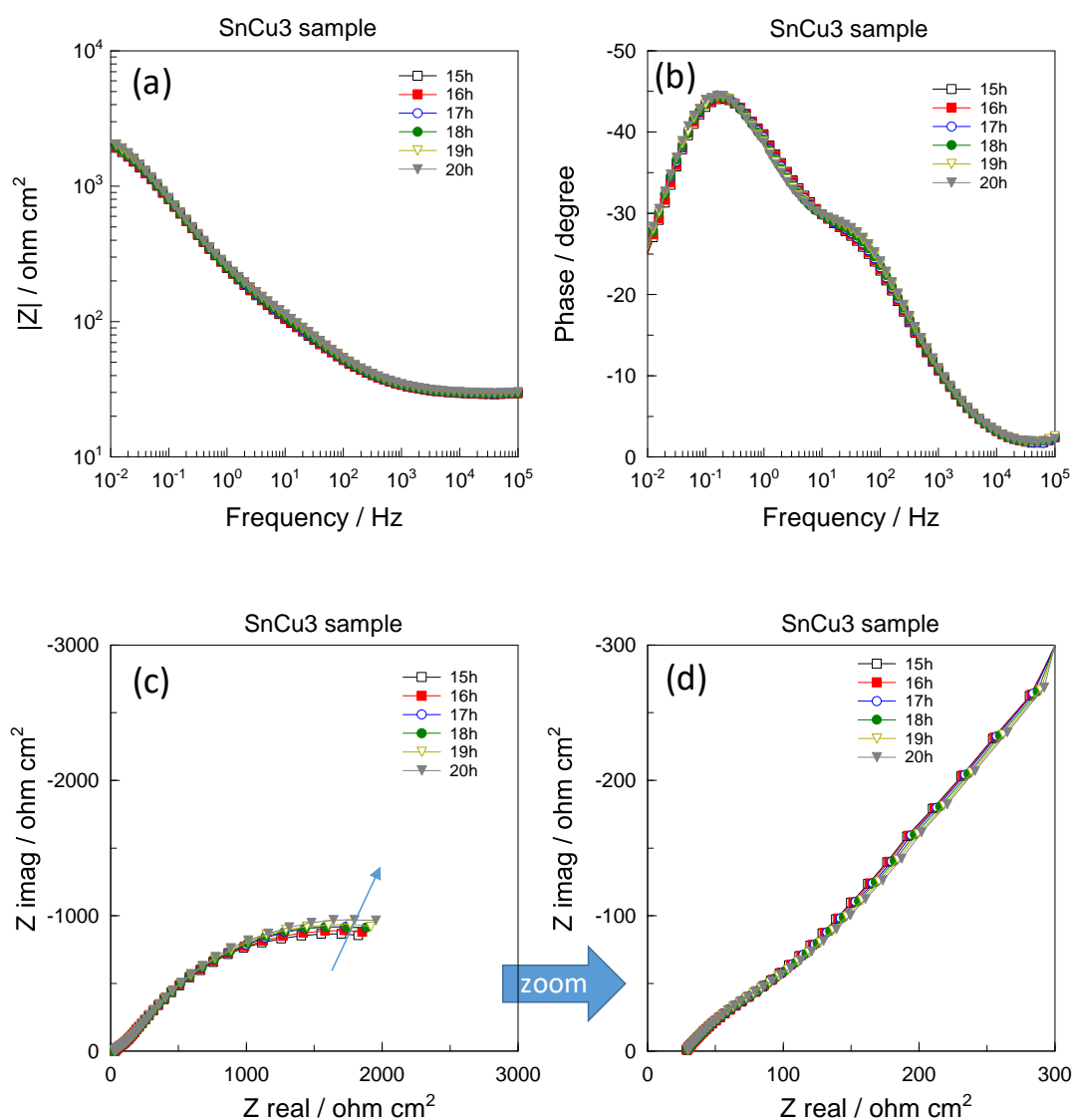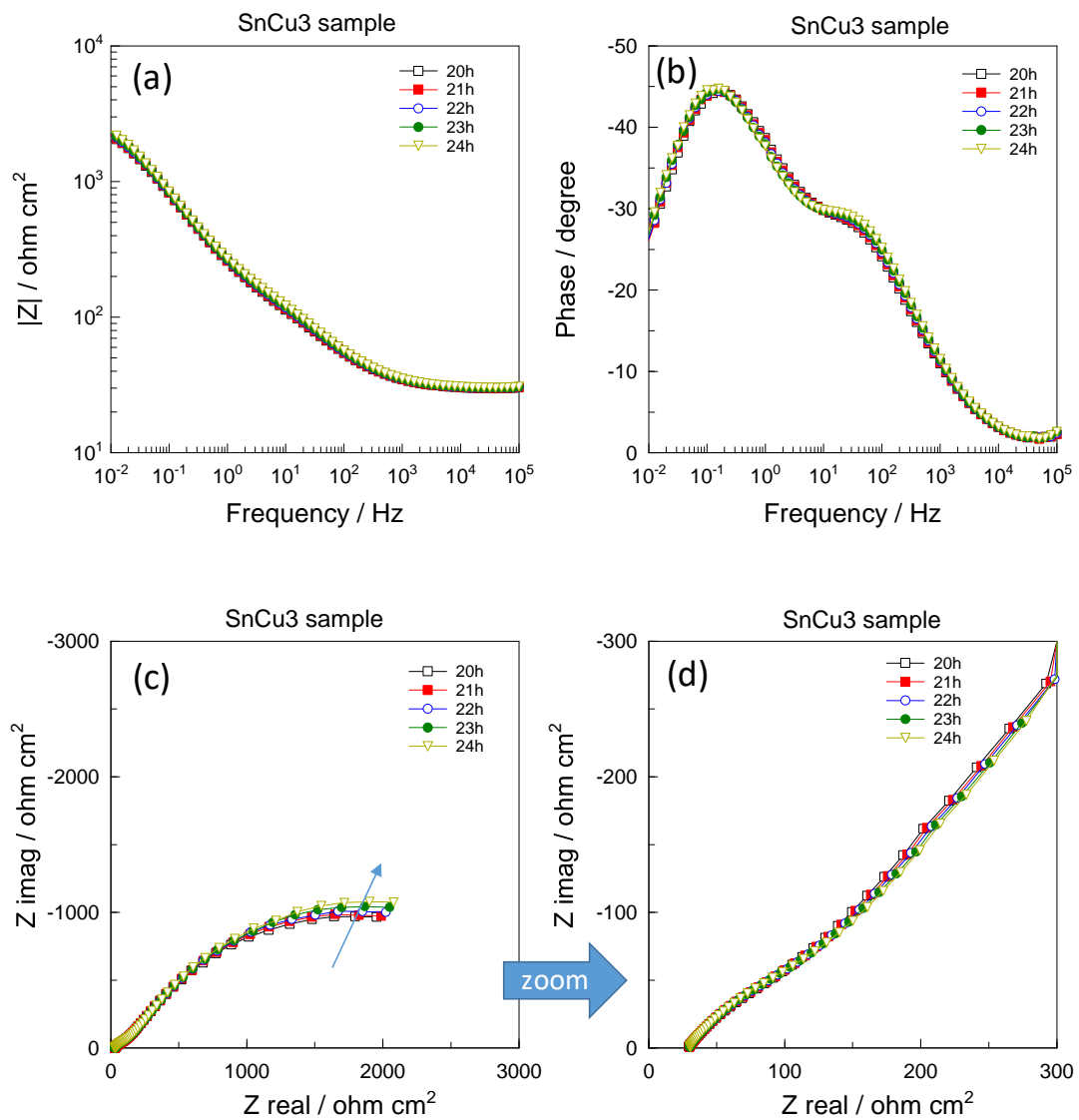*Nyquist diagram. 24h of immersion in aqueous solution of NaCl 0,6M.*

SnCu3 schoop

Evolution of Bode and Nyquist diagrams during 24h of immersion in aqueous solution of NaCl 0.6M.

ZnAl15 schoop

Evolution of Bode and Nyquist diagrams during 24h of immersion in aqueous solution of NaCl 0.6M.